A DATA-ESTIMATION-BASED APPROACH FOR QUASI-CONTINUOUS SEISMIC RESERVOIR MONITORING

A DISSERTATION
SUBMITTED TO THE DEPARTMENT OF GEOPHYSICS
AND THE COMMITTEE ON GRADUATE STUDIES
OF STANFORD UNIVERSITY
IN PARTIAL FULFILLMENT OF THE REQUIREMENTS
FOR THE DEGREE OF
DOCTOR OF PHILOSOPHY

Adeyemi Arogunmati
March 2011

I certify that I have read this dissertation and that, in my opinion, it is fully adequate in scope and quality as a dissertation for the degree of Doctor of Philosophy.

Jerry M. Harris
(Principal Adviser)

I certify that I have read this dissertation and that, in my opinion, it is fully adequate in scope and quality as a dissertation for the degree of Doctor of Philosophy.

Mark Zoback

I certify that I have read this dissertation and that, in my opinion, it is fully adequate in scope and quality as a dissertation for the degree of Doctor of Philosophy.

Franklin M. Orr, Jr.

I certify that I have read this dissertation and that, in my opinion, it is fully adequate in scope and quality as a dissertation for the degree of Doctor of Philosophy.

Tapan Mukerji

I certify that I have read this dissertation and that, in my opinion, it is fully adequate in scope and quality as a dissertation for the degree of Doctor of Philosophy.

Robert Clapp

Approved for the University Committee on Graduate Studies.

Abstract

Current strategies and logistics for seismic data acquisition impose restrictions on the calendar-time temporal resolution obtainable for a given time-lapse monitoring program. One factor that restricts the implementation of a quasi-continuous monitoring program using conventional strategies is the time it takes to acquire a complete survey. Here quasi-continuous monitoring describes the process of reservoir monitoring at short time intervals. This dissertation describes an approach that circumvents the restriction by requiring only a subset of a complete survey data each time an image of the reservoir is needed. Ideally, the time interval between survey subset acquisitions should be short so that changes in the reservoir properties are small. The accumulated data acquired are used to estimate the unavailable data at the monitoring time step, and the combined known and estimated data are used to produce an image of the subsurface for monitoring.

Quasi-continuous seismic monitoring can be used to monitor geologic reservoirs during the injection phase of a CO_2 sequestration project. It can also be used to monitor reservoir changes between injector and producer wells during the secondary recovery phase in an oil field. The primary advantage of a quasi-continuous monitoring strategy over the conventional strategy is the high temporal resolution of the reservoir changes obtainable. Naturally, the spatial resolution of the image obtained using a subset of the data from a full survey will be worse than the spatial resolution of the image obtained using the complete data from a full survey. However, if the unavailable data are estimated perfectly, the spatial resolution is not lost. The choice of estimation algorithm and the size of the known data play an important role in the success of the approach presented in this dissertation.

First, I demonstrate the practicability of my approach using synthetic and field surveys. Second, I demonstrate its efficiency with crosswell traveltime data, and full-trace surface-seismic data. For the crosswell traveltime data demonstration, I show, with synthetic and field data, how quasi-continuous reconstructions of the reservoir velocity model can be obtained. I use prediction-error filters (PEFs) in estimating unavailable seismic traveltimes. For the surface-seismic data demonstration, I show how quasi-continuous migrated images can be obtained from partial survey data. I use minimum-weighted-norm interpolation (MWNI) to estimate unavailable seismic traces.

Acknowledgements

First and foremost, I would like to thank my family for their financial and moral support that has helped me go through my many years as a student. I particularly would like to thank them for their emotional support which I needed in adjusting to the new environment after leaving Nigeria for graduate school in the US. I would like to thank my sister, Biola, for always being there for me and reminding me constantly that I was not on this journey alone, but that I had a family that felt everything I felt. I also thank members of my extended family, too many to list by name. They were there for me the entire time.

Many thanks to my adviser, Jerry Harris, for creating a conducive research environment at SWP lab. He was always there with exciting ideas and challenging questions that helped me think about aspects of my research that I overlooked. He was also there with suggestions on how to make my research argument stronger and how to communicate that argument to a scientific audience as well as a general audience. Finally, he always made sure I had access to the computational resources I needed to complete my PhD work.

I extend my gratitude to my thesis committee members who have been there from the start of this journey, Mark Zoback, Franklin M. Orr, Jr., Tapan Mukerji, and Robert Clapp. I appreciate their constant support and willingness to attend my annual reviews and qualifying exam. I have benefited from their numerous suggestions and recommendations on directions to take my research.

Youli Quan, research associate member of SWP has been there from my first day in the department. I appreciate the productive discussions we have had over the years. His door was always open and he was very helpful in locating SWP data and

software that have not been used in a long time. He gave me useful suggestions and recommendations regarding my research ideas and conference presentations. I would like to thank Raymond Abma for the numerous discussions we had on interpolation schemes, especially minimum weighted norm interpolation (MWNI). I worked with Raymond Abma, Richard Clarke, Olav Barkved, and Jean-Paul van Gestel during my internship at BP. With their help I was able to get the field data presented in this dissertation.

I will not forget the relationship I have built with current and past SWP students over the years. Jonathan Ajo-Franklin had graduated before I started here at Stanford. I met him during my prospective student visit at MIT and he has always been encouraging and supportive. We have had numerous conversations about research and I learned a lot from him. Chuntang Xu was in his Final year when I came in. He was always there when I needed advice on coping with the stress of being a first year student and being overly concerned about the qualifying exam. Jolene Robin McCaskill was always there to help me understand American culture. She was never out of words of encouragement and she knew who to point me toward when she could not provide direct assistance. We were officemates for one year and I remember many interesting conversations we had, both academic and non-academic.

Evan Um has been my officemate for the past three years. I have great respect for him and our friendship has grown over the years. I appreciate the calmness he brings to the group. We shared many similar adversities at the same time, and we formed a bond that allowed us to encourage each other to successfully pass through the adversities. Tieyuan Zhu is currently the youngest member of the group. I have watched him grow from a first-year grad student to a post-qualifying-exam grad student. Watching him grow has made me understand what I went through in my early years at Stanford. I appreciate the friendship we have built over the years and I appreciate the lessons I have learned from him about Chinese culture. Eduardo Santos and Bouko Vogelaar are past post-docs and Armando Sena is a current post-doc with SWP. Many thanks to them for their suggestions on how to make my research better and how to present it in such a way that it is easily understood. I

also want to thank Claudia Baroni for managing the administrative demands of the research group. She made sure paperwork for attending conferences and getting reimbursements were as easy as humanly possible.

I have made many friends over the years, at Obafemi Awolowo University, Rice University, and at Stanford University. Adeola Adeyemi, Ben Appiah, Mark Little, Dzifa Douse, Tumasang Fofang, Erion Plaku, Amarda Plaku, Priyank Jaiswal, Ravi Kumar, Ndubuisi Nebo, Nivedita Thiagarajan, Patrick Taha, Etosha Cave, Justin Brown, Jumoke Oduwole, Tunde Oduwole, Hamid Adesokan, Hui Liu, Voke Elstein, Daniel Elstein, and Eli Goldstein. The list goes on and on. I could not have asked for better friends. I have learned a lot from my friends and I appreciate their impact on my life.

Special thanks to Gboyega Ayeni, Tope Akinbehinje, Jerome Onwunalu, Chinyere Nwabugwu, Obinna Duru, Jide Kolade. These are members of my Stanford family and they have made my experience worthwhile. They are always there for me when I need them and they never let me down. I remember the parties and after-parties we have enjoyed and the enlightening discussions we have had over the years. Also special thanks to Oluyinka and Olutoyin Olutoye, and Ayowale and Ayodele Ogunye for the support they provided during my initial arrival to the US. It allowed me to settle into the new environment with ease. We have developed a good friendship over the years.

Finally, my gratitude goes to someone who has been there for me since my second quarter as a Stanford student, Patrinia Sandles. My entire Stanford experience would have been different without her. I appreciate her tolerance of my many pet peeves. She was always there to give me the emotional and spiritual support I have enjoyed on a daily basis. My special thanks go to her for being there and looking forward to the end of the PhD program with me.

Contents

List of Figures

List of Tables

Chapter 1

Introduction

1.1 Problem Overview

In the petroleum industry and in other fields of earth science, earth vibrations caused by sound wave propagation are measured. The measured signals can be processed so that it provides information about fluid properties in geologic reservoirs in the earth. If we repeat these measurements, we can observe changes in the fluid properties, provided sufficient time had elapsed between measurements. This is the idea behind time-lapse seismic monitoring.

Subsurface monitoring is needed for geologic CO_2 storage site licensing, assessing reservoir operations, assessing hazards, and monitoring subsurface fluids in a variety of applications. Time-lapse monitoring projects are designed to observe changes in a reservoir over a period of time. Traditionally, this period can vary from a few months to a few years (e.g. Landrø et al., 1999; Mathisen et al., 1995; Koster et al., 2000; Arts et al., 2004), and significant changes would have occured in the reservoir. Figure 1.1 is a synthetic example of traditional seismic time-lapse monitoring. Cost and survey time often imposes restrictions on how frequently time-lapse seismic surveys can be acquired. In some cases, particularly when monitoring subsurface reservoirs for hazard assessment, it is important to have shorter time-intervals between surveys. Short time intervals between time-lapse surveys will allow early detection of hazards. In this dissertation, I propose a method that

makes monitoring at short time intervals, or quasi-continuous seismic monitoring, practical. I define *quasi-continuous* monitoring as reservoir monitoring at a rate consistent with the changes in the reservoir.

The time interval between consecutive time-lapse surveys in quasi-continuous monitoring is significantly shorter than that in conventional monitoring. This time interval is on the order of a few days to a few months. The quasi-continuous reservoir monitoring approach I present in this dissertation targets monitoring projects where a good knowledge of the temporal changes in the physical properties of a reservoir is important. These projects include monitoring reservoirs with structural stability problems, geologic reservoirs used in storing CO_2, and reservoirs where management decisions have to be made as the project proceeds. My approach uses data-estimation-based quasi-continuous seismic reservoir monitoring to take advantage of the small changes expected to occur in a reservoir over a short time period.

Seismic imaging has played a large part in subsurface monitoring projects, especially in petroleum exploration (e.g. Harris et al., 1995; Rickett and Lumley, 2001). This is partly because seismic signals can penetrate to the typical burial depth of reservoirs in virtually any geologic setting to capture the changes that occur in reservoir rock properties (Wynn, 2003), and partly because seismic data processing theory is well developed and understood (see Yilmaz, 1987, 2001). In seismic time-lapse reservoir studies, changes in reflection amplitudes are used to determine the physical changes that have occurred in a reservoir (e.g. Burkhart et al., 2000; Arts et al., 2004). The use of seismic imaging and inversion in time-lapse monitoring takes advantage of the changes in the seismic properties of the reservoir rock during the time interval under consideration.

The use of dedicated ocean-bottom cables (OBCs) in time-lapse reservoir monitoring has increased in recent years, e.g. at the Valhall Field (Barkved et al., 2005), Clair Field (Foster et al., 2008), and the Chirag-Azeri Fields (Foster et al., 2008). The ability to use embedded receivers makes the proposed quasi-continuous monitoring approach even more appealing by eliminating the cost of repeated receiver deployment. Oil fields with embedded instrumentation are called instrumented oil fields (e.g. Ebrom et al., 2000; Hottman and Curtis, 2001; Maxwell and Urbancic,

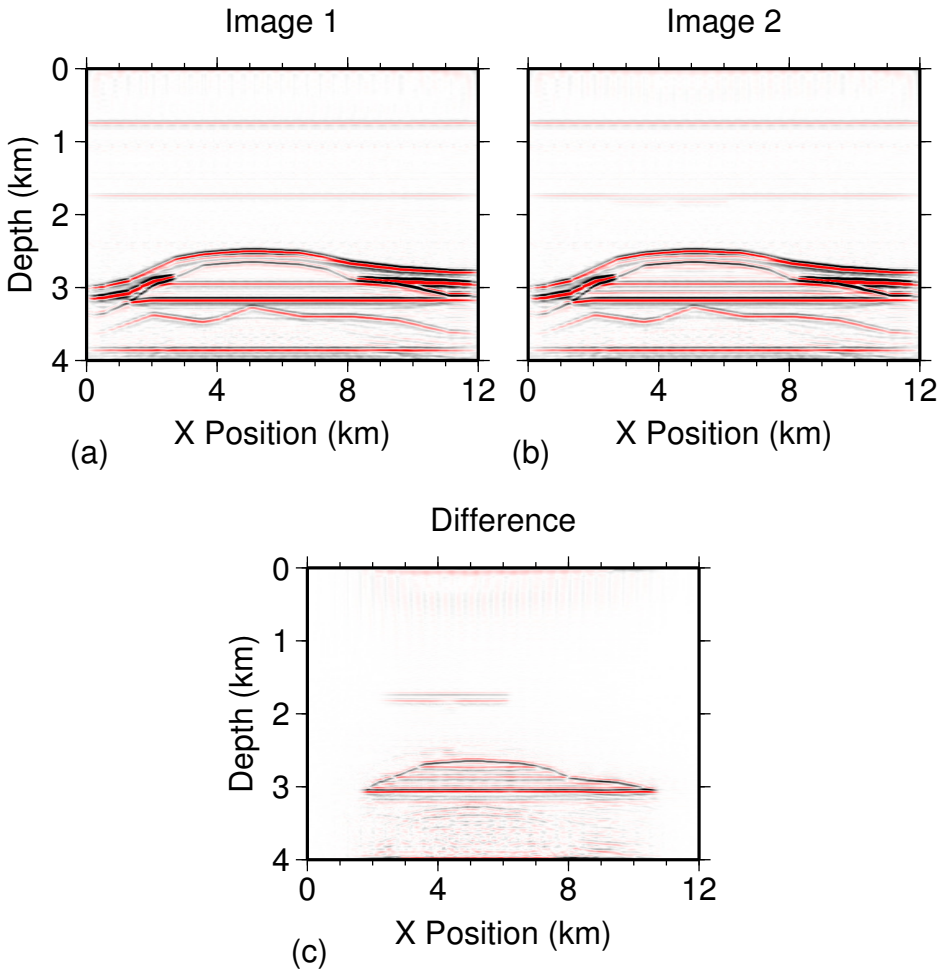

Figure 1.1: A synthetic example of time-lapse seismic monitoring. (a) Synthesized image of the subsurface at an initial survey time. (b) Synthesized image of the subsurface at a second survey time. (c) Difference between the image in (a) and the image in (b), showing changes in the subsurface geologic units.

2001).

The temporal frequency of time-lapse surveys is a key factor in designing a quasi-continuous monitoring project; therefore the ability to vary the data acquisition frequency is of the utmost importance. Attempts have been made to establish continuous and quasi-continuous seismic monitoring scenarios which have been primarily designed around quick turn-around of acquired conventional 3D survey sized seismic data volumes (.i.e., fast delivery of the final image after the data are acquired, as in Lumley (2001) and Clarke et al. (2005)). The difficulty in implementing a truly continuous time-lapse seismic monitoring project using conventional data acquisition parameters lies in the long time frame needed, i.e., the time it takes to acquire the required data volume in the field, and the time it takes to process it.

If implemented in the field, my approach would involve acquiring less data than required for conventional surveys but acquiring it more frequently. The recorded data volume at each survey time could be an order of magnitude less than what would be recorded for a conventional 2D or 3D survey, depending on the quasi-continuous survey frequency. My approach is somewhat similar to the recently developed concept of compressed seismic data acquisition (Candès and Romberg, 2007; Candès and Wakin, 2008; Herrmann and Hennenfent, 2008), in the sense that sparse data are acquired and then used to estimate unrecorded data.

Figure1.2 is an illustration of the approach presented in this dissertation. With a conventional time-lapse monitoring approach, large, complete datasets are acquired at each survey. With the approach presented in this dissertation, only a small subset of the conventional data is acquired at each incremental survey. Shot-receiver pairs used in each incremental survey vary throughout one complete survey cycle, such that the accumulated data acquired at the end of a cycle gives one full survey. The unrecorded data at each incremental survey are estimated and later combined with the sparse, recorded data to reconstruct geophysical images of the subsurface.

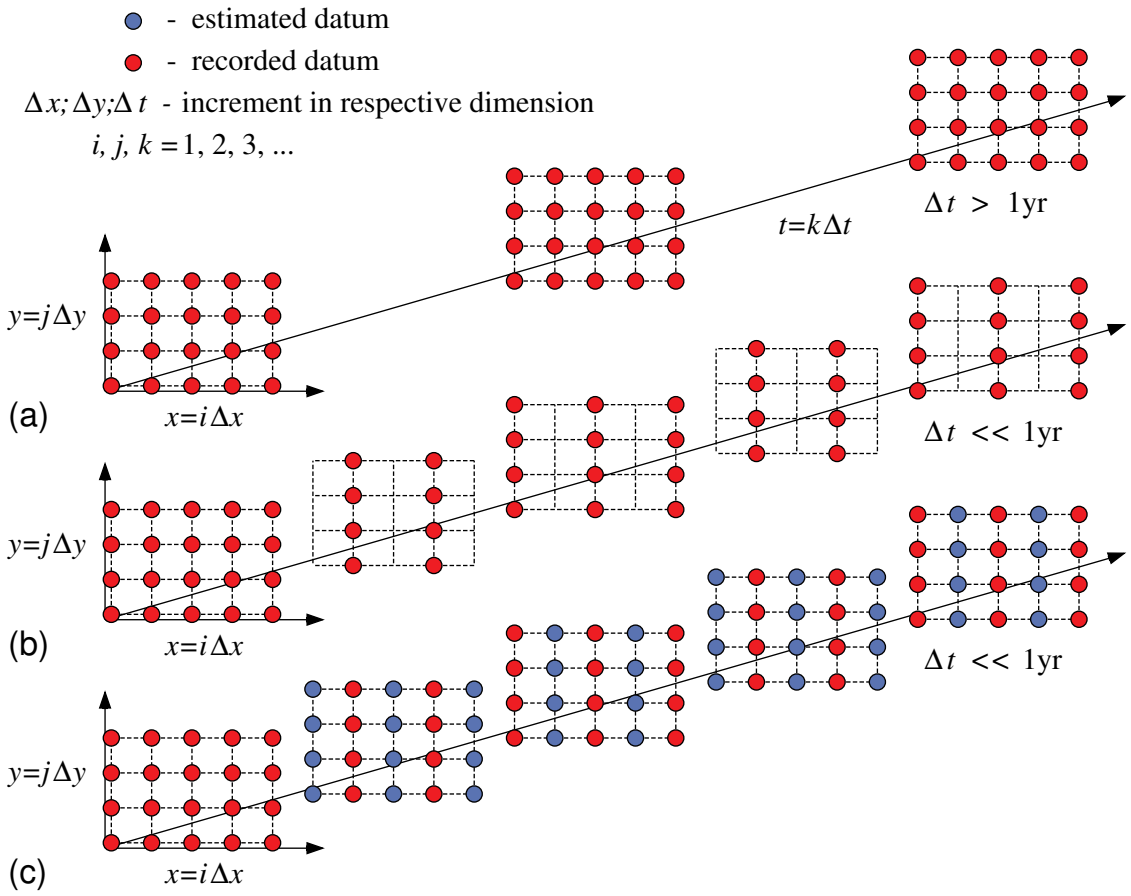

Figure 1.2: An illustration comparing the conventional time-lapse approach with the proposed quasi-continuous approach. (a) Complete datasets from the conventional acquisition strategy. (b) Sparse datasets from the proposed acquisition strategy. (c) Estimated datasets from the proposed acquisition strategy.

1.2 Background

Until now, seismic data estimation has involved computing unavailable or unknown data between available or known data within the same dataset (e.g. Spitz, 1991; Crawley, 2000; Abma and Kabir, 2006; Thomson et al., 2006; Zwartjes and Gisolf, 2007; Curry, 2008). I call this "single-dataset interpolation." The results are constrained by information only available in the incomplete dataset. The approach I present is based on multi-dataset interpolation, where a sequence of independent and incomplete datasets collected over a slowly changing field is used to estimate the unavailable data in the incomplete datasets. This is the strategy used in the electronic image processing field, where high-resolution video images are produced from a series of low-resolution images (e.g. Schultz and Stevenson, 1996; Hardie et al., 1997). This approach benefits from information present in multiple datasets. Since most time-lapse data changes occur in reservoirs and the reservoir makes up a small percentage of the subsurface imaged, we can take advantage the redundancy in the datasets.

In this dissertation, I apply the new strategy to time-lapse seismic data using existing data-estimation methods. I use two data-estimation methods that ignore the physics of wave propagation, and therefore requires no knowledge of the velocity field. These methods are described in Section 2.1.

Several techniques have been proposed for geophysical model reconstruction from time-lapse sparse data. These include dynamic imaging techniques, for example DynaSIRT (Santos and Harris, 2008), ensemble Kalman filter dynamic inversion (Quan and Harris, 2008), and temporal regularization joint inversion (Ajo-Franklin et al., 2005). DynaSIRT is a dynamic iterative reconstruction technique that uses weighted data from other surveys together with the data from the survey of interest to iteratively reconstruct a geophysical model for the survey of interest. On the other hand, dynamic inversion with ensemble Kalman filtering updates the geophysical model obtained from the current sparse data using the computed Kalman gain. The joint inversion approach presented by Ajo-Franklin et al. (2005) relies on regularization along the slow-time dimension to account for the sparsity of the

data.

The reconstruction techniques listed above rely on the inversion process to eliminate the effects of any changes in data acquisition patterns from one survey to another. With my approach, differences in the data acquisition footprint are accounted for in the data space prior to inversion or image processing. However, the benefit of processing sparse time-lapse data directly, using regularization or otherwise, is the small amount of data processed, thus requiring less computational resources.

1.3 Notable Reservoir Catastrophes

The notorious collapse of the Baldwin Hills dam on the 14th of December 1963 is thought to have been caused by oil production and injection of water for secondary recovery in the Inglewood oil field in Los Angeles (Hamilton and Meehan, 1971). These reservoir operations were responsible for an overall ground subsidence of 1.8 meters or more. Movement occurred along faults and surfaces of weakness that existed in the sediments below the dam once the accumulated strains were released. This led to failure of the dam, which collapsed, releasing approximately 945 million liters of water, along with mud and debris, onto the communities below the Baldwin Hills, damaging over 250 homes. Fortunately, millions of lives were saved because the communities were evacuated when indications of imminent failure were observed. Besides the loss of the dam, the collapse caused an estimated $12 million in property damage (Hamilton and Meehan, 1971).

The collapse of the Baldwin Hills dam makes a strong case for an efficient subsurface monitoring system, and more specifically, a quasi-continuous subsurface monitoring system. A quasi-continuous reservoir monitoring system at the Baldwin Hills dam would have provided an opportunity for early detection of the subsidence below the dam, which could have spurred preemptive action, probably in the form of a controlled release of the water in the dam long before the dam collapsed. Also, appropriate management decisions regarding production from and water injection to the oil field could have been made in response to the subsidence.

One of the climate change mitigation options aimed at controlling greenhouse gas contributions from anthropogenic activities is carbon dioxide capture and sequestration in geologic reservoirs (Benson et al., 2005), a procedure that carries its own possibilities for disaster. During the injection phase, when the reservoir pressure changes rapidly, faults may be reactivated, creating fluid flow conduits that can conduct CO_2 from the reservoir elsewhere.

In the event of a massive CO_2 leak to the surface in close proximity to human settlement, lives could be at great risk. An illustration of the danger, though in this case a natural disaster, is the 1986 Lake Nyos CO_2 gas release in Cameroon. About 1700 people and 3000 cattle are reported to have been killed by a sudden release of CO_2 gas from Lake Nyos, a crater lake, on August 21, 1986 (Kling et al., 1987). Upwelling mantle material containing dolomite, undergoes partial melting, releasing CO_2 as pressure drops. The released CO_2 from the degassed dolomitic materials accumulates in near-surface sites and can be released to the atmosphere instantaneously, as happened at Lake Nyos (Kling et al., 1987).

The Lake Nyos disaster provides a reference for potential effects of a failed CO_2 sequestration project. The timing of the accumulation and release of the CO_2 gas at Lake Nyos could not have been predicted, since it occurred naturally and unexpectedly. For CO_2 sequestration in geologic reservoirs, the timing of the accumulation is known. An effective monitoring program, able to detect potential catastrophes early, should be established before any sequestration project begins.

Seismic geophysical investigation methods can be used to detect changes in the seismic properties of geologic units induced by accumulation of CO_2 in the subsurface. For instance, unintended migration of buried CO_2 along faults or fractures into overlying geologic units, can be detected by seismic methods. Early detection is of utmost importance. The time required to collect and process conventional seismic surveys restricts how frequently the subsurface can be imaged. A continuous or quasi-continuous monitoring strategy that requires less time than the conventional approach is therefore needed.

1.4 Terminology

I make the distinction between the two-way traveltime axis of a seismic trace, which I call the *fast-time* axis, and the time axis of the surveys in a time-lapse data volume, which I call the *slow-time* axis.

I refer to a completely sampled dataset, which would normally be recorded for conventional seismic data studies, as a *complete* or *full* dataset, whereas a subset of the complete dataset is a *sparse*, *partial* or *incomplete* dataset.

I use the term *baseline* to describe the field project site prior to the beginning of the process being monitored. A *baseline seismic dataset* is the dataset acquired before monitoring began. The *baseline image* is the image obtained from the baseline dataset, and the *baseline velocity model* is the velocity model built for the baseline dataset.

I call the dataset collected from the time of the baseline survey to the time of a monitor survey, including all intermediate monitor surveys, the *accumulated dataset* of that monitor survey. This is different from the specific data subset collected at that survey.

I use the term *survey time* to describe an instance in time when all recorded data are collated. Accordingly, *incremental survey times* refer to consecutive survey times.

I make a distinction between the *image time* and the *estimation time*. The image time is the instant in time that a resulting processed seismic image or tomographic image represents, whereas the estimation time is the time when the most recent sparse dataset in the accumulated sparse dataset was acquired.

I refer to the difference between the image time and the estimation time as the *estimation slow-time lag*. Since unavailable data at any time are estimated using sparse data acquired at the time of interest, previously acquired sparse data, and sparse data acquired at later times if they exist, there is a lag time between the time of interest and the estimation time. Suppose I have six sparse datasets acquired at two-week intervals, and I estimate unavailable data for all sparse survey datasets at the sixth survey time; my estimation slow-time lag for survey three is six weeks.

I distinguish the terms *estimated traces* and *estimated traveltimes* from the term *estimated data*. Estimated traces or traveltimes are the previously unknown measurements in the sparse data which have now been estimated, while the estimated data are a combination of the estimated traces or traveltimes, and the true, known traces or traveltimes.

1.5 Quasi-continuous vs Sparse Data Monitoring

As explained in previous sections, this dissertation presents a data-estimation-based approach for time-lapse monitoring. This approach can be applied in one of two ways; quasi-continuous monitoring, or time-lapse monitoring with sparse data. In quasi-continuous monitoring, the time interval between successive survey times is small relative to the reservoir changes of interest. This interval is on the order of days or weeks or months, and acquired data are processed and interpreted as full survey data subsets are acquired. In contrast, in time-lapse monitoring with sparse data, the interval between successive surveys is large relative to the reservoir changes of interest, on the order of months or years. In both cases, newly acquired data are used to estimate unrecorded data at the current survey time as well as to re-estimate unrecorded data at previous survey times.

1.6 Practicability

Standard 3D surveys over hydrocarbon reservoirs could take anywhere from a few weeks to a few months to complete (e.g. MacLeod et al., 1999). Depending on the kind of changes occurring in the reservoir, its physical properties may vary between the first shot-time and the last shot-time. These short-term changes, if detected early, may provide useful information helpful in making decisions on reservoir project operations.

Designing a field survey for the approach presented in this dissertation could be challenging. Figure 1.3 shows a possible source deployment scenario for quasi-

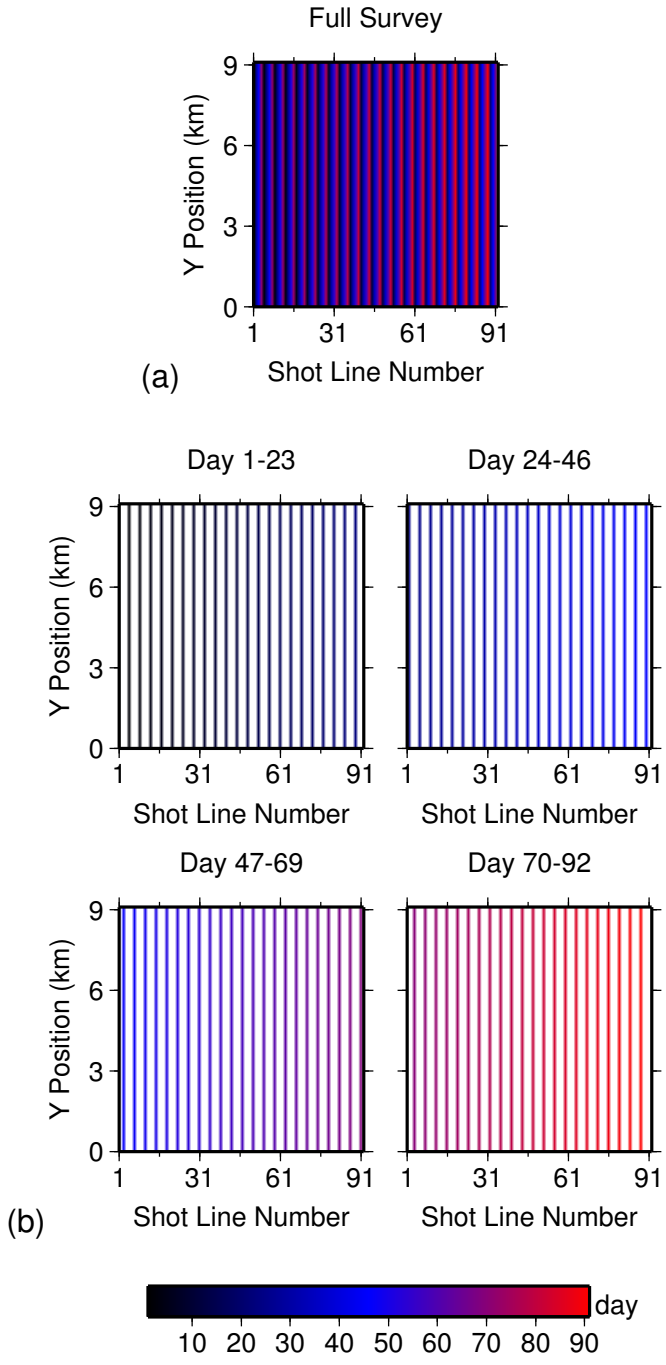

Figure 1.3: (a) An idealized illustration of seismic shot-lines from a standard full survey. (b) The survey shot-lines shown in (a) split into four groups based on shot times.

continuous imaging in a monitoring project over a period of three months. I have assumed that the field is an offshore field; the receivers are dedicated OBCs; and the airgun sources are towed by a source boat. With the conventional approach, one image will be produced from this survey. However, if a slow-time temporal resolution of three weeks for the reservoir changes is good enough, the deployed shots could be split into four groups as shown in Figure 1.3. Obviously, the approach can also be applied to land/onshore surveys. In this case, the receivers are geophones and can also be permanently installed.

Because each group is acquired within a period of three weeks, the slow-time temporal resolution of interest, four images of the reservoir over the course of three months can be produced. This strategy can be extrapolated to any time frame. Figure 1.4 shows an acquisition map from an OBC survey at the Valhall Field (van Gestel et al., 2008), with a time scale similar to that diagrammed in Figure 1.3. Even though the project was not designed for the approach presented, it is obvious that a field implementation of the approach described in Arogunmati and Harris (2009, 2010) is possible using this dataset. In Chapter 5, I present results obtained when my approach is applied to the Valhall time-lapse survey dataset as shown in Figure 1.4.

The data acquisition pattern proposed in this dissertation is equivalent to prolonging a conventional seismic survey. Prolonging a standard seismic data acquisition project to obtain quasi-continuous seismic data is attainable, since seismic surveys today are not acquired instantaneously, even though the data are processed as such.

A quasi-continuous seismic project is economically efficient if permanently installed seismic sources and receivers are used. This eliminates the equipment deployment costs associated with each seismic survey. In addition, it makes repeatability in the acquired data possible, and it favors flexibility in setting data-acquisition intervals. Projects with dedicated receivers are now common. Examples are the Valhall Field (Barkved et al., 2005) and the Clair Field (Foster et al., 2008), where permanently installed OBCs are used. Also, the availability of fiber-optic networks and broadband satellite systems (Houston and Grumman, 2003) means the data

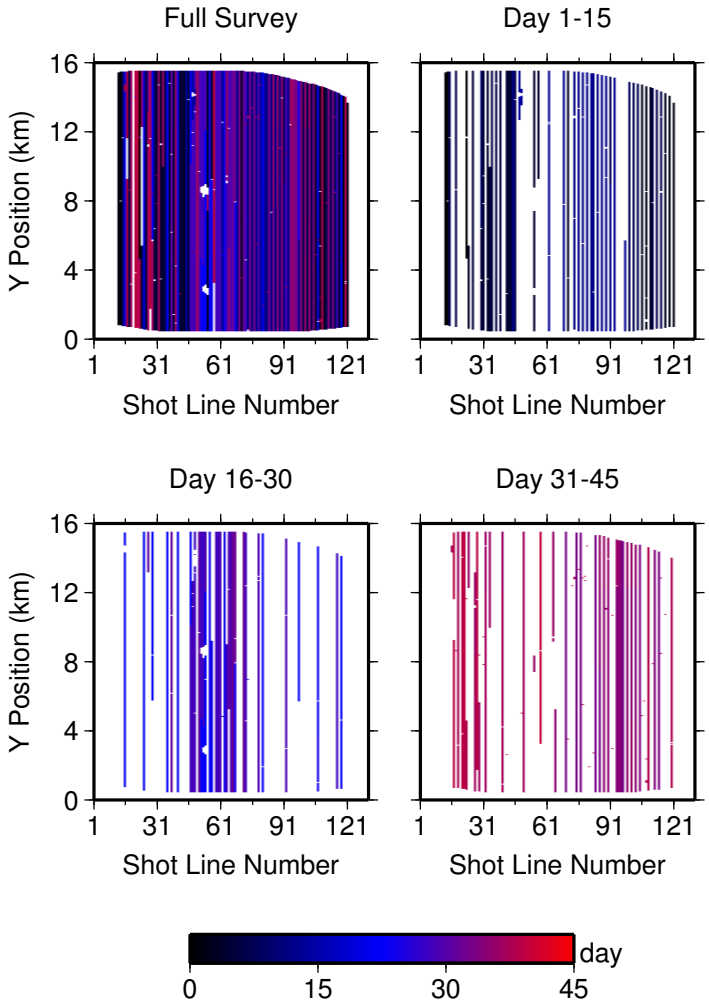

Figure 1.4: (a) Shot-lines for survey 4 of BP's Valhall LoFS project, a standard, full 3D field survey. (b) The survey shot-lines shown in (a) split into three groups based on shot times.

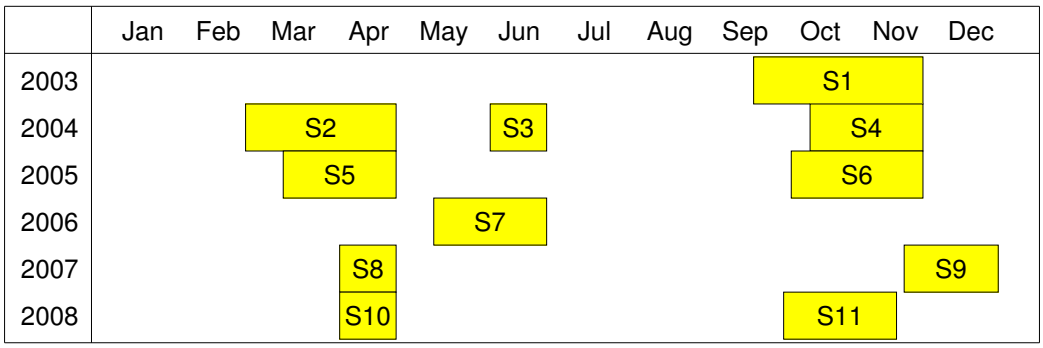

Table 1.1: Shot times for the first 11 surveys at the Valhall Field operated by BP. The data acquisition times for the surveys range from three weeks to two months.

processing station need not be close to the survey location.

The offshore seismic data obtained for the Valhall Life of Field Seismic (LoFS) project, a time-lapse reservoir monitoring project operated by BP at the Valhall Field in the North Sea, can be used as an example. Figure 1.1 shows the shot times for the first 11 surveys. The data acquisition times for the different surveys range from three weeks to two months. However, a single image was produced for each survey, as if it were an instantaneous seismic image of the subsurface.

1.7 Primary Contribution

In this dissertation, I present a seismic time-lapse monitoring strategy that allows easy variability in slow-time temporal resolution. It has the potential to be the foundation for continuous seismic reservoir monitoring. The strategy can be used on seismic traveltime or seismic full-trace data. I show with examples that it can be used to quasi-continuously monitor geologic CO_2 storage reservoirs and hydrocarbon reservoirs. The approach presented in this dissertation accounts for differences in the data acquisition footprint prior to imaging or inversion, in the data space. In addition, because operations are in data space, bad data are easily identified and can be removed prior to imaging or inversion. This makes quality control easier.

1.8 Thesis Overview

In Chapter 2, I introduce the primary methods and algorithms used in this dissertation for data estimation. These include data estimation using prediction-error filters (PEFs), and data estimation using minimum-weighted-norm interpolation (MWNI). I describe how the heterogeneity in the seismic data is overcome, and I use simple synthetic examples to show the efficiency of the data estimation methods. I also describe the error-analysis tool I developed for assessing the accuracy of my estimated data. This new tool addresses the fact that when a missing seismic trace is estimated, inaccuracies could exist in the form of amplitude errors or phase errors (or both) relative to the true missing trace. For a synthetic test, the true trace is usually known, and the estimation error can be established. For a field dataset with missing traces, the true trace may not be known; however, an analysis of the performance of the estimation algorithm on a synthetic dataset can provide insight into how well missing field data are estimated.

In Chapter 3, I apply my approach to synthetic and field crosswell traveltime data. I implement an iterative PEF/data estimation approach to the quasi-continuous monitoring problem. I describe the benefits of estimating missing data using PEFs, a stochastic approach. I illustrate my argument using a synthetic model simulating a monitored CO_2 geologic storage site over a period of 140 weeks. I allow the injected CO_2 to leak from the intended reservoir into a shallower geologic unit to show how quasi-continuous monitoring can be used in the early detection of the leak. I use synthetic velocity models derived from inverted data from the McElroy Field in West Texas, where CO_2 was used as the injected fluid in secondary recovery. In addition to showing results from synthetic examples, I also show results obtained after applying my approach to the McElroy time-lapse field data.

In Chapter 4, I apply my approach to full-trace seismic data. I use MWNI to estimate missing data from two unique synthetic time-lapse datasets. The first is a time-lapse 2D dataset synthesized using velocity models that represent a CO_2 sequestration site monitored over a period of 20 months at one-month intervals. As I did with the example shown in Chapter 3, I allowed the injected CO_2 to leak

from the intended reservoir to a geologic unit above the reservoir. The ability of my approach to track the changes caused by the CO_2 shows its efficiency. The second dataset is a time-lapse 3D dataset synthesized using velocity models that represent a petroleum reservoir undergoing secondary recovery. In this example, the injected water is monitored to ensure it travels in the intended direction. In a real world scenario, a quasi-continuous project could be established to ensure that the right injection rate and pressure are used, and operational decisions can be made accordingly.

In Chapter 5, I introduce the Valhall Field dataset. I present two possible applications of my approach to the Valhall Field. In the first application, I subsample and reorganize the dataset from surveys 9, 10, and 11 into three quasi-continuous datasets and use my approach to monitor the changes in the reservoir during the period over which surveys 9, 10, and 11 were acquired. In the second application, I organize the dataset from survey 4 of the time-lapse data volume into three quasi-continuous datasets and use my approach to monitor the changes in the reservoir during the period over which survey 4 was acquired. In the first case, the monitoring time-scale is the same as the time-scale in the original dataset. In the second case, the monitoring time-scale is significantly smaller than the time-scale in the original dataset. The time interval between images using my approach is 15 days, and the average time interval between surveys in the original dataset is six months.

Finally, in Chapter 6, I conclude the thesis, bringing together the ideas presented in the previous chapters and making recommendations regarding future directions for the idea presented in this dissertation. I also summarize the strengths, weaknesses, and limitations of my approach.

1.9 3D seismic image and data display

In chapters 4 and 5, I illustrate the efficiency of my proposed approach using 3D surface-seismic data. Unlike 2D data, 3D data volumes cannot be efficiently displayed in their entirety on paper. I display 3D data by showing selected 2D slices from the data volume in the *xy* plane, *xz* plane, and *yz* plane. On each displayed

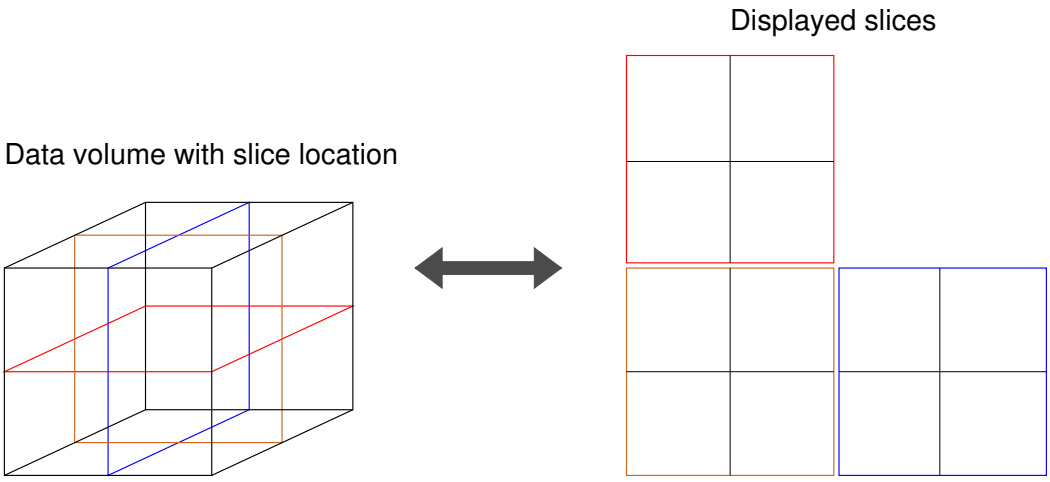

Figure 1.5: Template for displaying 3D seismic data and velocity models used in this dissertation. The 3D volume is shown using slices along all three planes.

slice, its intersection with the other two slices will be indicated. An illustration of this template is show in Figure 1.5.

1.10 Assumptions

The quasi-continuous monitoring strategy presented in this dissertation assumes that the slow-time temporal resolution of the changes in the physical properties of the reservoir has a higher priority than the spatial resolution of the same changes in the reservoir; therefore we can sacrifice some spatial resolution for a higher slow-time temporal resolution. The spatial resolution is reduced relative to the high resolution obtainable when completely sampled datasets are used in image reconstruction. However, my approach uses missing data estimation to partially restore the spatial resolution compromised by recording sparse data.

I also assume that a completely sampled baseline dataset exists. I make this assumption because field project sites are studied extensively before being selected,

and the seismic dataset used in site selection is often completely sampled. Since the sparse data recorded at short time intervals are intended to track small changes in the reservoir, the baseline dataset provides information on the non-changing background structure of the subsurface.

Finally, I assume that the recorded data are repeatable from one time-lapse survey to the other within a very narrow error range. In other words, recorded seismic data do not vary significantly from survey to survey if there are no physical changes in the subsurface; therefore, any changes in the recorded data from one survey to another are attributed to changes in the reservoir and not to inconsistencies in data recording parameters.

Chapter 2

Time-Lapse Data-Estimation Methodology

2.1 The Data-Estimation Problem

In this dissertation, I present a quasi-continuous seismic reservoir monitoring approach. I assume that a dataset can be recorded either completely or partially. I call the partially acquired dataset a *sparse dataset*. A complete dataset is recorded over a period of time, and at each incremental survey time, the recorded data subset can be categorized as a sparse dataset.

For clarity, I will represent the spatial domain with number subscripts and the slow-time temporal domain with number superscripts. Also, I will represent completely sampled data with the letter subscript c, sparsely sampled data with the letter subscript s, and unrecorded data with the letter subscript u. Using these rules, I can represent complete datasets from the first and second surveys as,

$$\mathbf{d}_c^1 = [\ d_1^1\ d_2^1\ d_3^1\ \cdots\ d_n^1\ ]^T; \quad n = \textit{last sample number}\ , \tag{2.1}$$

and

$$\mathbf{d}_c^2 = [\ d_1^2\ d_2^2\ d_3^2\ \cdots\ d_n^2\ ]^T; \quad n = \textit{last sample number}\ , \tag{2.2}$$

respectively. The sum of the sparse dataset and the unrecorded dataset gives the

complete dataset; i.e.,

$$\mathbf{d}_c^k = \mathbf{d}_s^k + \mathbf{d}_u^k \,, \tag{2.3}$$

where $\mathbf{d}_s^k$ is the sparse data recorded at time k, and $\mathbf{d}_u^k$ is the unrecorded data at time k. An example of sparse, unrecorded, and complete datasets at time $k = 2$ is

$$\begin{aligned} \mathbf{d}_s^2 &= [\ d_1^2\ \ 0\ d_3^2\ d_4^2\ \ 0\ \ 0\ \ d_7^2\ \ 0\ \ d_9^2\ ]^T \,, \\ \mathbf{d}_u^2 &= [\ \ 0\ d_2^2\ \ 0\ \ 0\ \ d_5^2\ d_6^2\ \ 0\ \ d_8^2\ \ 0\ ]^T \,, \\ \mathbf{d}_c^2 &= [\ d_1^2\ d_2^2\ d_3^2\ d_4^2\ d_5^2\ d_6^2\ d_7^2\ d_8^2\ d_9^2\ ]^T \,. \end{aligned} \tag{2.4}$$

By writing an identity equation for (2.3),

$$\mathbf{d}_c^k = \mathbf{S}\mathbf{d}_c^k + (\mathbf{I} - \mathbf{S})\mathbf{d}_c^k \,, \tag{2.5}$$

we observe that

$$\mathbf{d}_s^k = \mathbf{S}\mathbf{d}_c^k \,; \quad \mathbf{d}_u^k = (\mathbf{I} - \mathbf{S})\mathbf{d}_c^k \,, \tag{2.6}$$

where $\mathbf{S}$ is a data selection operator that selects which data are recorded.

If the accumulated complete dataset consisting of data from k surveys is written as,

$$\mathbf{t}_c^k = [\ \mathbf{d}_c^1\ \mathbf{d}_c^2\ \mathbf{d}_c^3\ \cdots\ \mathbf{d}_c^k\ ]^T \,, \tag{2.7}$$

then

$$\mathbf{t}_c^k = \mathbf{t}_s^k + \mathbf{t}_u^k \,, \tag{2.8}$$

where $\mathbf{t}_s^k$ is the accumulated sparse dataset at time k, and $\mathbf{t}_u^k$ is the accumulated unrecorded dataset at time k. The quasi-continuous monitoring strategy requires measuring sparse data at short time intervals, i.e., measuring $\mathbf{t}_s^k$. This implies that we estimate the unrecorded $\mathbf{t}_u^k$ using the measured $\mathbf{t}_s^k$. To estimate the unrecorded data using the autoregressive model, I make the ergodicity assumption: I assume that the statistics of the recorded seismic trace in space are equivalent to the statistics of one repeatedly recorded trace. This assumption is fundamental to seismic data estimation using prediction-error filters (PEFs). Since this assumption is valid

only in small regions of space, I use the non-stationary formulation of the autoregressive data-estimation method. The goal of my estimation problem is to obtain, by inversion (see Menke, 1984; Tarantola, 1987), an estimate of the accumulated complete data, $\tilde{\mathbf{t}}_c^k$, using the accumulated recorded sparse data, $\mathbf{t}_s^k$, at time k; that is,

$$\tilde{\mathbf{t}}_c^k = \mathbf{t}_s^k + \tilde{\mathbf{t}}_u^k \ , \tag{2.9}$$

where $\tilde{\mathbf{t}}_u^k$ is the estimate of the accumulated unrecorded data at time k.

2.1.1 Optimal Linear Prediction

My derivation for the optimal linear predictor follows that described in Gilgen (2006). Let the series d_i, $i = 1, 2, ..., n-1$, be a realization of the stochastic process, D_i, with a variance σ^2, and let D_n be a random variable for data measured at time n. Also, let $\hat{d}_n$ be a realization of the estimator $\hat{D}_n = \hat{D}_n(D_1, D_2, ..., D_{n-1})$. Then $\hat{d}_n$ is called a predicted value of D_n, and $\hat{D}_n$ is a prediction of D_n. An optimal prediction of d_n minimizes the mean square of the prediction error, $\hat{e}_n$, where $\hat{e}_n = D_n - \hat{D}_n$. The variance of $\hat{e}_n$, $Var\ \hat{e}_n$, is defined as,

$$Var\ \hat{e}_n = E\{[D_n - \hat{D}_n]^2\} \ , \tag{2.10}$$

where the symbol E is the expected value symbol.

Given the above definitions, we can write

$$\hat{D}_n = a_1 D_{n-1} + a_2 D_{n-2} + ... + a_{n-1} D_1 \ , \tag{2.11}$$

$$\hat{D}_n = \sum_{k=1}^{n-1} a_k D_{n-k} \ . \tag{2.12}$$

Equation (2.12) is called an optimal linear prediction if $\mathbf{a} = [a_1, a_2, \cdots, a_{n-1}]^T$ minimizes the prediction error defined in (2.10). From (2.12), we can deduce

$$\hat{d}_n = \sum_{k=1}^{n-1} a_k d_{n-k} \ . \tag{2.13}$$

Optimal linear prediction is the foundation of autoregressive data estimation. Autoregressive models have been applied in many data prediction and data estimation problems (e.g. Takanami and Kitagawa, 1991; Schultz et al., 1998; Myers and Schultz, 2000). A random sequence, d_n, with zero mean is an autoregressive process of order p when the most recent p outputs and the current input can be used to recursively generate the next output (Jain, 1998). This can be stated as follows:

$$\begin{gathered} d_n = \textstyle\sum_{k=1}^{p} a_k d_{n-k} + \epsilon_n \ , \\ E[\epsilon_n] = 0; \, E\{[\epsilon_n]^2\} = \beta^2; \, E[\epsilon_n \epsilon_m] = \beta^2 \delta_{n-m}; \, E[\epsilon_n d_m] = 0, m < n, \end{gathered} \tag{2.14}$$

where ϵ_n is a zero-mean, stationary input sequence independent of previous outputs, and a_k are the elements of a PEF. Based on only the past p samples, the quantity

$$\bar{d}_n \triangleq \sum_{k=1}^{p} a_k d_{n-k} \tag{2.15}$$

is the best linear mean-square predictor of d_n (Jain, 1998). This implies that

$$d_n = \bar{d}_n + \epsilon_n \ . \tag{2.16}$$

We can rewrite (2.14) as

$$\epsilon_n = d_n - \sum_{k=1}^{p} a_k d_{n-k} \ . \tag{2.17}$$

In matrix-vector form, (2.17) can be expressed as

$$\begin{bmatrix} \epsilon_1 \\ \epsilon_2 \\ \vdots \\ \epsilon_n \end{bmatrix} = \begin{bmatrix} d_1 \\ d_2 \\ \vdots \\ d_n \end{bmatrix} - \begin{bmatrix} d_0 & 0 & \cdots & 0 \\ d_1 & d_0 & \ddots & 0 \\ \vdots & \vdots & \ddots & \vdots \\ d_{n-1} & d_{n-2} & \cdots & d_{n-p} \end{bmatrix} \begin{bmatrix} a_1 \\ a_2 \\ \vdots \\ a_n \end{bmatrix} \tag{2.18}$$

or

$$\begin{bmatrix} d_0 \\ \epsilon_1 \\ \epsilon_2 \\ \vdots \\ \epsilon_n \end{bmatrix} = \begin{bmatrix} d_0 & 0 & 0 & \cdots & 0 \\ d_1 & d_0 & 0 & \ddots & 0 \\ d_2 & d_1 & d_0 & \ddots & 0 \\ \vdots & \vdots & \ddots & \ddots & \vdots \\ d_n & d_{n-1} & d_{n-2} & \cdots & d_{n-p} \end{bmatrix} \begin{bmatrix} 1 \\ -a_1 \\ -a_2 \\ \vdots \\ -a_p \end{bmatrix} . \tag{2.19}$$

If we assume that $d_0 = 0$, and that $d_i = 0$ for $i > n$, we can write

$$\begin{bmatrix} \epsilon_1 \\ \epsilon_2 \\ \vdots \\ \epsilon_n \\ \vdots \\ \epsilon_{n+p-1} \end{bmatrix} = \begin{bmatrix} d_1 & 0 & 0 & \cdots & 0 \\ d_2 & d_1 & 0 & \ddots & 0 \\ \vdots & \vdots & \ddots & \ddots & \vdots \\ d_n & d_{n-1} & d_{n-2} & \cdots & d_{n-p} \\ 0 & d_n & d_{n-1} & \cdots & d_{n-p+1} \\ 0 & 0 & d_n & \cdots & d_{n-p+2} \\ \vdots & \vdots & \ddots & \ddots & \vdots \\ 0 & 0 & 0 & \cdots & d_n \end{bmatrix} \begin{bmatrix} 1 \\ -a_1 \\ -a_2 \\ \vdots \\ -a_p \end{bmatrix} . \tag{2.20}$$

The right hand side of (2.20) is a convolution operation; therefore we can use the

commutative property of convolution to rewrite (2.20) as

$$\begin{bmatrix} \\ \epsilon_1 \\ \epsilon_2 \\ \vdots \\ \epsilon_n \\ \vdots \\ \epsilon_{n+p-1} \end{bmatrix} = \begin{bmatrix} 1 & 0 & 0 & \cdots & 0 \\ -a_1 & 1 & 0 & \ddots & 0 \\ -a_2 & -a_1 & 1 & \ddots & \vdots \\ \vdots & -a_2 & -a_1 & \cdots & 1 \\ -a_p & \vdots & -a_2 & \cdots & -a_1 \\ 0 & -a_p & \vdots & \cdots & -a_2 \\ \vdots & \vdots & \ddots & \ddots & \vdots \\ 0 & 0 & 0 & \cdots & -a_p \end{bmatrix} \begin{bmatrix} d_1 \\ d_2 \\ d_3 \\ \vdots \\ d_n \end{bmatrix} . \tag{2.21}$$

Using boldface, uppercase letters to represent matrices and boldface lowercase letters to represent vectors, (2.20) and (2.21) can be written as

$$\epsilon = \mathbf{Da} \tag{2.22}$$

and

$$\epsilon = \mathbf{Ad} \tag{2.23}$$

respectively. The matrix $\mathbf{A}$ contains row-shifted copies of the PEF coefficient vector $\mathbf{a}$, while the matrix $\mathbf{D}$ contains row-shifted copies of the data vector $\mathbf{d}$.

While data prediction deals primarily with computing yet-to-be-measured data samples from previously measured data samples, data estimation deals with computing missing data samples in an incomplete set of data samples. To estimate missing data using the autoregressive model, (2.22) and (2.23) are satisfied by minimizing the prediction error, ϵ, according to (2.16).

Claerbout (1998) suggests a two-stage process for filling in missing data using autoregression. In the first stage, the optimal PEF for the incomplete data is estimated. In the second stage, the estimated PEF is used to estimate the missing data. To compute the optimal PEF, we use a training dataset. This training dataset can be the incomplete dataset with the missing data masked out or a different dataset with similar statistical properties to the one we wish to estimate. The PEF is obtained

with (2.22) by minimizing the residual (prediction error), $\mathbf{r_d}$:

$$\mathbf{0} \approx \mathbf{r_d} = \mathbf{DKa} + \mathbf{d} \ . \tag{2.24}$$

where $\mathbf{K}$ is a masking operator that ensures that the constrained filter coefficients remain unchanged. These include the zero-lag coefficient of the filter, $\mathbf{a}$, which has a value of 1. $\mathbf{K}$ is similar to the identity matrix but has a value of zero at positions corresponding to constrained filter coefficients. Equation (2.24) assumes that the data vector, $\mathbf{d}$, is stationary and can be described by a single PEF.

Guitton (2003) presented an approach for estimating PEFs for non-stationary data. This approach allows the PEF coefficients to vary smoothly from one end of the data to the other during the convolution operation. In this case, we solve for a non-stationary PEF of the following form:

$$\mathbf{f_{ns}} = [\ \mathbf{a}_0 \mid \mathbf{a}_1 \mid \mathbf{a}_2 \mid \cdots \mid \mathbf{a}_n\ ]^T \ , \tag{2.25}$$

where

$$\mathbf{a}_k = [\ 1 \ -a_{1,k} \ -a_{2,k} \ -a_{3,k} \ \cdots \ -a_{p,k}\ ]^T \ . \tag{2.26}$$

We solve by minimizing the residual,

$$\mathbf{0} \approx \mathbf{r_d} = \mathbf{D}_0\mathbf{K}\mathbf{a}_0 + \mathbf{D}_1\mathbf{K}\mathbf{a}_1 + \cdots + \mathbf{D}_n\mathbf{K}\mathbf{a}_n + \mathbf{d} = \mathbf{D_{ns}}\mathbf{K_{ns}}\mathbf{f_{ns}} + \mathbf{d} \ , \tag{2.27}$$

where $\mathbf{a}_0$, $\mathbf{a}_1$, $\mathbf{a}_2$, $\cdots$, $\mathbf{a}_n$, are distinct stationary PEFs; $\mathbf{f_{ns}}$ is a non-stationary PEF with the vertical lines separating distinct PEFs; and $\mathbf{D}_k$ contains the subset of $\mathbf{d}$ to be convolved with $\mathbf{a}_k$. $\mathbf{D_{ns}}$ and $\mathbf{K_{ns}}$ are non-stationary representations of $\mathbf{D}$ and $\mathbf{K}$ respectively. The objective functions for the least-squares minimization of (2.24) and (2.27) are

$$\mathbf{\Phi} = ||\mathbf{r_d}||^2 = ||\mathbf{DKa} + \mathbf{d}||^2 \tag{2.28}$$

and

$$\mathbf{\Phi} = ||\mathbf{r_d}||^2 + \alpha^2||\mathbf{r_r}||^2 = ||\mathbf{D_{ns}}\mathbf{K_{ns}}\mathbf{f_{ns}} + \mathbf{d}||^2 + \alpha^2||\mathbf{R}\mathbf{K_{ns}}\mathbf{f_{ns}}||^2 \tag{2.29}$$

respectively, where $\mathbf{r_r} = \mathbf{RK_{ns}f_{ns}}$, $\alpha^2||\mathbf{r_r}||^2$ is a regularization term, $\mathbf{R}$ is a roughening operator, and α is a scaling constant. The regularization term is used to ensure that we obtain a smoothly varying, non-stationary PEF. Minimizing (2.28) with respect to $\mathbf{a}$ and rearranging the terms give

$$\mathbf{a} = -\left(\mathbf{K}^\dagger\mathbf{D}^\dagger\mathbf{DK}\right)^{-1}\mathbf{K}^\dagger\mathbf{D}^\dagger\mathbf{d}\ , \tag{2.30}$$

where the symbol, †, denotes the complex conjugate transpose. Minimizing (2.29) with respect to $\mathbf{f_{ns}}$ and rearranging the terms give

$$\mathbf{a} = -\left(\mathbf{K}^\dagger_{\mathbf{ns}}\mathbf{D}^\dagger_{\mathbf{ns}}\mathbf{D_{ns}K_{ns}} + \alpha^2\mathbf{K}^\dagger_{\mathbf{ns}}\mathbf{R}^\dagger\mathbf{RK_{ns}}\right)^{-1}\mathbf{K}^\dagger_{\mathbf{ns}}\mathbf{D}^\dagger_{\mathbf{ns}}\mathbf{d}\ . \tag{2.31}$$

For a given image, a non-stationary PEF takes a longer time to compute than a stationary PEF, because there are many more independent unknowns in the inverse problem.

After computing the PEF, $\mathbf{a}$, the missing data are estimated by minimizing the residual:

$$\begin{aligned} \mathbf{0} \approx \mathbf{r_a} &= \mathbf{ASd} + \mathbf{AHd}\ , \\ \mathbf{H} &= \mathbf{I} - \mathbf{S}\ , \end{aligned} \tag{2.32}$$

where $\mathbf{S}$ is a masking operator similar to the identity matrix, except that it has values of 1 in the diagonal positions corresponding to known data and zeros in the diagonal positions corresponding to missing data locations. $\mathbf{I}$ is the identity matrix, and $\mathbf{H}$ is the masking operator for the unknown data. In the non-stationary case, $\mathbf{f_{ns}}$, the residual of the non-stationary convolution operation is used to estimate the missing data:

$$\mathbf{0} \approx \mathbf{r_f} = \mathbf{A}_0\mathbf{S}_0\mathbf{d}_0 + \mathbf{A}_0\mathbf{H}_0\mathbf{d}_0 + \mathbf{A}_1\mathbf{S}_1\mathbf{d}_1 + \mathbf{A}_1\mathbf{H}_1\mathbf{d}_1 + \cdots = \mathbf{F_{ns}Sd} + \mathbf{F_{ns}Hd}\ , \tag{2.33}$$

where $\mathbf{A}_k$ is a matrix representing convolution with $\mathbf{a}_k$, $\mathbf{d}_k$ is the subset of $\mathbf{d}$ convolved with $\mathbf{a}_k$, and $\mathbf{F_{ns}}$ is a matrix representing convolution with $\mathbf{f_{ns}}$. The objective

functions for the least-squares minimization of (2.32) and (2.33) are

$$\mathbf{\Phi} = ||\mathbf{r_a}||^2 = ||\mathbf{ASd} + \mathbf{AHd}||^2 \tag{2.34}$$

and

$$\mathbf{\Phi} = ||\mathbf{r_f}||^2 = ||\mathbf{F_{ns}Sd} + \mathbf{F_{ns}Hd}||^2 \tag{2.35}$$

respectively. Minimizing (2.34) with respect to the data $\mathbf{d}$ and rearranging the terms give

$$\begin{aligned} \mathbf{d} &= -\left(\mathbf{H}^\dagger\mathbf{A}^\dagger\mathbf{AH}\right)^{-1}\mathbf{H}^\dagger\mathbf{A}^\dagger\mathbf{r}_0 \ , \\ \mathbf{r}_0 &= \mathbf{ASd} \ , \end{aligned} \tag{2.36}$$

where $\mathbf{r}_0$ is a constant vector that holds the output of the PEF convolved with the known data, $\mathbf{Sd}$. Minimizing (2.35) with respect to the data $\mathbf{d}$ and rearranging the terms give

$$\begin{aligned} \mathbf{d} &= -\left(\mathbf{H}^\dagger{\mathbf{F_{ns}}}^\dagger\mathbf{F_{ns}H}\right)^{-1}\mathbf{H}^\dagger{\mathbf{F_{ns}}}^\dagger\mathbf{r}_0 \ , \\ \mathbf{r}_0 &= \mathbf{F_{ns}Sd} \ , \end{aligned} \tag{2.37}$$

where $\mathbf{r}_0$ is a constant vector that holds the output of the non-stationary PEF convolved with the known data $\mathbf{Sd}$. Equations (2.36) and (2.37) are used to compute the estimated data. I use the non-stationary form of the autoregression model to compute $\tilde{\mathbf{t}}_u^k$ in (2.9).

Data covariance information (see Journel and Huijbregts, 1978; Cressie, 1993) for a given dataset are approximated by its PEF. A PEF can be constructed in any number of dimensions. Figure 2.1 shows PEF shapes in 1-, 2- and 3-dimensions. Ideally we would like the filter to be causal. Notice that the leading values of the 2- and 3-dimensional PEF shapes are not at the corners of the PEFs. This is because we would like to predict as many slopes as possible in the incomplete data being reconstructed with the PEF. Having the leading value at the corner limits the number of slopes or trends predictable by the PEF.

In Chapter 3, PEFs will be used to estimate unavailable crosswell-seismic traveltimes in a quasi-continuous sparse dataset. Because a seismic arrival is deterministic and is hyperbolic for horizontal layers, it cannot readily be described as a random

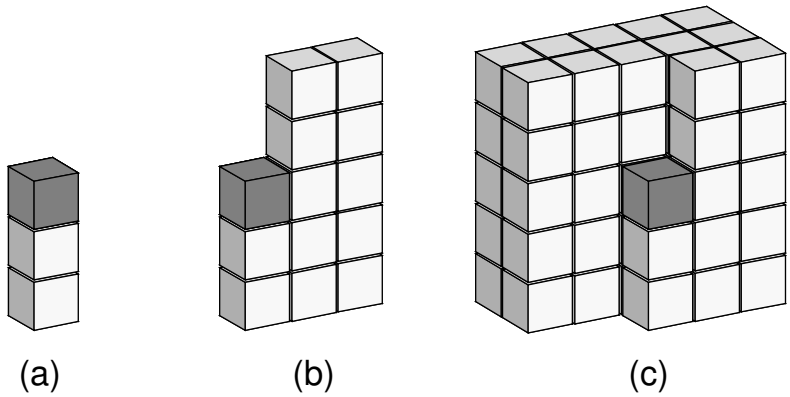

Figure 2.1: Shapes of prediction-error filters. (a) 3-term 1-dimensional PEF. (b) 13-term 2-dimensional PEF. (c) 63-term 3-dimensional PEF. This figure was modified from Curry (2008).

sequence with zero mean. However, the arrival can be flattened by applying a moveout correction (e.g. de Bazelaire, 1988; Castle, 1994; Tsvankin, 1995; Yilmaz, 1987) or by computing and subtracting the hyperbolic trend from the arrival. If the mean is now removed from the picked flattened arrival traveltimes, the result can be described as a random sequence with zero mean. This is illustrated in Figures 2.2 and 2.3.

2.1.1.1 Helical Coordinate

Seismic data used in geophysical studies are usually multidimensional, combining one or more spatial dimensions and a fast-time dimension. Autoregressive methods, on the other hand, are often used in one-dimensional problems. An efficient algorithm for solving inverse problems is the conjugate gradient algorithm (Hestenes and Stiefel, 1952). This algorithm requires computing forward and adjoint operations. Equations (2.20) and (2.21) show that the forward operation in estimating missing data using autoregressive methods is convolution. The adjoint operation to

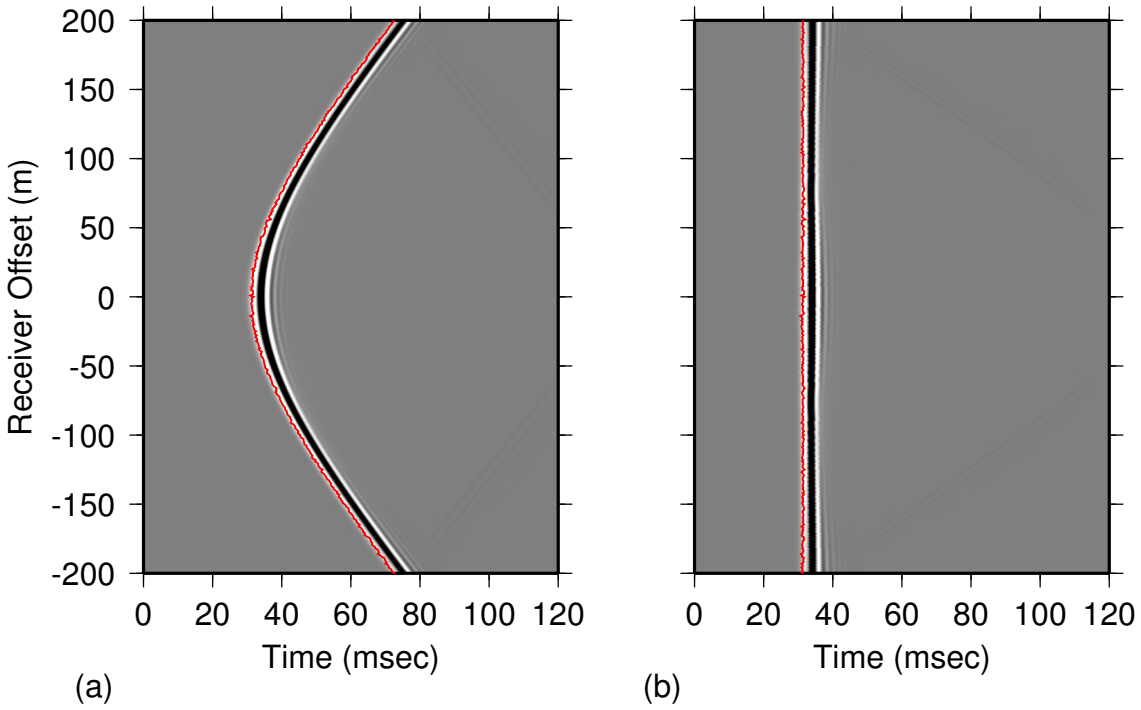

Figure 2.2: (a) shot gather from a synthetic crosswell acquisition experiment showing a direct arrival. (b) The shot gather in (a) with the direct arrival flattened. The red lines in both images are the direct arrival traveltime picks.

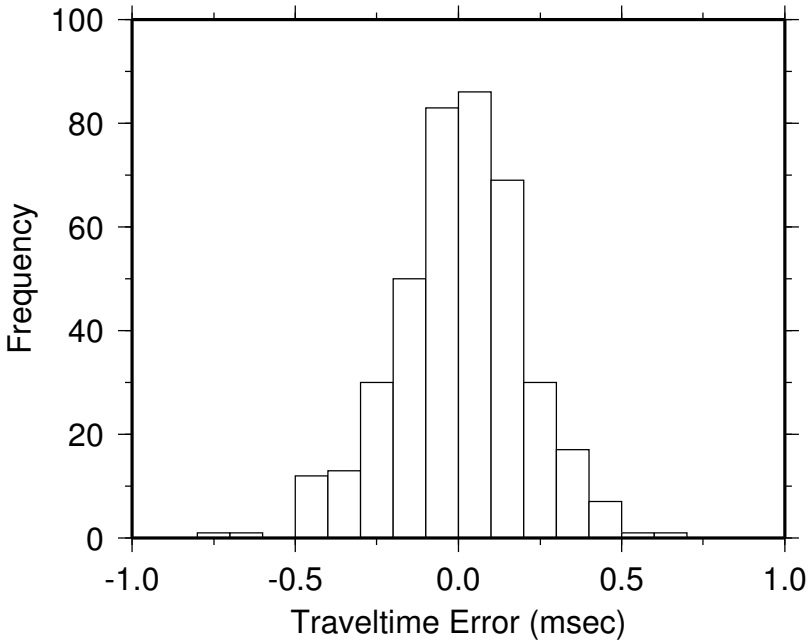

Figure 2.3: Picking-error histogram for the traveltimes shown in Figure 2.2(b) after removing the mean traveltime value.

convolution is deconvolution. Convolution can be done in any number of dimensions, but deconvolution is stable only in 1-dimensional computations (Claerbout, 1998).

Claerbout (1998) presented a helical coordinate system which allows the implementation of multi-dimensional convolution and deconvolution as one-dimensional operations. For a multidimensional array, transformation into a helical coordinate system is implemented by rearranging the elements along each dimension to form a long one-dimensional vector. A visual illustration of the helical transformation is shown in Figure 2.4. It starts with a matrix which is then wound to form a cylinder, with the end of one column connected to the top of the next column. Finally, the cylinder is unwound to form a strip. This strip is the helical coordinate transform

of the initial matrix. For example, the two-dimensional array,

$$\begin{pmatrix} a & d \\ b & e \\ c & f \end{pmatrix} \tag{2.38}$$

has the following helical coordinate transform:

$$M = [\, 0\, 0\, a\, b\, c\, 0\, \cdots\, 0\, d\, e\, f\, 0\, 0\,] \,. \tag{2.39}$$

The additional zeros in the array are used to remove edge effects introduced by the coordinate transform. Claerbout (1998) showed that filtering on the helix is equivalent to filtering in the multi-dimensional space.

2.1.1.2 PEF Estimation Example

Let us look an example of PEF estimation for simple images. I synthesized a 200x200-element, 2D image with two linear events having conflicting dips and different amplitudes. This image is shown in Figure 2.5. I estimated both stationary and a non-stationary 5x5-element, 2D PEFs. For the non-stationary PEF, I allowed the coefficients to vary smoothly over the image at every other pixel in both dimensions. Figure 2.6 shows the residual norm, $\mathbf{r_d}$, after convolving the PEFs with the synthetic image. From (2.24), the residual norm should be uncorrelated. It should have a white spectrum and be approximately zero. The non-stationary PEF does a better job at whitening the synthetic image.

Figure 2.7 shows the results obtained when a random, uncorrelated image is divided by the stationary and non-stationary PEFs. From (2.24), the result of this operation should be the original synthetic image. As expected, the stationary PEF produces a homogeneous output different from the original image. Although the image in its entirety is wrong, it contains linear events with the same slopes as those present in the original image. The non-stationary PEF on the other hand, produces an output similar to the original synthetic image. However, the amplitudes are

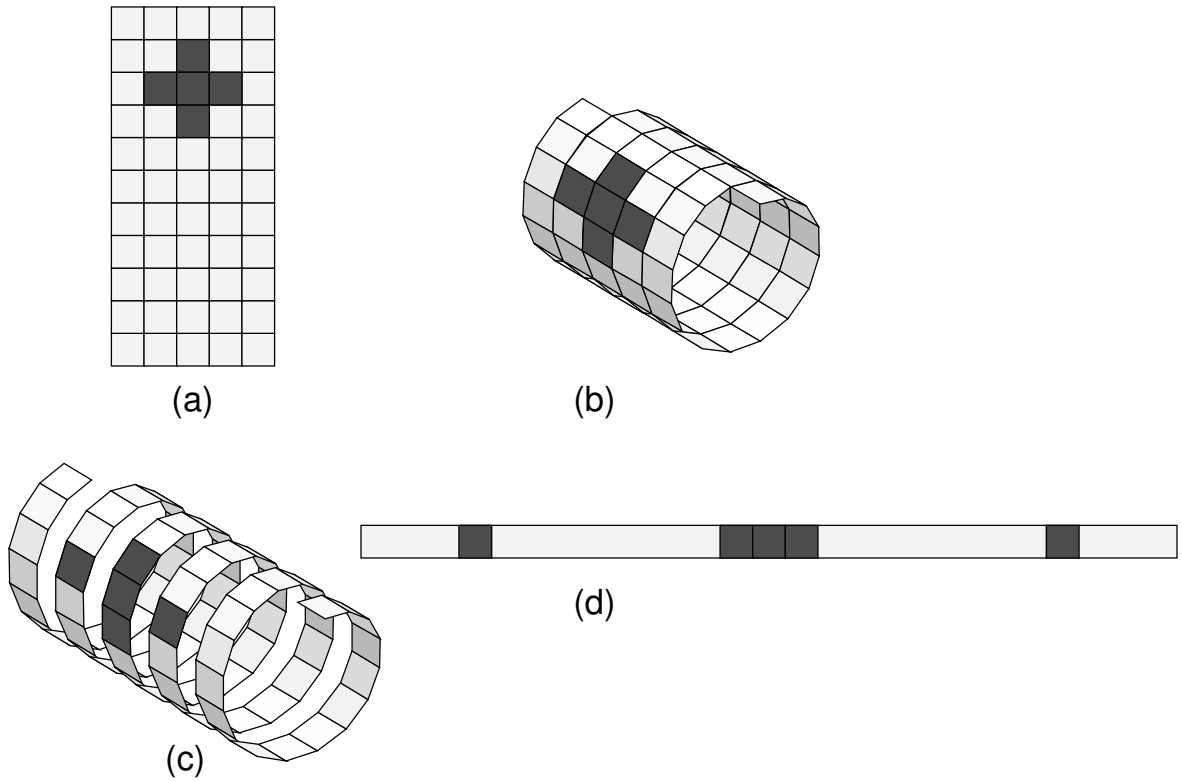

Figure 2.4: Conceptual steps involved in converting a 2-dimensional matrix to its helical coordinate transform. (a) 2-dimensional matrix. (b) Matrix in (a) wound into cylinder with the bottom of one column connected to the top of the next column. (c) Helix formed by stretching out the cylinder in (b). (d) Strip formed by unwinding the helix in (c). The strip in (d) is the helical transform of the matrix in (a). This figure was modified from Fomel and Claerbout (2003).

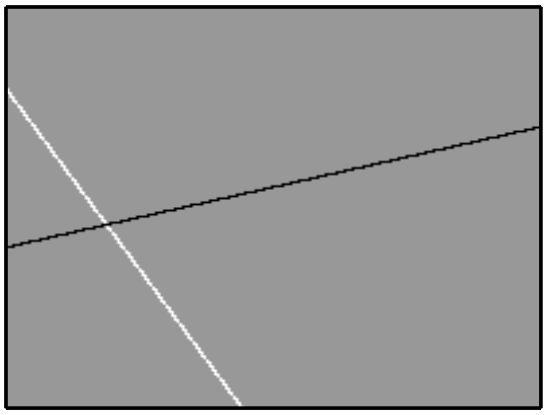

Figure 2.5: 2D synthetic image with two linear events that have conflicting dips and different amplitudes.

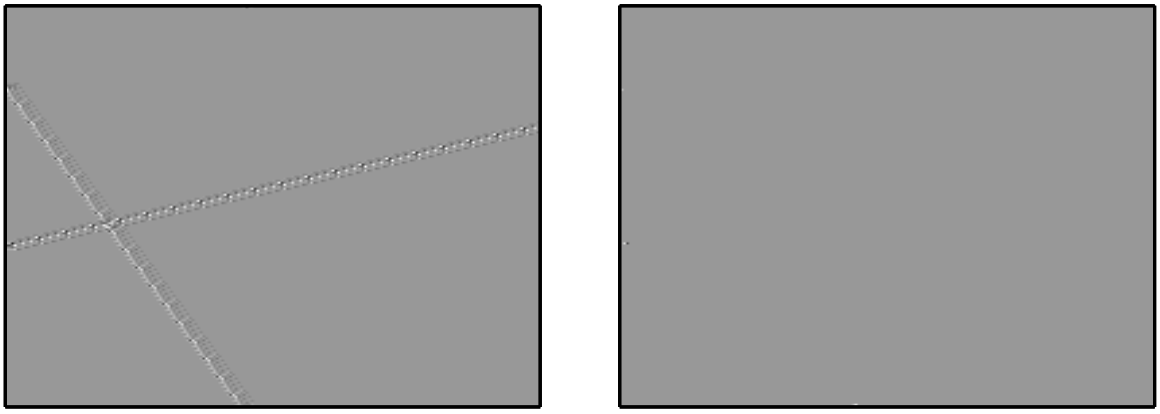

Figure 2.6: The residual image obtained after convolving the 2D image in Figure 2.5 with its stationary PEF (a); and its non-stationary PEF (b).

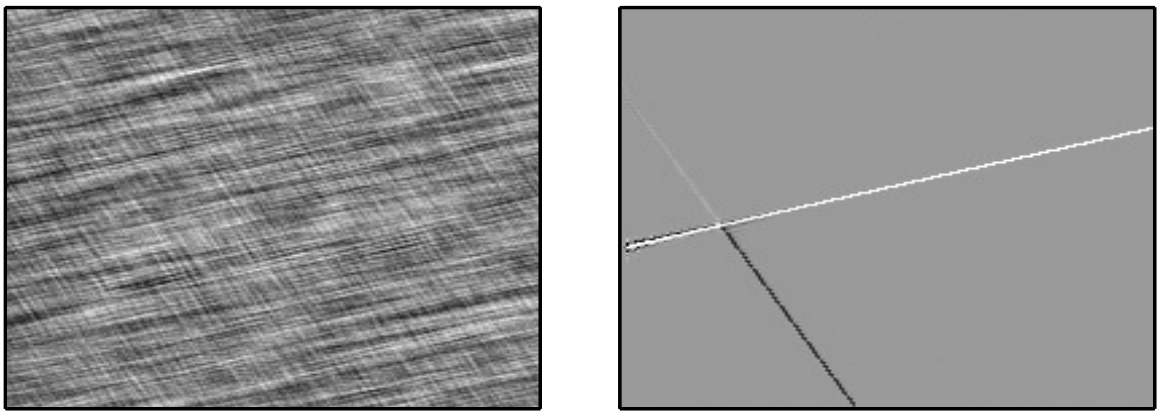

Figure 2.7: The synthesized image obtained after dividing a random incoherent image with (a) the stationary PEF of the image shown in Figure 2.5; and (b) the non-stationary PEF of the image shown in Figure 2.5.

wrong. This is because PEFs do not store amplitude information.

2.1.1.3 Data Estimation Example

Now that we have seen an example where a PEF is estimated, let us look at an example where missing data in an incomplete dataset are estimated. The first example uses the two-slope synthetic image presented in Figure 2.5. Figure 2.8 shows a 90% sparse subset of the complete image and the reconstructed images using a stationary PEF and a non-stationary PEF. The 90% sparse image is created by randomly discarding 10% of the data points in the image. I used the same PEFs presented in the previous section. With only 10% of the data missing, both PEFs do a good job at reconstructing the complete image. However, if we subsample the image to a 20% sparse image by discarding 80% of the data points, the reconstructed images (Figure 2.9) show significant differences. The reconstructed image with the stationary PEF shows streaks not present in the original image. The streaks on each event in the image have the same slope as the other event. As expected, the image

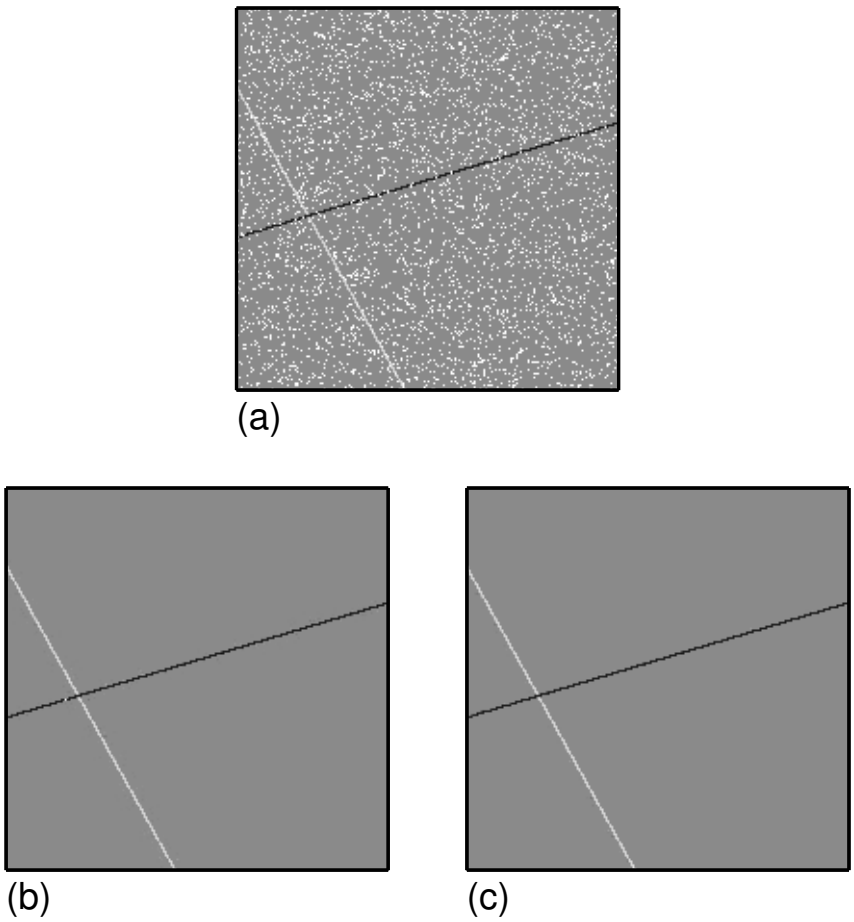

Figure 2.8: (a) A 90% sparse image subsampled from the image shown in Figure 2.5. (b) Reconstructed image using a stationary PEF. (c) Reconstructed image using a non-stationary PEF.

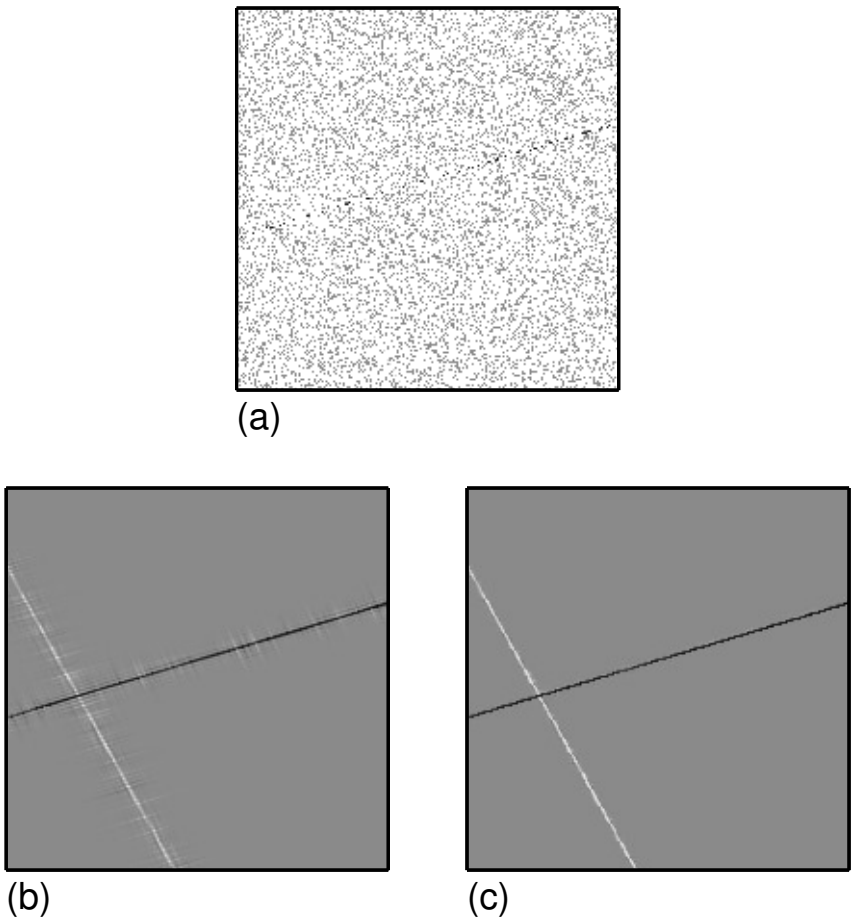

Figure 2.9: (a) A 20% sparse image subsampled from the image shown in Figure 2.5. (b) Reconstructed image using a stationary PEF. (c) Reconstructed image using a non-stationary PEF.

reconstructed using the non-stationary PEF is closer to the true image. The events are better resolved and are devoid of the streaks present in the image reconstructed using a stationary PEF.

The second example is a black and white image of my friend's car's tire. This image consists of smoothly varying features with sharp boundaries. As I did with the previous example, I computed 5x5-element, 2D, stationary and non-stationary PEFs using the complete image. The complete image and the images obtained by dividing a random, incoherent dataset by the PEFs are shown in Figure 2.10. With the stationary PEF, I obtained a smooth image that varies gradually from dark to light gray, left to right. With the non-stationary PEF, I obtained an image that is mostly similar to the original image. The non-stationary PEF does a good job in reconstructing distinct features in the image, including small features such as the grooves around the tire. After computing the PEF, I proceeded to estimate missing data from subsampled images. Figure 2.11 shows 10% and 50% sparse images. Reconstructed images using stationary PEFs are shown in Figure 2.12, and reconstructed images using non-stationary PEFs are shown in Figure 2.13. The reconstructed images obtained using the stationary PEFs are smoother than the true images when the input data are highly subsampled.

In the third example, I examine the effect of using an imperfect PEF in reconstructing missing data. I used the tire image presented in the previous example. Before computing the PEFs, I scaled the image by a factor of -0.01. I computed PEFs with the same size as those constructed earlier and used them to estimate the missing data in the same sparse images shown in the previous section. Results are shown in Figure 2.14. Simple inspection shows that they are in good agreement with the results obtained when perfect training images are used. The difference between the reconstructed images from the 10% and 50% sparse images using the perfect and imperfect PEFs are shown in Figure 2.15. In general, PEFs are insensitive to data amplitudes.

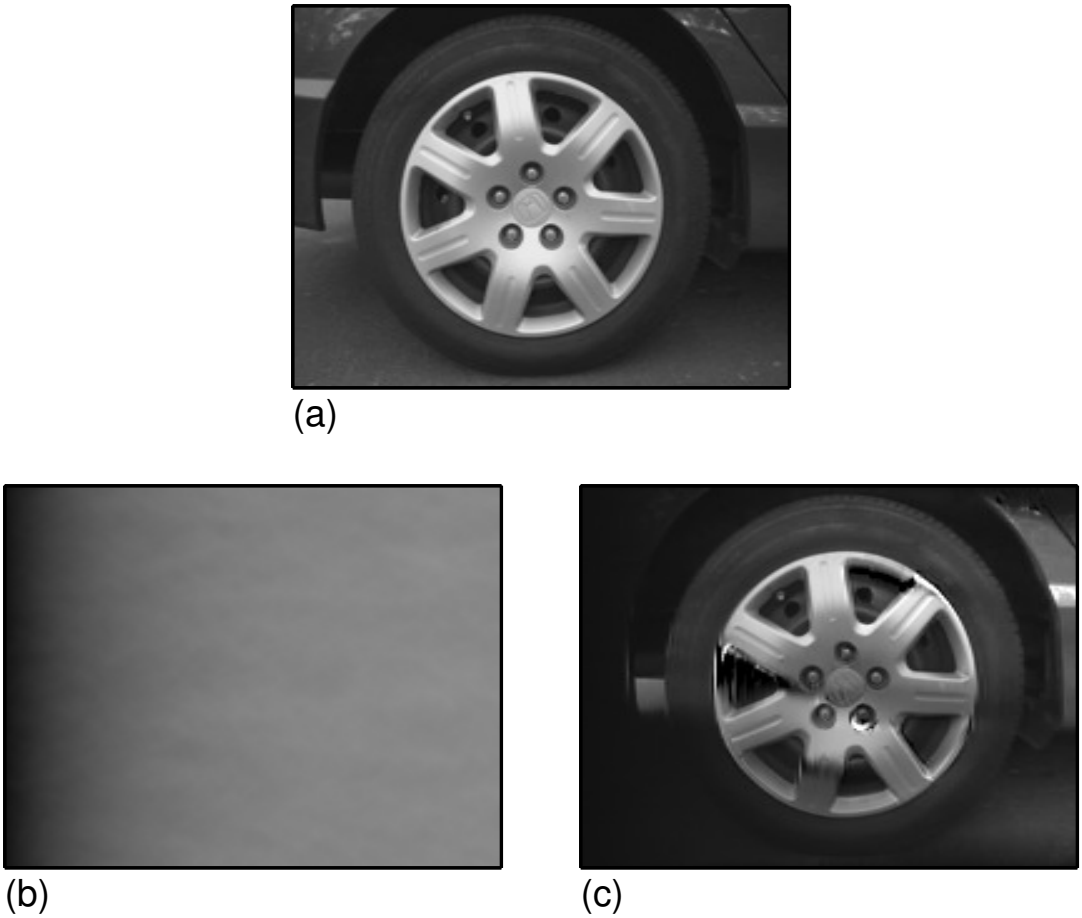

Figure 2.10: (a) A complete black and white image of a tire. (b) Synthesized image produced by dividing an incoherent random image by the stationary PEF for the image in (a). (c) Synthesized image produced by dividing an incoherent random image by the non-stationary PEF for the image in (a).

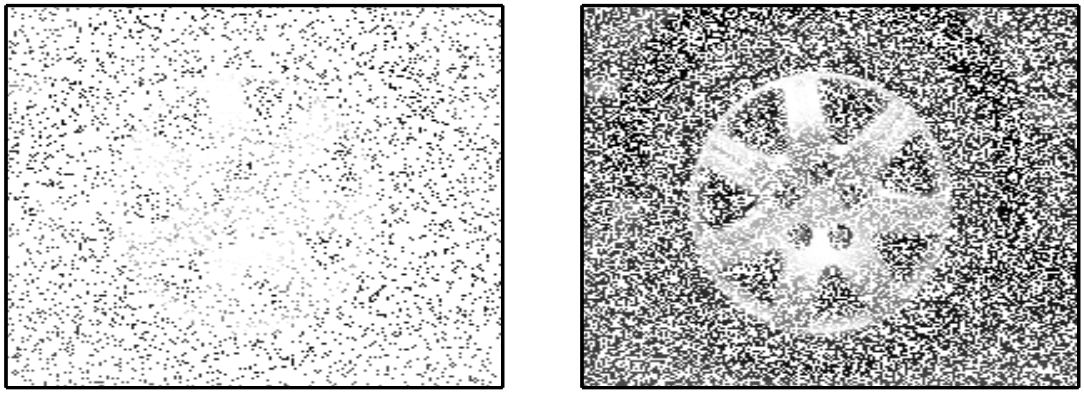

Figure 2.11: (a) The car tire image subsampled to 10%. (b) The car tire image subsampled to 50%.

Figure 2.12: The reconstructed car tire image using a stationary PEF. (a) From 10% sparse image. (b) From 50% sparse image.

(a) (b)

Figure 2.13: The reconstructed car tire image using a non-stationary PEF. (a) From 10% sparse image. (b) From 50% sparse image.

(a) (b)

Figure 2.14: The reconstructed car tire image using an imperfect, non-stationary PEF. (a) From 10% sparse image. (b) From 50% sparse image.

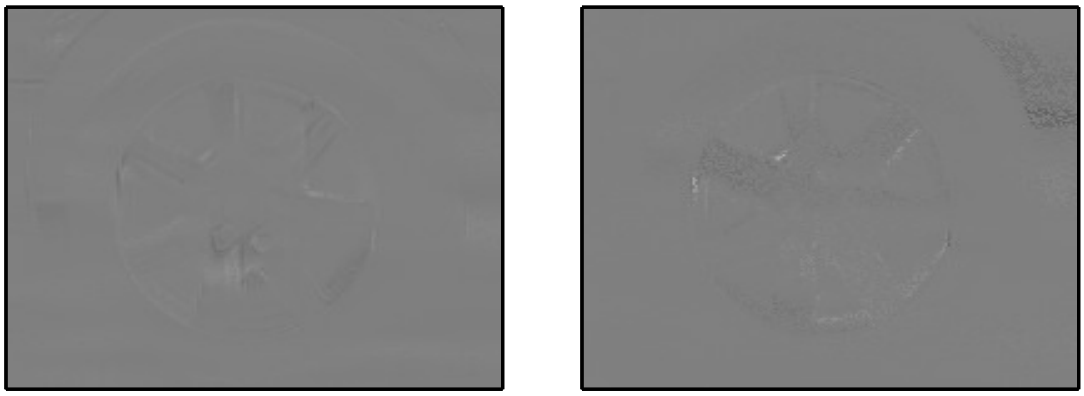

Figure 2.15: Difference between the images shown in Figure 2.13 and Figure 2.14 for (a) the 10% case; and (b) the 50% case. The color scale has range from minus to plus 10% of the maximum values in Figure 2.13.

2.1.1.4 Time-lapse Data-Estimation Implementation

The proposed approach assumes that a completely sampled baseline dataset exists in every time-lapse monitoring project. This dataset could be the one used in the site-selection process for the project under study. To obtain an estimate of the accumulated unrecorded data at each time k, I use an iterative strategy. The strategy begins with estimating the initial non-stationary PEF using a training dataset. I use the completely sampled baseline dataset as an initial estimate of the completely sampled dataset at each survey time. I then use the initial PEF to estimate the accumulated unrecorded dataset from the accumulated sparse dataset.

In the second iteration, I use the resulting estimated accumulated dataset from the first iteration to re-estimate the non-stationary PEF. This PEF is an improvement over the PEF obtained in the first iteration, since the new sparse measurements at each survey time are used. The updated PEF is then used to re-estimate the accumulated unrecorded dataset. The resulting estimate is an improvement over the previous estimate, because an improved PEF is used. I repeat this process until convergence is reached, that is, until the improvement in the estimated PEF or estimated data is negligible.

I repeat the entire iterative process each time new sparse datasets, $\mathbf{d}_s^k$, are added to the accumulated datasets, $\mathbf{t}_s^k$. By doing so, previously estimated unrecorded datasets, $\tilde{\mathbf{d}}_u^k$, are re-estimated. I repeat the iterative process because each additional sparse dataset provides data to further constrain the estimates of unrecorded data at previous times. Of course, after a certain amount of time, the improvement in the estimates of previously unrecorded data becomes negligible.

The equations solved in each iteration are described below.

Iteration 1

At time k, I compute the PEF with

$$\mathbf{f}_1^k = -\left(\mathbf{K}^{k\dagger}\mathbf{T}_c^{1\dagger}\mathbf{T}_c^1\mathbf{K}^k + \alpha^2\mathbf{K}^{k\dagger}\mathbf{R}^{k\dagger}\mathbf{R}^k\mathbf{K}^k\right)^{-1}\mathbf{K}^{k\dagger}\mathbf{T}_c^{1\dagger}\mathbf{t}_c^1\,, \tag{2.40}$$

where $\mathbf{f}_1^k$ is the non-stationary filter computed in the first iteration, $\mathbf{K}^k$ is the constrained filter-coefficient masking operator at time k, $\mathbf{R}^k$ is the regularization operator at time k, $\mathbf{t}_c^1$ is the completely sampled data at time 1 (the baseline data), and $\mathbf{T}_c^1$ is the convolution matrix for $\mathbf{t}_c^1$. The subscript representing non-stationarity used earlier, $\mathbf{ns}$, has been removed for clarity.

I estimate the missing data with

$$\tilde{\mathbf{t}}_{u,1}^k = -\left(\mathbf{H}^{k\dagger}\mathbf{F}_1^{k\dagger}\mathbf{F}_1^k\mathbf{H}^k\right)^{-1}\mathbf{H}^{k\dagger}\mathbf{F}_1^{k\dagger}\mathbf{F}_1^k\mathbf{t}_s^k\,, \tag{2.41}$$

where $\tilde{\mathbf{t}}_{u,1}^k$ is the estimated accumulated unrecorded data in the first iteration; and $\mathbf{F}_1^k$ is the convolution matrix for the non-stationary filter $\mathbf{f}_1^k$, at time k.

The estimated accumulated data is obtained using

$$\tilde{\mathbf{t}}_{c,1}^k = \mathbf{t}_s^k + \tilde{\mathbf{t}}_{u,1}^k\,, \tag{2.42}$$

which can also be written as

$$\tilde{\mathbf{t}}_{c,1}^k = \mathbf{t}_s^k - \left(\mathbf{H}^{k\dagger}\mathbf{F}_1^{k\dagger}\mathbf{F}_1^k\mathbf{H}^k\right)^{-1}\mathbf{H}^{k\dagger}\mathbf{F}_1^{k\dagger}\mathbf{F}_1^k\mathbf{t}_s^k\,. \tag{2.43}$$

Iteration 2

I compute the new PEF as follows:

$$\mathbf{f}_2^k = -\left(\mathbf{K}^{k\dagger}\tilde{\mathbf{T}}_{c,1}^{k\dagger}\tilde{\mathbf{T}}_{c,1}^{k}\mathbf{K}^k + \alpha^2\mathbf{K}^{k\dagger}\mathbf{R}^{k\dagger}\mathbf{R}^k\mathbf{K}^k\right)^{-1}\mathbf{K}^{k\dagger}\tilde{\mathbf{T}}_{c,1}^{k\dagger}\tilde{\mathbf{t}}_{c,1}^{k}\,, \tag{2.44}$$

where $\mathbf{f}_2^k$ is the non-stationary filter computed in the second iteration, $\tilde{\mathbf{t}}_{c,1}^k$ is the estimated accumulated data obtained in iteration 1, and $\tilde{\mathbf{T}}_{c,1}^k$ is the convolution matrix for $\tilde{\mathbf{t}}_{c,1}^k$.

I estimate the missing data with

$$\tilde{\mathbf{t}}_{u,2}^k = -\left(\mathbf{H}^{k\dagger}\mathbf{F}_2^{k\dagger}\mathbf{F}_2^k\mathbf{H}^k\right)^{-1}\mathbf{H}^{k\dagger}\mathbf{F}_2^{k\dagger}\mathbf{F}_2^k\mathbf{t}_s^k\,, \tag{2.45}$$

where $\tilde{\mathbf{t}}_{u,2}^k$ is the estimated accumulated unrecorded data in the second iteration, and $\mathbf{F}_2^k$ is the convolution matrix for the non-stationary filter $\mathbf{f}_2^k$ at time k.

The estimated accumulated data is obtained using

$$\tilde{\mathbf{t}}_{c,2}^k = \mathbf{t}_s^k + \tilde{\mathbf{t}}_{u,2}^k\,, \tag{2.46}$$

which can also be written as

$$\tilde{\mathbf{t}}_{c,2}^k = \mathbf{t}_s^k - \left(\mathbf{H}^{k\dagger}\mathbf{F}_2^{k\dagger}\mathbf{F}_2^k\mathbf{H}^k\right)^{-1}\mathbf{H}^{k\dagger}\mathbf{F}_2^{k\dagger}\mathbf{F}_2^k\mathbf{t}_s^k\,. \tag{2.47}$$

Iteration 3

I compute the new PEF as follows:

$$\mathbf{f}_3^k = -\left(\mathbf{K}^{k\dagger}\tilde{\mathbf{T}}_{c,2}^{k\dagger}\tilde{\mathbf{T}}_{c,2}^{k}\mathbf{K}^k + \alpha^2\mathbf{K}^{k\dagger}\mathbf{R}^{k\dagger}\mathbf{R}^k\mathbf{K}^k\right)^{-1}\mathbf{K}^{k\dagger}\tilde{\mathbf{T}}_{c,2}^{k\dagger}\tilde{\mathbf{t}}_{c,2}^{k}\,, \tag{2.48}$$

where $\mathbf{f}_2^k$ is the non-stationary filter computed in the third iteration, $\tilde{\mathbf{t}}_{c,2}^k$ is the estimated accumulated data obtained in iteration 2, and $\tilde{\mathbf{T}}_{c,2}^k$ is the convolution matrix for $\tilde{\mathbf{t}}_{c,2}^k$.

I estimate the missing data with

$$\tilde{\mathbf{t}}_{u,3}^{k} = -\left(\mathbf{H}^{k\dagger}\mathbf{F}_{3}^{k\dagger}\mathbf{F}_{3}^{k}\mathbf{H}^{k}\right)^{-1}\mathbf{H}^{k\dagger}\mathbf{F}_{3}^{k\dagger}\mathbf{F}_{3}^{k}\mathbf{t}_{s}^{k}\,, \tag{2.49}$$

where $\tilde{\mathbf{t}}_{u,3}^{k}$ is the estimated accumulated unrecorded data in the second iteration, and $\mathbf{F}_{3}^{k}$ is the convolution matrix for the non-stationary filter $\mathbf{f}_{3}^{k}$, at time k.

The estimated accumulated data is obtained using,

$$\tilde{\mathbf{t}}_{c,3}^{k} = \mathbf{t}_{s}^{k} + \tilde{\mathbf{t}}_{u,3}^{k} \tag{2.50}$$

which can also be written as

$$\tilde{\mathbf{t}}_{c,3}^{k} = \mathbf{t}_{s}^{k} - \left(\mathbf{H}^{k\dagger}\mathbf{F}_{3}^{k\dagger}\mathbf{F}_{3}^{k}\mathbf{H}^{k}\right)^{-1}\mathbf{H}^{k\dagger}\mathbf{F}_{3}^{k\dagger}\mathbf{F}_{3}^{k}\mathbf{t}_{s}^{k}\,. \tag{2.51}$$

We can summarize the above iteration process as follows:

$$\mathbf{f}_{i}^{k} = \begin{cases} -\left(\mathbf{K}^{k\dagger}\mathbf{T}_{c}^{1\dagger}\mathbf{T}_{c}^{1}\mathbf{K}^{k} + \alpha^{2}\mathbf{K}^{k\dagger}\mathbf{R}^{k\dagger}\mathbf{R}^{k}\mathbf{K}^{k}\right)^{-1}\mathbf{K}^{k\dagger}\mathbf{T}_{c}^{1\dagger}\mathbf{t}_{c}^{1} & ;\ i=1 \\ -\left(\mathbf{K}^{k\dagger}\tilde{\mathbf{T}}_{c,i-1}^{k\dagger}\tilde{\mathbf{T}}_{c,i-1}^{k}\mathbf{K}^{k} + \alpha^{2}\mathbf{K}^{k\dagger}\mathbf{R}^{k\dagger}\mathbf{R}^{k}\mathbf{K}^{k}\right)^{-1}\mathbf{K}^{k\dagger}\tilde{\mathbf{T}}_{c,i-1}^{k\dagger}\tilde{\mathbf{t}}_{c,i-1}^{k} & ;\ i>1 \end{cases} \tag{2.52}$$

$$\tilde{\mathbf{t}}_{c,i}^{k} = \mathbf{t}_{s}^{k} - \left(\mathbf{H}^{k\dagger}\mathbf{F}_{i}^{k\dagger}\mathbf{F}_{i}^{k}\mathbf{H}^{k}\right)^{-1}\mathbf{H}^{k\dagger}\mathbf{F}_{i}^{k\dagger}\mathbf{F}_{i}^{k}\mathbf{t}_{s}^{k} \quad ;\ \forall i \tag{2.53}$$

where the subscript i represents the iteration number.

2.1.2 Minimum-Weighted-Norm Interpolation

Minimum-weighted-norm interpolation (MWNI) (Liu, 2004; Liu and Sacchi, 2004), like the algorithms presented in Spitz (1991) and Wang (2002), is a frequency-domain estimation algorithm. With MWNI, missing data are estimated along spatial dimensions, one temporal frequency at a time.

Following the derivation in Liu (2004), let $\mathbf{d}$ be the frequency-domain representation of a completely sampled dataset, such that

$$\mathbf{d} = [\ d_0\ d_1\ d_2\ \cdots\ d_{N-1}\ ]^T\ ; \quad \textit{N-1 = last sample number}\ . \tag{2.54}$$

We can define a sampling operator, $\mathbf{S}$, that selects a set of measured samples from a complete set of samples, such that

$$\mathbf{d}_s = \mathbf{S}\mathbf{d}\ . \tag{2.55}$$

where $\mathbf{d}_s$ is the sparse, measured data. I define the set of unrecorded data samples, $\mathbf{d}_u$, that satisfies

$$\mathbf{d} = \mathbf{d}_s + \mathbf{d}_u\ . \tag{2.56}$$

MWNI is used to compute the set of samples $\tilde{\mathbf{d}}_u$, that gives an estimate of the completely sampled dataset $\tilde{\mathbf{d}}$:

$$\tilde{\mathbf{d}} = \mathbf{d}_s + \tilde{\mathbf{d}}_u\ . \tag{2.57}$$

Note that the slow-time indices have been excluded in (2.54), (2.55), (2.56), and (2.57). This is because I begin by deriving the MWNI equation for the non-time-lapse case. Slow-time indices will be included later in this section, when the MWNI equation for the time-lapse case is given.

I define the discrete Fourier transform (DFT) of $\mathbf{d}$ as follows:

$$D_k = \frac{1}{\sqrt{N}} \sum_{n=0}^{N-1} d_n e^{-2\pi i \frac{kn}{N}} \qquad k = 0, 1, 2, \cdots, N-1 \tag{2.58}$$

and

$$\mathbf{D} = [\ D_0\ D_1\ D_2\ \cdots\ D_{N-1}\ ]^T\ . \tag{2.59}$$

I also define the inverse discrete Fourier transform (IDFT) of $\mathbf{D}$ as

$$d_n = \frac{1}{\sqrt{N}} \sum_{k=0}^{N-1} D_k e^{2\pi i \frac{kn}{N}} \qquad k = 0, 1, 2, \cdots, N-1 \; . \tag{2.60}$$

Using compact notation, I represent the DFT and IDFT in (2.58) and (2.60) as,

$$\mathbf{D} = \mathbf{F}\mathbf{d} \tag{2.61}$$

and

$$\mathbf{d} = \mathbf{F}^H \mathbf{D} \tag{2.62}$$

respectively, where $\mathbf{F}$ is the DFT unitary matrix, and the superscript H denotes the complex conjugate transpose. The missing-data problem can be solved using the method of Lagrange multipliers by minimizing

$$\mathbf{\Phi} = \lambda^T \left(\mathbf{S}\tilde{\mathbf{d}} - \mathbf{d}_s \right) + \left|\left| \tilde{\mathbf{d}} \right|\right|_W^2 \; . \tag{2.63}$$

where $\left|\left| \tilde{\mathbf{d}} \right|\right|_W^2$ is the weighted norm of $\tilde{\mathbf{d}}$, and λ is a vector of Lagrange multipliers. Equation (2.63) implies that we minimize

$$\left|\left| \tilde{\mathbf{d}} \right|\right|_W^2 \tag{2.64}$$

subject to

$$\mathbf{S}\tilde{\mathbf{d}} - \mathbf{d}_s = 0 \; . \tag{2.65}$$

The wave-number-domain norm used is defined as

$$\left|\left| \tilde{\mathbf{d}} \right|\right|_W^2 = \sum_{k \in \mathcal{K}} \frac{\tilde{D}_k^* \tilde{D}_k}{P_k^2} \; , \tag{2.66}$$

where $\mathcal{K}$ represents the region of spectral support, and the coefficient P_k is the spectral power at wave number k (Cabrera and Parks, 1991).

We proceed with the derivation by introducing a diagonal matrix, $\mathbf{\Lambda}$, with elements

$$\Lambda_k = \begin{cases} P_k^2, & k \in \mathcal{K} \\ \\ 0, & k \notin \mathcal{K} \end{cases} , \tag{2.67}$$

and a pseudo inverse defined as

$$\Lambda_k^\dagger = \begin{cases} 1/P_k^2, & k \in \mathcal{K} \\ \\ 0, & k \notin \mathcal{K} \end{cases} . \tag{2.68}$$

Combining (2.66) and (2.68), we get

$$\left|\left|\tilde{\mathbf{d}}\right|\right|_W^2 = \tilde{\mathbf{D}}^H \mathbf{\Lambda}^\dagger \tilde{\mathbf{D}} \, . \tag{2.69}$$

Using (2.62) in (2.69), we get

$$\left|\left|\tilde{\mathbf{d}}\right|\right|_W^2 = \tilde{\mathbf{d}}^H \mathbf{F}^H \mathbf{\Lambda}^\dagger \mathbf{F} \tilde{\mathbf{d}} \, , \tag{2.70}$$

$$= \tilde{\mathbf{d}}^H \mathbf{Q}^\dagger \tilde{\mathbf{d}} \, , \tag{2.71}$$

where $\mathbf{Q}^\dagger = \mathbf{F}^H \mathbf{\Lambda}^\dagger \mathbf{F}$. Note that $\mathbf{Q} = \mathbf{F}^H \mathbf{\Lambda} \mathbf{F}$. Operators $\mathbf{Q}$ and $\mathbf{Q}^\dagger$ are band-limiting operators, and they annihilate spectral components $k \notin \mathcal{K}$.

Now that the pieces of the puzzle are set, we restate (2.63) as

$$\mathbf{\Phi} = \lambda^T \left(\mathbf{S} \tilde{\mathbf{d}} - \mathbf{d}_s \right) + \tilde{\mathbf{d}}^H \mathbf{Q}^\dagger \tilde{\mathbf{d}} \, . \tag{2.72}$$

Minimizing (2.72) by differentiation with respect to $\tilde{\mathbf{d}}$ and setting it to 0 gives

$$0 = \mathbf{S}^T \lambda + 2 \mathbf{Q}^\dagger \tilde{\mathbf{d}} \, . \tag{2.73}$$

This implies

$$\tilde{\mathbf{d}} = - \left(2 \mathbf{Q}^\dagger \right)^{-1} \mathbf{S}^T \lambda = - \frac{1}{2} \mathbf{Q} \mathbf{S}^T \lambda \, . \tag{2.74}$$

Substituting $\tilde{\mathbf{d}}$ from (2.74) in (2.65), we obtain

$$\lambda = -2\left(\mathbf{S}\mathbf{Q}\mathbf{S}^T\right)^{-1}\mathbf{d}_s\ . \tag{2.75}$$

Substituting λ from (2.75) in (2.74), we obtain

$$\tilde{\mathbf{d}} = \mathbf{Q}\mathbf{S}^T\left(\mathbf{S}\mathbf{Q}\mathbf{S}^T\right)^{-1}\mathbf{d}_s\ . \tag{2.76}$$

Equation (2.76) is the MWNI equation used to obtain a completely populated estimated dataset, $\tilde{\mathbf{d}}$, from a sparsely populated dataset, $\mathbf{d}_s$.

If the sparsely sampled data contain some noise, and we wish to obtain the least-squares estimate of the missing data, the objective function minimized is

$$\mathbf{\Phi} = \left|\left|\mathbf{S}\tilde{\mathbf{d}} - \mathbf{d}_s\right|\right|^2 + \alpha^2\left|\left|\tilde{\mathbf{d}}\right|\right|_W^2\ , \tag{2.77}$$

which can be rewritten as

$$\mathbf{\Phi} = \left(\mathbf{S}\tilde{\mathbf{d}} - \mathbf{d}_s\right)^2 + \alpha^2\tilde{\mathbf{d}}^H\mathbf{Q}^\dagger\tilde{\mathbf{d}}\ , \tag{2.78}$$

$$\mathbf{\Phi} = \left(\mathbf{S}\tilde{\mathbf{d}} - \mathbf{d}_s\right)^T\left(\mathbf{S}\tilde{\mathbf{d}} - \mathbf{d}_s\right) + \alpha^2\tilde{\mathbf{d}}^H\mathbf{Q}^\dagger\tilde{\mathbf{d}}\ , \tag{2.79}$$

where α^2 is the trade-off parameter of the problem. We can write an equivalent equation for the least squares MWNI equation:

$$\begin{pmatrix}\mathbf{S}\\ \alpha\mathbf{W}\end{pmatrix}\tilde{\mathbf{d}} \approx \begin{pmatrix}\mathbf{d}_s\\ \mathbf{0}\end{pmatrix}\ , \tag{2.80}$$

where the matrix of weights $\mathbf{W}$ is expressed as

$$\mathbf{W} = \mathbf{\Lambda}^{\dagger 1/2}\mathbf{F}\ . \tag{2.81}$$

In the numerical implementation of (2.80) we introduce a new variable: $\mathbf{z} = \mathbf{W}\tilde{\mathbf{d}}$.

Equation (2.80) becomes

$$\begin{pmatrix} \mathbf{S}\mathbf{W}^{\dagger} \\ \alpha \end{pmatrix} \mathbf{z} \approx \begin{pmatrix} \mathbf{d}_s \\ \mathbf{0} \end{pmatrix} . \tag{2.82}$$

If we set the trade-off parameter to $\alpha = 0$, we obtain

$$\mathbf{S}\mathbf{W}^{\dagger}\mathbf{z} \approx \mathbf{d}_s . \tag{2.83}$$

I solve (2.83) for $\mathbf{z}$ using the conjugate-gradient method (Hestenes and Stiefel, 1952). By setting the trade-off parameter to $\alpha = 0$, we allow the number of iterations in the conjugate gradient method to serve as the regularization parameter (Hansen, 1998).

Since the spectrum of the complete data is needed to compute the matrix of weights, $\mathbf{\Lambda}$, but the complete data is unknown, $\mathbf{\Lambda}$ is obtained iteratively, starting with an initial guess. In my implementation, I start with an initial guess of $P_k = 1,\ k \in \mathcal{K}$. I calculate $\mathbf{P}$ using the broad shape of the estimated spectrum. This is done by convolving the estimated data spectrum in the frequency domain with the DFT of a Hanning window. That is,

$$\mathbf{P} = \mathbf{A} \otimes \mathbf{D} , \tag{2.84}$$

where $\mathbf{A}$ is the DFT of the Hanning window, $\mathbf{a}$, and $\otimes$ denotes convolution.

In the time-lapse data-estimation problem, $\mathbf{d}_s$ in (2.76) and (2.83) is a frequency slice through the 1D Fourier transform (along the fast-time axis) of the accumulated sparse dataset at time k. If we call this quantity $\mathbf{t}_s^k$, (2.76) and (2.83) for the time-lapse data-estimation problem are

$$\tilde{\mathbf{t}}_c^k = \mathbf{Q}^k \mathbf{S}^{kT} \left(\mathbf{S}^k \mathbf{Q}^k \mathbf{S}^{kT} \right)^{-1} \mathbf{t}_s^k , \tag{2.85}$$

and

$$\mathbf{S}^k \mathbf{W}^{k\dagger} \mathbf{z}^k \approx \mathbf{t}_s^k , \tag{2.86}$$

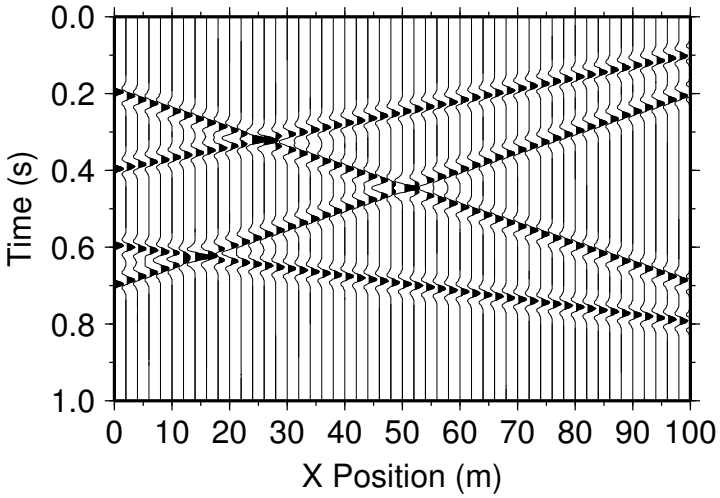

Figure 2.16: Complete 2D synthetic seismic section with linear events.

respectively. In (2.85), $\tilde{\mathbf{t}}_c^k$ is the corresponding frequency slice through the 1D Fourier transform (along the fast-time axis) of the accumulated estimated dataset at time k.

2.1.2.1 2D Synthetic examples

To demonstrate the efficiency of MWNI in reconstructing missing seismic traces, I present two examples. In the first example, I show the method's efficiency in reconstructing linear events in a seismic section. Figure 2.16 shows a complete seismic section with linear events of different slopes. The complete section is made up of 50 traces. I simulate incomplete data by discarding some traces from the complete dataset to produce 90%, 70%, 50%, 30%, 20% and 10% sparse datasets. Both regularly spaced and randomly spaced missing traces were simulated. The resulting incomplete datasets are shown in Figures 2.17 and 2.18. In the real world, we might need to estimate regularly spaced missing traces when a completely sampled dataset is needed for a processing step like migration. Likewise, we might need to estimate randomly spaced missing traces in a situation where some receivers on a

receiver cable had failed. To estimate the missing traces in Figures 2.17 and 2.18, I first perform a Fourier transform along the time axes and use the results as input into the MWNI algorithm, where estimation is done separately for each frequency. Even though the input data for each reconstruction is two-dimensional, estimation is done in one dimension, the spatial dimension. Figures 2.19 and 2.20 show the corresponding interpolation results.

In Figures 2.21 and 2.22, I show the spectral weights, P_k^2, obtained at iterations 0 through 5 of the reconstructions for the 30% sparse dataset with linear events. In Figure 2.21, the frequency is 5 Hz, and in Figure 2.22, it is 25 Hz. Notice how the shapes of the spectral weights approach the shapes of the power spectra of the true dataset at those frequencies. The flat shape at iteration 0 is a result of an initial guess of 1. As the iteration continues and the weights are re-estimated, the estimated shapes move closer to the true shapes.

In the second example, I show the efficiency of MWNI in reconstructing non-linear events in a seismic section. Figure 2.23 shows a complete seismic section with non-linear events. In this case, the complete section is made up of 100 traces. As was the case with the first example, I simulated incomplete data by discarding some traces from the complete dataset to produce 90%, 70%, 50%, 30%, 20% and 10% sparse datasets. Both regularly spaced and randomly spaced missing traces were simulated. The resulting incomplete datasets are shown in Figures 2.24 and 2.25. Using the same data-estimation steps as in the first example, I obtain the reconstructed sections shown in Figures 2.26 and 2.27.

Figures 2.19, 2.20, 2.26, and 2.27 show that MWNI does not adequately reconstruct extremely sparse datasets like the 10% sparse data sections in my example. This is not surprising, since reconstructing datasets that sparse would require some prior information for improved accuracy. In addition, a comparison of the results with linear events and hyperbolic events shows that MWNI does a better job at predicting linear events. This is evident in the signal-to-noise ratios of the resulting reconstructed sections in both cases.

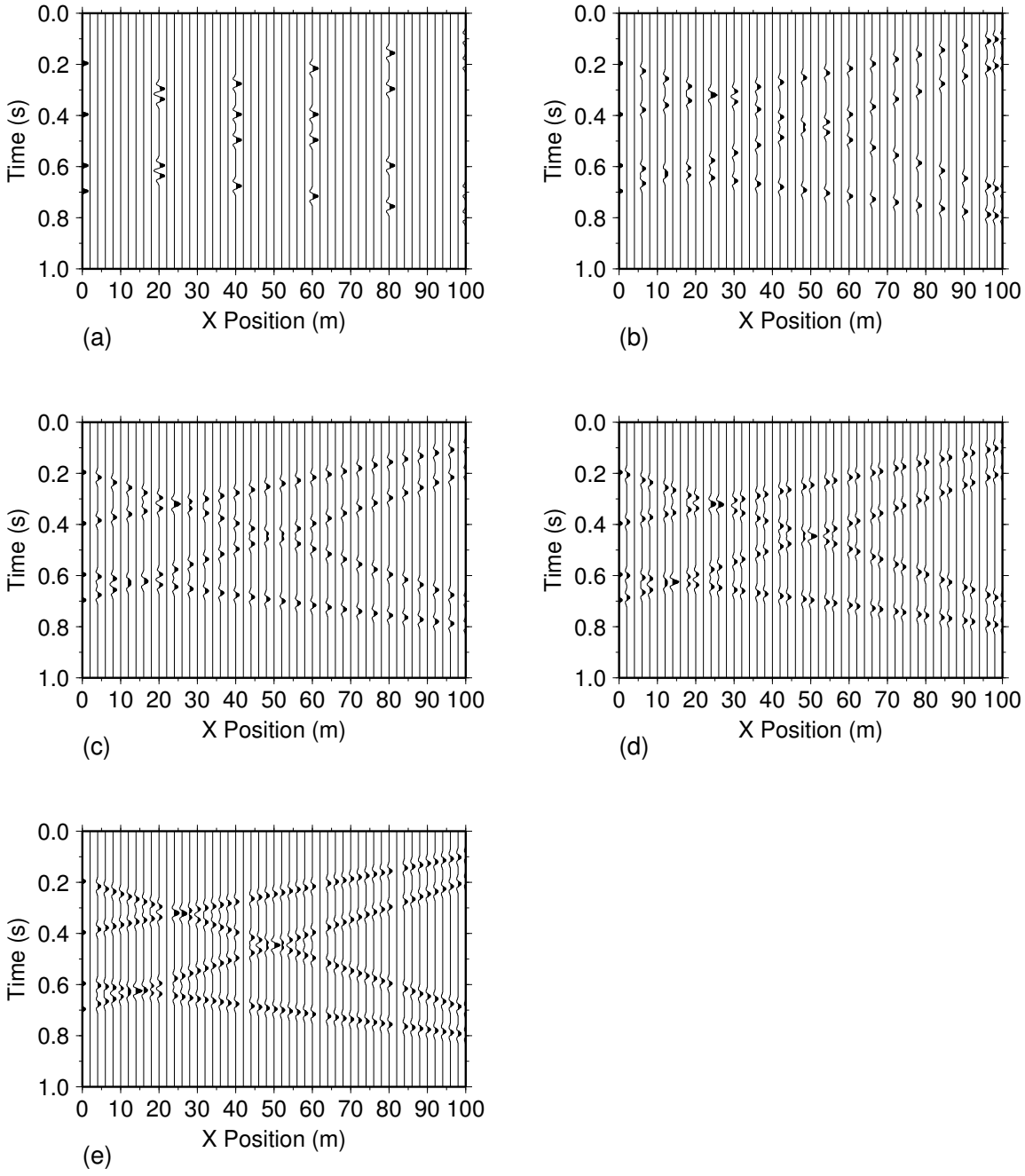

Figure 2.17: Sparse seismic sections derived from the section shown in Figure 2.16 with regularly spaced missing traces. (a) 10% sparse data. (b) 30% sparse data. (c) 50% sparse data. (d) 70% sparse data. (e) 90% sparse data.

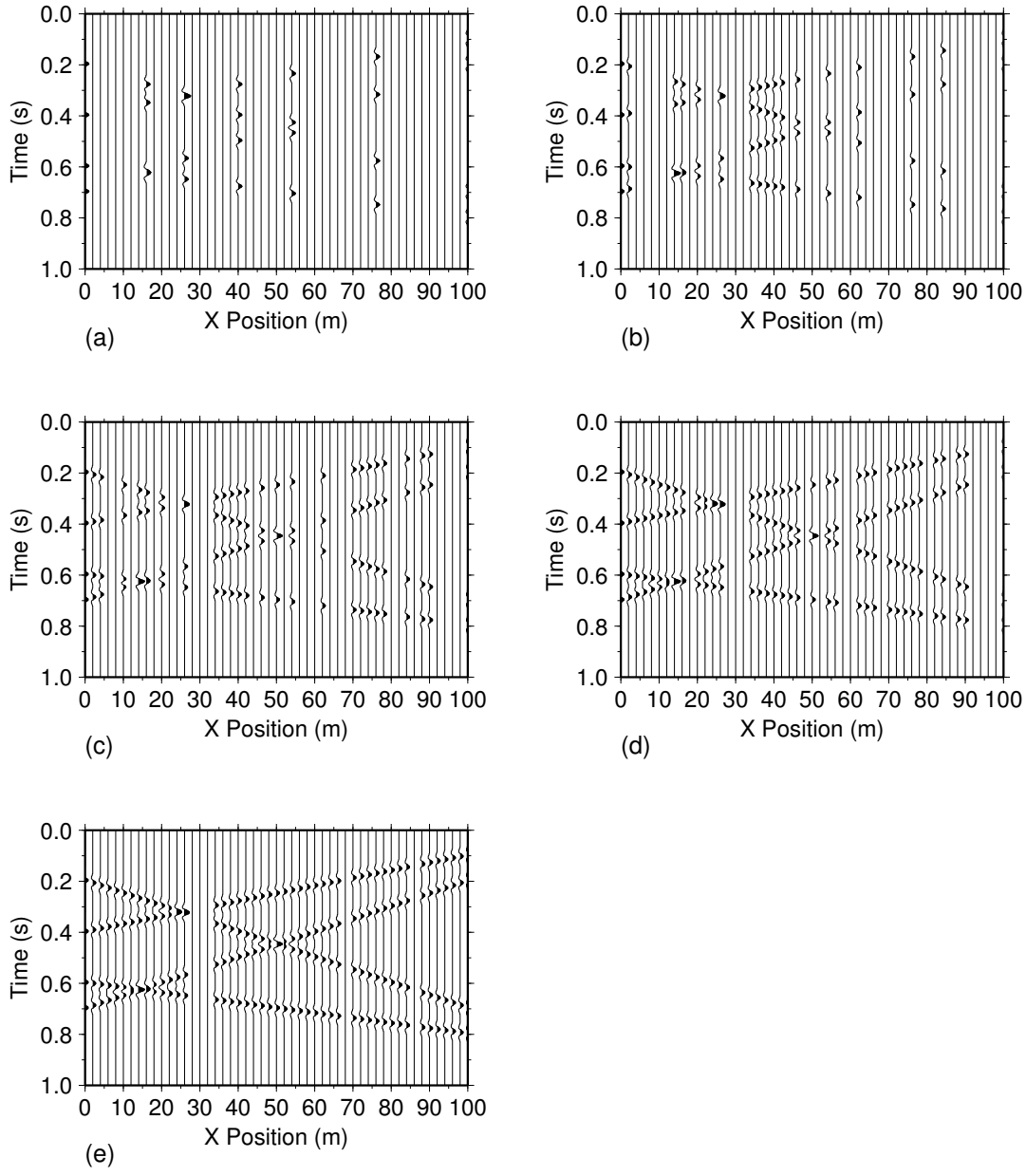

Figure 2.18: Sparse seismic sections derived from the section shown in Figure 2.16 with randomly spaced missing traces. (a) 10% sparse data. (b) 30% sparse data. (c) 50% sparse data. (d) 70% sparse data. (e) 90% sparse data.

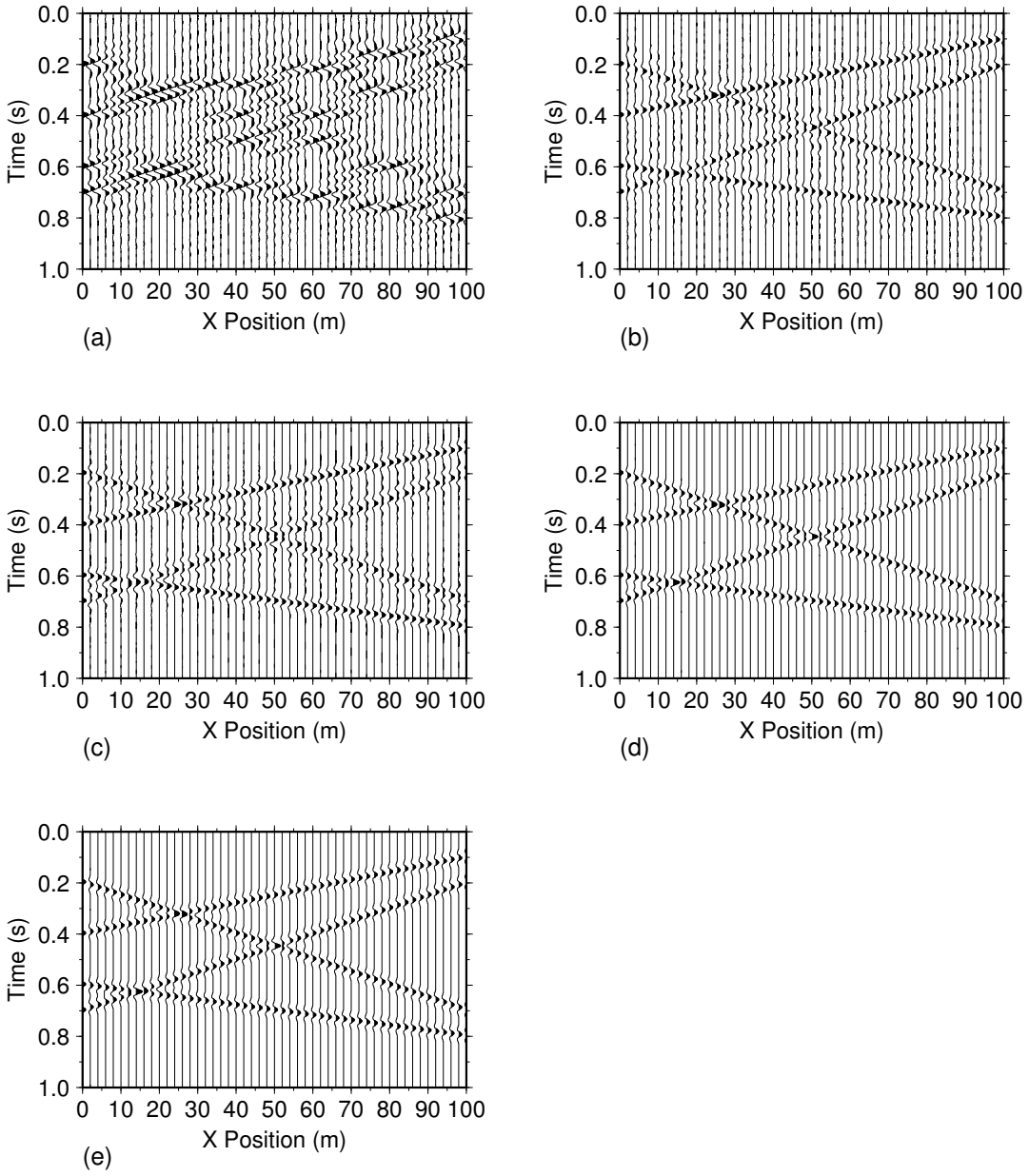

Figure 2.19: Reconstructed seismic sections from the sparse sections shown in Figure 2.17 with regularly spaced missing traces. (a) Reconstructed section from 10% sparse data. (b) Reconstructed section from 30% sparse data. (c) Reconstructed section from 50% sparse data. (d) Reconstructed section from 70% sparse data. (e) Reconstructed section from 90% sparse data.

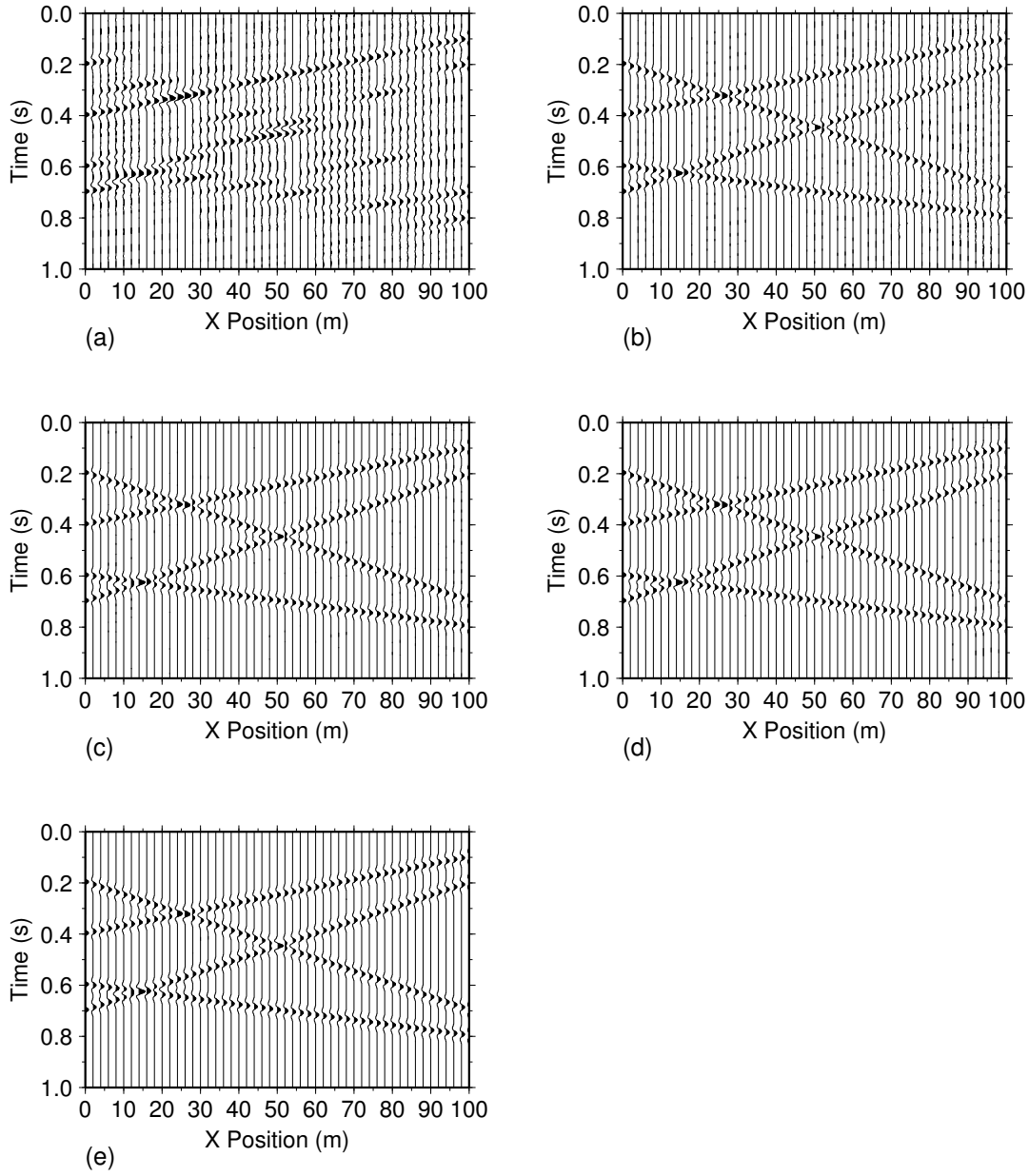

Figure 2.20: Reconstructed seismic sections from the sparse sections shown in Figure 2.18 with randomly spaced missing traces. (a) Reconstructed section from 10% sparse data. (b) Reconstructed section from 30% sparse data. (c) Reconstructed section from 50% sparse data. (d) Reconstructed section from 70% sparse data. (e) Reconstructed section from 90% sparse data.

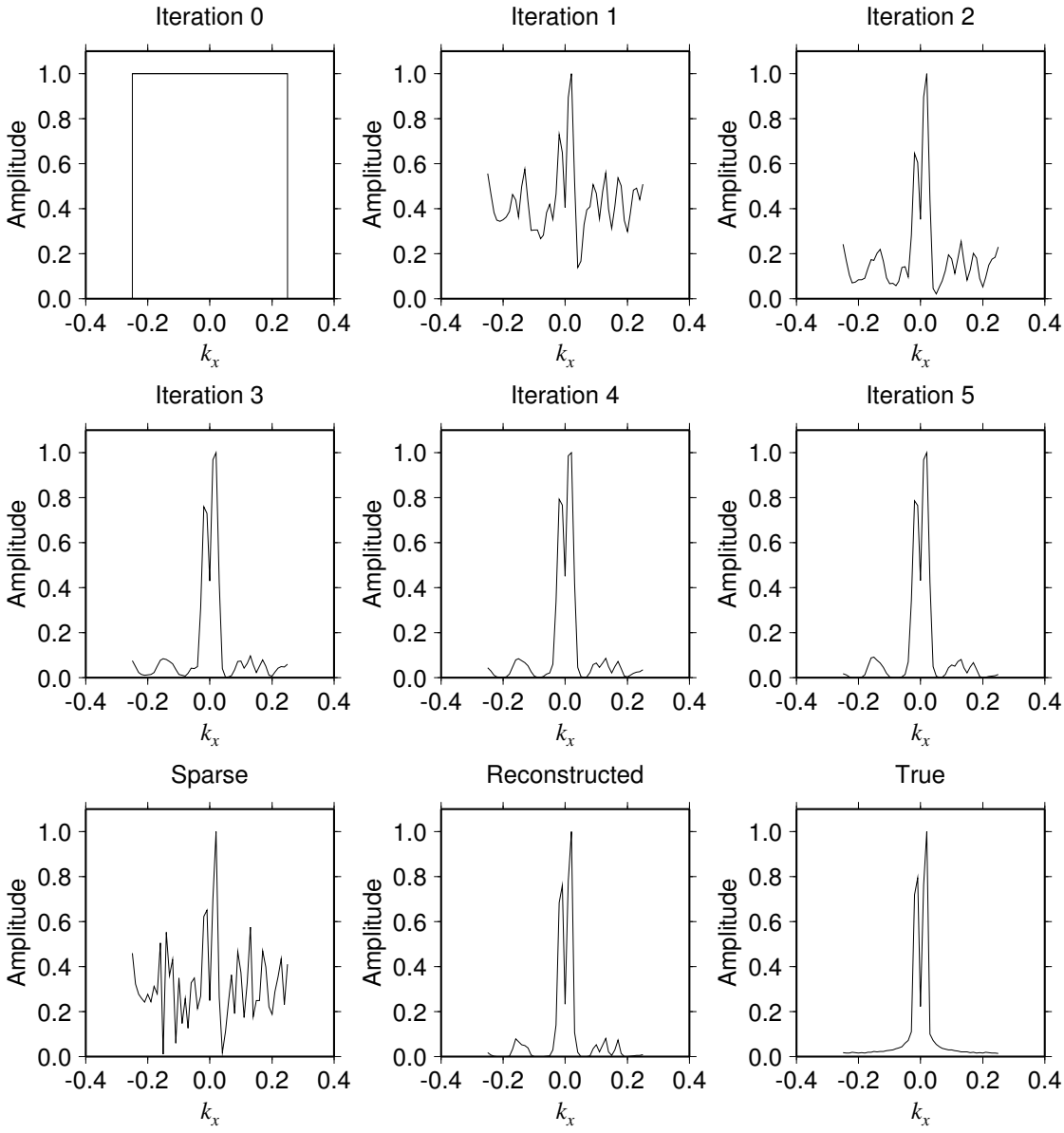

Figure 2.21: The spectral weights P_k^2, obtained at iterations 0 through 5 for the 30% sparse data section with linear events at 5Hz, compared to the power spectra of the sparse data, final reconstructed data, and the true data at the same frequency.

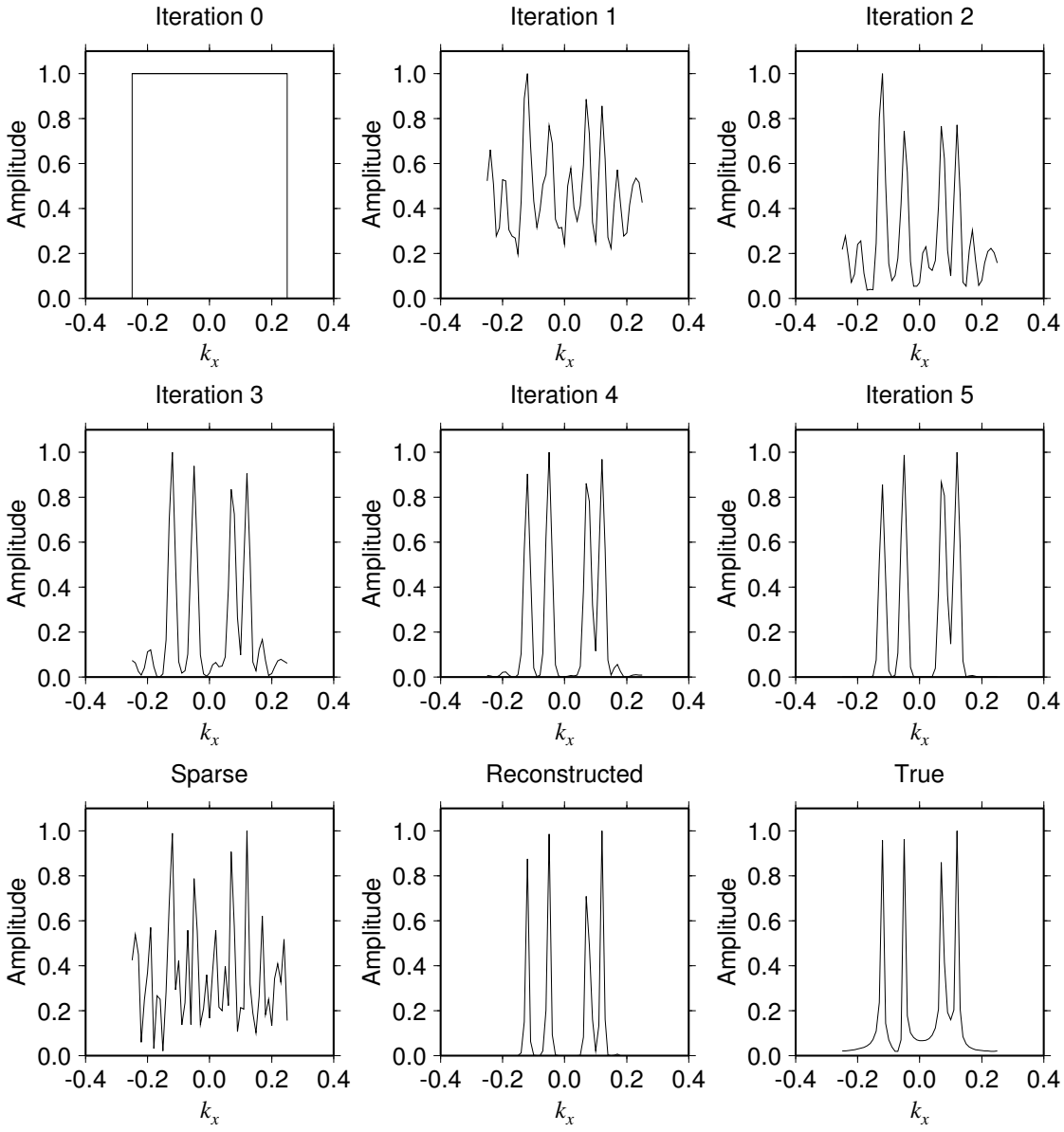

Figure 2.22: The spectral weights P_k^2, obtained at iterations 0 through 5 for the 30% sparse data section with linear events at 25Hz, compared to the power spectra of the sparse data, final reconstructed data, and the true data at the same frequency.

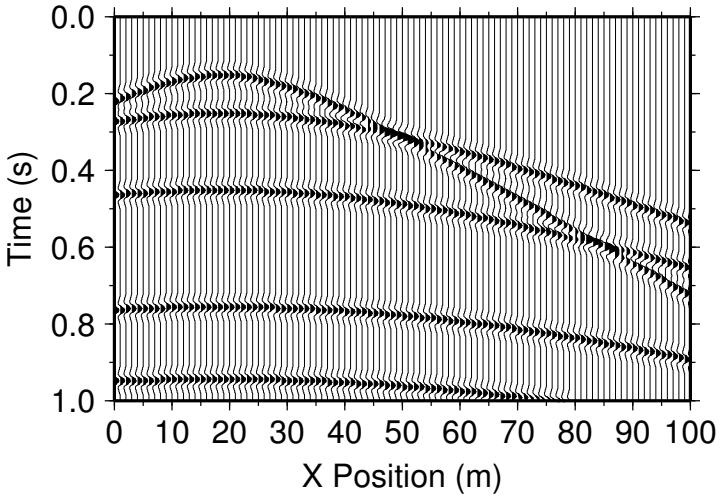

Figure 2.23: Complete 2D synthetic seismic section with non-linear events.

2.1.2.2 3D Synthetic examples

In order to reconstruct a dataset with many non-linear events, the patching technique (Claerbout, 2008) can be used. This technique involves splitting the dataset into subsets, operating on those subsets, and then returning them to their original positions. In this case, the dataset is split into subsets where events are close to being linear. To illustrate this, I use the 3D quarter-dome synthetic dataset (Claerbout, 2008). Sections through the 3D complete, 30% sparse, and reconstructed quarter-dome volume are shown in Figure 2.28. It is evident in Figure 2.28(c) that the reconstruction in the regions with severe curvature is inaccurate. If we apply the patching technique to the 30% sparse data volume, isolate a subset of the badly reconstructed region and reconstruct the missing traces, we get the result shown in Figure 2.29. Unlike the non-patched case, the reflectors in the patched reconstruction case are clearly visible.

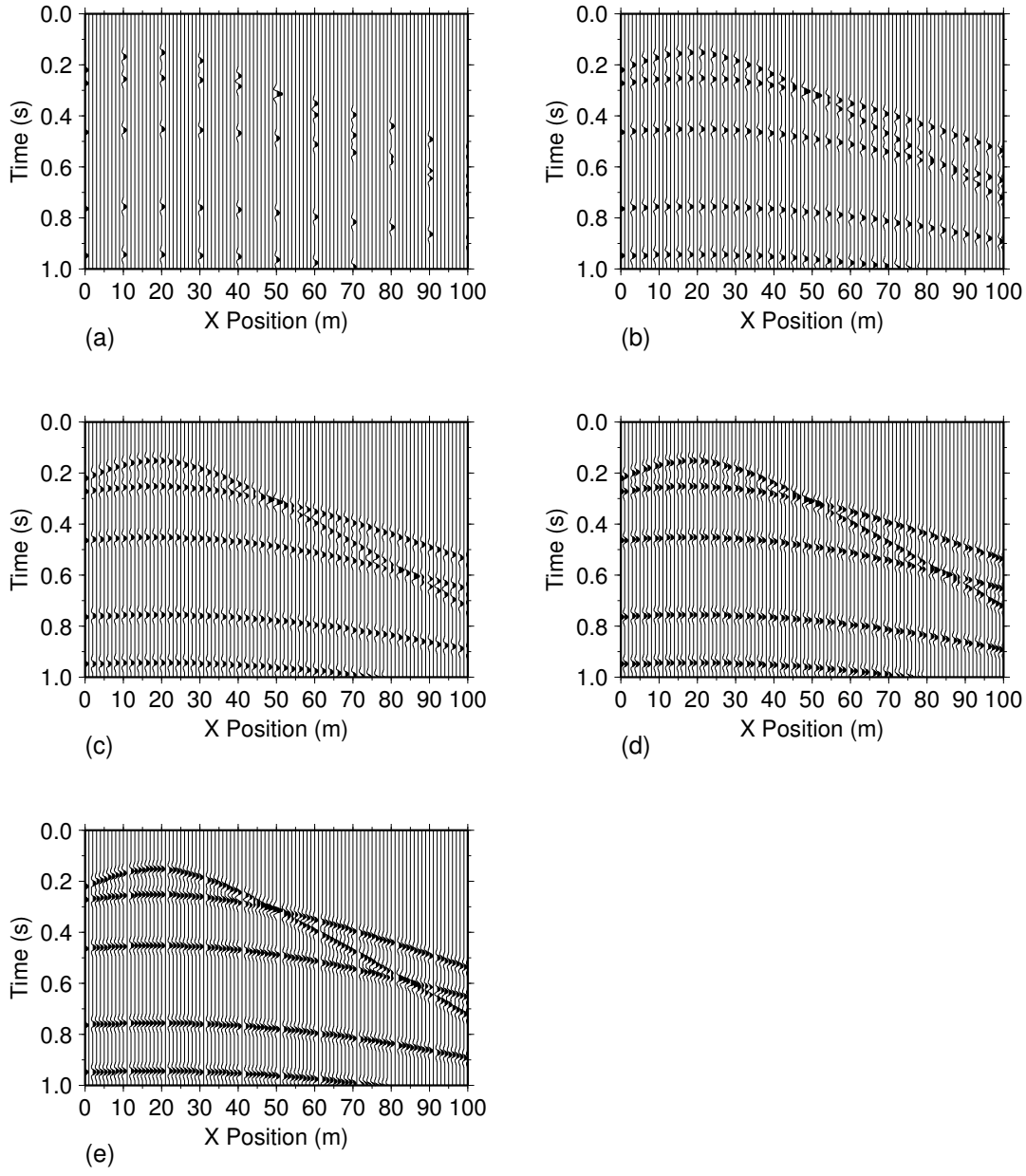

Figure 2.24: Sparse seismic sections derived from the section shown in Figure 2.23 with regularly spaced missing traces. (a) 10% sparse data. (b) 30% sparse data. (c) 50% sparse data. (d) 70% sparse data. (e) 90% sparse data.

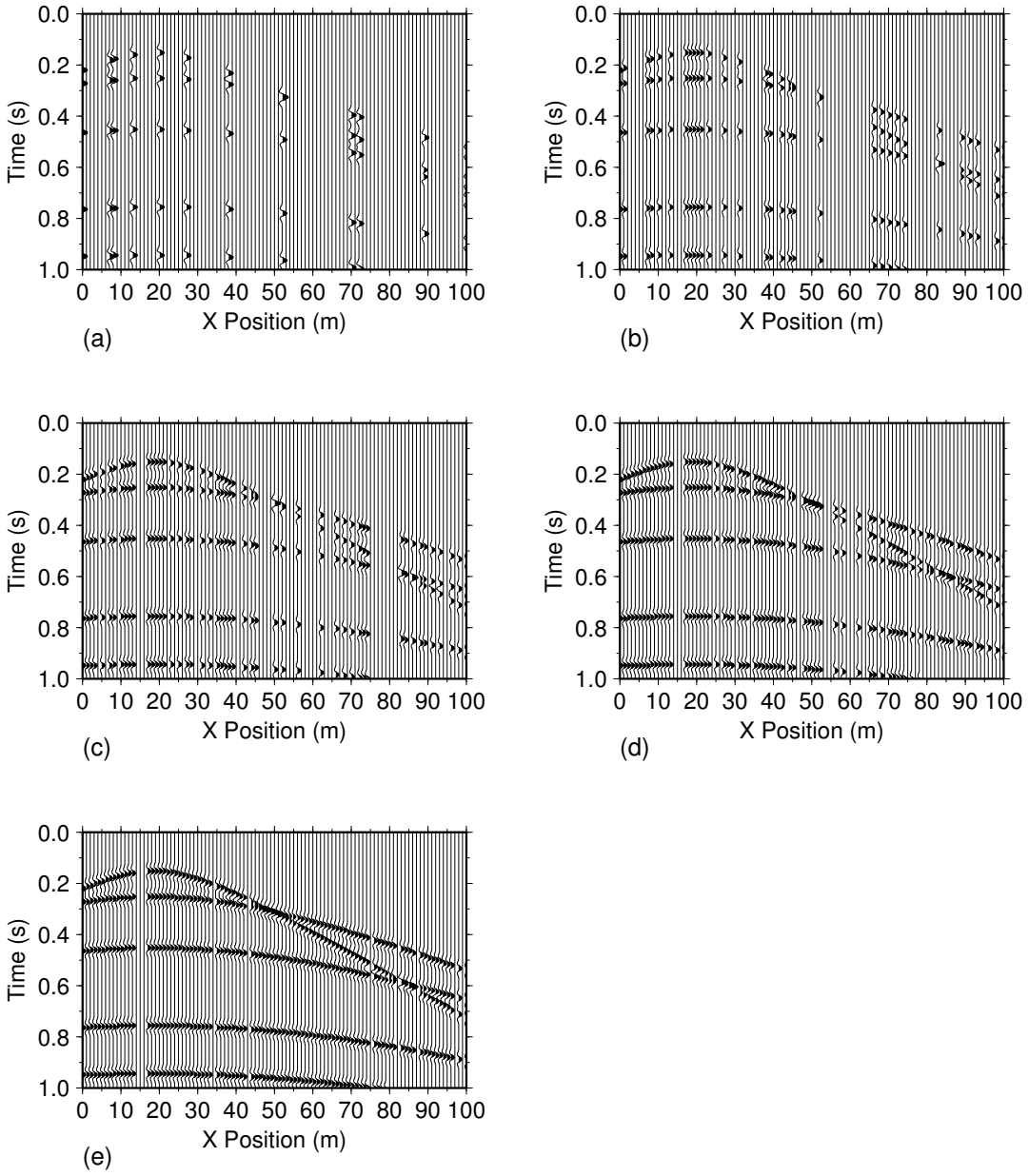

Figure 2.25: Sparse seismic sections derived from the section shown in Figure 2.23 with randomly spaced missing traces. (a) 10% sparse data. (b) 30% sparse data. (c) 50% sparse data. (d) 70% sparse data. (e) 90% sparse data.

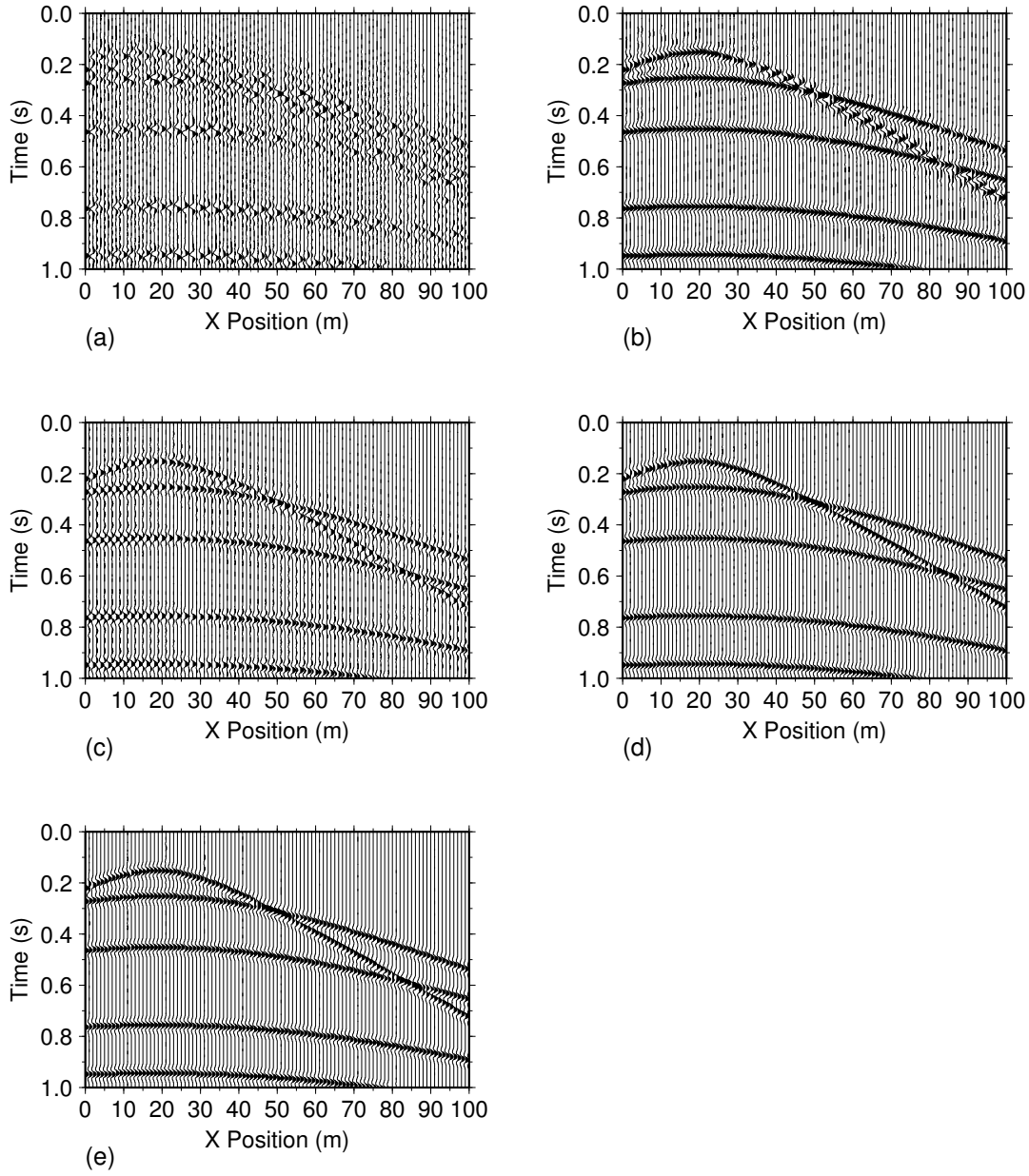

Figure 2.26: Reconstructed seismic sections from the sparse sections shown in Figure 2.24 with regularly spaced missing traces. (a) Reconstructed section from 10% sparse data. (b) Reconstructed section from 30% sparse data. (c) Reconstructed section from 50% sparse data. (d) Reconstructed section from 70% sparse data. (e) Reconstructed section from 90% sparse data.

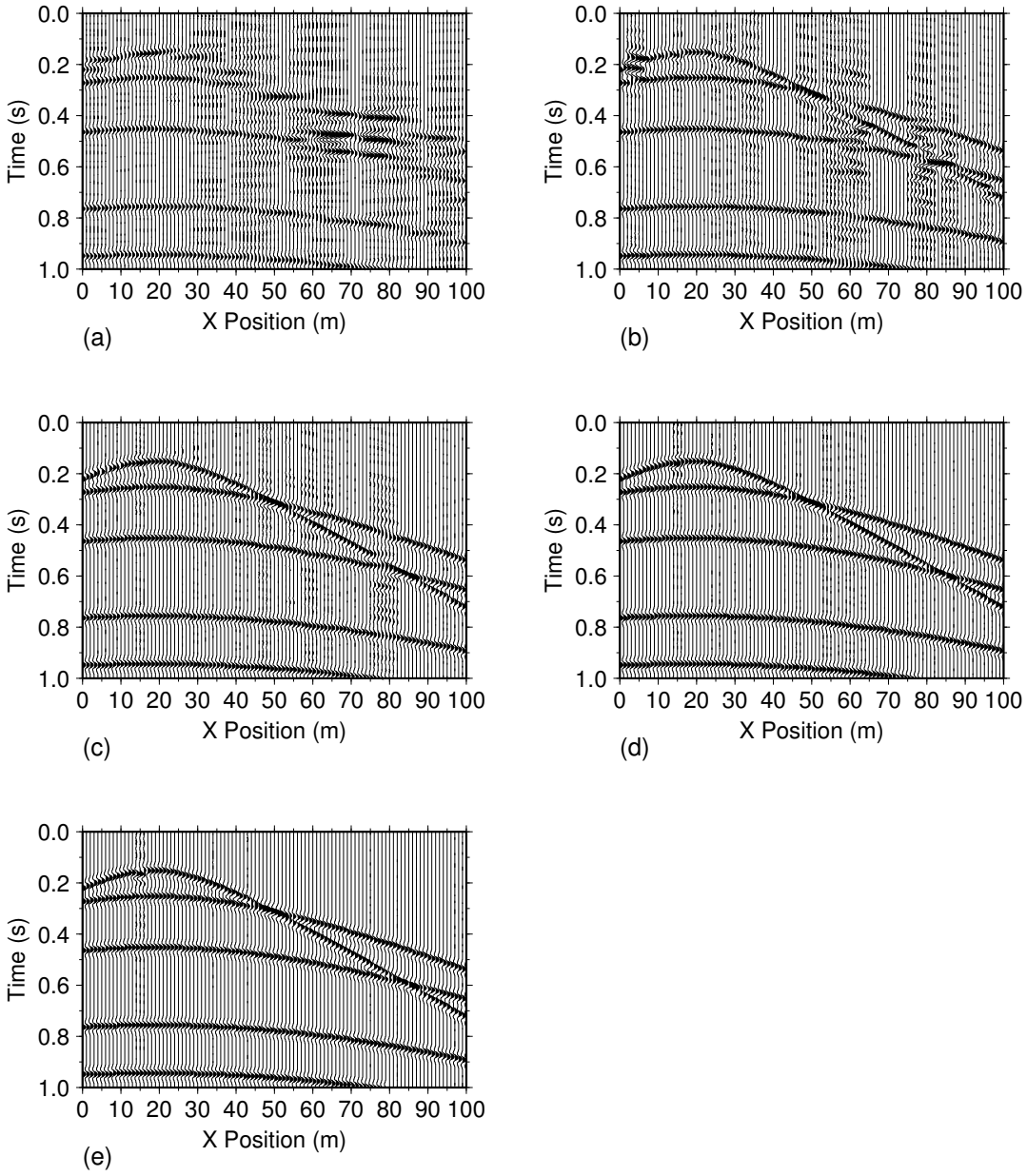

Figure 2.27: Reconstructed seismic sections from the sparse sections shown in Figure 2.25 with randomly spaced missing traces. (a) Reconstructed section from 10% sparse data. (b) Reconstructed section from 30% sparse data. (c) Reconstructed section from 50% sparse data. (d) Reconstructed section from 70% sparse data. (e) Reconstructed section from 90% sparse data.

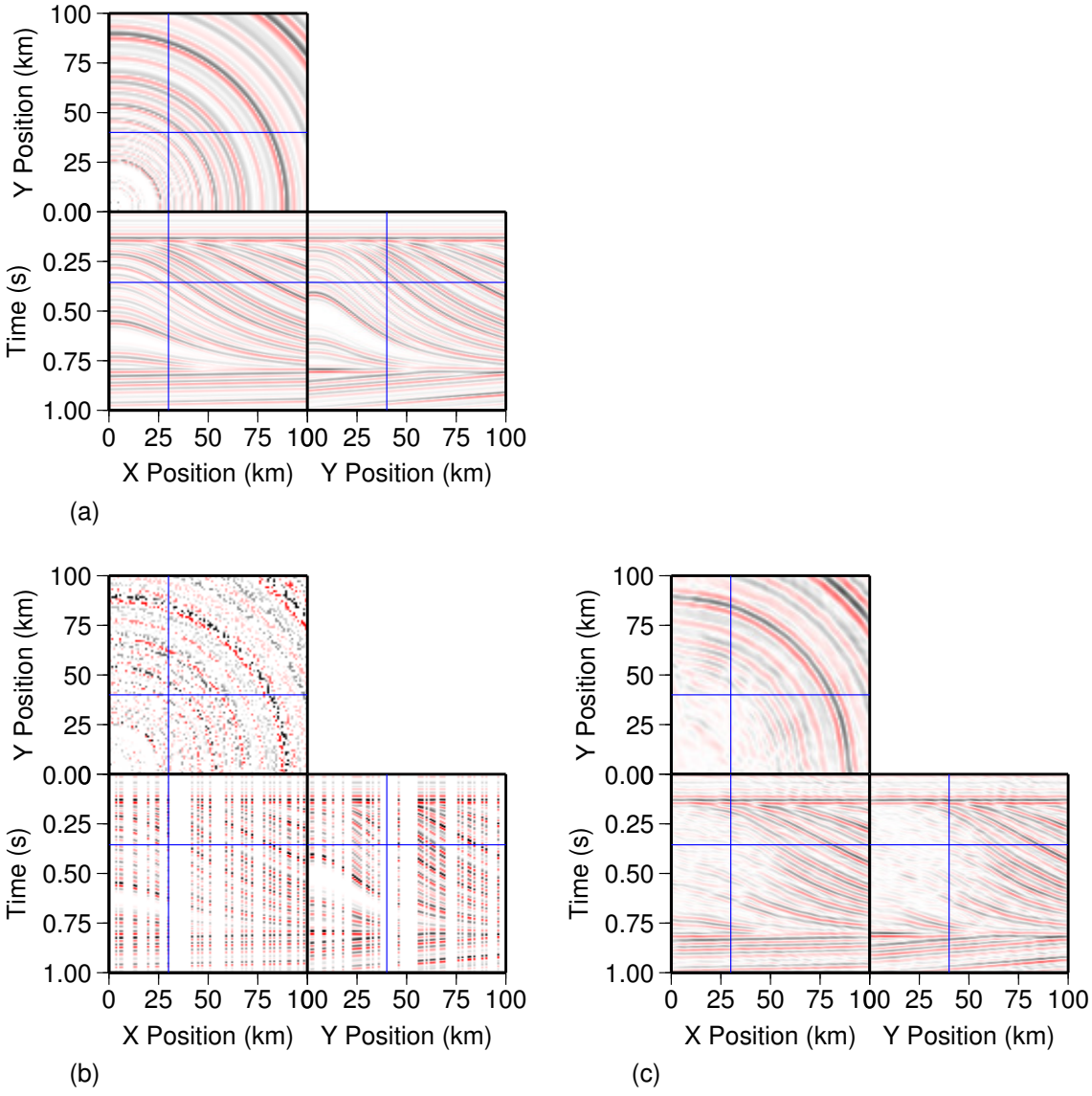

Figure 2.28: Reconstructing a sparse 3D quarter-dome. (a) A complete dataset. (b) 30% sparse dataset. (c) A reconstruction of the complete dataset from the 30% sparse dataset shown in (b).

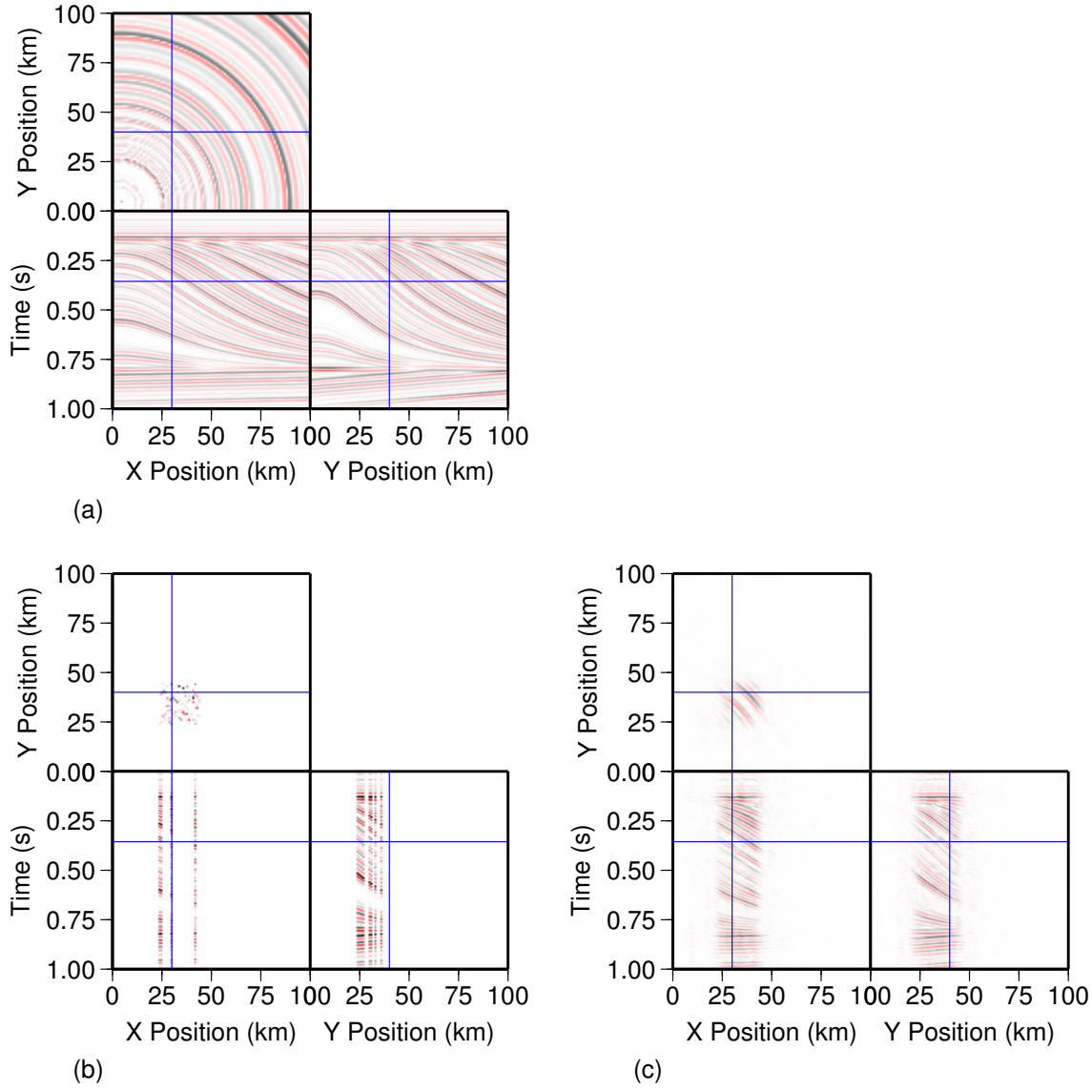

Figure 2.29: Reconstructing a sparse 3D quarter-dome patch. (a) A complete dataset. (b) 30% sparse dataset patch. (c) A reconstruction of the complete dataset patch from the 30% sparse dataset patch shown in (b).

2.1.3 Choice of Estimation Algorithm

In this dissertation, I use the two data estimation methods described in the previous subsections. I use autoregression (prediction error filtering) as the estimation tool in Chapter 3, and minimum weighted norm interpolation as the estimation algorithm in Chapters 4 and 5. Data estimation with autoregression works best when a very good training dataset exists. This is especially true when the incomplete data is very sparse. The training data is used to compute the initial PEF in the iterative estimation process. In Chapter 3, I apply the proposed approach to crosswell traveltime tomography. The traveltimes extracted from the complete baseline datasets is good training dataset for estimation missing data in time-lapse datasets. When seismic arrival traveltimes are extracted from a full trace dataset, the traveltime data size is significantly less than the full trace data size. Computation time in this case, is reasonable.

In Chapters 4 and 5, I apply my approach to full trace seismic data. Computation time of an autoregression estimation of missing data for an accumulated sparse, full trace seismic data can be prohibitive. With MWNI, prior information used to constrain the estimated data is obtained from the incomplete data even if the incomplete data is very sparse. In addition, data estimation using MWNI is done in the frequency domain. Computation time is often faster because full trace seismic data can shrink significantly in size when converted from time domain to frequency domain. For these two reasons, I use MWNI as my estimation algorithm for the full trace seismic data examples presented in Chapters 4 and 5.

2.2 Error-Analysis Tool for Seismic-Trace Reconstruction

2.2.1 Introduction

Within the past few decades, several seismic data-estimation (interpolation and extrapolation) techniques have been presented to the seismic geophysics community.

These include time-domain techniques like autoregression (Claerbout, 1998) and frequency-domain techniques like the f-x interpolation scheme (Spitz, 1991), and the minimum-weighted-norm interpolation scheme (Liu and Sacchi, 2004). The need for good data-estimation algorithms arise because in many cases, uncontrollable circumstances prevent certain traces from being recorded in the field. However, some key seismic data-processing steps work optimally when traces are regularly and densely spaced. In addition, smart seismic monitoring techniques such as estimation-based quasi-continuous reservoir monitoring (Arogunmati and Harris, 2009) rely on data-estimation algorithms. The character of the recorded data used to estimate the unrecorded data greatly influences the character of the estimated traces.

The data-estimation-based quasi-continuous seismic monitoring method proposed by Arogunmati and Harris (2009) uses time-lapse data from an additional, survey in addition to sparse, recorded data at a survey of interest, to estimate unrecorded data. In such a case, differences in the true and estimated data may result from varied source signatures and recording fidelity in the different surveys. Once the missing data have been estimated, it is not possible to differentiate errors due to data-recording differences from shortcomings in the data-estimation algorithm or scheme.

It is common practice to present data-estimation errors either by displaying the true and estimated data and identifying portions of the data that are reconstructed imperfectly, or by simply showing the difference between the two datasets (e.g. Spitz, 1991; Crawley, 2000; Liu and Sacchi, 2004; Curry, 2008). With such representations, one is limited by the number of plots that can be shown. Either the best estimation or the worst estimation results may be shown. A single shot gather from an entire seismic data volume may be shown. The data shown is often referred to as the typical result. There is often no quantitative description summarizing the estimation errors of all test cases.

In this section, I present a tool for assessing inaccuracies in estimated data. Using this tool, it is possible to efficiently demonstrate how effective an estimation

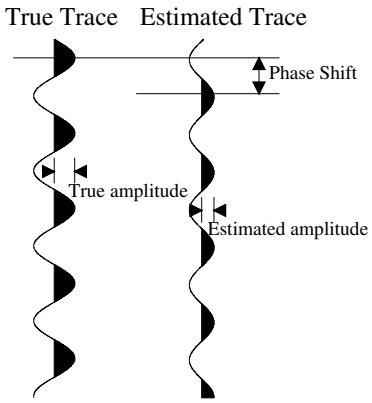

Figure 2.30: An illustration of a true trace and its estimate. When an unknown trace is estimated, the inaccuracies are expressed as amplitude errors and phase-shift errors.

algorithm or scheme is in specific situations with quantities that have intuitive interpretation. This tool assumes the true data is known and some traces have been intentionally discarded and then estimated. While the ultimate goal of an estimation algorithm or scheme is its application to field data with unknown missing traces, it is important to have reference cases where the missing traces are in fact, known. Quantifying the inaccuracies in these reference cases give an idea of how effective the estimation algorithm is. I can relate errors in data estimation to errors in a processed image. In the following sections, I describe the mathematical background for the tool presented, and then I show an example of its use.

2.2.2 Methodology

When an unknown trace is estimated, it is intended to be as close to the true trace as possible. Depending on the algorithm and the known data used in the estimation process, this trace may or may not be a good representation of the true data. The trace may be out of phase with the true trace, or its amplitudes may be incorrect. Figure 2.30 illustrates this point.

Computing the difference between the amplitudes in two datasets is trivial. However, if both datasets are out of phase, computing the difference directly is

meaningless. Computing the phase-shift is an integral part of the proposed tool. Methods such as cross-correlation (e.g. Knapp and Carter, 1976) and Taylor expansion (e.g. Hatchell et al., 2003; Naeini et al., 2009) are currently used to compute phase-shifts between multiple datasets. The most commonly used are cross-correlation based algorithms. In their simplest forms, these algorithms use the discrete signal cross-correlation equation to compute the cross-correlation coefficients between segments of corresponding traces for each sample point, and locate the position of the maximum cross-correlation coefficient. Cross correlation of two discrete time signals is expressed as

$$h(\tau) = \sum_{\tau=-N}^{N} f(t)g(t+\tau) \ , \tag{2.87}$$

where $f(t)$ and $g(t)$ are the input signals as a function of time t, h is the output cross-correlation coefficient function as a function of the lag-time τ, and N is the length of the input signal. The sample point under consideration is then moved to its corrected position using the lag time of the maximum cross-correlation coefficient.

Naeini et al. (2009) noted that several issues may affect the efficiency of cross-correlation based techniques. For example, when a very short time window is used in computing the cross-correlation coefficients, the maximum cross-correlation coefficient may be biased towards the largest amplitudes in the trace. The bias can easily be eliminated by using large enough computation windows, or by applying automatic gain control (AGC) to the traces prior to computing the cross-correlation coefficients. For speed and computational efficiency, cross-correlation may be implemented in the Fourier domain. This is done using the equation

$$H(k) = \overline{F(k)}G(k) \ , \tag{2.88}$$

where $F(k)$ is the Fourier transform of the first signal $f(t)$, $G(k)$ is the Fourier transform of the second signal $g(t)$, and $\overline{F(k)}$ is the complex conjugate of $F(k)$.

In analyzing the estimation errors in the reconstructed datasets shown in this dissertation, I used a cross-correlation-based method to compute phase-shifts.

2.2.3 Synthetic Example

As an example, I use the migrated image from an estimated dataset. This dataset was estimated from a sparse dataset with 80% of its traces missing. In Figure 2.31, I show the true image, the image from the estimated data, the difference between the true and estimated data before depth correction, and the difference between the true and estimated data after depth correction. The computed depth-shifts are shown in Figure 2.32.

Using these results, an assessment can be made of the gross error in the image. This could be in the form of a mean shift or root-mean-square shift, along with the corresponding amplitude measure. The advantage of this approach comes when a large number of datasets are reconstructed. The error measures can be used to track trends in the reconstructed dataset.

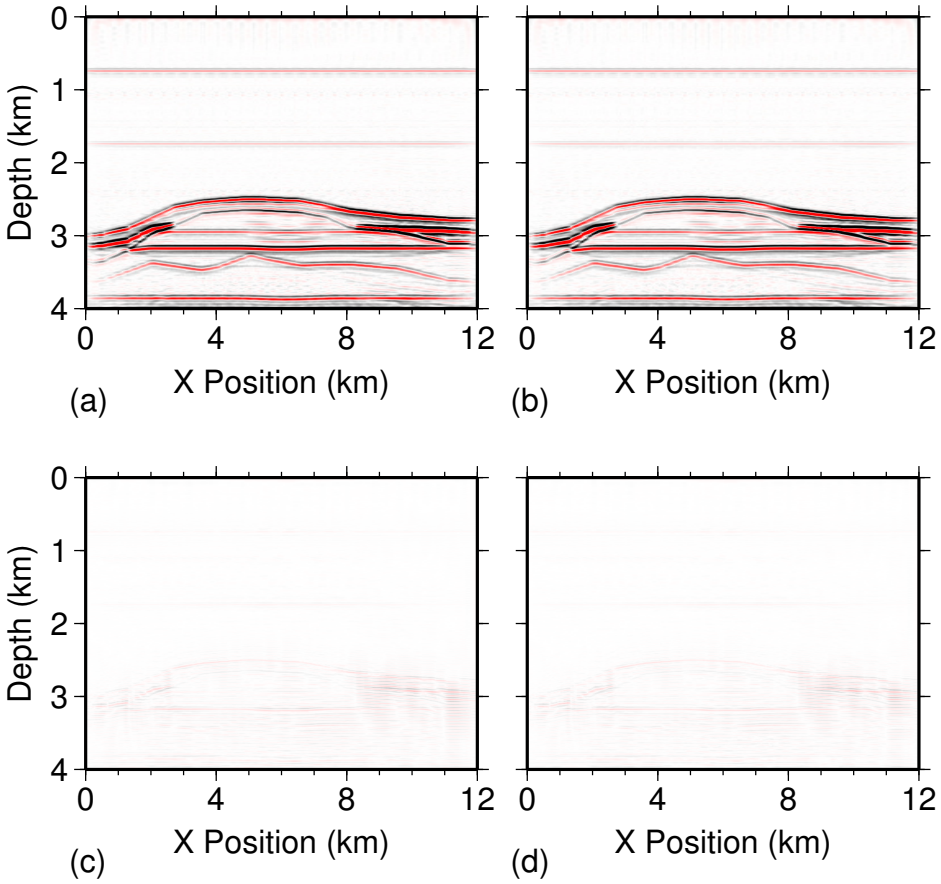

Figure 2.31: An application of the error-analysis tool presented: (a) Migrated image from complete true data. (b) Migrated image from combined 20% true and 80% estimated data. (c) The difference between the images in (a) and (b) before depth correction. (d) The difference between the images in (a) and (b) after depth correction.

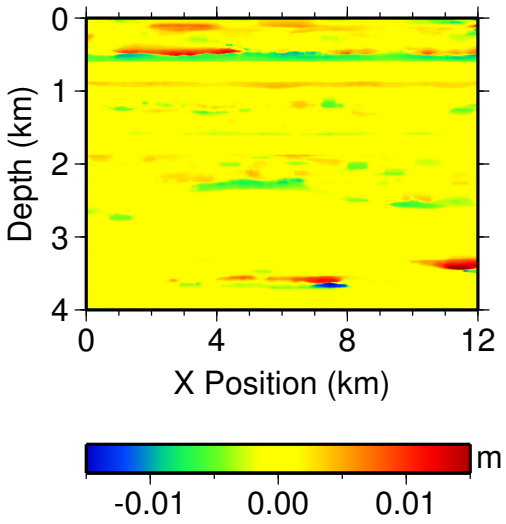

Figure 2.32: An application of the error-analysis tool presented: The computed depth-shifts for the image shown in Figure 2.31(b).

Chapter 3

Quasi-continuous Monitoring with Crosswell Traveltime Tomography

3.1 Introduction

In this chapter, I present an application of the quasi-continuous, seismic monitoring approach to crosswell traveltime data for tomography. I show that it is an efficient strategy for reconstructing seismic velocity changes in a reservoir. The data-estimation tool I use is the iterative PEF/data scheme described in Section 2.1.1. I apply the approach to both synthetic and field crosswell-seismic traveltime data. In the synthetic example, I simulate a CO_2 reservoir monitored over a period of 140 weeks. In the field example, I use data acquired at the McElroy Field in West Texas, where a pilot project for enhanced recovery using CO_2 was implemented. Only the baseline dataset and one monitor dataset were available.

3.2 Synthetic Crosswell Traveltime Example

I use a synthetic baseline velocity model, as well as flow-simulation models to simulate a time-lapse monitoring study at a CO_2 injection site. Beginning with a baseline velocity model (Figure 3.1), I create additional 70 synthetic velocity models

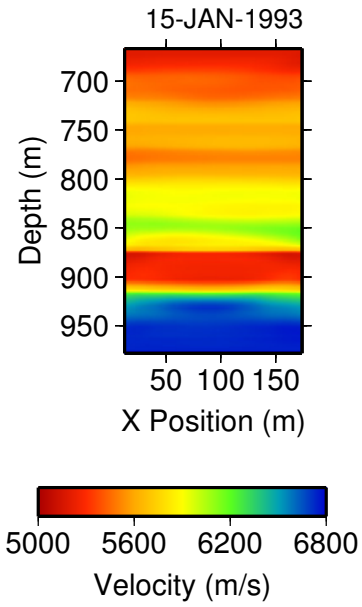

Figure 3.1: Synthetic baseline velocity model.

representing snapshots of the seismic velocity field between two wells at two week intervals over a period of 140 weeks, starting January 1, 1993. I allow a leak to occur after approximately 40 weeks of CO_2 injection.

3.2.1 Conventional Time-Lapse Monitoring

To represent conventional time-lapse monitoring, I use only two velocity models, with a time interval of 140 weeks between the baseline and monitor surveys. In other words, I use the baseline and the 70th time-lapse velocity model. I compute first-arrival traveltimes for a crosswell geometry using the finite-difference method described in Hole and Zelt (1995). I use a source and receiver configuration that mirror the McElroy Field configuration (Figure 3.2). Gaussian noise corresponding to a picking error of 2 msec, is added to the synthetic traveltimes. Figure 3.3 shows the computed baseline and time-lapse traveltime datasets. The traveltime datasets are displayed on a grid with the x- and y-axes represented by the shot and receiver

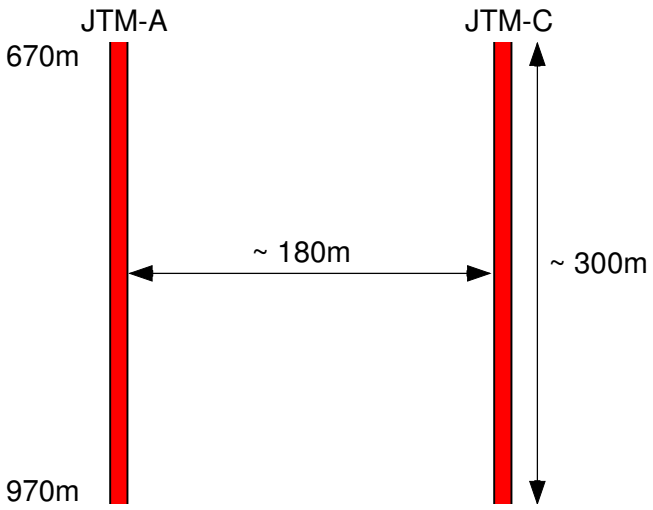

Figure 3.2: Crosswell data-acquisition configuration for the McElroy Field dataset.

depths, respectively.

To reconstruct the velocity models, I use the regularized tomography algorithm described in Zelt and Barton (1998). The true and reconstructed velocity difference models are shown in Figure 3.4. The rms error shown in Figure 3.4 is the rms error between 800 m and 900 m depth. Although the time-lapse velocity difference is well resolved, the leak is first detected long after it started. In a real CO_2-sequestration project, that could be catastrophic.

3.2.2 Quasi-Continuous Time-Lapse Monitoring

For each of the 70 time-lapse velocity models synthesized, I compute first-arrival traveltimes for a crosswell-seismic geometry. I use the same source and receiver configuration as the conventional example described in the previous section, which mirrors the configuration used in the McElroy Field. Gaussian noise, corresponding to a picking error of 2 msec, is added to the synthetic traveltimes. I then sub-sample the synthetic datasets following the quasi-continuous monitoring strategy described. This is accomplished by discarding large portions of each dataset.

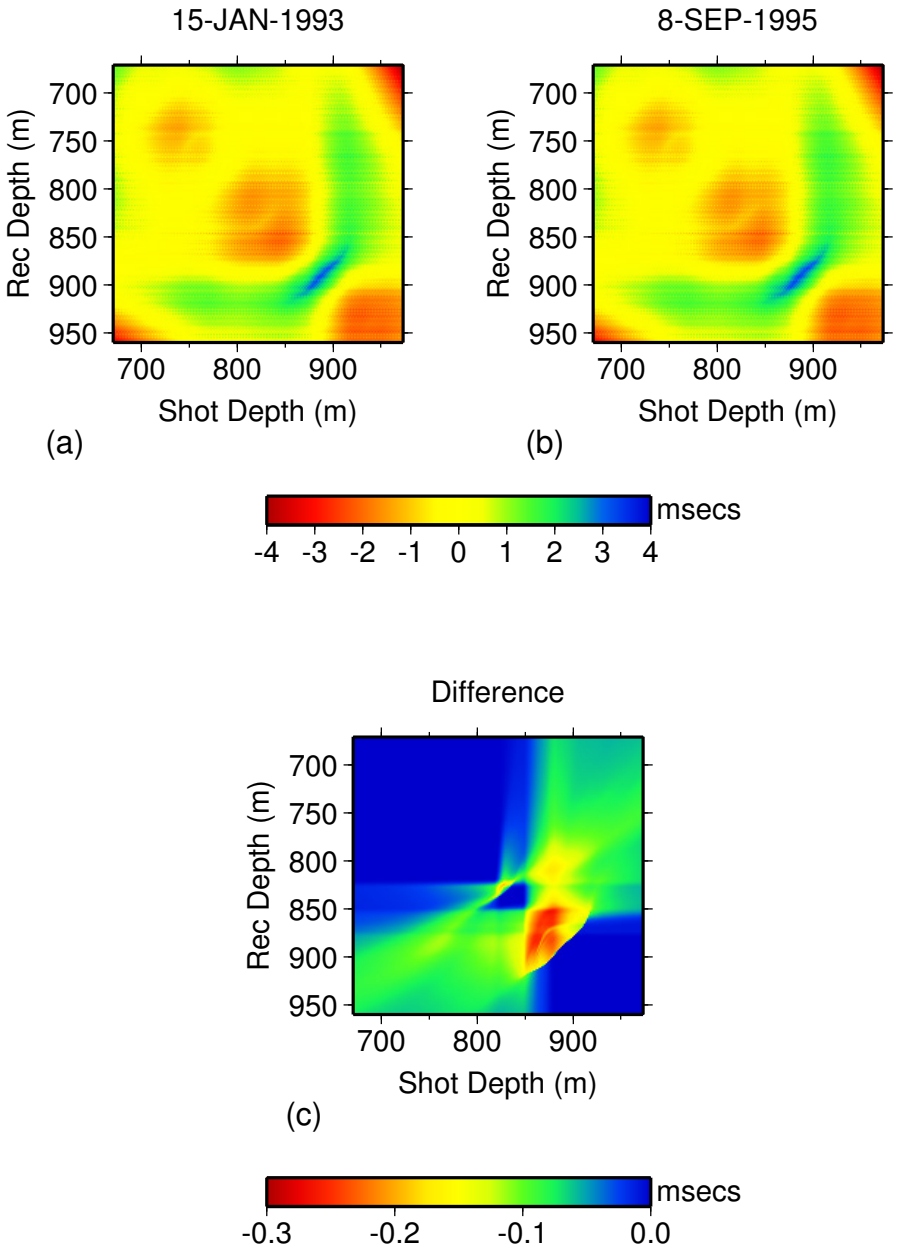

Figure 3.3: (a) Synthetic baseline traveltime dataset. (b) Monitor traveltime dataset. (c) The difference between (a) and (b). The data shown in (a) and (b) have been reduced by a constant velocity of 5800m/s.

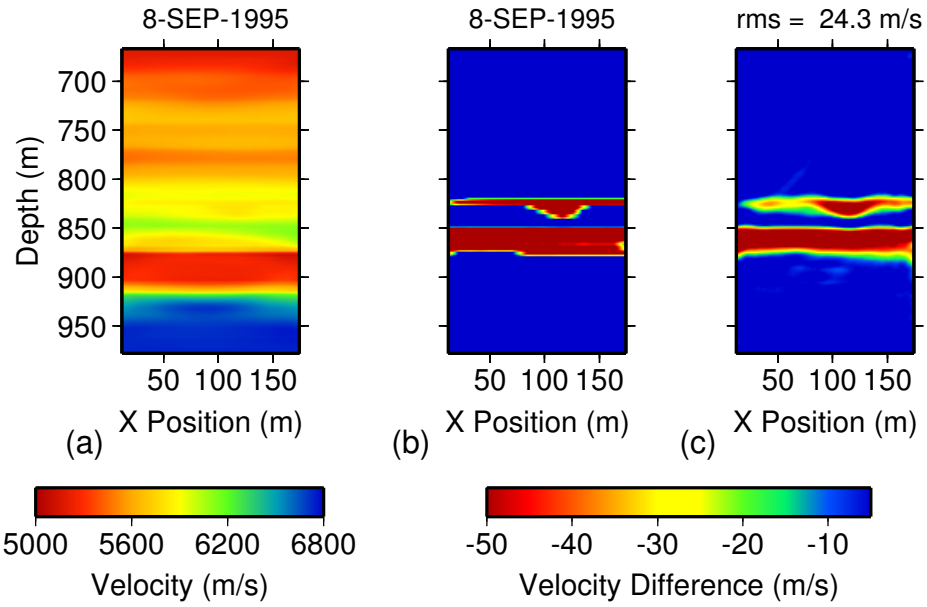

Figure 3.4: (a) The true velocity model after 140 weeks. (b) The true time-lapse velocity-difference model after 140 weeks. (c) The reconstructed velocity-difference model after 140 weeks. The injected CO_2 is well resolved, but the leak is first detected after 140 weeks.

Four groups of subsampled (sparse) datasets are created: 1%, 2%, 5%, and 10% of the original data volume. For comparison, I ensure that the cumulative sizes of the sub-sampled datasets at the end of the two-year period are equal. For the 1% case, I sample 1% of each of the 70 synthetic datasets, discarding 99% of the dataset; for the 2% case, I sample 2% of every other dataset, discarding 98% of the data from alternating datasets and 100% of the others; for the 5% case, I sample 5% of every 5th dataset, discarding 95% from every 5th dataset and 100% of the others; and for the 10% case, I sample 10% of every 10th dataset, discarding 90% from every 10th dataset, and 100% of the others. Both random and regular sampling scenarios are tested. I also test both selection without replacement and selection with replacement.

Figure 3.5 shows selected true velocity-difference models alongside models reconstructed from complete, true synthetic datasets. Reconstructing velocity models from the sparse subsampled datasets produces geologically unreasonable models, showing significant artifacts. This is because the inverse problem is severely underdetermined. A first-order fix for a severely underdetermined problem is to reduce the number of model parameters estimated in the inverse problem. The consequence of this action is that the smallest model feature recoverable becomes significantly larger. In geophysical reconstructions, that means reducing spatial resolution. Estimating unrecorded data helps to retain spatial resolution.

I construct time-lapse data volumes by concatenating datasets from different surveys along the slow-time axis. This produces 3D data volumes having two spatial dimensions and one slow-time dimension. I then use the iterative PEF/data approach described in Section 2.1.1 to estimate the discarded data for the 3D, time-lapse, sparse traveltime data volumes. As the starting guess for the iterative process, I use an initial data volume that assumes that the traveltimes do not change within the period of interest. I then estimate a PEF from the resulting time-lapse data volume. I use this PEF to estimate the missing data. This process is repeated until convergence, or until a tolerance measure is met as described in Section 2.1.1. Sample estimated and true datasets are shown in Figure 3.6. It is obvious in Figure 3.6 that the approach presented is an effective approach in estimating the discarded

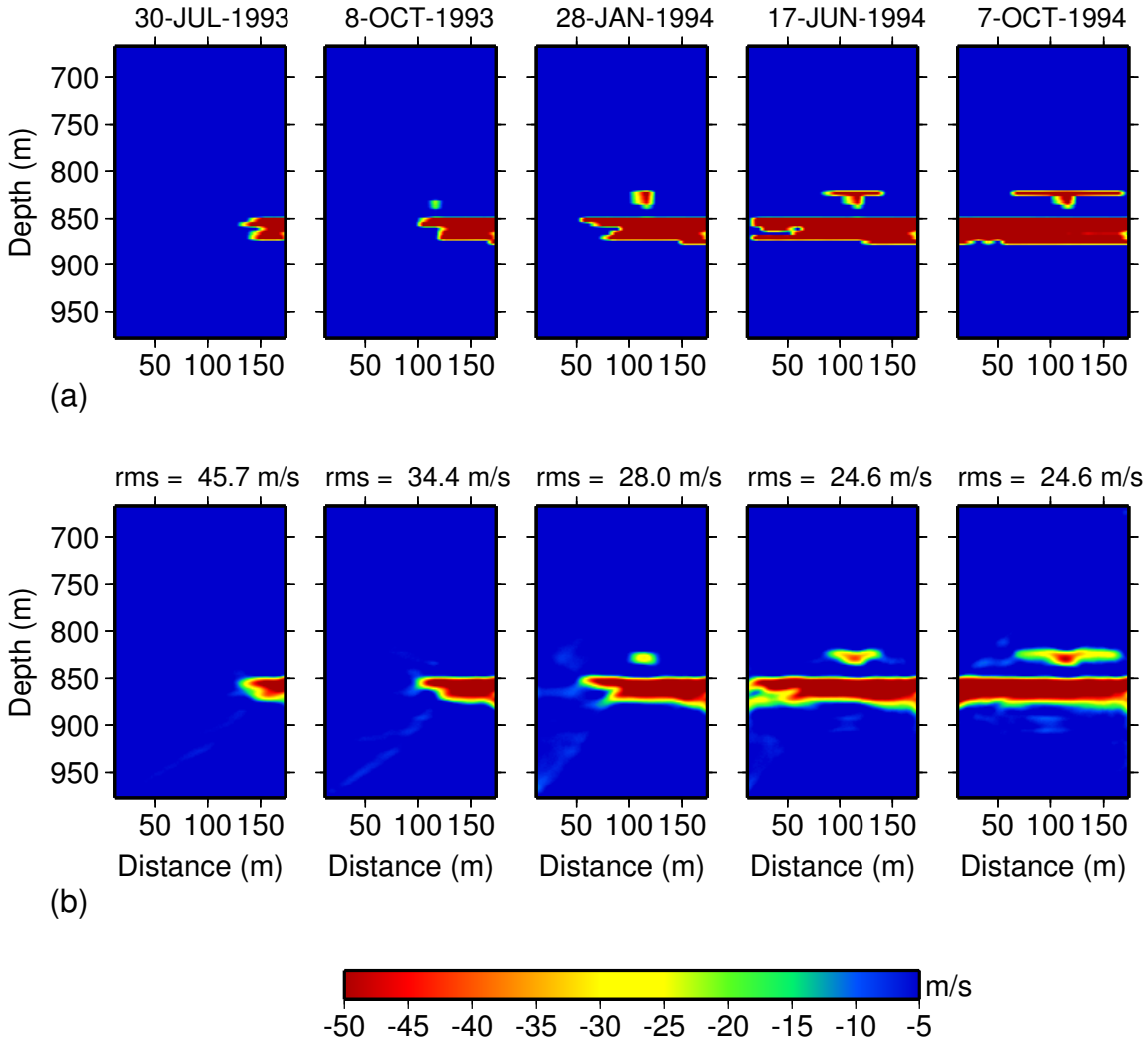

Figure 3.5: (a) Selected true synthetic velocity-difference models. The model dates are shown above each model. (b) Selected reconstructed velocity-difference models from complete true synthetic traveltimes. These represent the best images that can be reconstructed from the synthetic traveltimes. The model rms errors are shown above each reconstructed velocity model.

data.

Figure 3.7 shows the rms errors obtained when a complete data-estimation cycle is implemented as new data become available. In Figure 3.7, N is the number of sparse time-lapse datasets (surveys) used in the estimation process. One key observation is that the errors are similar, regardless of the sparsity of datasets. This implies that the same level of model accuracy can be obtained with a smaller data size using the approach presented in this dissertation (i.e., by acquiring less data more frequently). In addition, by sampling more frequently, we increase the slow-time temporal resolution.

The error plots in Figure 3.8 show that the accuracy of the reconstructed velocity models improves as the number of iterations increases. This shows a convergence towards the true model shown in Figure 3.7. Finally, we see a decrease in rms error as data size increases. As more data are acquired, the accuracy of the estimated data increases. The improvement, however, decreases as data are accumulated.

In Figures 3.7 and 3.8, it is obvious that after some time, adding new datasets does not improve the estimation error for previously estimated datasets. For these estimated datasets, convergence has been reached. This implies that a smaller, moving estimation-window can be used instead of estimating all data volumes at all times. If a moving estimation-window is used, the first indication of abnormalities may warrant expanding the time-window backward in time for confirmation. Also, a converged dataset can be used instead of the baseline dataset as the initial guess in the iterative process, since we expect it to be more similar to the most recent dataset than the baseline dataset is.

To examine the benefits of calculating a new PEF when new sparse datasets are added, I reconstruct the synthetic velocity models using previously estimated PEFs and then compare them to the results obtained when a new PEF is recalculated. In Figure 4, I show rms slowness errors obtained after the second and third iterations when the estimated traveltime data used in the reconstruction process are from 1% true data. The rms errors are lowest when the PEF used is calculated from a time-lapse data volume that includes all available datasets. In addition, the rms errors of the slowness model reconstructed from the data estimated using the PEF calculated

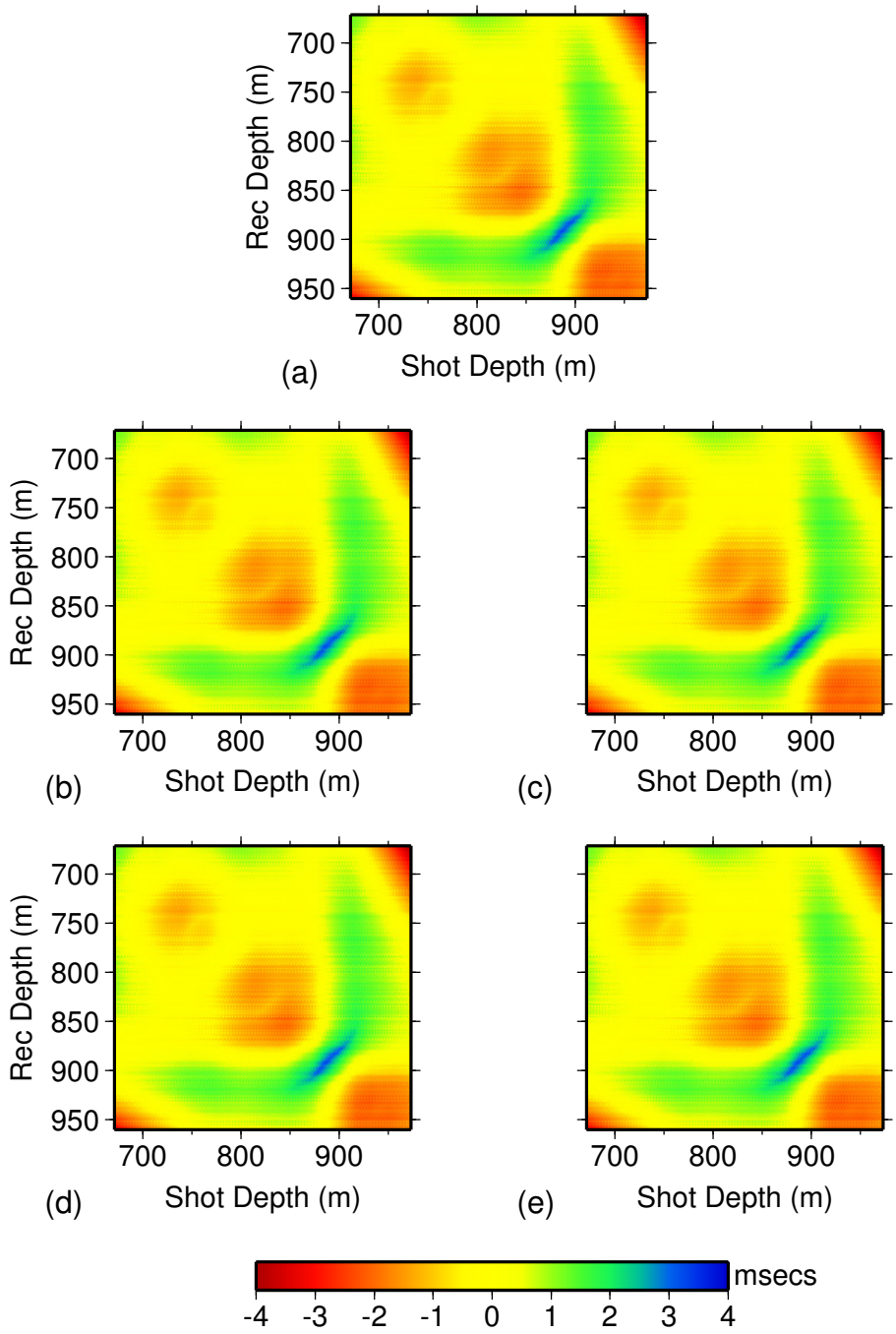

Figure 3.6: A selected true synthetic dataset and the corresponding estimated dataset from different sparse datasets. (a) True synthetic data. (b) 10% true + 90% estimated data. (c) 5% true + 95% estimated data. (d) 2% true + 98% estimated data. (e) 1% true + 99% estimated data. The algorithm clearly does a good job in reconstructing the missing data.

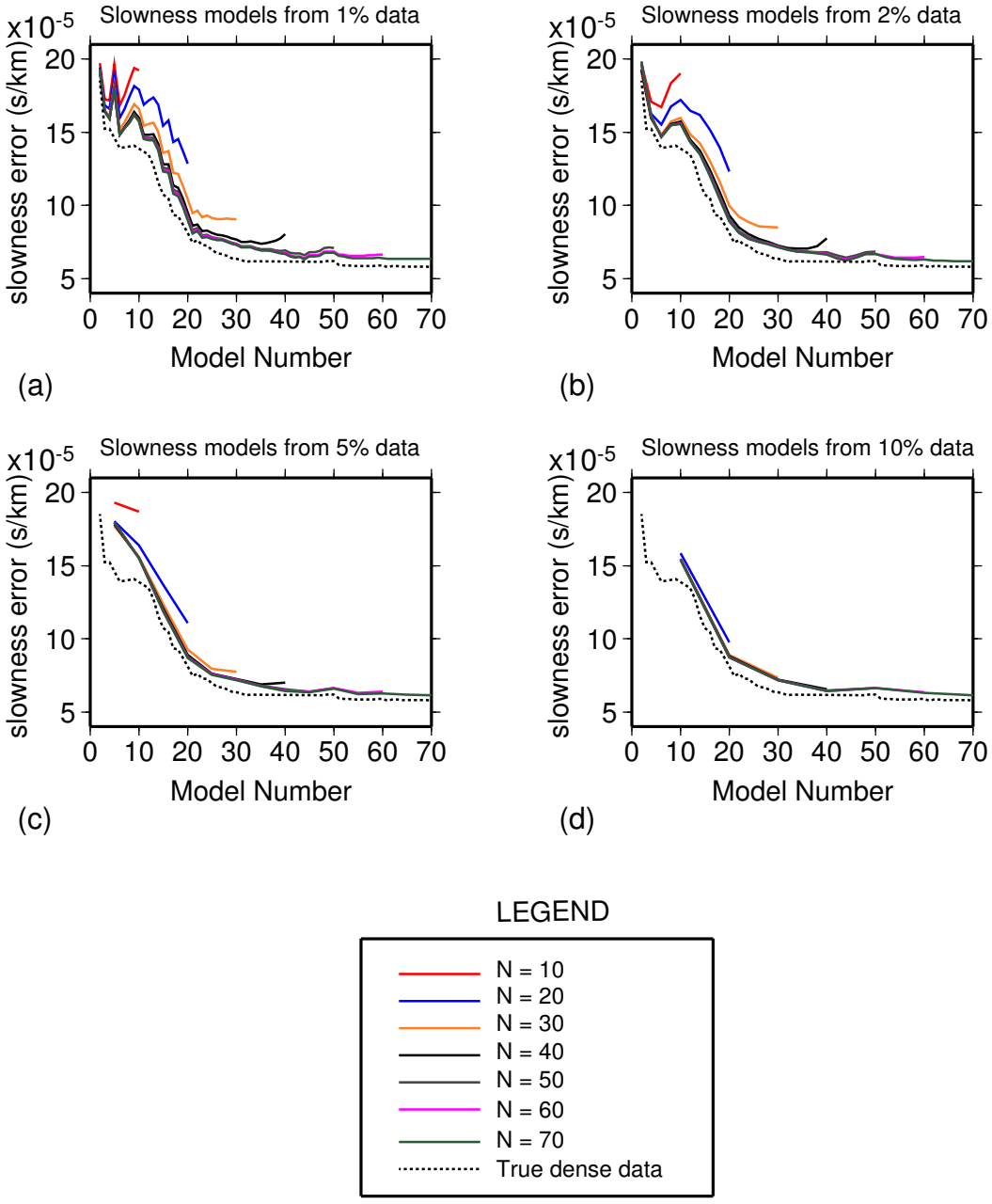

Figure 3.7: RMS error plots of the reconstructed slowness models from estimated traveltime datasets grouped by the size of the original sparse datasets; only the third iteration results are shown. The dashed line in each plot shows the result obtained using true complete data. (a) 1% true data. (b) 2% true data. (c) 5% true data. (d) 10% true data. The plots are color-coded by the number of sparse, time-lapse datasets (N) used in the estimation of missing data.

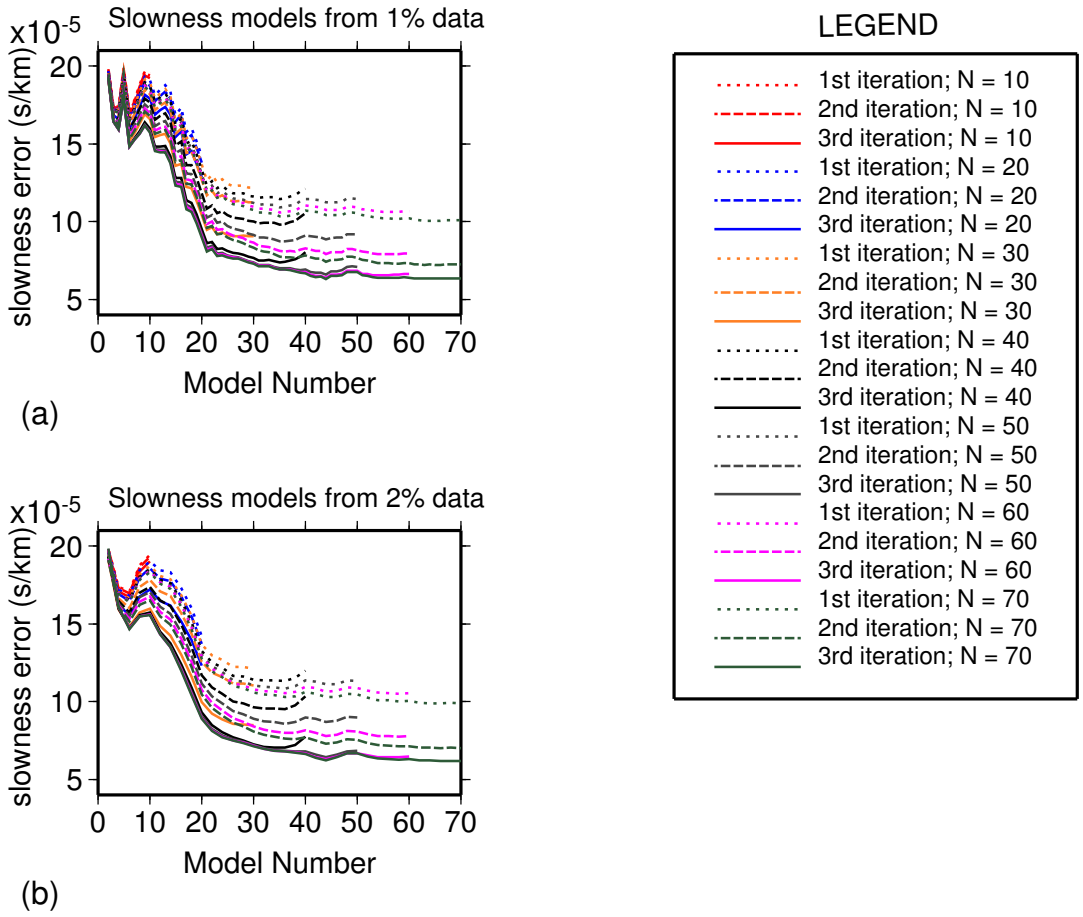

Figure 3.8: RMS error plots of the reconstructed slowness models from estimated traveltime datasets grouped by the size of the original sparse datasets, showing all three iteration results. Data are estimated using (a) 1% true data, and (b) 2% true data. The plots are color-coded by the number of sparse, time-lapse datasets (N) used in the estimation of missing data.

from the first 10 datasets are worse than those using the PEF calculated from the first 20 datasets, and so on. The errors are seen to shrink with data completeness, implying convergence. This shows that as the reservoir properties evolve and more data are acquired, the estimated PEF gets closer to the true PEF. From the plots, we also see that convergence is faster in the third iteration than in the second iteration.

In Figures 3.10 and 3.11, I compare a series of reconstructed velocity models using the estimated datasets from different sparse datasets. The selected velocity models represent the period around the time the leak started, i.e. 22nd October 1993 (21st velocity model). Because the slow-time sampling rate of the reconstructed velocity models from data estimated using 2% true data is higher than the sampling rates of the velocity models reconstructed using data estimated from 5% and 10% true data, the leak is detected much earlier in the 2% case than in the 5% or 10% cases. In addition, because the data sparsity of the 1% case is very high, the leak is not detected early. This shows that using the right data sparsity is as important as obtaining the right slow-time resolution. Although this approach to continuous time-lapse monitoring is effective, the fact that the error shrinks as more datasets are acquired gives it the property of delayed accuracy. Because the data are estimated from future and past data, accuracy increases as more data are acquired.

3.3 Reservoir Monitoring at the McElroy Field

A time-lapse monitoring project was conducted in the McElroy Field in Texas with crosswell acquisition geometry. The baseline dataset was acquired in 1993, and a monitor dataset was acquired in 1995 (Harris et al., 1995; Lazarotos and Marion, 1997). Selected shot gathers are shown in Figure 3.12. The project was executed as a pilot study to monitor changes in the reservoir in response to CO_2 injection into the reservoir. I use data collected between wells JTM-A and JTM-C. In the 1993 survey, JTM-C was the source well and JTM-A was the receiver well. The reverse was the case in the 1995 survey. The wells are separated by about 180 m. A total of

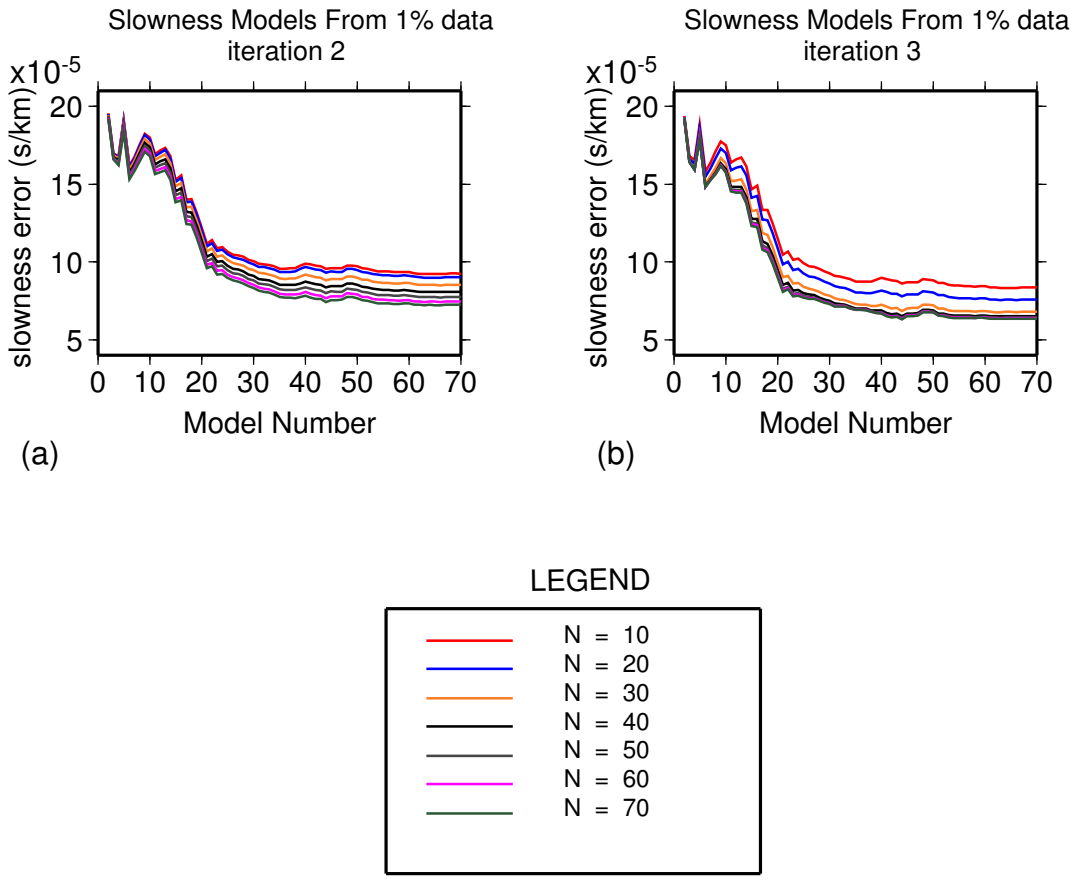

Figure 3.9: RMS error plots of the reconstructed velocity models from estimated traveltime datasets. The plots are color-coded by the number of datasets used in estimating the PEFs applied (a) after the second iteration, and (b) after the third iteration.

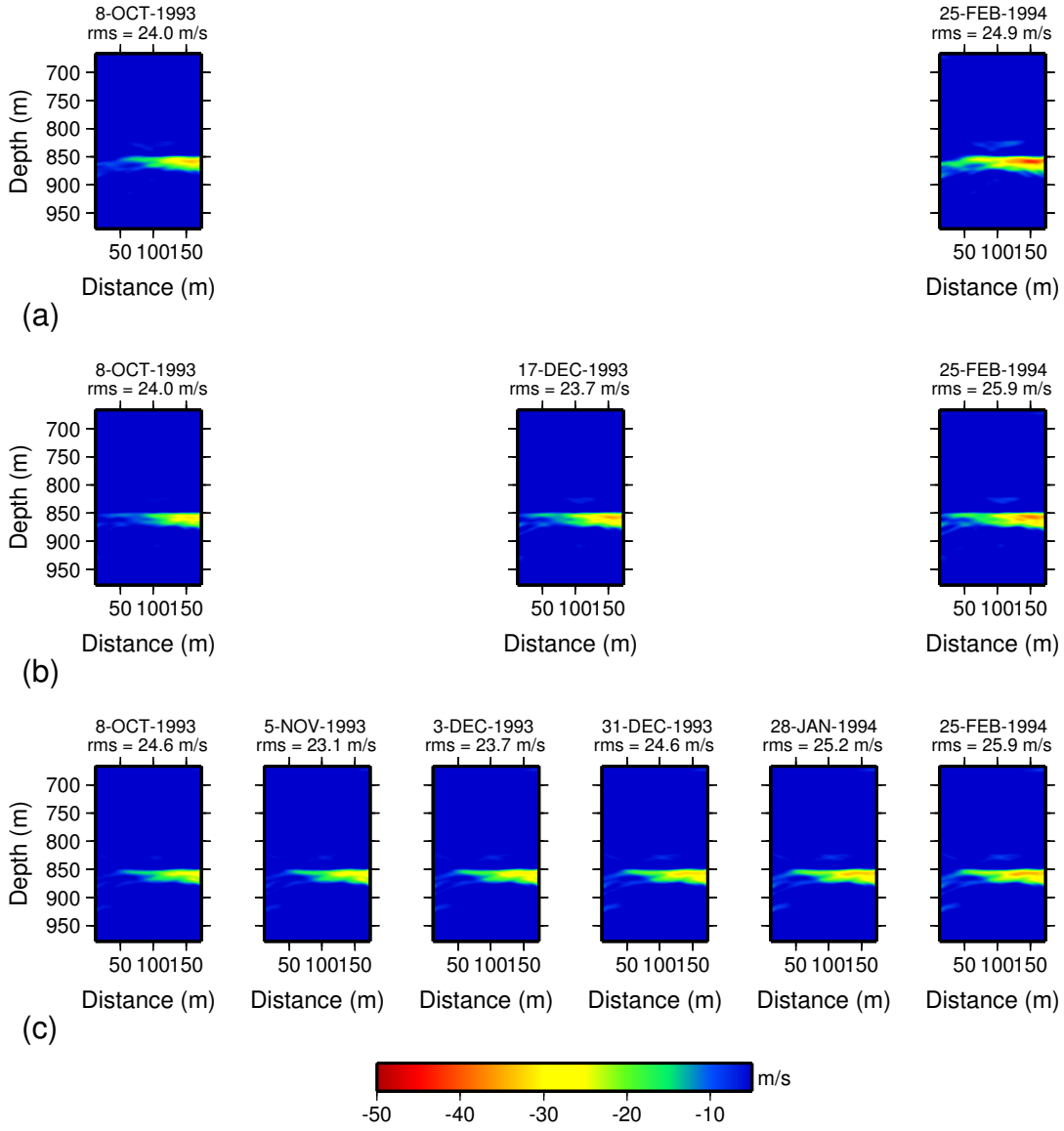

Figure 3.10: Selected reconstructed velocity-difference models from the data estimated from (a) 10% datasets, (b) 5% datasets, and (c) 2% datasets. These models are sampled around the beginning of the leak. Because the data space is sampled more frequently in time, the leak is detected earlier with estimated data using 2% data than with the estimated data using 5% or 10% data.

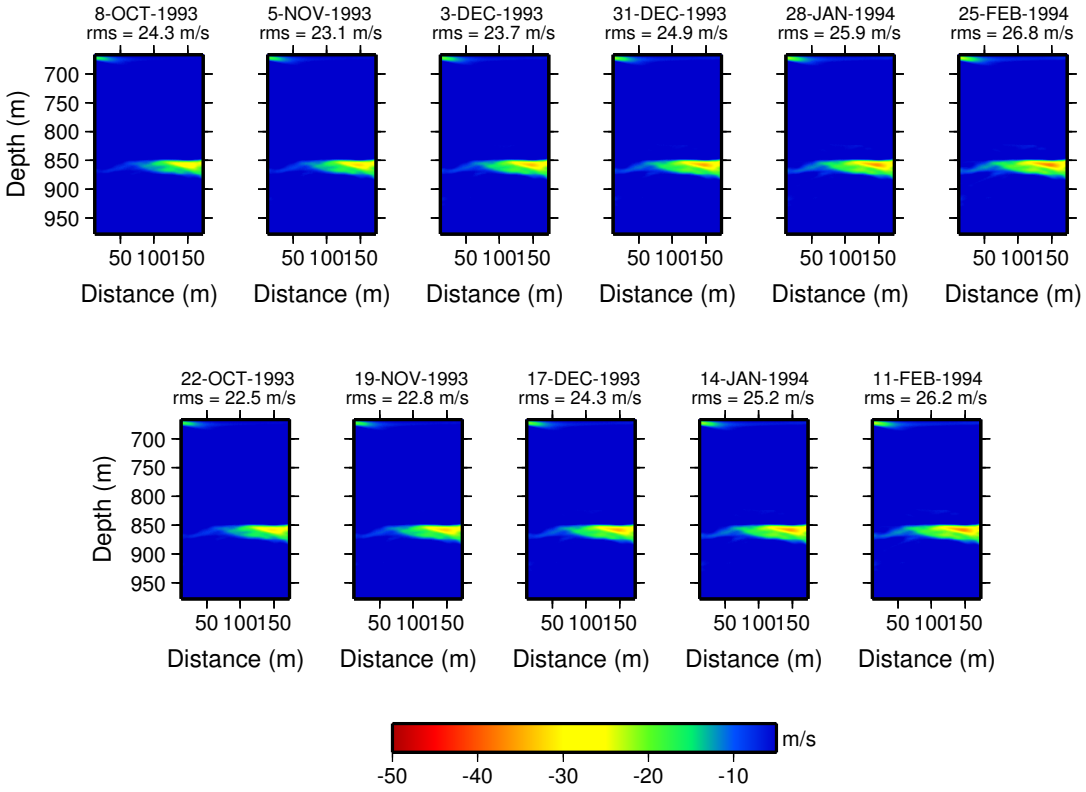

Figure 3.11: Selected reconstructed velocity-difference models from the data estimated from 1% datasets. Because of the sparsity of the data, the velocity models reconstructed using data estimated with 1% data do not capture the leaked CO_2.

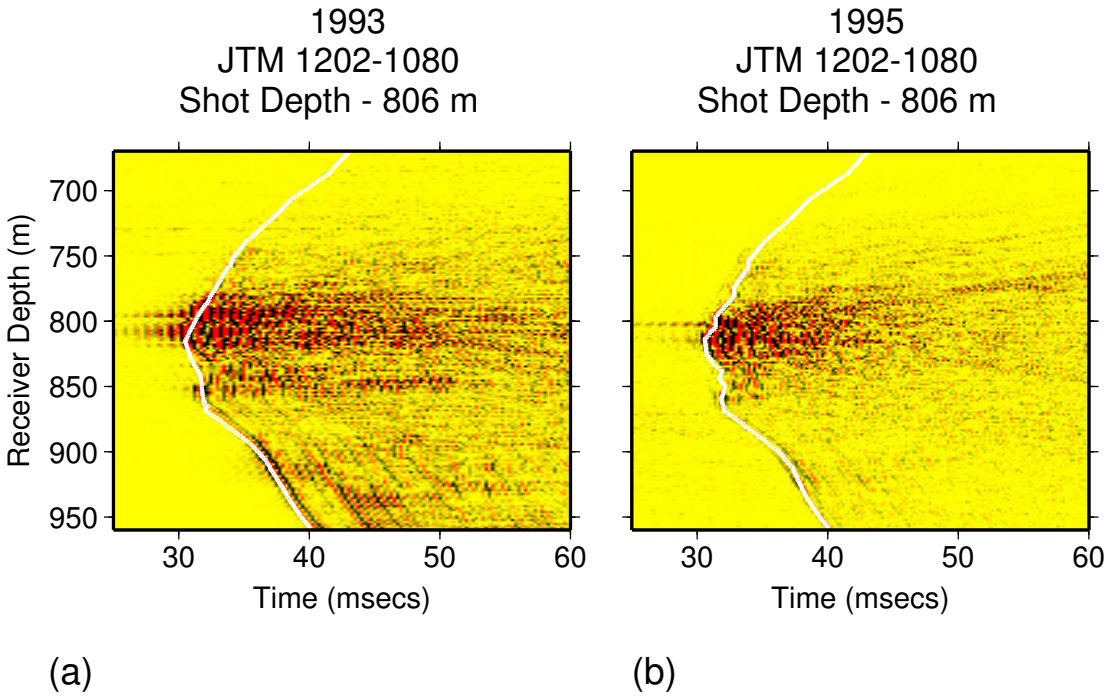

Figure 3.12: Common-source gathers from the 1993 and 1995 surveys in the McElroy Field. The thick, white curves are first-arrival traveltimes picked on the gathers.

201 sources and 191 receivers were deployed in the first survey, while 200 sources and 192 receivers were deployed in the second survey.

3.3.1 Conventional Time-Lapse Monitoring

To reconstruct a 2D, p-wave velocity model between the two wells, I pick first-arrival traveltimes on the seismic sections. The traveltime data are shown in Figure 3.13. The axes of the data grids in Figure 3.13 represent shot and receiver depths. As expected, we observed the largest traveltime differences at the depths corresponding to the location of the reservoir. The traveltime increase is caused by a decrease in reservoir seismic velocity. The decreased velocity is a result of the injection of CO_2 into the reservoir. I reconstruct velocity models using the tomography algorithm described in Zelt and Barton (1998). Figure 3.14 shows the difference between

the 1993 model and the 1995 model. The reduction in velocity can be seen in the velocity-difference model.

3.3.2 Time-Lapse Monitoring with Sparse Data

After successfully applying the proposed time-lapse monitoring approach to synthetic data, I apply it to the McElroy Field data. In this case, I use 5% of the 1995 monitor dataset. The results are shown in Figure 3.15. Without data estimation, the reservoir velocity change resulting from the injection of CO_2 is grossly underestimated. Using the complete baseline dataset and the sparse monitor dataset, I estimate the discarded data. The velocity model reconstructed using the estimated data is good. This result shows the efficiency of the proposed approach for cross-well traveltime field data. An ideal field implementation of our approach will utilize more than two surveys for optimal results.

3.4 Summary

To examine the effectiveness of my approach, I created synthetic time-lapse traveltime datasets from field datasets recorded in the McElroy Field in Texas. The field data were recorded to monitor a reservoir flooded with CO_2 for secondary recovery. I created 70 synthetic time-lapse velocity models representing the state of the field every two weeks from the date of first data acquisition, and I also create their corresponding traveltime datasets. The synthetic models showed CO_2 being injected into the reservoir and leaking into a shallower reservoir 10 months after injection began.

I kept the total size of the data at the end of the surveys constant while varying both the size of the sparse data acquired at each time and the length of the time interval between datasets. I used 1%, 2%, 5%, and 10% of the individual complete datasets as my sparse datasets. The data intervals in these datasets were 2, 4, 10, and 20 weeks, respectively. After the unrecorded datasets were estimated, traveltime tomography was used to reconstruct the velocity models. The errors in the

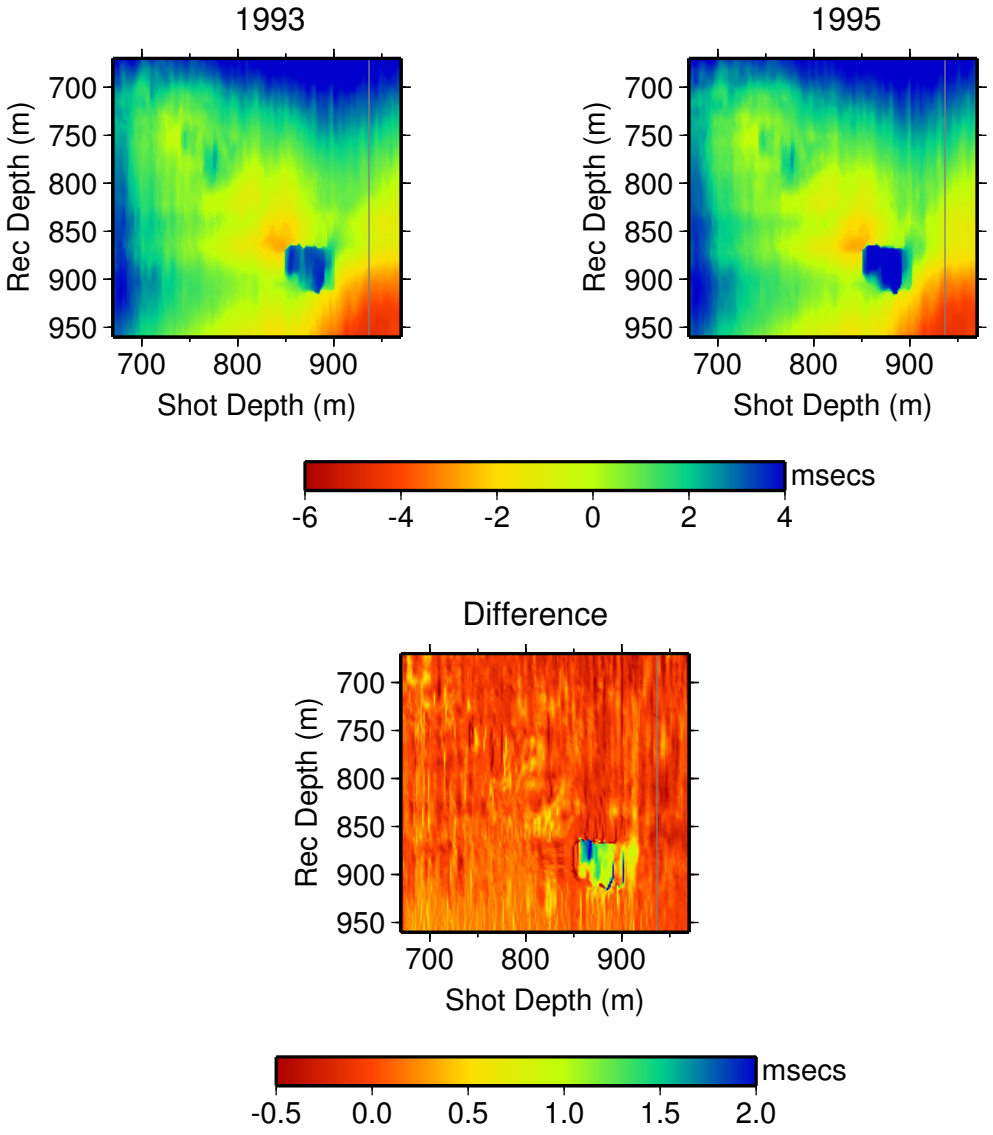

Figure 3.13: Traveltime data grids picked from the baseline (1993) and monitor (1995) surveys, and the difference between the two datasets.

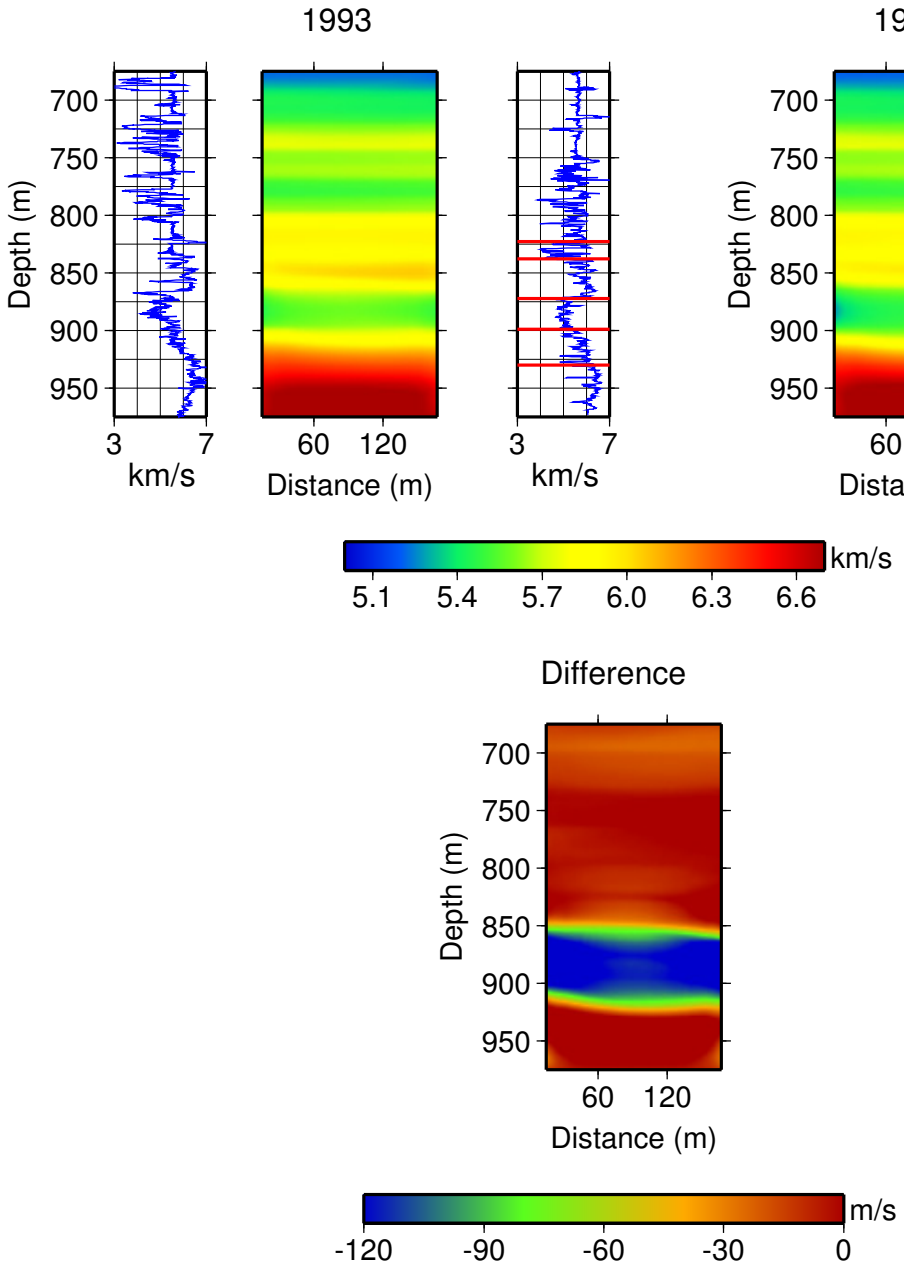

Figure 3.14: Reconstructed velocity models from the baseline (1993) and monitor (1995) surveys, and the velocity-difference model. The velocity models are reconstructed using the datasets shown in Figure 3.13. 1-D velocity logs shown are produced from sonic delta-transit time well logs. Geologic markers are indicated by horizontal red lines on the logs. There is good agreement between the velocity model and the well logs.

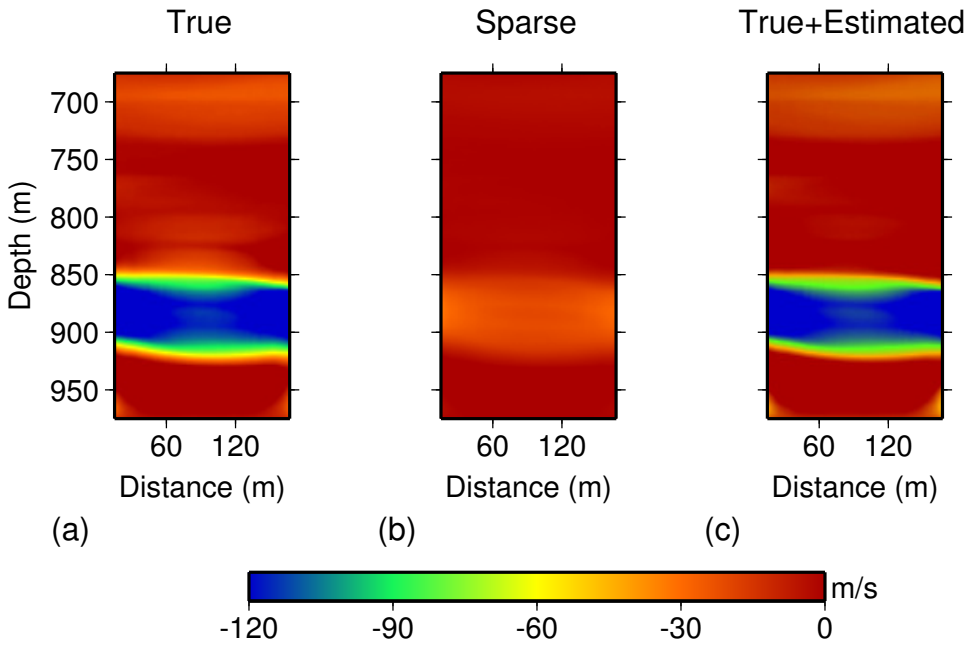

Figure 3.15: Reconstructed velocity-difference models from (a) the complete field dataset, (b) the sparse field data (5% of the complete dataset), and (c) 5% true + 95% estimated dataset.

reconstructed models were then analyzed.

The synthetic example showed that only a small number of iterations are needed to produce reliable reconstructed velocity models; in my case, only three iterations were needed. As more sparse datasets are acquired, estimates of previously acquired sparse datasets improve in accuracy. The accuracy improves because the newer sparse datasets continue to add information to the older datasets.

Because the reconstructed time-lapse models converge after some time, a moving estimation window can be used to reduce computational time. Furthermore, because total data size increases with time, once a certain reconstructed velocity model has converged, its data need not be re-estimated when new data are available. In the synthetic data example, the CO_2 leak is detected two weeks after it occurred. However, this time delay is much smaller than the conventional time-lapse data acquisition interval.

I also applied the proposed approach to field data. Here, I use the baseline and monitor data from the McElroy Field. I discarded 95% of the monitor dataset and then estimated the discarded data from the baseline data and the sparse monitor data. The results show the efficiency of this approach on crosswell field data. With only the baseline and the sparse monitor dataset, the reconstructed reservoir velocity change is underestimated. With the baseline and estimated monitor datasets, the reconstructed reservoir velocity change is close to the true model.

Chapter 4

Quasi-continuous Monitoring with Surface-Seismic Data: Synthetic Data Example

4.1 Introduction

In the preceding chapter, I presented an application of the quasi-continuous seismic monitoring approach to crosswell-seismic traveltime data. I showed that my approach is efficient at tracking small changes in the velocity model of a reservoir at short time intervals. To estimate the unrecorded traveltime data at each incremental survey time, I used non-stationary PEFs as my data estimation tool.

In this chapter, I shift my focus to surface-seismic data. Surface-seismic reservoir monitoring is common practice today. Surface-seismic exploration is less invasive than crosswell-seismic exploration from the reservoir point of view, which makes it a better option in projects where the integrity of the reservoir is very important. An example is CO_2 sequestration in geologic reservoirs, where an abundance of wells penetrating the reservoir might compromise its containment capability. Furthermore, surface-seismic survey configurations provide more flexibility for source-receiver distribution than crosswell-seismic survey configurations, and survey boundaries can be extended with minimal cost.

I present two synthetic tests of quasi-continuous surface-seismic monitoring. The first is a 2D CO_2-sequestration example designed to ensure that the injected gas remains contained within the reservoir, and the second is a 3D enhanced-recovery example designed to verify that the injected fluid flows in the direction intended.

4.2 2D surface-seismic Synthetic Example

The monitoring scenario in this example is similar to that presented in Chapter 3, although the geologic setting is different. The reservoir here is a layered sedimentary unit overlain by a chalk layer and underlain by layered sedimentary units. It is separated from the geologic units below by an unconformity. The baseline velocity model is perturbed to produce 20 time-lapse velocity models. The perturbation is defined by velocity decrease in the reservoir. The velocity decrease represents the injected CO_2 in the reservoir (see Mavko et al., 1998). I let a leak occur in the reservoir after the 11th month, and allow the leaked CO_2 to accumulate in a reservoir above the containment reservoir. One of the benefits of a quasi-continuous monitoring strategy is that it may detect the leak as soon as it occurs so that remedial steps can be taken.

I use the elastic wave equation algorithm described in Wu (2005) to simulate the synthetic seismic data with velocity and density models created for this example. I use a source wavelet with a peak frequency of 25Hz. Although computationally time-consuming, the elastic wave equation algorithm allows the simulation of a more realistic seismic dataset with primary- and secondary-wave arrivals.

4.2.1 Survey Setup

I simulate 2D seismic data using 31 receivers measuring data from 481 shots. The shots are spaced 25 m apart, while the receivers are spaced 400 m apart along the survey line. To demonstrate a conventional survey, I use data from all sources and all receivers. To demonstrate a quasi-continuous survey, I use data from about 96 evenly spaced shots for each partial survey. The quasi-continuous survey is designed

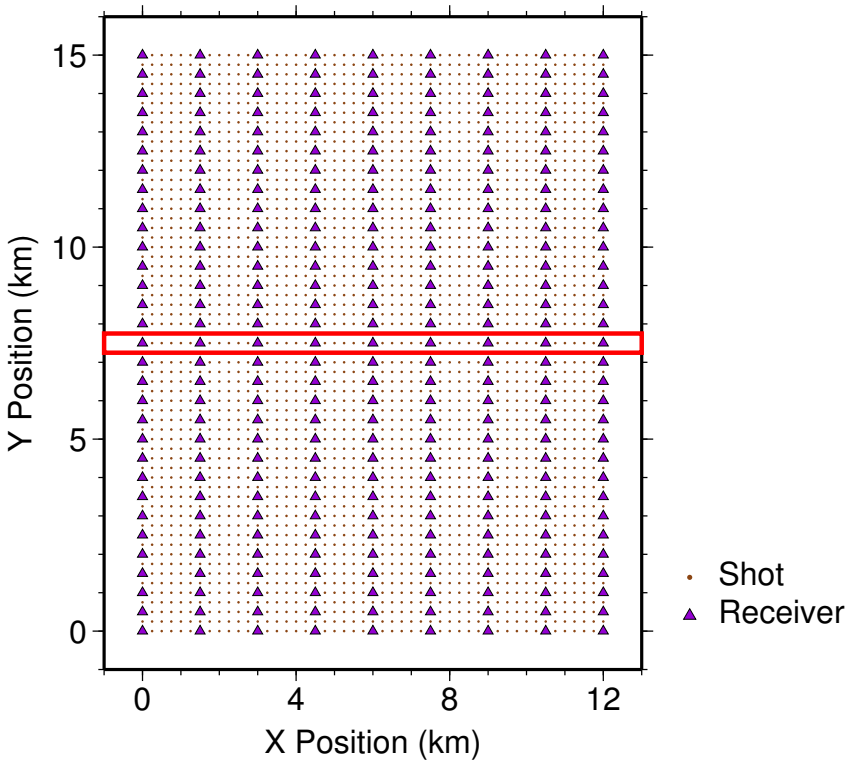

Figure 4.1: An illustration showing the 2D acquisition pattern described in Section 4.2 as an extraction from a 3D survey. The rectangle with the thick red border indicates the extracted 2D line.

in such a way that five partial surveys produce the same data volume and coverage as one complete survey.

The source-receiver distribution described in this 2D example can be viewed as a 2D slice through an 3D survey, where the receivers are ocean-bottom cables (OBCs) and the sources are airgun shots distributed on a regular grid as shown in Figure 4.1. In the quasi-continuous monitoring case, some shot-lines are skipped in each partial survey.

4.2.2 Conventional Time-Lapse Monitoring

In today's industry, conventional time-lapse monitoring surveys may occur as infrequently as every two years. I adopt a time interval of 20 months for my conventional survey. Figure 4.2 shows the baseline velocity model, the velocity model after 20 months, and the time-lapse change between the two velocity models. Figure 4.3 shows wavefield-propagation snapshots from one of the shots through the baseline velocity model, overlain on a background image of the baseline velocity model. The primary and mode-converted waves can be seen propagating through the velocity model. In Figure 4.4, I show sample shot gathers from the baseline survey, the time-lapse survey, and the difference between them. We can easily identify the primary reflectors, and the mode converted arrivals on the shot gathers. The mode converted waves are identified by their moveouts and their significantly reduced amplitudes at zero offset.

I use a source-receiver migration algorithm (see Biondi, 2007) to produce seismic images from the shot gathers. These images are shown in Figure 4.5, together with the difference between them. Because I migrated both datasets with the baseline velocity model, as is the industry practice, the reflectors below the injected CO_2 are not located at the right depth. This effect can be removed by calculating the reflector depth-shifts and relocating the reflectors to the correct depths. The computed shifts are shown in Figure 4.7, and the corrected images are shown in Figure 4.6.

4.2.3 Quasi-Continuous Time-Lapse Monitoring

We saw in Section 4.2.2 that the conventional time-lapse monitoring strategy is not ideal for all monitoring scenarios, especially in cases where a late discovery of an abnormality can be catastrophic. A more appropriate strategy allows short time intervals between surveys. To facilitate data acquisition, we acquire subsets of the entire survey at each survey time, as described in Chapter 1, until a full survey has been completed.

If we assume that a slow-time resolution of one month is good enough for this

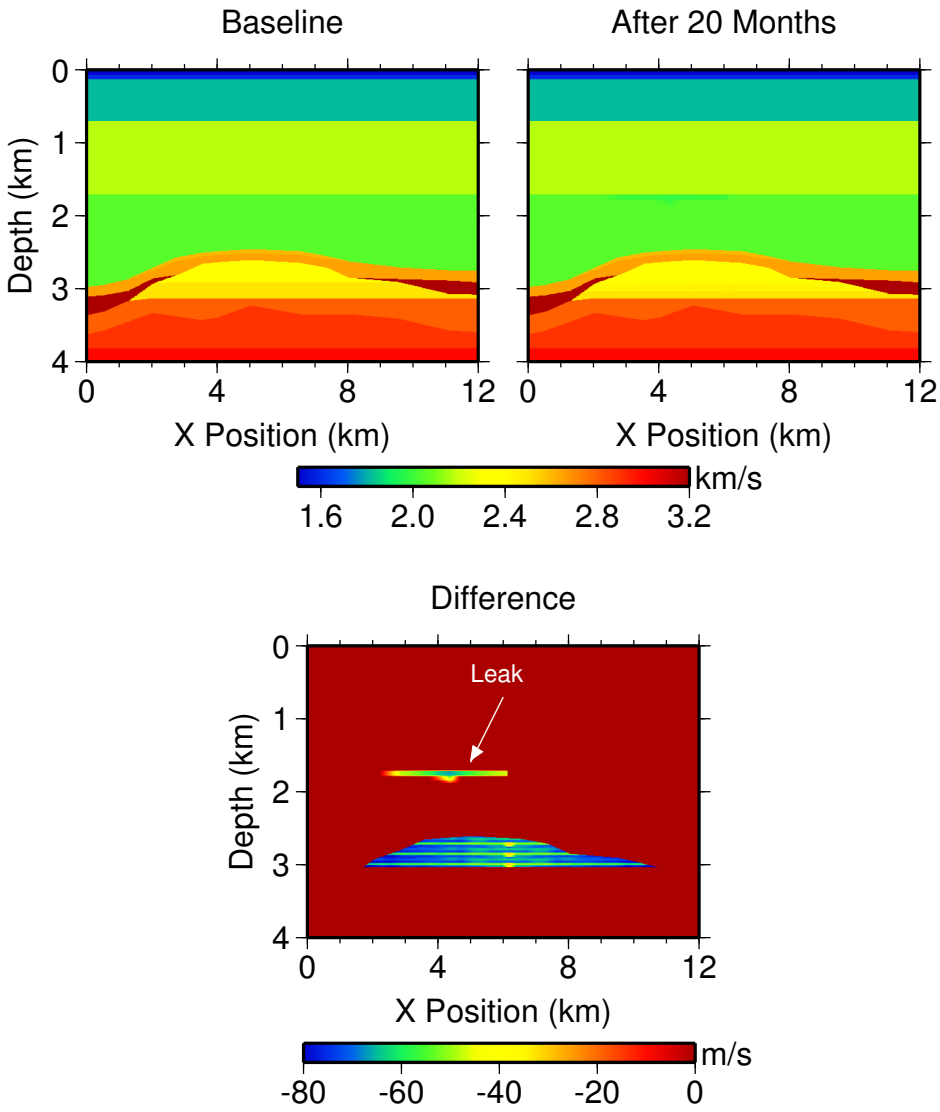

Figure 4.2: The 2D synthetic baseline velocity model, the velocity model after 20 months, and the difference between the two velocity models.

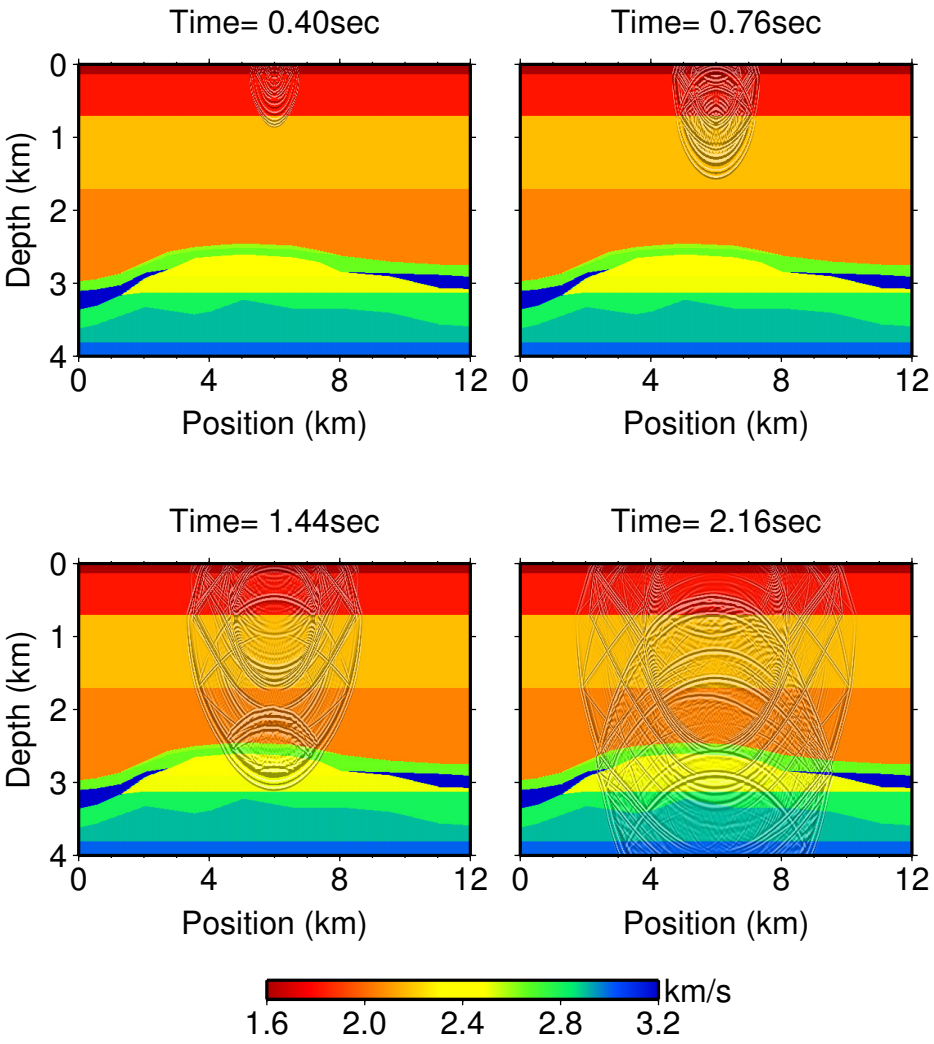

Figure 4.3: Snapshots of the wavefield propagated through the baseline velocity model.

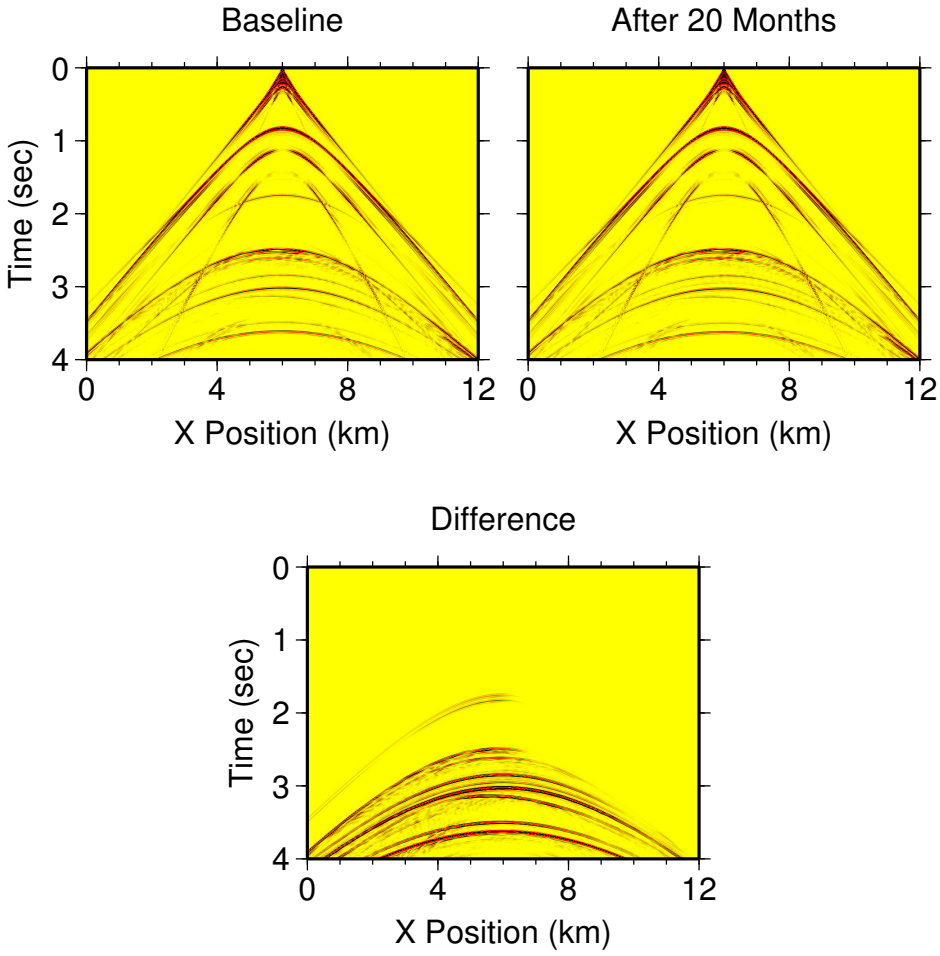

Figure 4.4: Selected synthesized receiver gathers from the baseline dataset, the dataset after 20 months, and the difference between them.

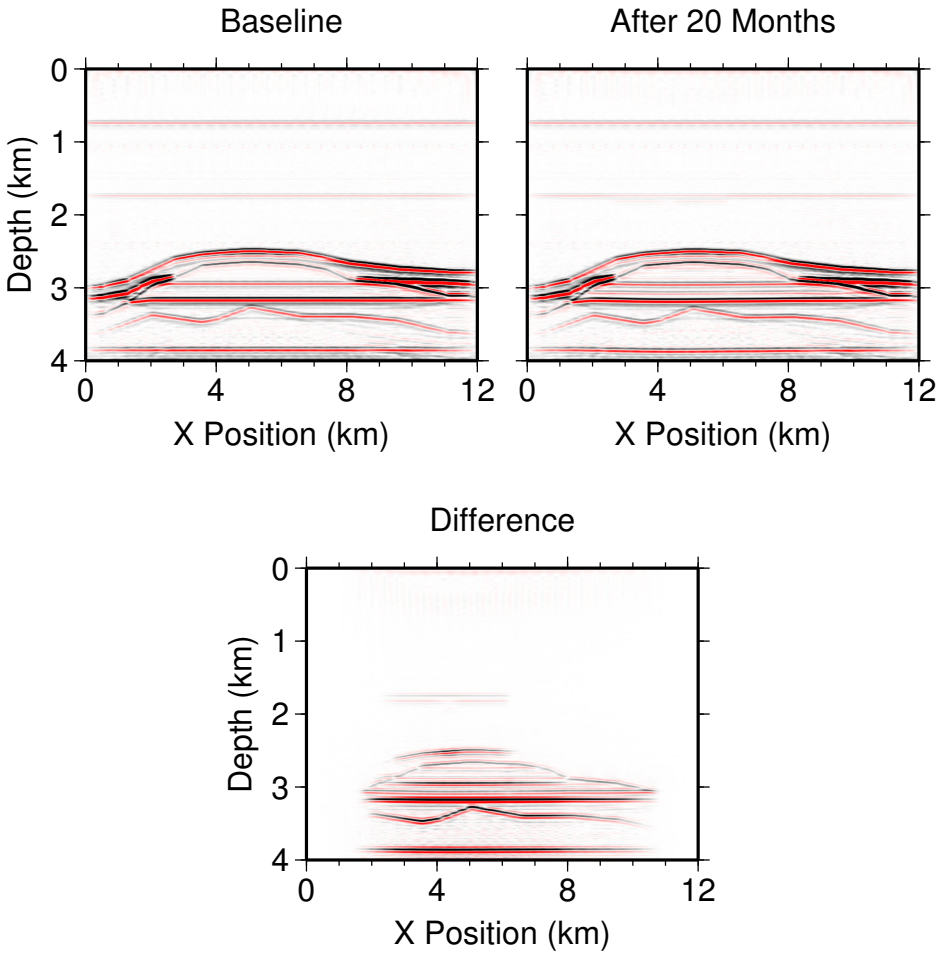

Figure 4.5: The migrated baseline image, the image after 20 months, and the time-lapse difference image. Notice the reflector depth errors introduced by using the baseline velocity model in migrating the image.

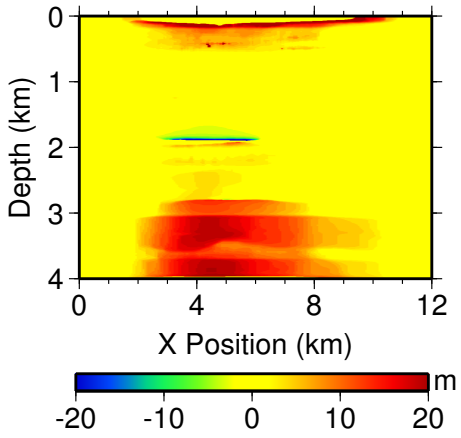

Figure 4.6: Computed depth-shifts for the migrated image after 20 months.

2D seismic time-lapse monitoring simulation, we can assess the ability of the monitoring approach described in this dissertation to detect the leak shortly after its occurrence. I assume that 20% of the data described in the previous section can be acquired and processed within a month. The objective now becomes using 20% of the synthesized datasets for each of the 20 synthetic velocity models to estimate the discarded 80%.

In creating the sparse datasets, I use realistic seismic source-receiver distributions (see Section 4.2.1 on page 94). The synthetic sparse datasets consist of regularly spaced traces. Four in five consecutive traces from the original complete dataset are discarded. The selected traces vary from survey to survey so that a complete survey is acquired after five surveys. Figure 4.8 shows sparse receiver gathers from two different surveys.

In order to perform time-lapse data estimation, I create time-lapse data volumes by concatenating receiver gathers along the slow-time dimension, producing 3D data volumes from 2D sections. At each incremental survey time, I add receiver gathers from the current sparse dataset to the accumulated time-lapse data volume for each receiver. Accordingly, all unknown traces in the accumulated sparse datasets are estimated at each incremental survey time. I use, as the input to the

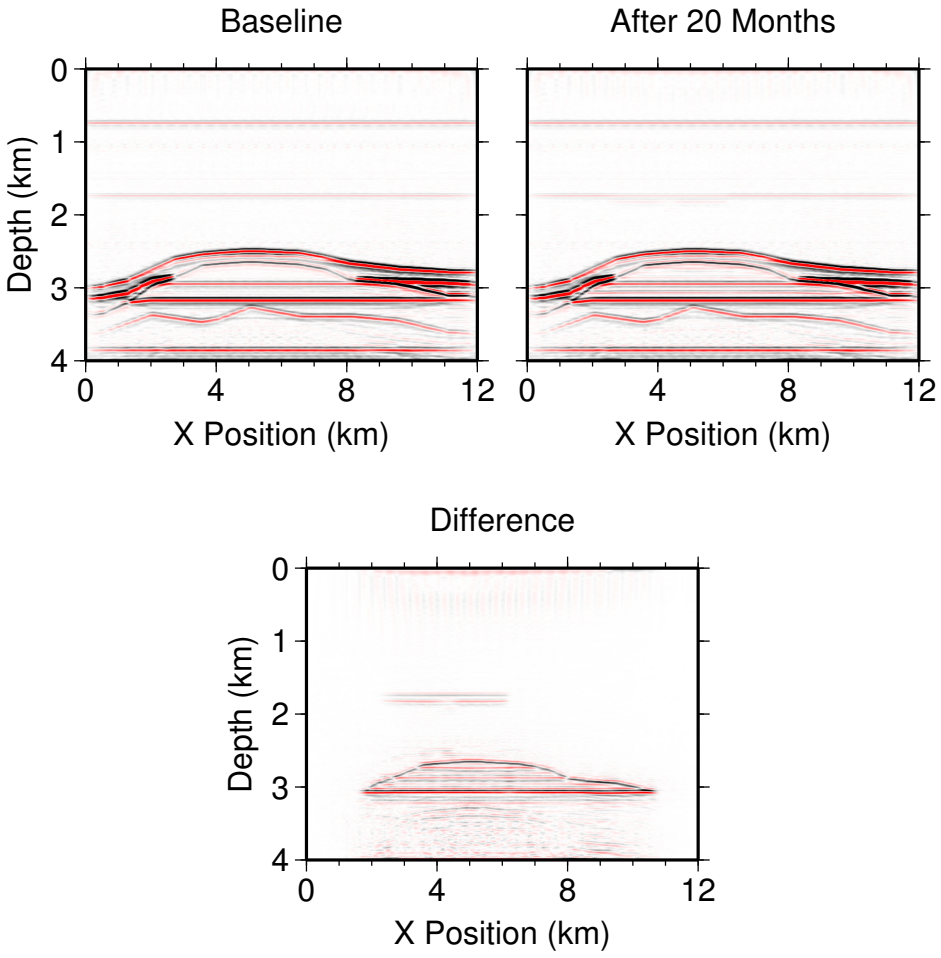

Figure 4.7: The baseline image, the corrected image after 20 months, and the time-lapse difference image. Notice that the reflectors have been relocated to their correct depths.

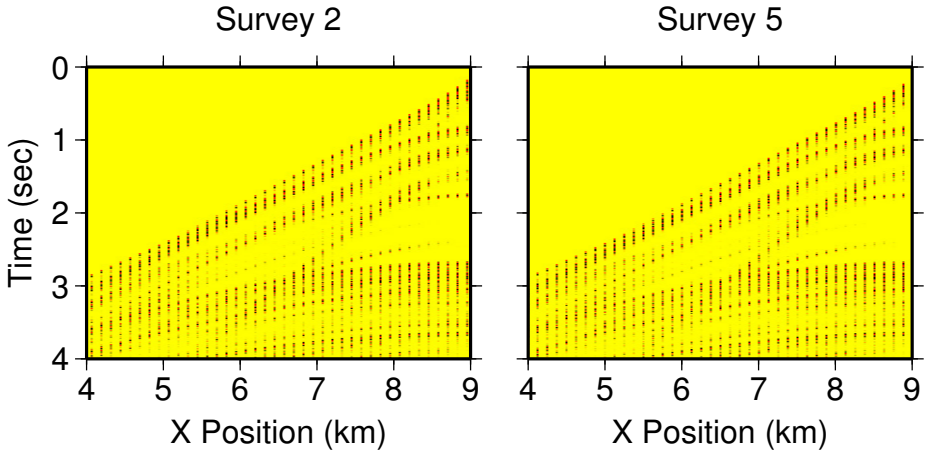

Figure 4.8: 20% sparse receiver gathers from the same receiver location for surveys 2 and 5.

minimum-weighted-norm interpolation (MWNI) algorithm, the 1D Fourier transform of overlapping 3D window patches, with 700 samples in the frequency dimension and 16 samples in the x-dimension. The number of samples in the slow-time dimension depend on the number of surveys in the accumulated dataset. In Figure 4.9, I show a selected sparse receiver gather; the corresponding true and estimated receiver gather; and the difference between the true and estimated datasets. MWNI does a good job at reconstructing the unknown traces.

I migrate the estimated datasets using the source-receiver migration algorithm mentioned earlier to produce corresponding seismic images. Figure 4.10 shows the subsurface image for the 12th month, obtained by estimating 80% unknown data from 20% known data accumulated up to the 14th month, together with time-lapse difference images. Here, I compare the time-lapse difference images from the estimated datasets to the true time-lapse difference images. Before computing the difference images, I relocate the reflectors to their correct depths using the cross-correlation algorithm described in Chapter 2.

By migrating the sparse data without estimating unavailable traces, an image close enough to the true image is produced. However, the time-lapse image obtained by subtracting the monitor image from the baseline image is less than adequate for monitoring the changes in the reservoir (Figure 4.11). The inadequacy

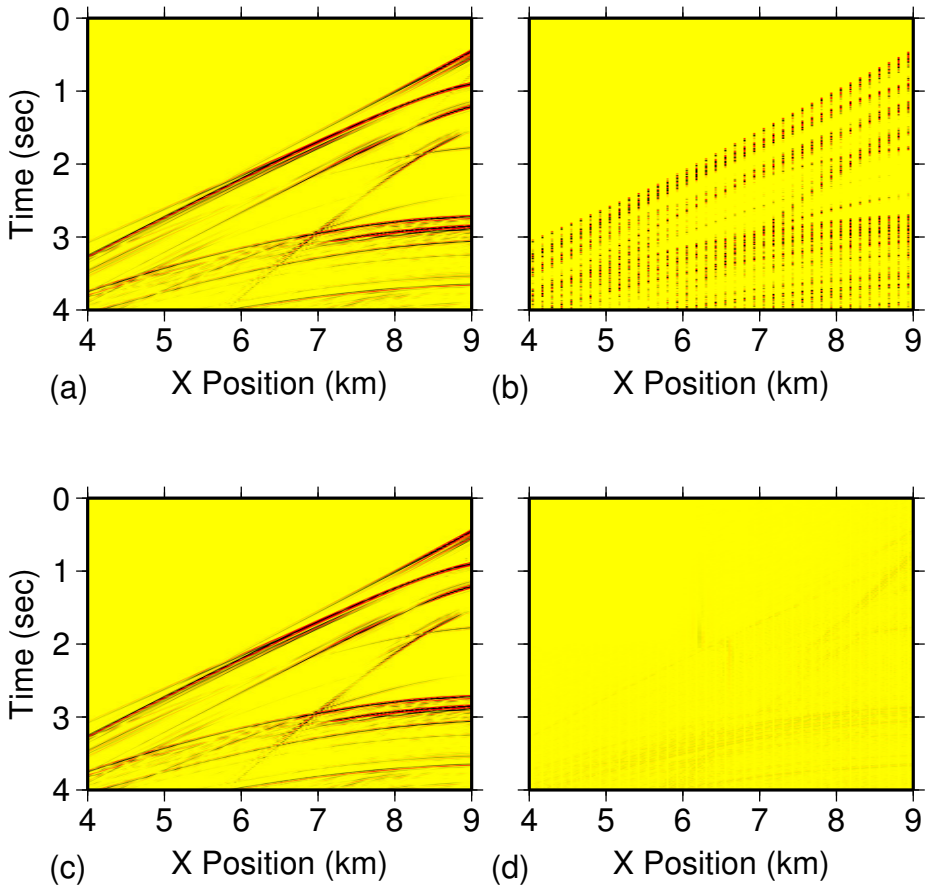

Figure 4.9: A comparison of the true, sparse, and estimated data for one receiver gather from the 12th-month data estimated in the 14th month. (a) The complete true data. (b) The 20% sparse data. (c) The estimated data. (d) The estimation error computed by taking the difference between the data in (a) and the data in (c).

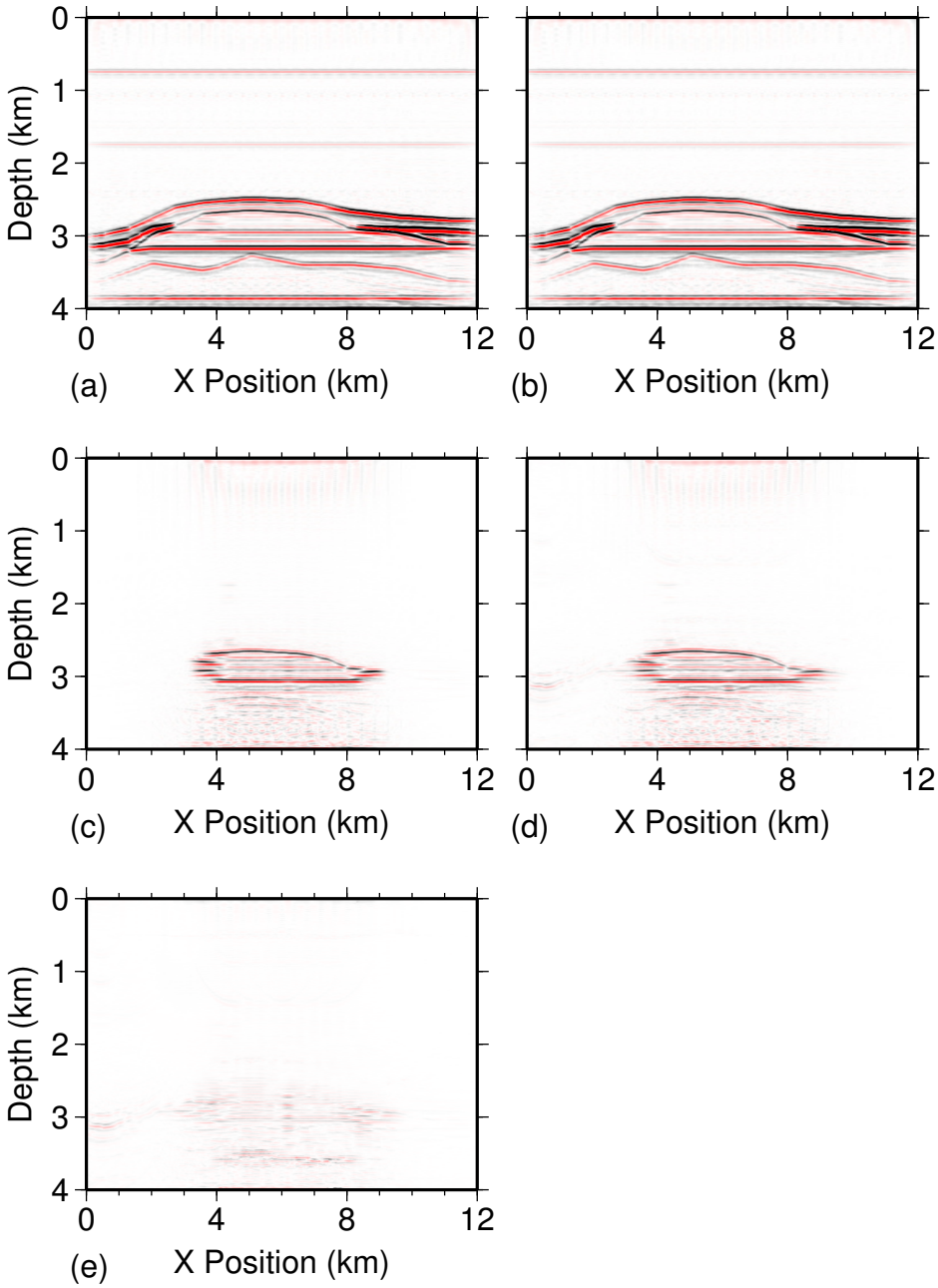

Figure 4.10: (a) The 12th-month subsurface image obtained from complete true data. (b) The 12th-month subsurface image obtained from the estimated data computed in the 14th month. (c) The 12th-month subsurface time-lapse difference image obtained from complete true data. (d) The 12th-month subsurface time-lapse image obtained from the estimated data computed in the 14th month. (e) The estimation error computed by taking the difference between the image in (a) and the image in (b).

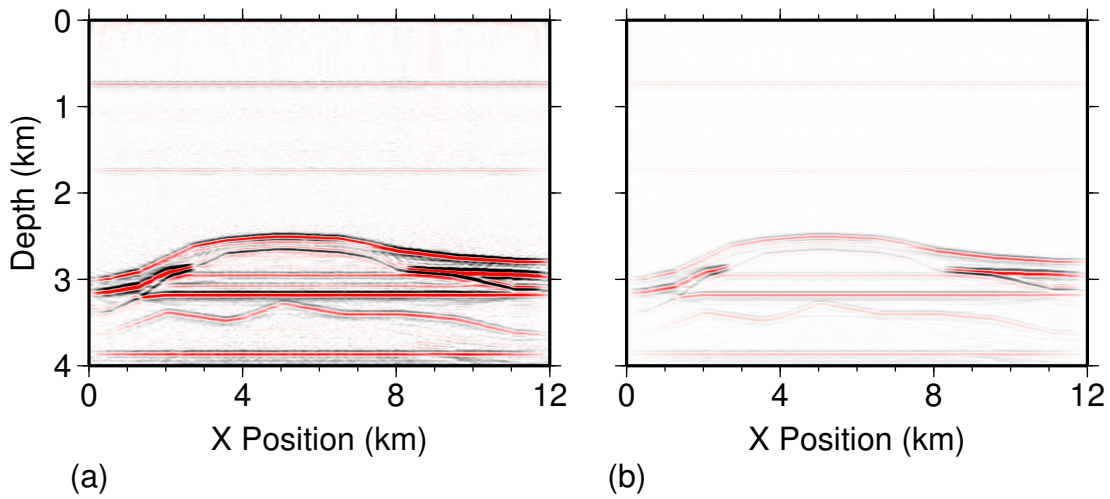

Figure 4.11: (a) The 15th-month subsurface image obtained from 20% sparse data. (b) The 15th-month time-lapse difference image obtained by subtracting the image in (a) from the baseline image.

results because images obtained from data with different number of seismic traces are differenced. By estimating the unavailable data, we compensate for the difference in data size.

Images obtained using the complete true data show that the CO_2 leak can be detected in the 11th month. Figure 4.12 shows the time-lapse images obtained using complete true data for months 10 through 15. The leak can be seen to increase in size starting from the 11th month. Figures 4.13, 4.14, and 4.15 show the time-lapse images obtained from the 10th to 15th using the estimated data with ESLs of 0, 1 and 2 months respectively. The leak is detected with the 11th-month data, but not until the 12th month; in other words, the leak is detected with the 11th-month data when there is a one-month estimation slow-time lag. We can compare Figure 4.13(b) and Figure 4.14(b) to see the improvement in our ability to detect the leak by using data from a later time than the time of interest in the estimation process. In this example, the quasi-continuous monitoring strategy presented in this dissertation can detect the leaked CO_2 one month after it occurs.

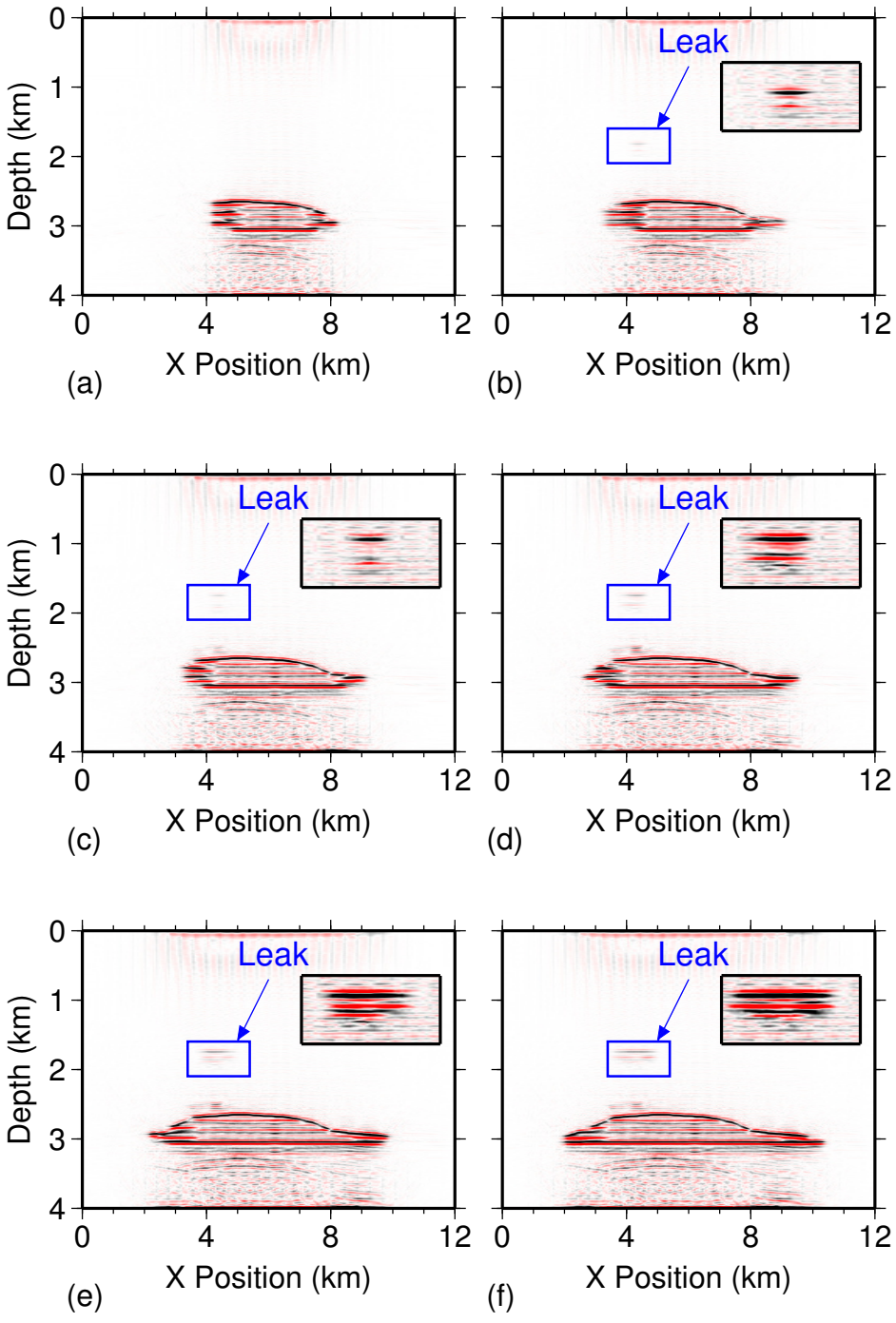

Figure 4.12: Time-lapse difference images obtained from complete data for the (a) 10th month, (b) 11th month, (c) 12th month, (d) 13th month, (e) 14th month, (f) 15th month.

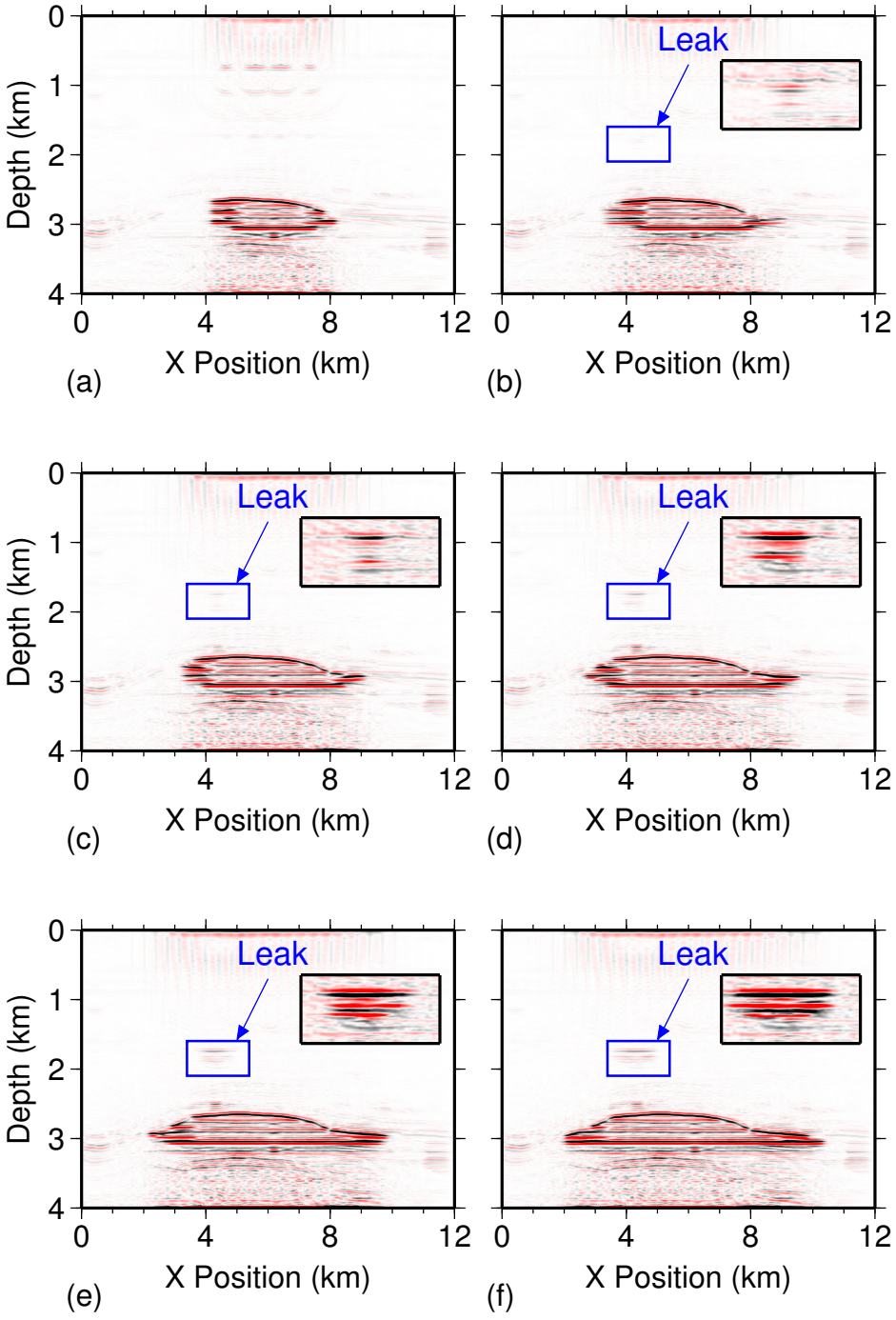

Figure 4.13: Time-lapse difference images obtained from estimated data with an ESL of 0 months for the (a) 10th month, (b) 11th month, (c) 12th month, (d) 13th month, (e) 14th month, (f) 15th month.

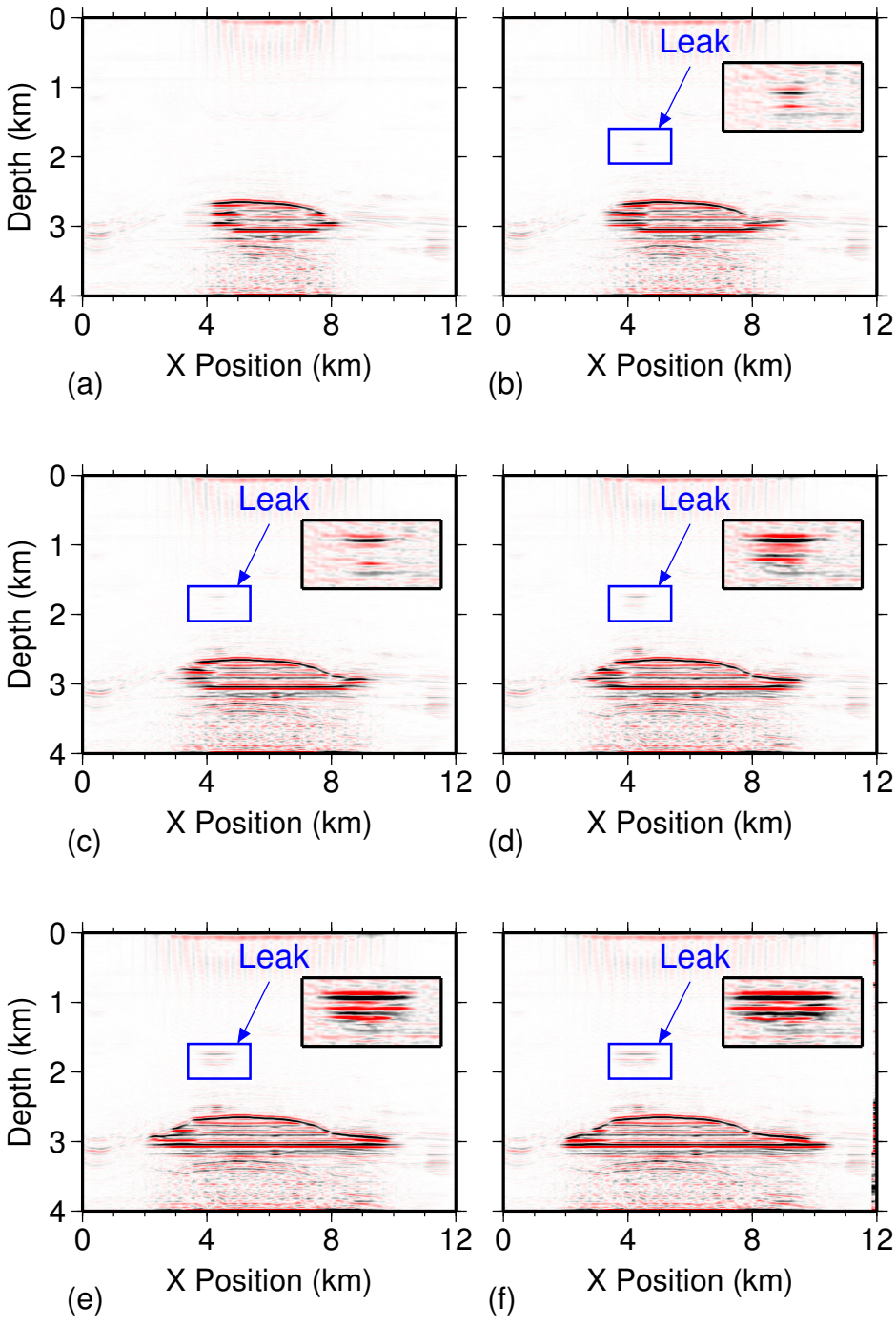

Figure 4.14: Time-lapse difference images obtained from estimated data with an ESL of 1 month for the (a) 10th month, (b) 11th month, (c) 12th month, (d) 13th month, (e) 14th month, (f) 15th month.

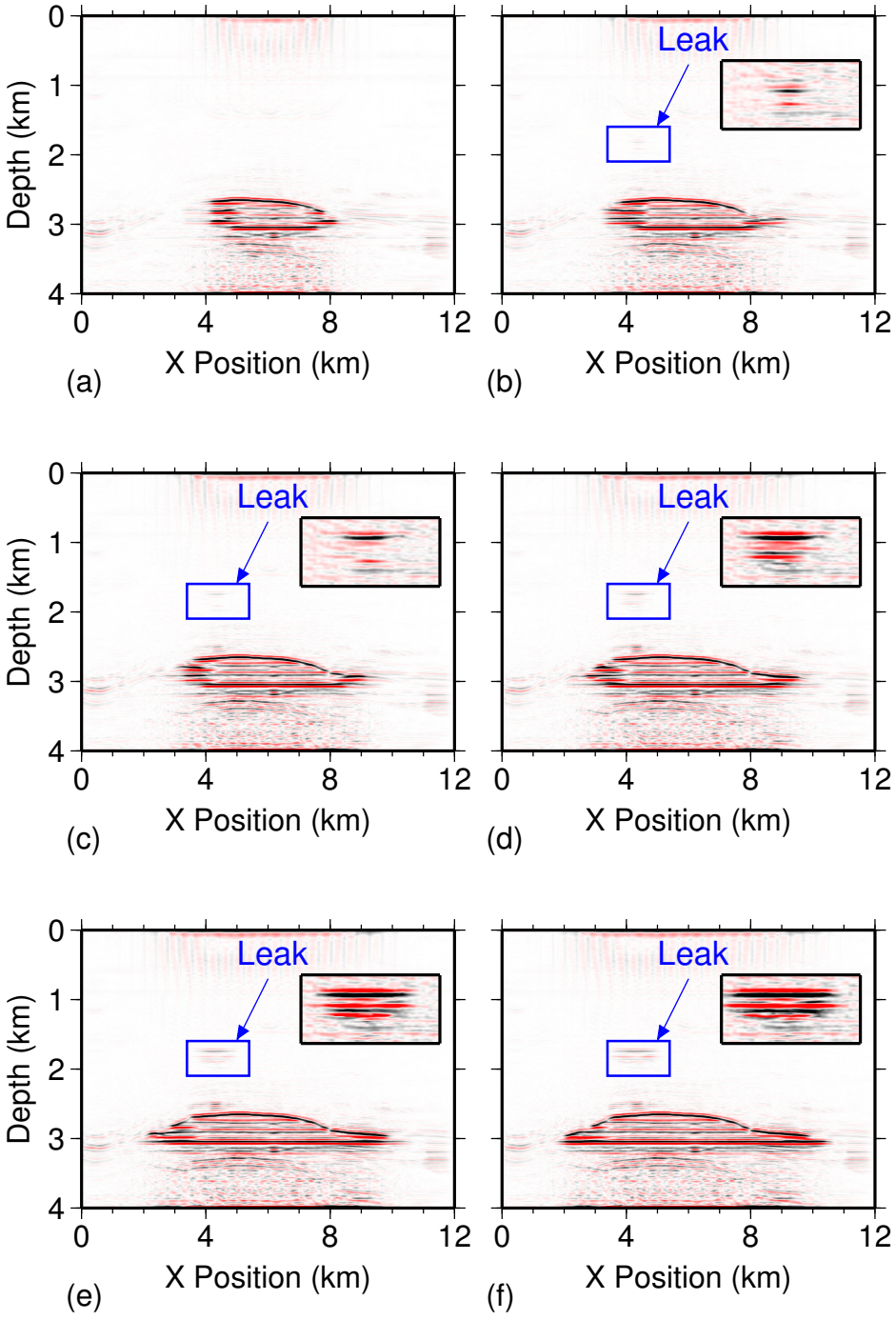

Figure 4.15: Time-lapse difference images obtained from estimated data with an ESL of 2 months for the (a) 10th month, (b) 11th month, (c) 12th month, (d) 13th month, (e) 14th month, (f) 15th month.

Figure 4.16 shows time-lapse difference images obtained for month six using estimated data from accumulated sparse datasets in months 6, 8, 10, 12, 15, and 20. In general, we see a reduction in imaging artifacts, caused by data-estimation errors, with time. The same can be said for Figure 4.17, which shows time-lapse difference images obtained for month 11 using estimated data from accumulated sparse datasets in months 11, 13, 15, 17, 19, and 20. As I explained in Chapter 3, estimation errors (artifacts) may be introduced when long estimation windows are used. This occurs because real features which exist in later datasets but are not present in earlier datasets are introduced into earlier datasets. Short, moving estimation windows can be used to avoid this problem.

It should be noted that the estimation error introduced by features present in sparse datasets at later times in estimated datasets at earlier times do not affect decisions made at earlier times, because of the irreversibility of time. The interpreter of the images obtained using estimated data must take this into account. The interpreter must be able to distinguish between a real feature and an introduced feature.

Figure 4.18 shows the ratio of the sum of the absolute amplitudes in the estimated-data images to the sum of the absolute amplitudes in the true-data images. Figure 4.19 shows the average reflector depth-shifts in the estimated-data images respectively. These are measures obtained with the estimation-error tool described in Section 2.2. The plotted curves are color-coded by the estimation slow-time lag (see Section 1.4 on page 9 for definition).

In addition to showing that estimation errors in this example are very small, the plots show that the most accurate estimates do not occur when the estimated data of interest is most recently acquired data, i.e. when the estimation slow-time lag is zero months. The most accurate estimates occur, in general, when the estimation slow-time lag is two months. Before and after two months of estimation slow-time lag, the estimates are less accurate. This is more apparent in the amplitude ratio plots than in the depth-shift error plots. Unlike the amplitude ratio, the depth-shift error for an estimation slow-time lag of zero months does not conform to this rule. This may be because the estimated traces at zero months of estimation slow-time lag are extrapolated in the slow-time direction, and as such, are not fully constrained

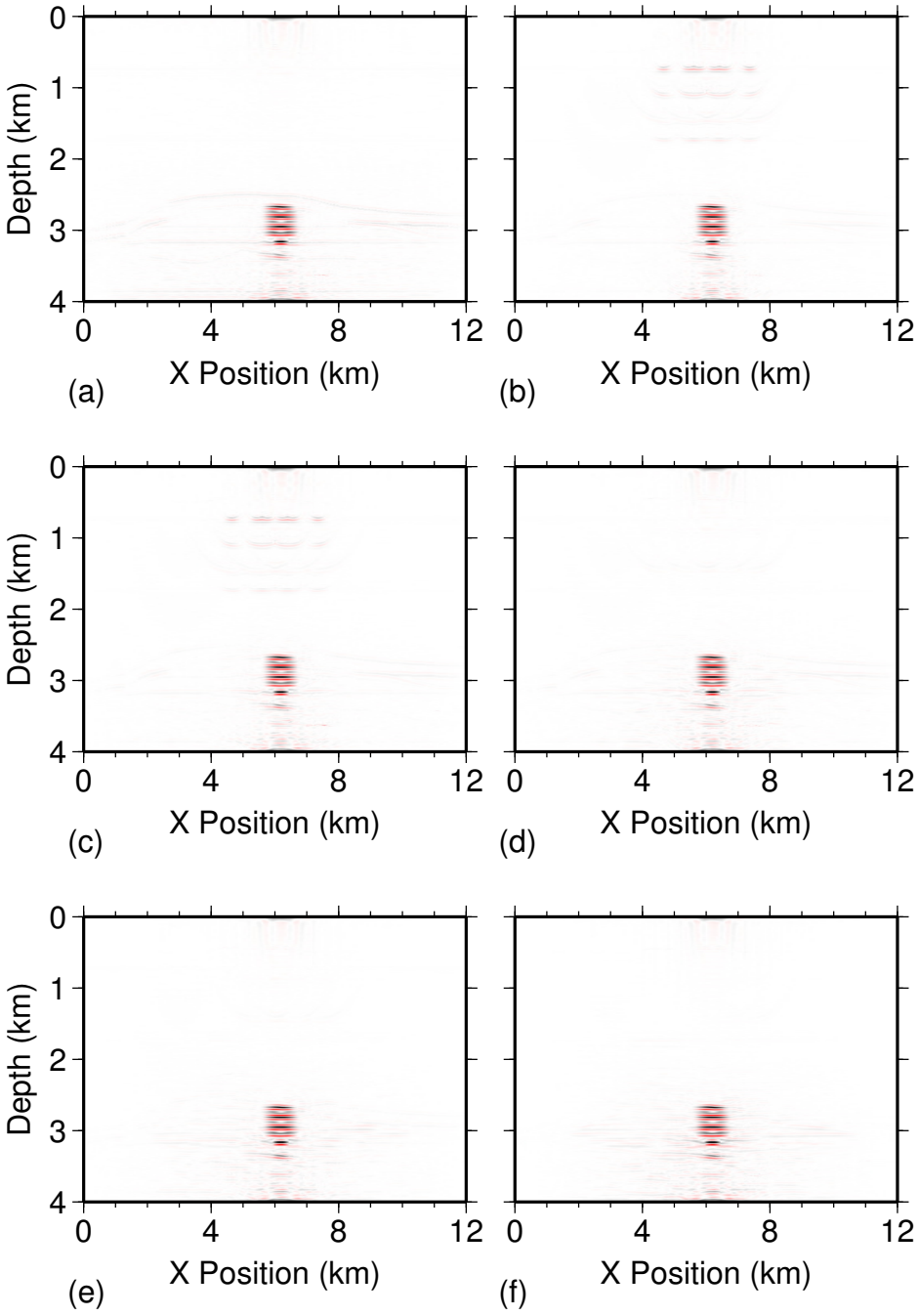

Figure 4.16: Time-lapse difference images obtained for month six using data estimated from accumulated sparse datasets in (a) month six, (b) month eight, (c) month 10, (d) month 12, (e) month 15, and (f) month 20.

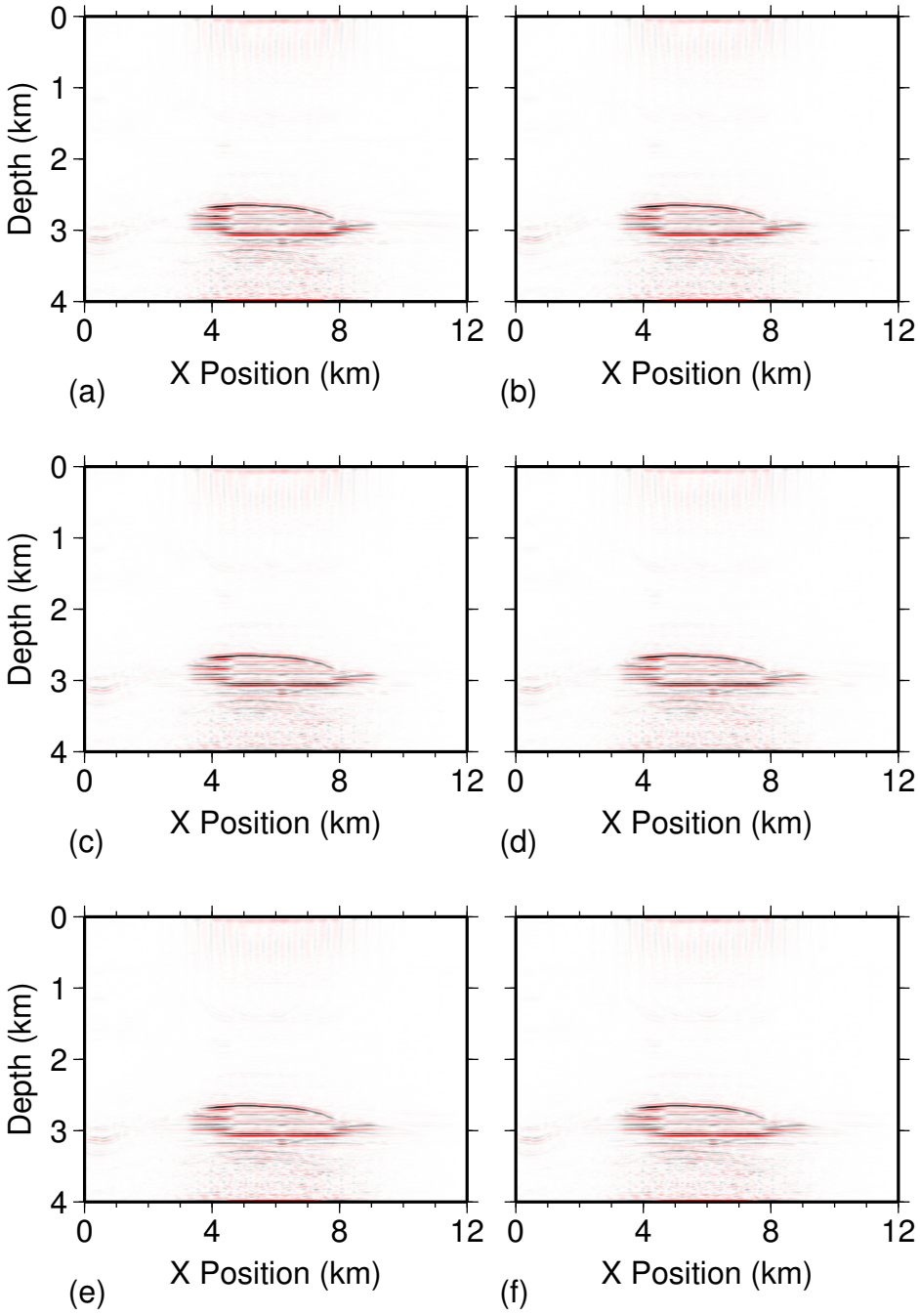

Figure 4.17: Time-lapse difference images obtained for month 11 using data estimated from accumulated sparse datasets in (a) month 11, (b) month 13, (c) month 15, (d) month 17, (e) month 19, and (f) month 20.

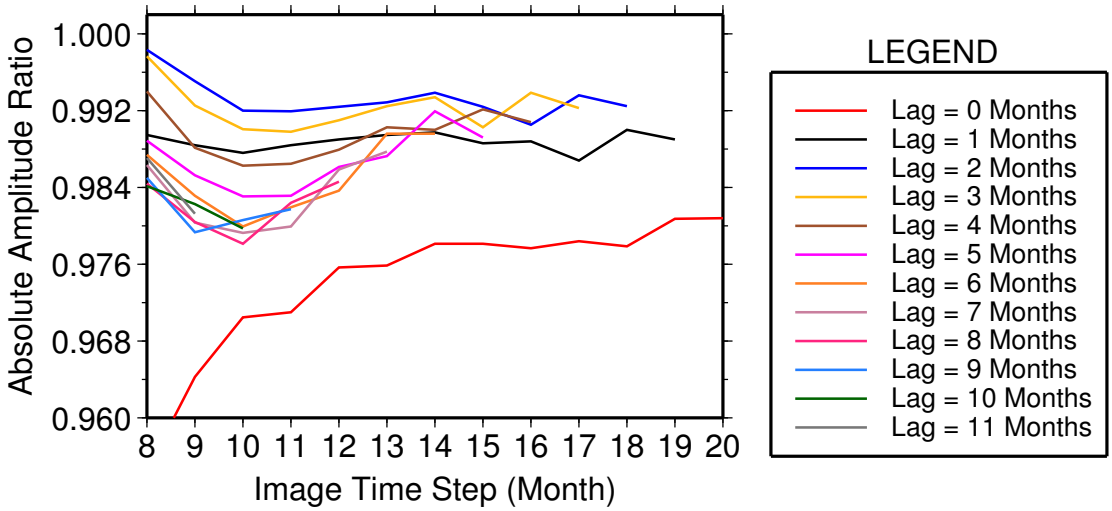

Figure 4.18: The ratio of the sum of the absolute amplitudes in the estimated-data images to the sum of the absolute amplitudes in the true-data images, color-coded by estimation slow-time lag (see Section 1.4 on page 9 for definition). Notice how the highest ratios occur, in general, at two months of estimation slow-time lag.

to follow a pattern.

Knowledge of the optimal estimation slow-time lag is useful when interpreting images obtained using data-estimation-based time-lapse monitoring. For a field project, where the true data are unknown and errors cannot be determined, a synthetic test, with acquisition parameters and noise level similar to those of the field data, can be used to determine the optimal estimation slow-time lag.

4.3 3D Surface-Seismic Synthetic Example

In this section, I apply my approach to a 3D synthetic model that simulates an oil field during enhanced recovery by water injection. Continuous monitoring during water injection would be required if decisions on injection rate and pressure must be made on the fly, which could happen if uncertainties exist regarding pressure gradients or structural integrity within the reservoir. The reservoir in this synthetic velocity model is a folded and partially faulted unit overlain by two folded and

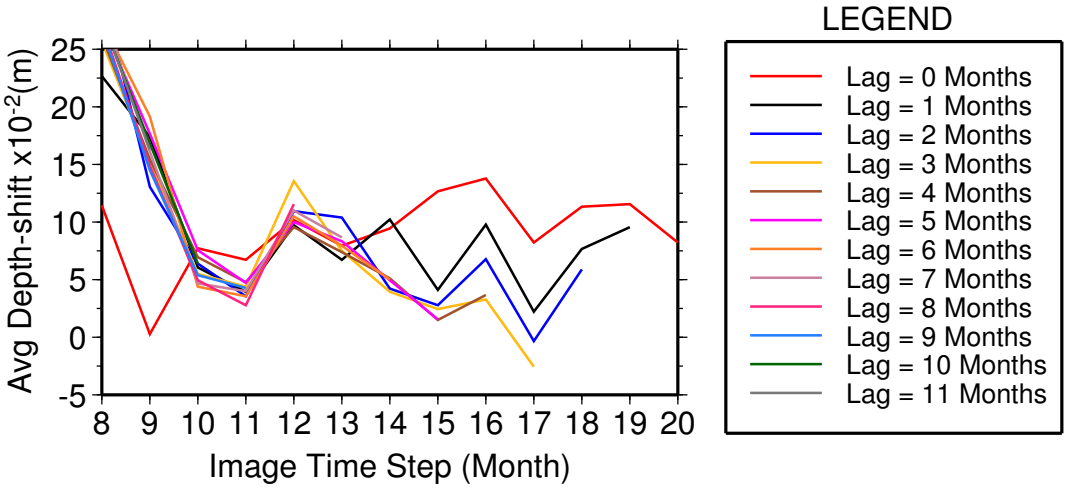

Figure 4.19: The average reflector depth-shift errors in the estimated-data images, color-coded by estimation slow-time lag.

completely faulted units. The baseline velocity model is perturbed to produce four time-lapse velocity models. The perturbation in these models consists of an increase in velocity, caused by water injection (see Wang and Nur, 1988; Mavko et al., 1998). The injected water is made to flow radially in the reservoir from a hypothetical well. The size of the radial patch indicating injected water increases from the first time-lapse velocity model to the fourth time-lapse velocity model. Slices through the baseline and time-lapse difference velocity models are shown in Figure 4.20 and Figure 4.21 respectively.

The goal of this synthesized time-lapse seismic monitoring project is to observe the flow pattern of the injected water as it comes in contact with the fault. It is expected that there will be no flow across the boundary, therefore any deviation will force a change in management decisions.

4.3.1 Survey Setup

The 3D synthetic survey is simulated using a 107 x 107 shot grid with 12 m inline and crossline shot spacing, and both 10 x 10 and 11 x 11 staggered receiver grids

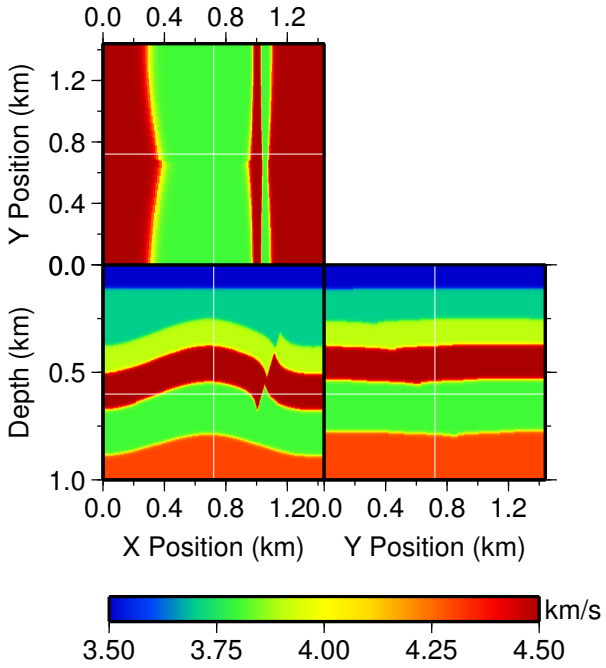

Figure 4.20: The baseline velocity model synthesized for the 3D example.

with 120 m inline and crossline spacing. I simulate a complete survey in the baseline case and partial (sparse) surveys in the time-lapse cases. The quasi-continuous partial surveys are acquired over a period of 20 months. The data size for the simulated complete survey is four times larger than for the simulated partial survey. Combining the data from all four synthetic time-lapse partial surveys produces a dataset with the same size as the complete survey for a conventional monitoring design. An illustration of the complete shot-receiver spatial distribution and the partial survey patterns are shown in Figure 4.22 and 4.23 respectively.

I assume that a seismic-receiver cable is used, therefore data sparsity in the partial surveys exists in the crossline direction but not in the inline direction. The quasi-continuous monitoring design is set up with four shot-grid patterns with 12 m spacing in the inline direction and 48 m spacing in the crossline directions; however, each pattern is shifted 12 m from the previous one in the crossline direction. The partial surveys represent time intervals of five months. Using the conventional strategy, the complete dataset composed of data from the four partial surveys will

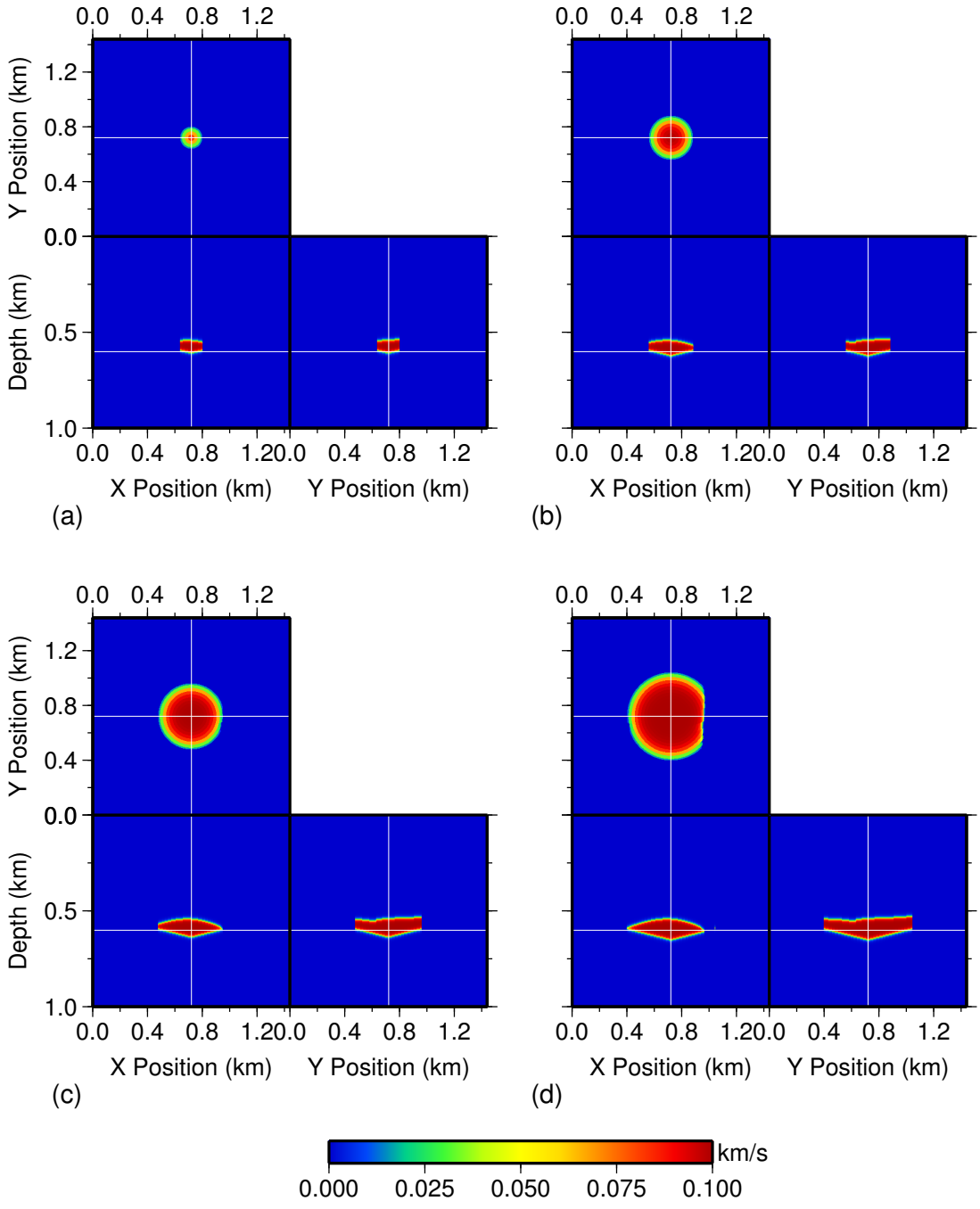

Figure 4.21: Time-lapse velocity changes in the synthetic velocity models. (a) After five months. (b) After 10 months. (c) After 15 months. (d) After 20 months.

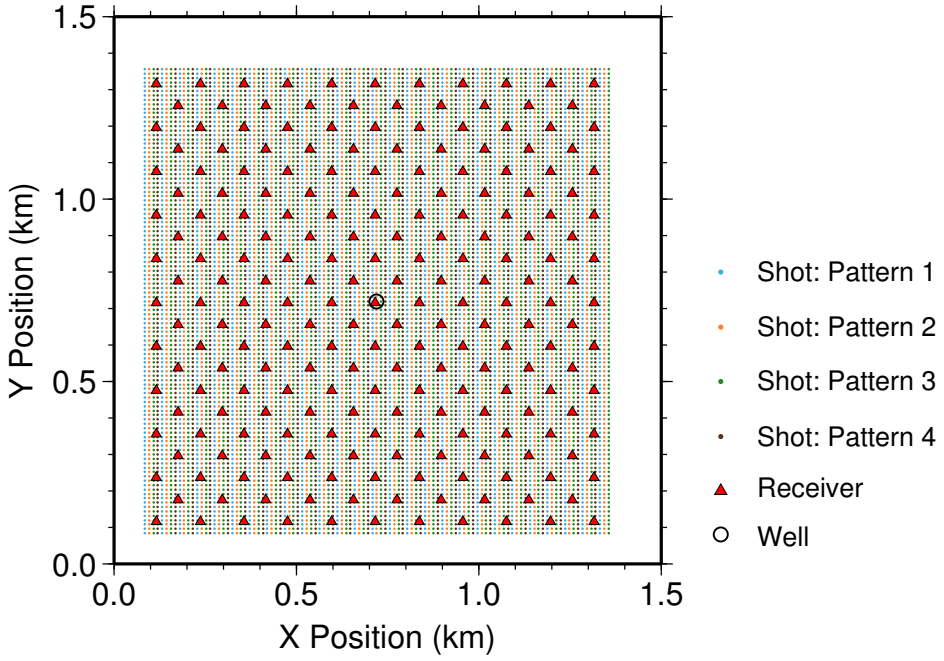

Figure 4.22: The source-receiver distribution for a complete survey. A complete survey is a combination of four different patterns alternated at each survey time.

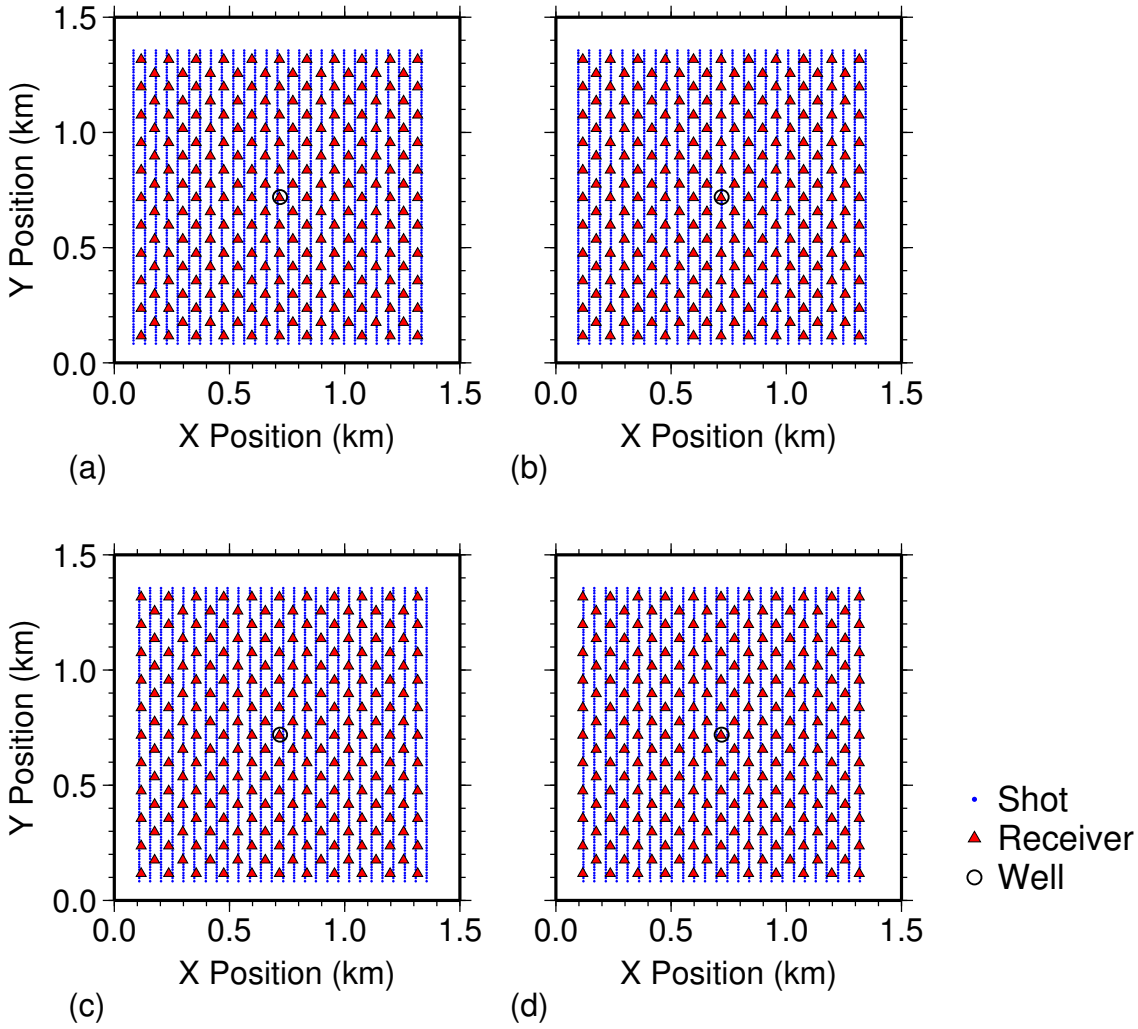

Figure 4.23: Individual survey patterns for the partial surveys.

be used to produce one image of the reservoir, whereas the quasi-continuous strategy described in this dissertation will be used to produce four time-lapse images of the reservoir, allowing operational and management decisions to be made sooner. In Figure 4.24, I show a sample receiver gather from the baseline survey.

4.3.2 Conventional Time-Lapse Monitoring

In Chapter 1 I showed how a conventional 3D seismic survey is acquired over a period of time rather than instantaneously. If we apply this knowledge to the synthesized time-lapse data described in the previous section, we produce a complete survey composed of partial surveys acquired as the reservoir changes occurred. Even though there are changes in the reservoir, there appear to be no discontinuities in the main reflectors in the combined data. A sample section through this combined dataset is shown in Figure 4.25.

I migrate the baseline and the combined time-lapse datasets using the baseline velocity model and move the reflectors in the monitor image to their correct positions with the cross-correlation method described in Chapter 2. Figure 4.26 shows the common mid-point (CMP) fold map of the input data to the migration algorithm. With a maximum fold of 36, a good-quality migrated image is produced. Sections through the migrated image and the time-lapse difference image are shown in Figure 4.27. A comparison of the time-lapse difference image and the last time-lapse velocity model (i.e. Figure 4.21d) shows that the shape and lateral extent of the injected water boundary is accurate; however its lower boundary is not well resolved. The high amplitude of the upper boundary occurs because of the constructive summing effect caused by the fixed position of the upper boundary. On the other hand, the lower boundary is not fixed, so there is no constructive summing effect.

If we choose to simulate current acquisition techniques, where surveys are acquired as quickly as possible, such that a complete survey can be acquired within six weeks, we obtain a more instantaneous image of the reservoir 20 months after injection began. Figure 4.28 shows the resulting instantaneous time-lapse difference

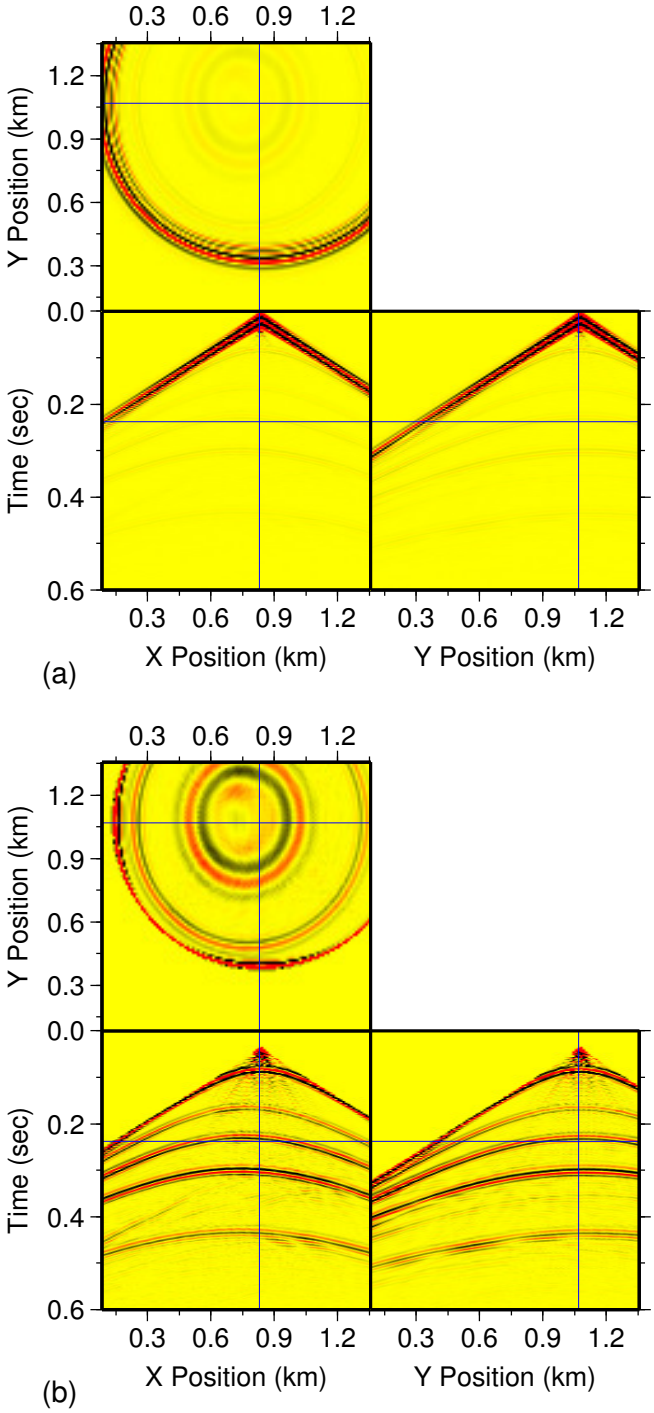

Figure 4.24: (a) Slices through a receiver gather from the baseline dataset. (b) The same dataset in (a) after muting the direct arrival.

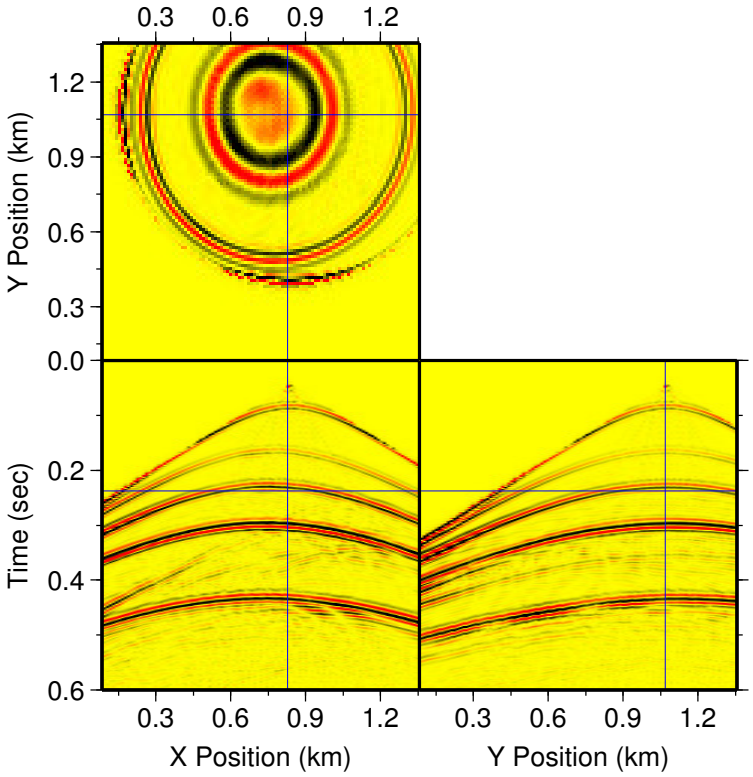

Figure 4.25: Slices through a receiver gather from the complete dataset obtained after combining all four partial datasets.

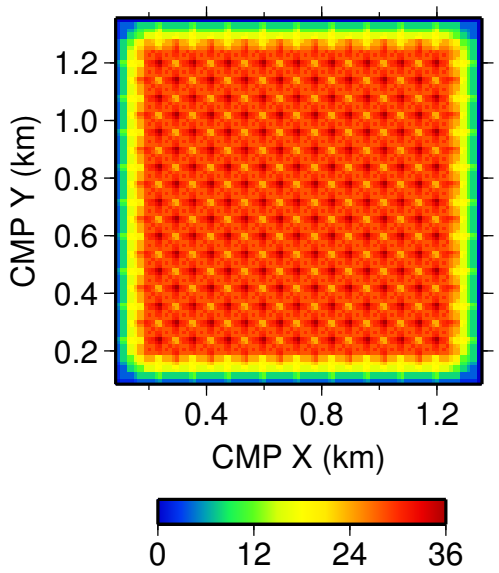

Figure 4.26: The fold map of the migrated datasets.

image. This strategy does not provide the best opportunity to detect what happens as the injected water reaches the fault. Figure 4.29 shows a 3D visualization of the top of the injected water flood.

4.3.3 Quasi-Continuous Time-Lapse Monitoring

If we use a quasi-continuous monitoring strategy in tracking the injected water, we are able to observe the reservoir changes at a better slow-time temporal resolution. At each survey time, I create 25% sparse datasets. In this example, the time interval between survey times of interest is five months. Sample sparse datasets are shown in Figure 4.30. I create accumulated, sparse, time-lapse seismic volumes at each survey time by concatenating receiver gathers along the slow-time dimension. The 1D Fourier transforms (along the fast-time axis) of these sparse seismic gathers are the inputs to the MWNI algorithm. To reduce the effect of event curvature on the estimation results, I use overlapping windows; the dimensions of the windows are 150 samples in the frequency dimension, 10 samples in the x-dimension, 10 samples in the y-dimension, and all available samples in the slow-time dimension.

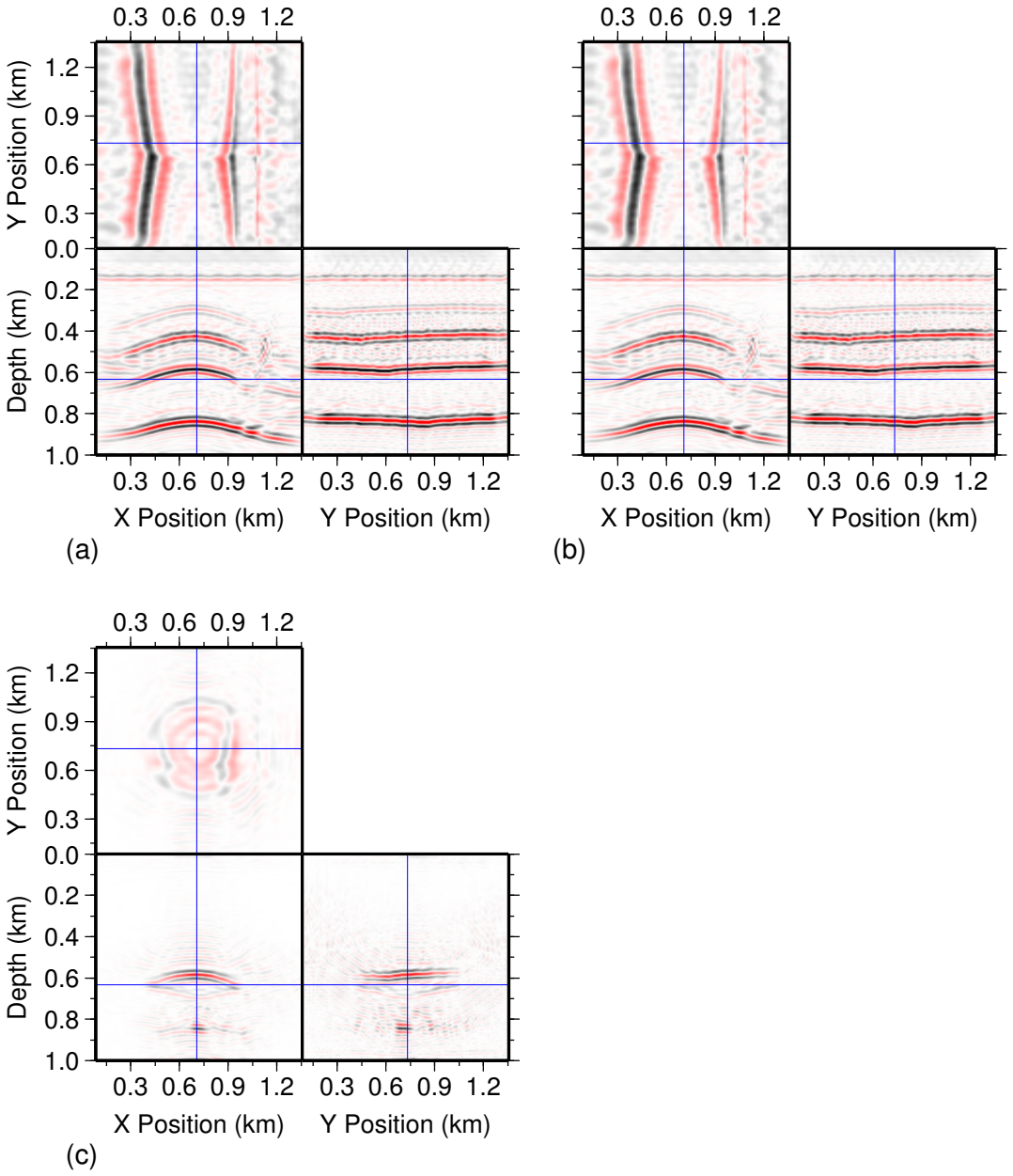

Figure 4.27: (a) Slices through the baseline image. (b) Slices through the image obtained by migrating the combined partial data. (c) Slices through the resulting time-lapse difference image.

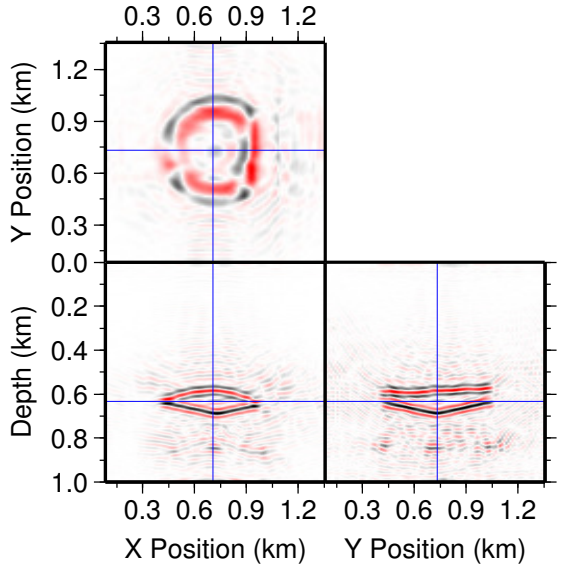

Figure 4.28: Time-lapse difference image obtained if we assume instantaneous data acquisition 20 months after water injection begins.

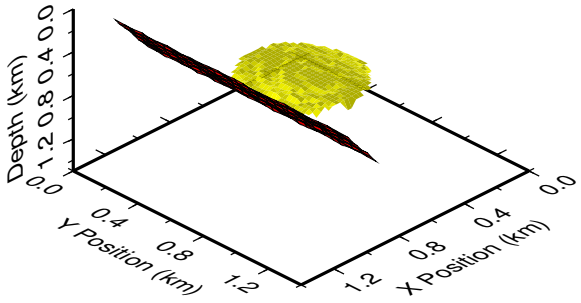

Figure 4.29: 3D visualization of the interpreted top of the injected water flood, based on the time-lapse difference images obtained from the instantaneous complete true data after 20 months.

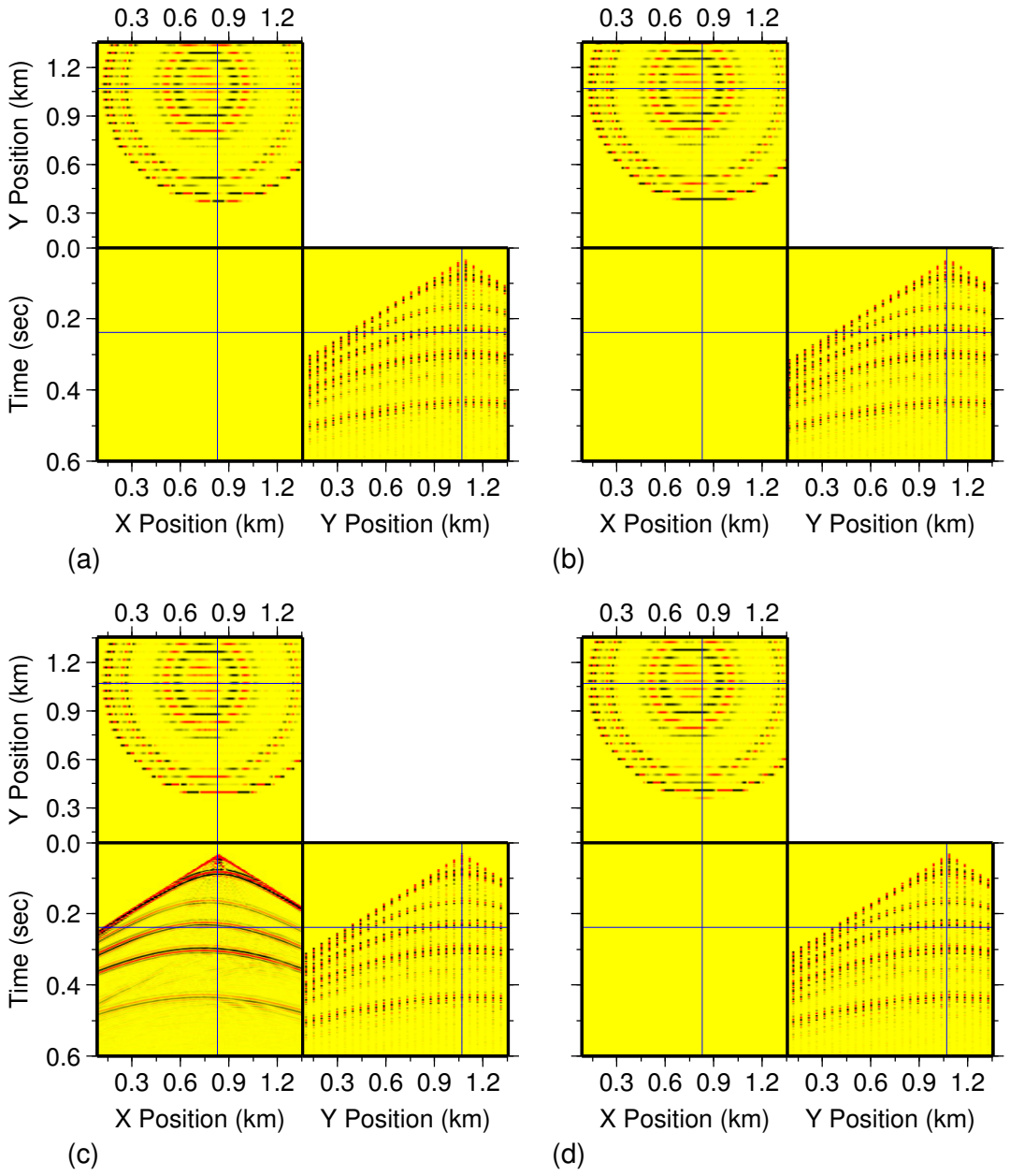

Figure 4.30: Slices through the partial datasets from (a) Pattern 1, (b) Pattern 2, (c) Pattern 3, and (d) Pattern 4.

Example estimated datasets for the first survey are shown in Figure 4.31. Difference estimated datasets, showing estimation inaccuracies, are shown in Figure 4.32. Comparing the results at each incremental survey time to the true dataset, we notice that the estimation errors reduce as the number of individual sparse datasets increase from one to two. This happens because of the added constraints introduced by the additional datasets. With three and four sparse datasets, we notice amplitude errors in the lower reflector. This occurs because the lower reflectors in the added datasets have significant amplitude differences from the lower reflectors in the dataset for the first survey. For this example, results show that an estimation window of one previous and one later time-lapse sparse dataset (or 10 months of accumulated datasets) produces the optimal estimation results.

Each estimated dataset is migrated using the same parameters as the conventional monitoring example, and the computed time-lapse difference images are shown in Figure 4.33. Compare these images with the time-lapse difference velocity models shown in Figure 4.21. It is obvious that the quasi-continuous monitoring strategy does a good job at tracking the incremental changes in the reservoir. Whereas the conventional strategy gives a result that sums up all the changes occurring in the reservoir throughout the data-acquisition period, the quasi-continuous strategy shows the incremental changes during the data acquisition process.

Figure 4.34 shows a 3D visualization of the interpreted top of the injected water flood based on the time-lapse difference images. The figure shows the water flood expanding during the 20-month monitoring period. It also shows the water flood making contact with the fault surface without leaking through the fault surface.

For comparison, the true time-lapse images are shown in Figure 4.35. Note that the primary difference between the images occurs in the shallow layers. This difference is a result of errors introduced by inaccurate estimation of the high-amplitude direct arrivals, as well as the near-offset data-estimation errors visible in Figure 4.32. The shapes and sizes of the boundaries of the reservoir changes are delineated correctly in the images from the estimated datasets.

Computed absolute amplitude ratios and depth-shift errors in the images obtained from the estimated data are shown in Tables 4.1 and 4.2. Only two of the 10

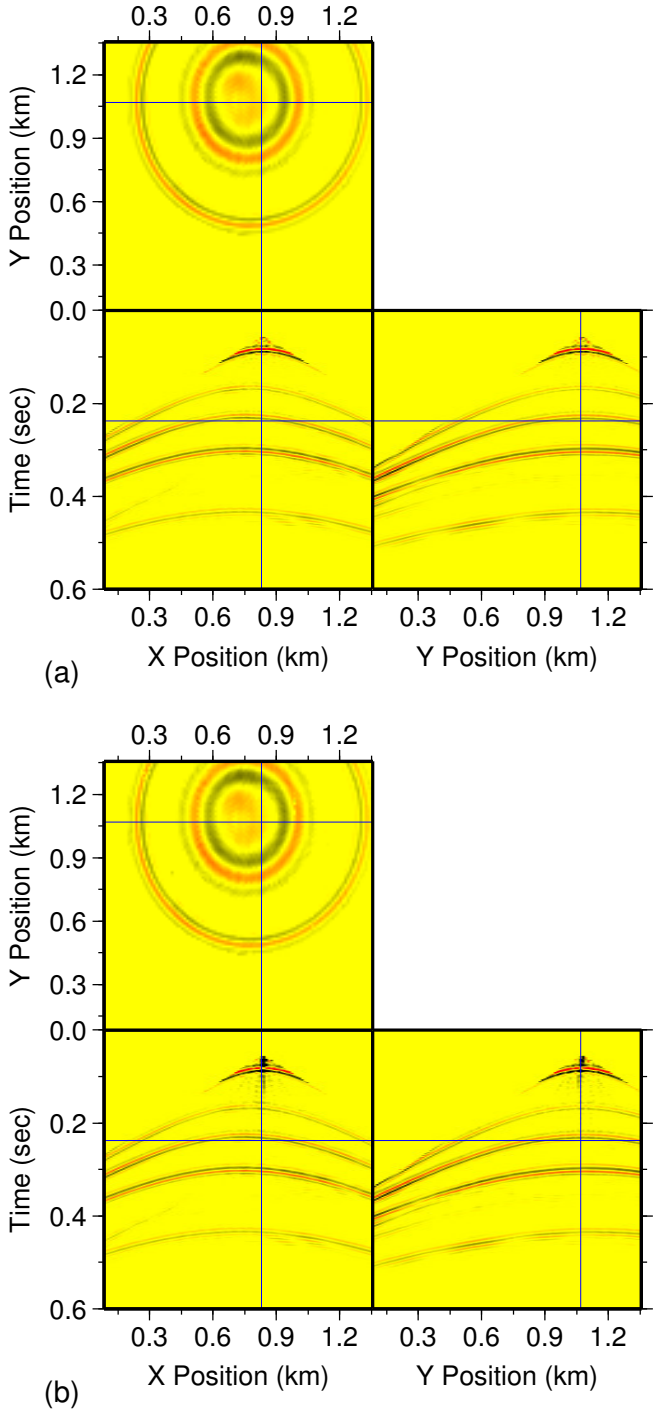

Figure 4.31: (a) Slices through a receiver gather with complete true data. (b) Slices through an estimated receiver gather from a 25% sparse receiver gather. (a) and (b) show receiver gathers from the same receiver position.

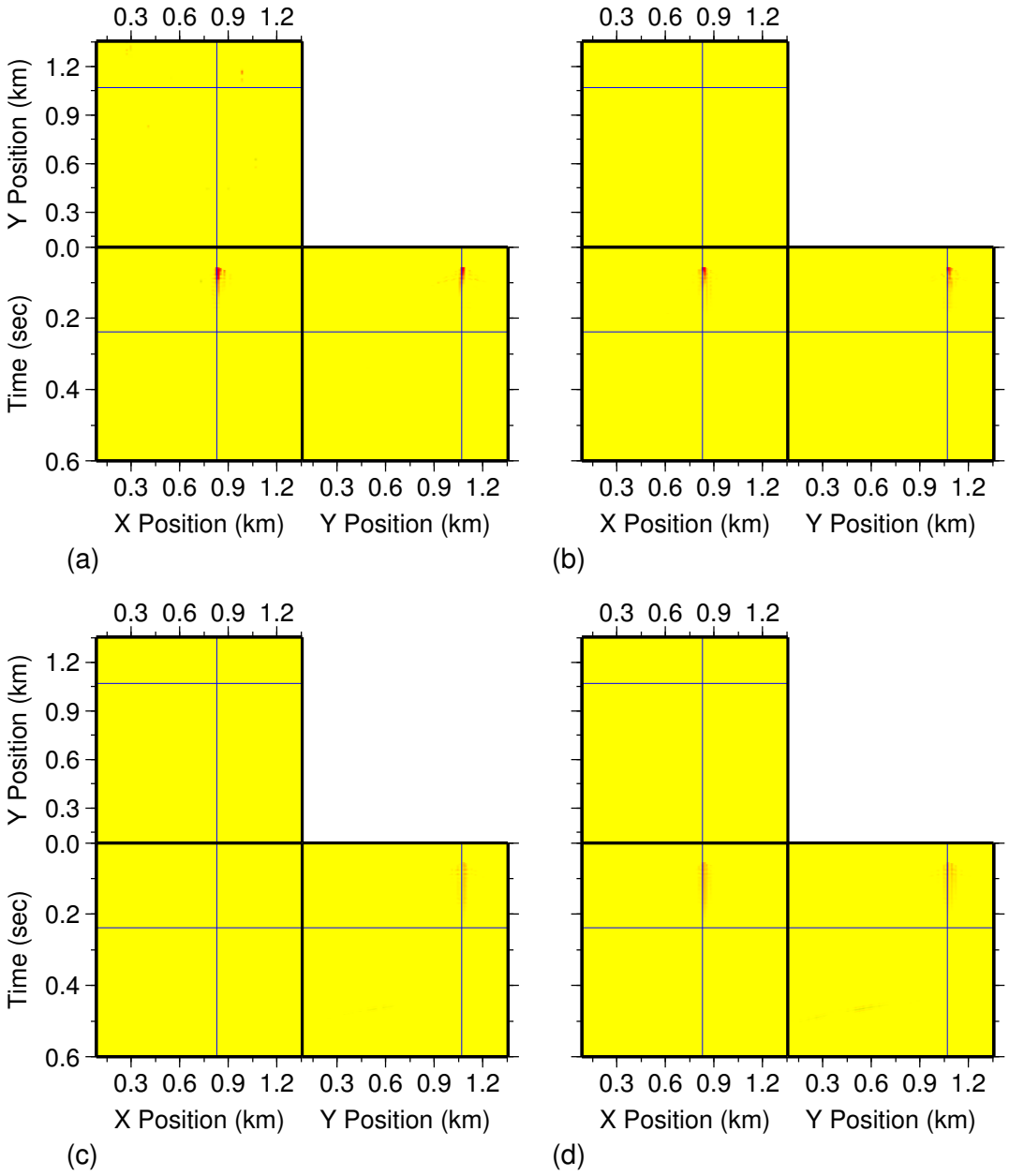

Figure 4.32: Section showing the estimation errors for the estimated dataset after 5 months at (a) estimation slow-time lag of zero months, (b) estimation slow-time lag of five months, (c) estimation slow-time lag of 10 months, and (d) estimation slow-time lag of 15 months.

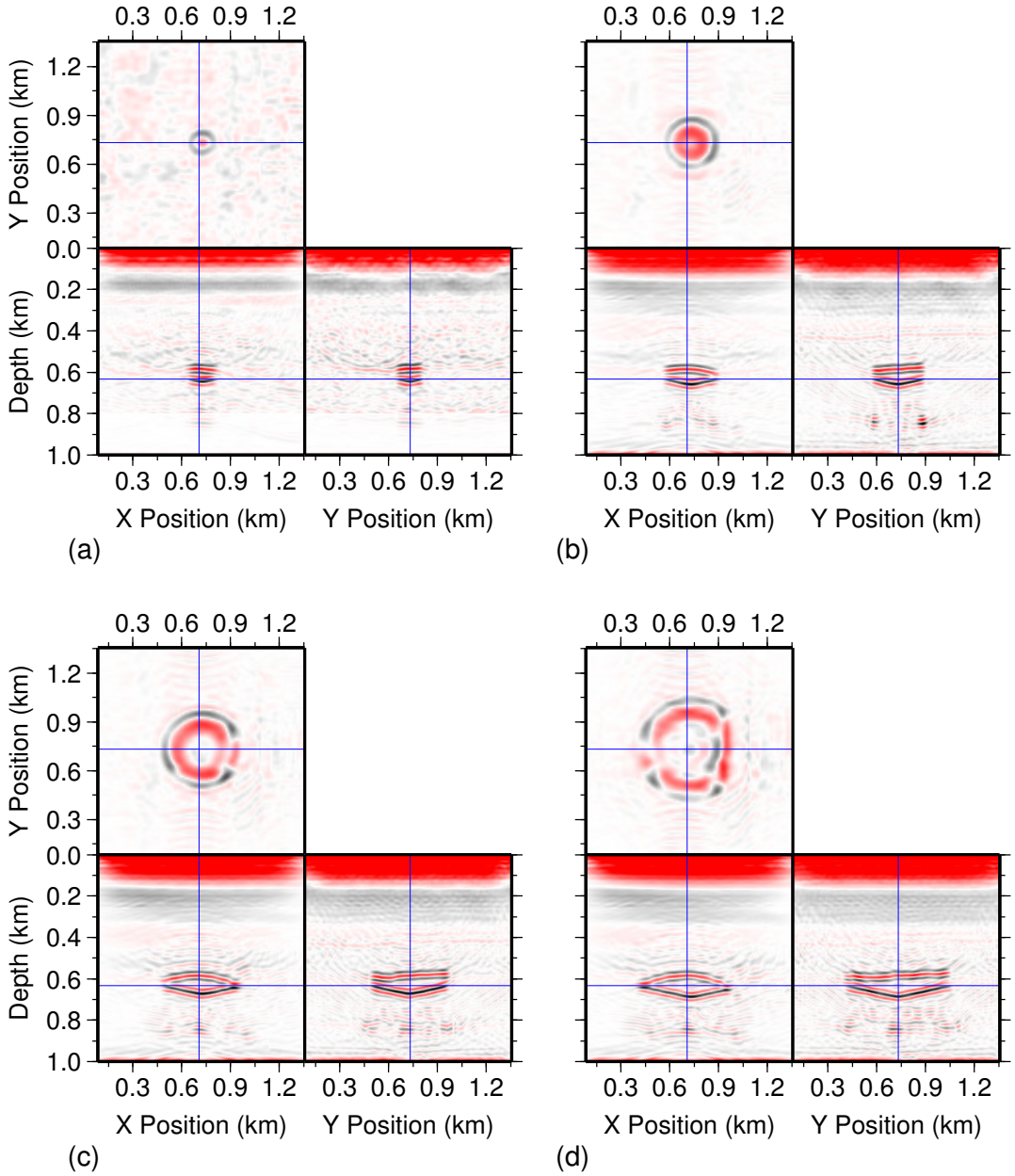

Figure 4.33: Time-lapse difference images computed for the images obtained using estimated data from 25% sparse datasets. (a) The time-lapse image after five months and estimation slow-time lag of zero months. (b) The time-lapse image after 10 months and estimation slow-time lag of zero months. (c) The time-lapse image after 15 months and estimation slow-time lag of zero months. (d) The time-lapse image after 20 months and estimation slow-time lag of zero months.

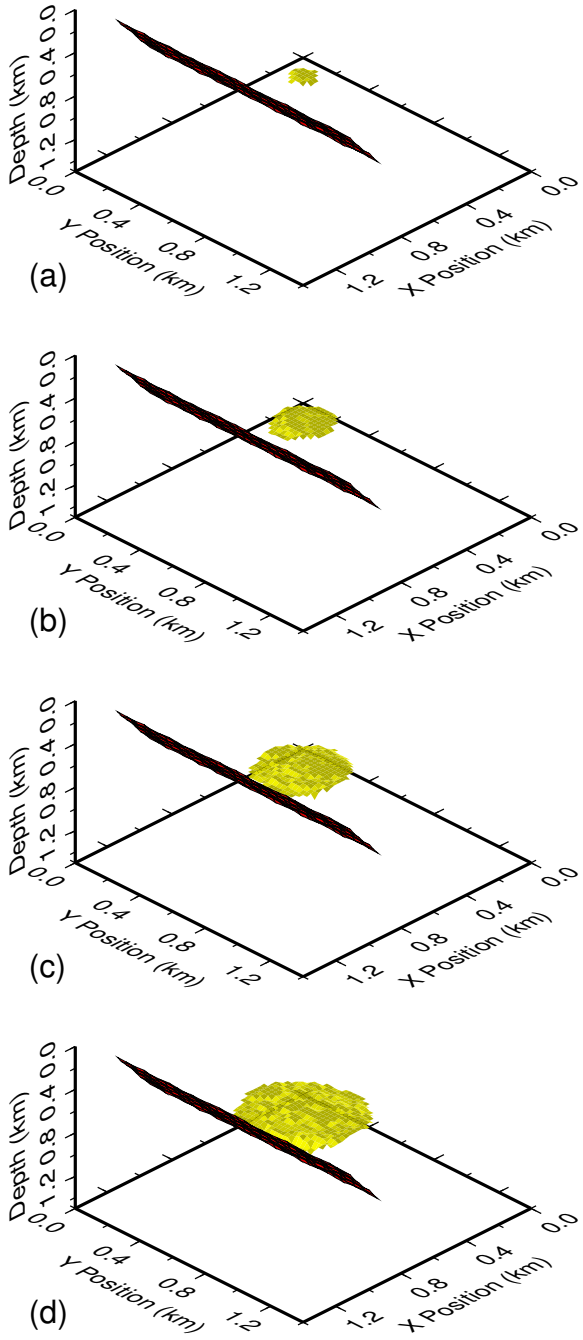

Figure 4.34: 3D visualization of the interpreted top of the injected water flood based on the time-lapse difference images obtained from the estimated datasets. (a) After five months. (b) After 10 months. (c) After 15 months. (d) After 20 months.

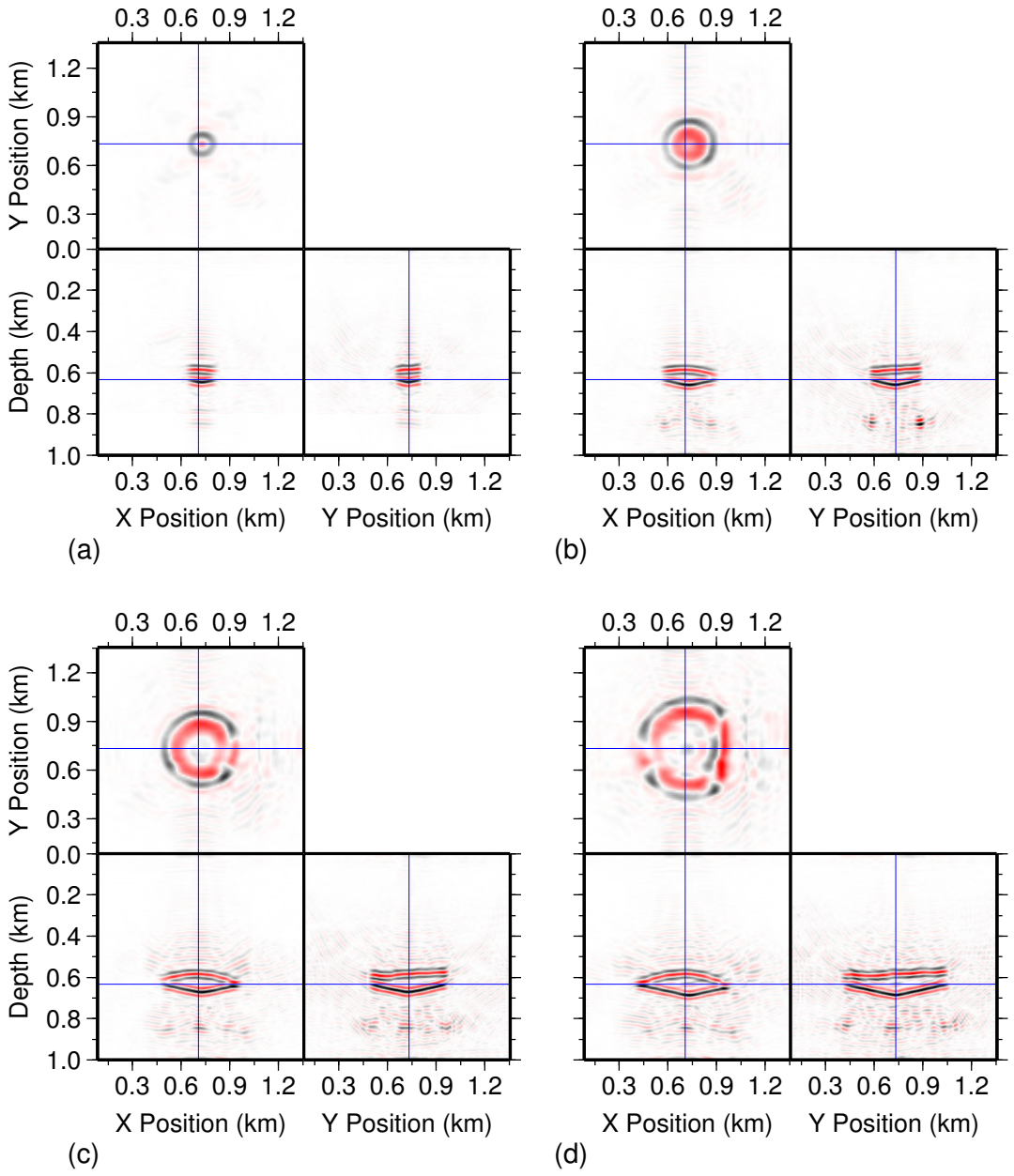

Figure 4.35: Time-lapse difference images computed for the images obtained using complete datasets. (a) After five months. (b) After 10 months. (c) After 15 months. (d) After 20 months.

ESL / IT	0 Months	5 Months	10 Months	15 Months
Month 5	0.951	0.920	0.910	0.919
Month 10	0.919	0.909	0.918	
Month 15	0.907	0.916		
Month 20	0.913			

ESL - Estimation Slow-time Lag

IT - Image Time

Table 4.1: Absolute amplitude ratios for the estimated-data images (see Section 1.4 on page 9).

images obtained from the estimated time-lapse datasets have absolute amplitude ratios less than 0.91. The error values in Table 4.2 show that depth-shift errors in the images obtained from the estimated time-lapse datasets are very small. Overall the estimated datasets compare well with the true datasets, even though I use only 25% of the true datasets.

4.4 Summary

In this chapter, I applied the quasi-continuous strategy introduced in Chapter 1 to two surface-seismic synthetic examples. In the first example, I simulated a CO_2 geologic reservoir where the injected CO_2 had leaked. I showed how my proposed method can be used in the early detection of such a leak. In the second example, I simulated a faulted hydrocarbon reservoir undergoing secondary recovery. I showed how my proposed approach can be used to monitor the injected water to ensure that the predicted flow patterns actually occur. Also, I show that the estimation errors computed using the method described in Section 2.2 are very small.

x10^{-1}m

ESL / IT	0 Months	5 Months	10 Months	15 Months
Month 5	0.788	1.530	1.601	1.533
Month 10	1.604	1.790	1.696	
Month 15	1.908	1.970		
Month 20	2.140			

ESL - Estimation Slow-time Lag

IT - Image Time

Table 4.2: depth-shift errors in the estimated-data images.

Chapter 5

Quasi-continuous Monitoring with surface-seismic Data: Field-Data Example

5.1 Introduction

In this chapter, I apply the methodology presented in previous chapters to the BP partnership's Valhall Life of Field Seismic (LoFS) project 4D dataset. I start by introducing the dataset, describing the acquisition process and parameters, and explaining the reason for implementing the Valhall LoFS project. I follow by showing the results obtained for a data-estimation-based quasi-continuous monitoring project at Valhall with the same survey time intervals as the Valhall LoFS project. In this case I subsample data from three consecutive time-lapse surveys to mimic one full survey acquired over the time interval for all three surveys. I then show results obtained after applying the methodology in a strict sense to one of the surveys. For this example, the quasi-continuous monitoring data are extracted from the Valhall LoFS dataset by splitting one full 3D survey into three time-lapse surveys to monitor changes in the reservoir over the data acquisition period of that survey.

5.2 The Valhall Time-Lapse Monitoring Project

The Valhall Field, operated by BP Norge AS, is located off the coast of Norway in the North Sea. Water depth at the Valhall Field averages 70 m (van Gestel et al., 2008). The reservoir at the Valhall Field is a highly porous, low-permeability, Cretaceous chalk layer at a depth of about 2400 m, with a thickness of 0 m to 70 m. The chalk layer has porosity values of 35-50% and matrix-permeability values of 1-10 mD under initial reservoir conditions (Barkved and Kristiansen, 2005). Overall, the reservoir is complex, with gas-charged sediments in the overburden (Munns, 1985). Gas within the overburden has formed a gas cloud above the crest of the field, creating an imaging challenge. Because of the the high porosity of the reservoir, there is significant compaction during pressure depletion (van Gestel et al., 2008). This compaction causes subsidence in the overburden. As a result, reservoir depletion creates significant 4D responses in time-lapse seismic data. The current rate of subsidence is 0.25 m/yr and overall subsidence has exceeded 5.4 m since production started (Barkved and Kristiansen, 2005).

Production at the Valhall Field began in 1982. In 2003, the Life of Field Seismic project (LoFS) was implemented to monitor production and water injection using permanently installed ocean-bottom cables (OBCs) (van Gestel et al., 2008). The Valhall LoFS project was designed to monitor water injection because of the horizontal orientation of the injectors and producers. Monitoring the interaction between the horizontal wells was a top priority. Another reason for implementing the Valhall LoFS project is the dynamic nature of the overburden units. Areas with large lateral changes in pore pressure and stress had to be avoided during well planning.

A total of about 120 km of cable was installed with approximately 2500 receiver stations. The receivers are separated by a nominal distance of 50 m in the inline direction and 300 m in the crossline direction. About 50,000 shots were deployed in each survey, with a nominal spacing of 50 m in both the inline and crossline directions. A 1976 interpretation of the chalk reservoir-top structure (Munns, 1985) is shown in Figure 5.1.

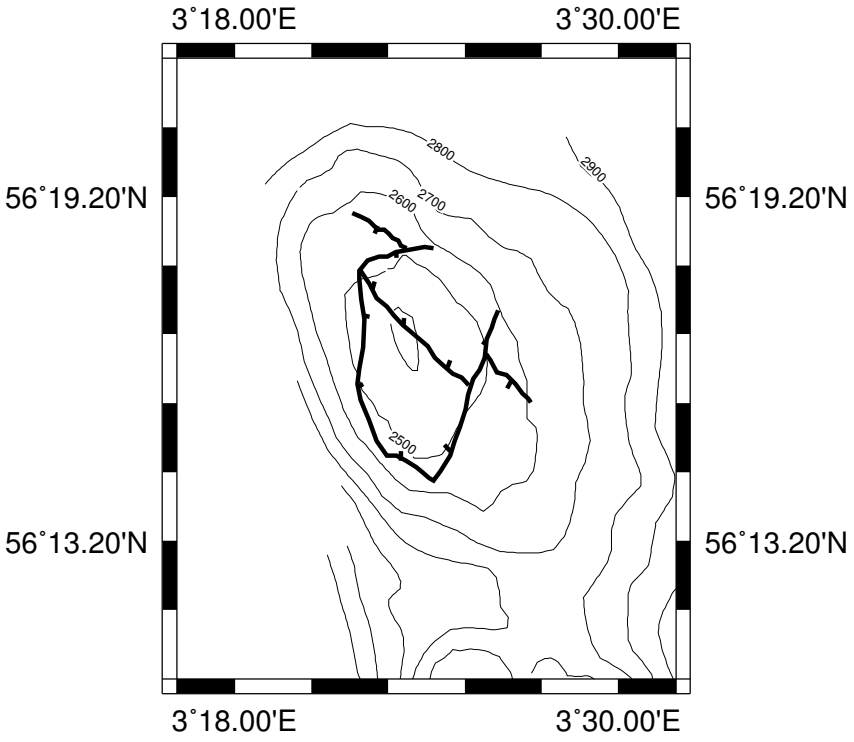

Figure 5.1: A 1976 interpretation of the chalk reservoir-top structure at Valhall (Munns, 1985).

To date, 11 surveys have been acquired (see Table 1.1 on page 14 for survey dates). The baseline survey was acquired in September 2003, and the 11th survey was acquired in October 2008. Dedicated water injection started in early 2006, before the 7th survey. Van Gestel et al. (2008) noted that data from production logging tools were in agreement with time-lapse changes observed in seismic data. The time interval between consecutive surveys varies from one to seven months. For a conventional time-lapse project, this temporal resolution is high. The duration of individual field surveys vary from three weeks at the shortest to two months at the longest. This large variation in the data-acquisition duration is in large part due to varying weather conditions. Sometimes, the weather is conducive to field operations, and sometimes it is not. Finally, I use the baseline velocity described in Sirgue et al. (2010) to migrate the Valhall Field data. Sections through this velocity model are shown in Figure 5.2.

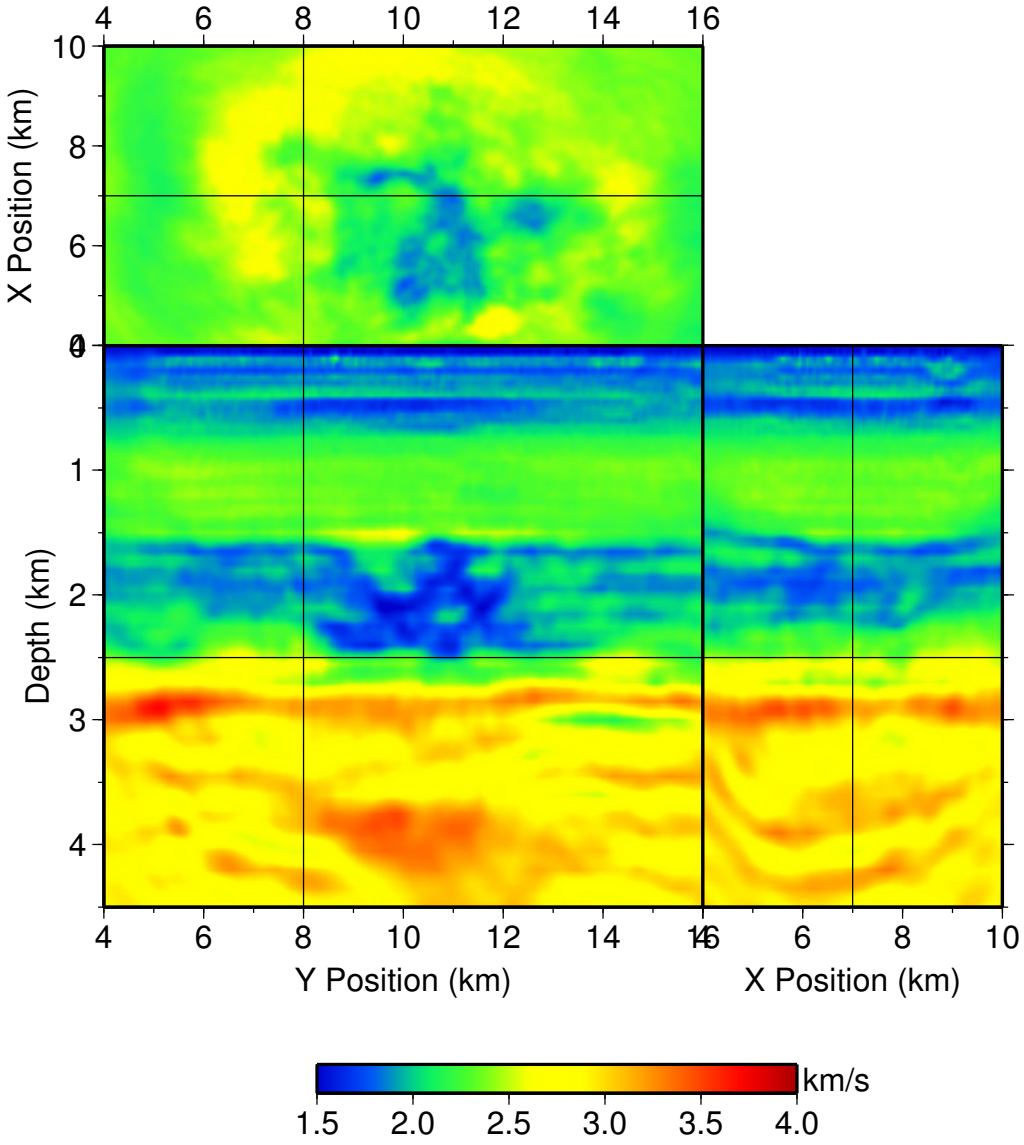

Figure 5.2: The Valhall LoFS project baseline velocity model (Sirgue et al., 2010).

5.3 Survey Setup

To demonstrate the efficiency of the method presented in this dissertation on field seismic data, I used data from subsets of the full Valhall LoFS surveys. These subsets consist of data from about 470 receivers, covering the lower portion of the survey map (geographically the south-eastern end). Each receiver gather consist of traces from shots within a 5 km radius from the receiver position. The portion of the field covered by the data subsets is unaffected by the gas clouds in the overburden sedimentary layers. The primary reason for selecting this subset is that the complexity involved in imaging sedimentary layers below a gas cloud is beyond the scope of this dissertation.

In the inline direction, both shots and receivers are separated by a nominal distance of 50 m; in the crossline direction, shots are separated by 50 m, but receivers are separated by a nominal distance of 300 m. The original survey map and the survey subset maps are shown in Figures 5.3 and 5.4. In the first quasi-continuous monitoring simulation, I use every third shot-line in the inline direction from surveys 9, 10, and 11. I change the first shot-line preserved in each survey. A sum of all the data subsets gives one complete dataset. Data sparsity occurs in the crossline direction but not in the inline direction. Sparsity in the inline direction would imply the some shot points are skipped during a survey, despite the fact that the source boat arrives at their locations. Skipping shot points in the inline direction while acquiring offshore seismic data is an inefficient acquisition strategy. In the second quasi-continuous monitoring simulation, the distribution of the receivers is left unchanged, but the distribution of the shots is varied depending on the shot time. I separate the shots into three groups representing 15-day shot intervals (see Figure 1.4 on page 13).

5.4 Conventional Time-Lapse Monitoring

The Valhall time-lapse LoFS project has unusually short time intervals between surveys, even though the monitoring strategy is conventional. On average, the interval

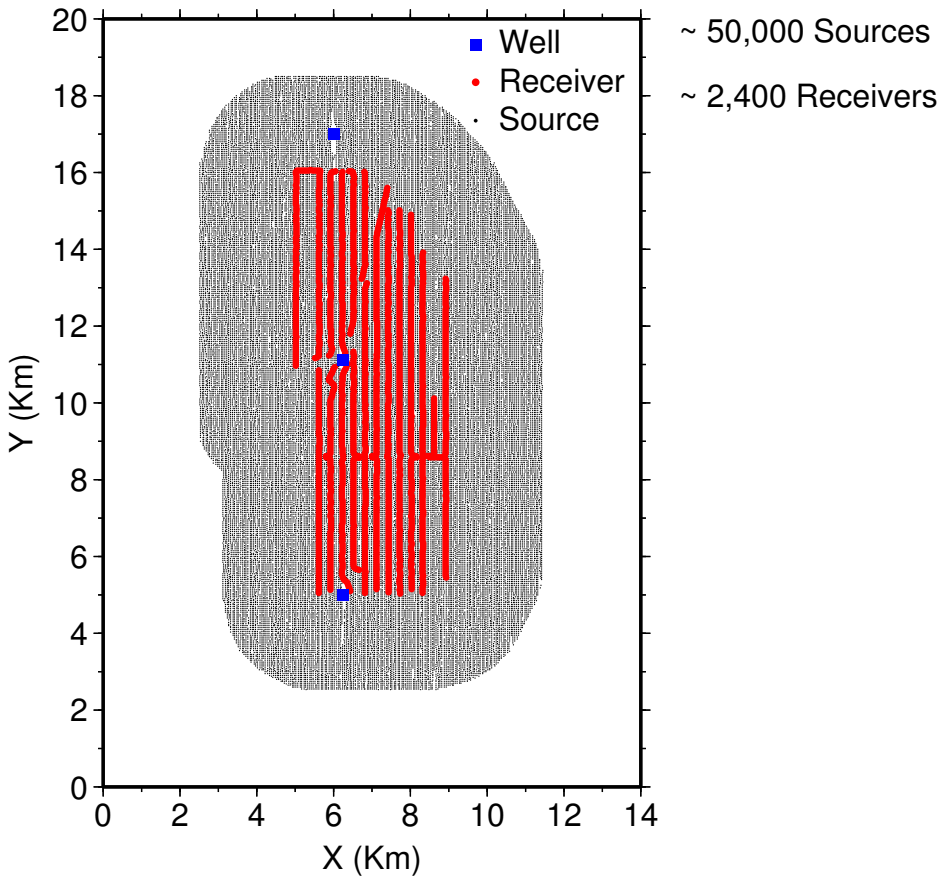

Figure 5.3: The original complete survey map of the Valhall LoFS project.

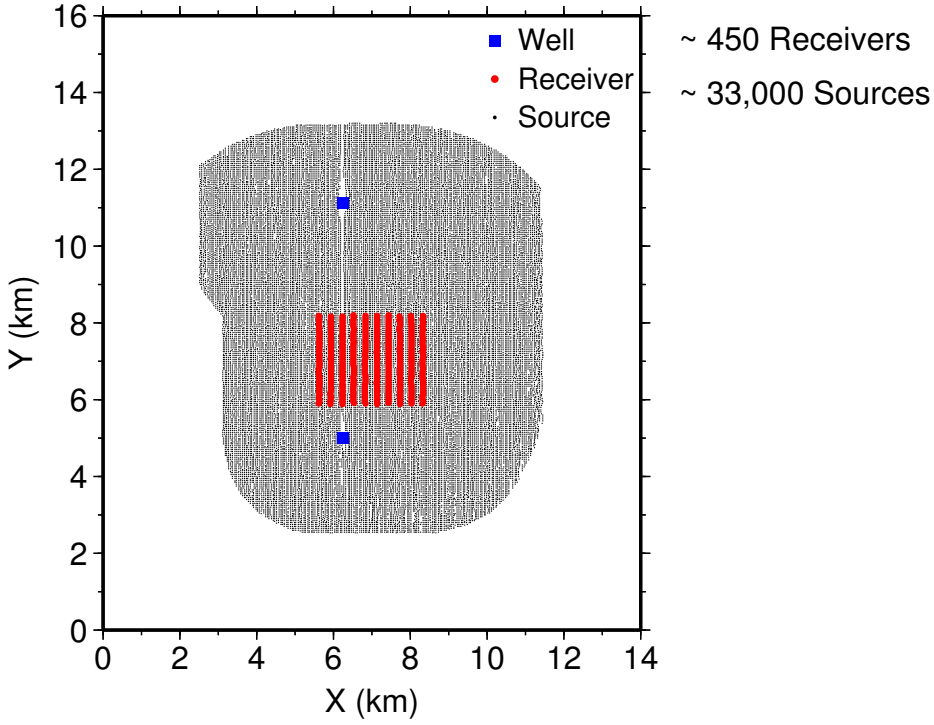

Figure 5.4: The survey map for the Valhall LoFS project data subsets used in this dissertation.

is six months. This is short by today's standards; however there are changes within the reservoir with a time scale far shorter than six months. These changes cannot be delineated using the conventional strategy. Sample datasets from surveys 1, 4, 9, 10, and 11 are shown in Figures 5.5, 5.6, 5.7, 5.8, and 5.9. As I did with the synthetic examples, I migrated the data with source-receiver wave equation migration. 2D slices through the baseline and monitor images are shown in Figures 5.10, 5.11, 5.12, and 5.13, and the time-lapse difference images are shown in Figures 5.14, 5.15, and 5.16. The reservoir top is easily identified in the images by a high-amplitude reflector around 2700 m depth in Figures 5.10 through 5.13. We see on the time-lapse difference images the amplitude changes in the reservoir reflector caused by the injected water from the time of the 9th survey to the time of the 11th survey in Figures 5.14 through 5.16.

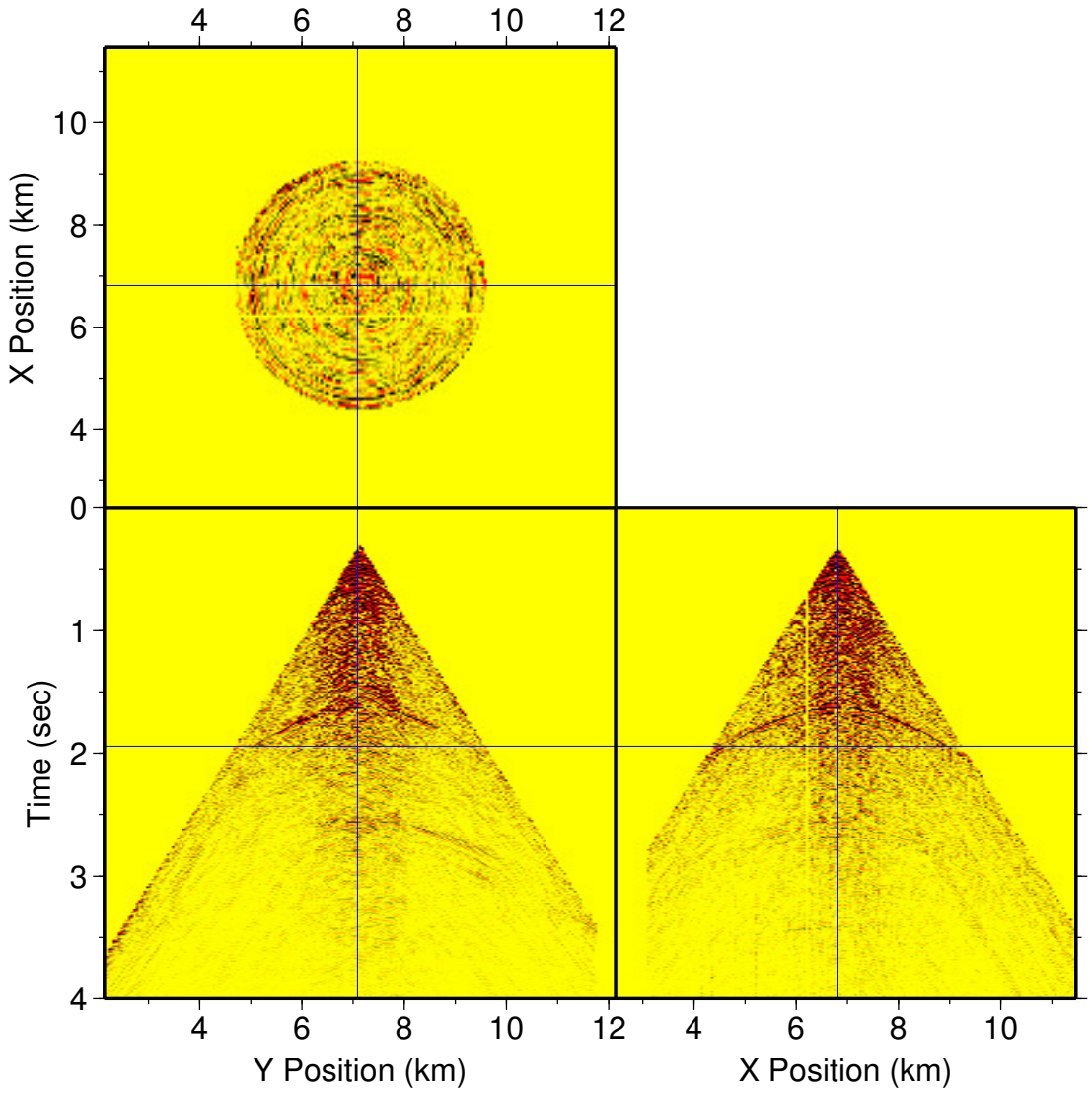

Figure 5.5: Sample receiver gather from the baseline survey. Direct arrivals have been muted.

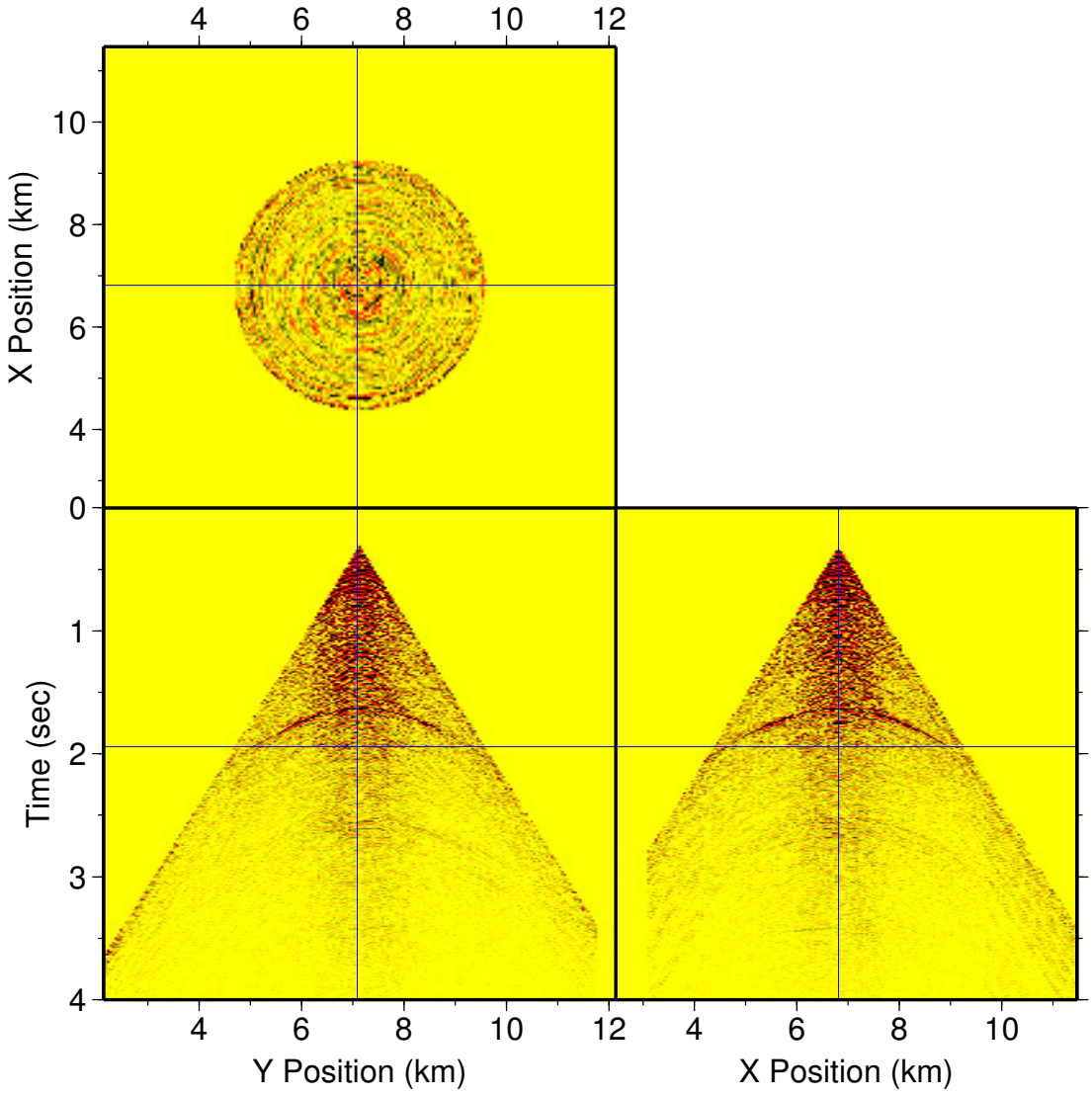

Figure 5.6: Sample receiver gather from survey 4. Direct arrivals have been muted.

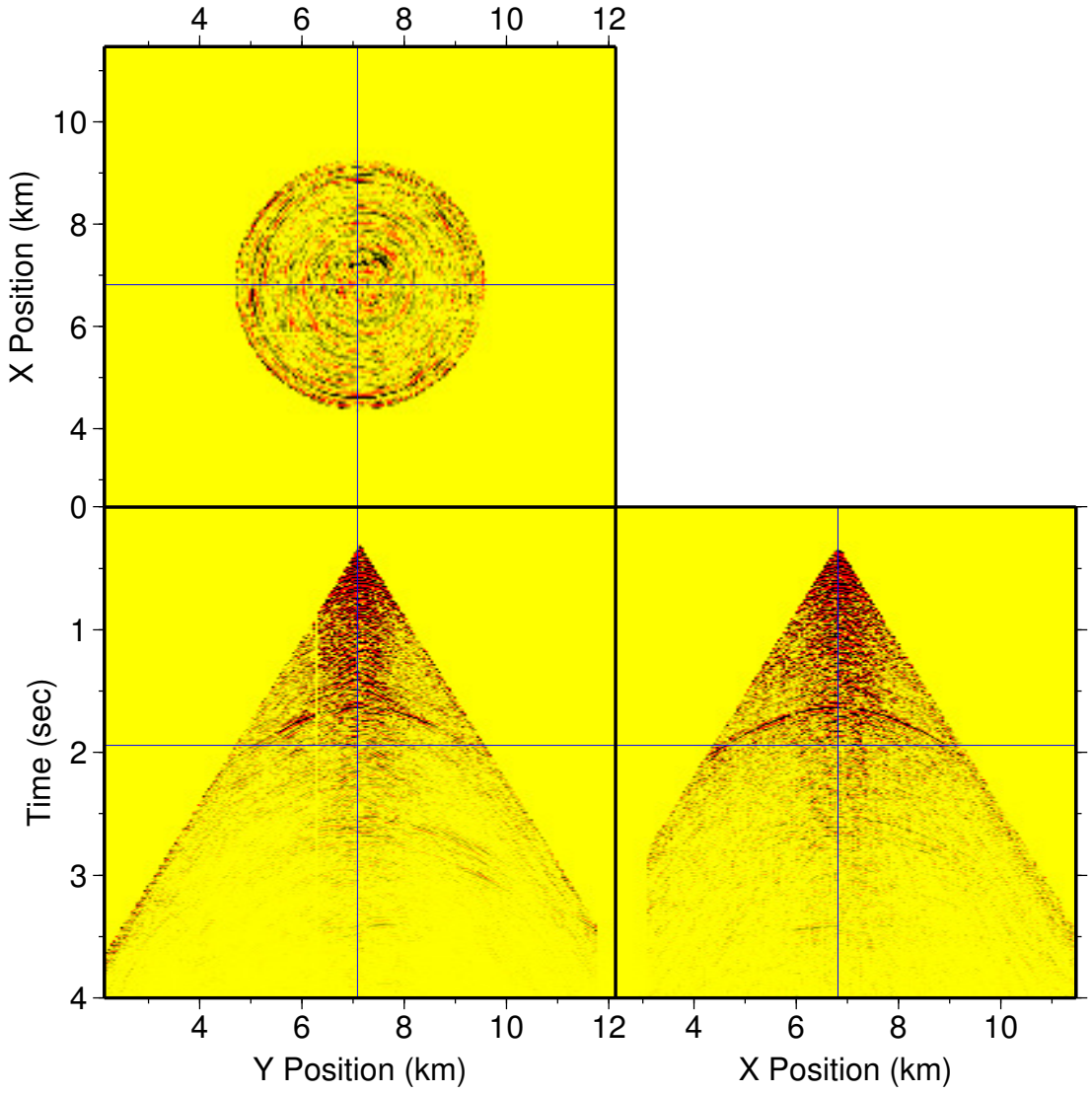

Figure 5.7: Sample receiver gather from survey 9. Direct arrivals have been muted.

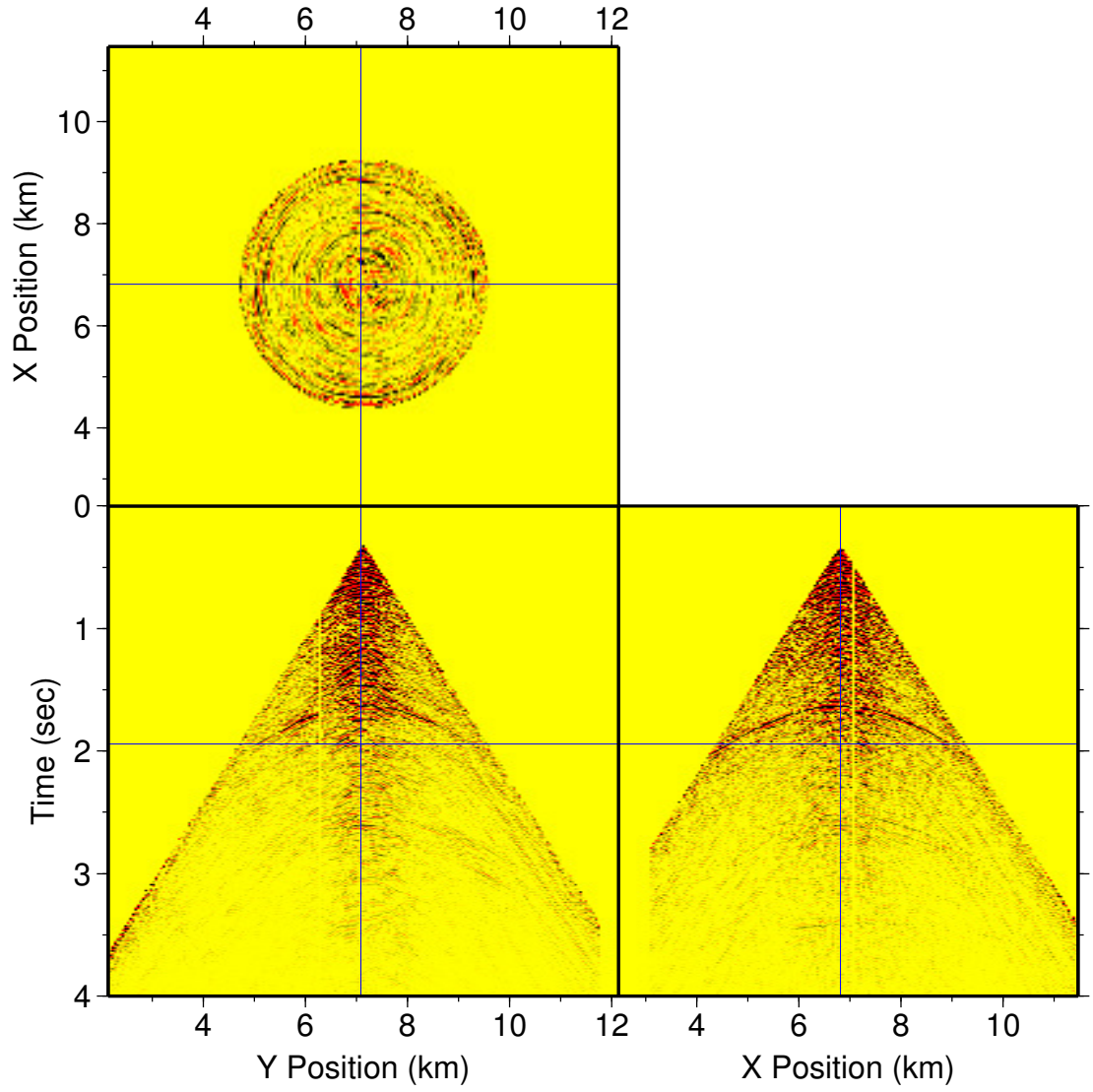

Figure 5.8: Sample receiver gather from survey 10. Direct arrivals have been muted.

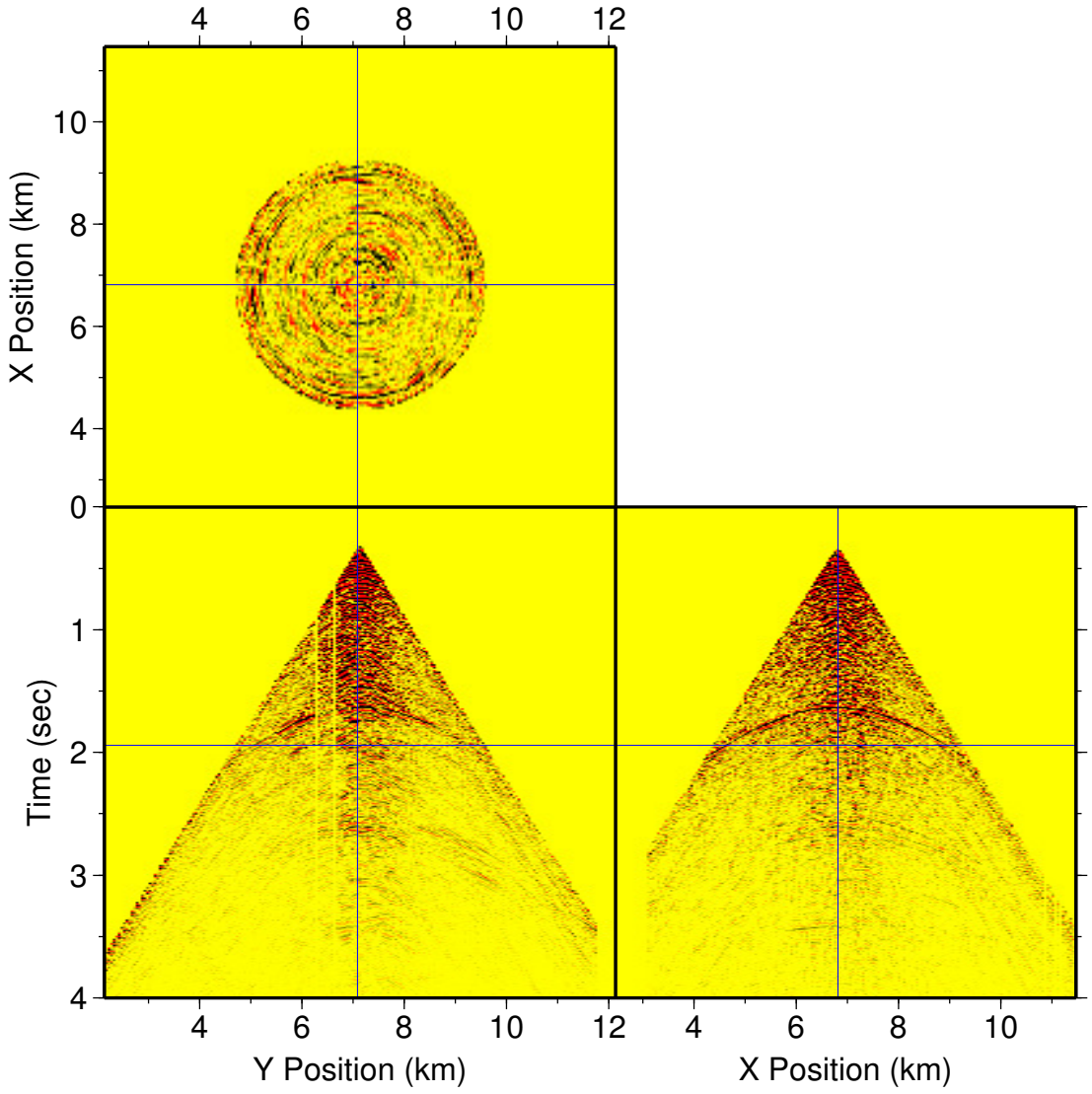

Figure 5.9: Sample receiver gather from survey 11. Direct arrivals have been muted.

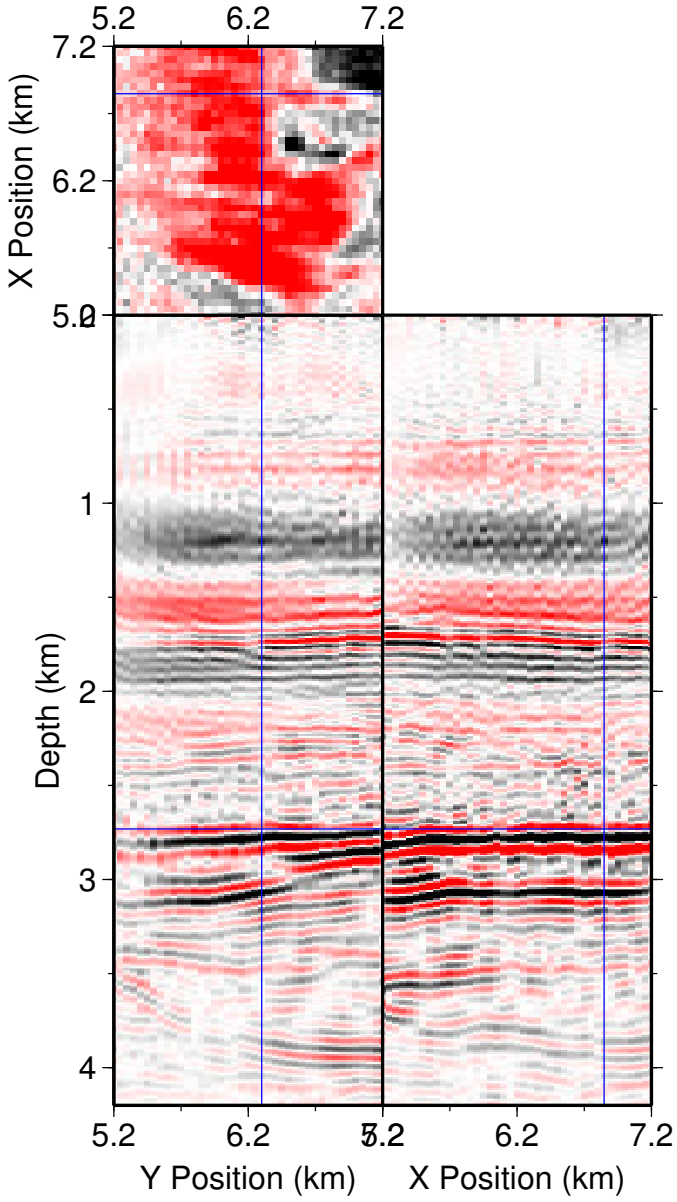

Figure 5.10: Valhall LoFS project migrated baseline image obtained using the subset dataset.

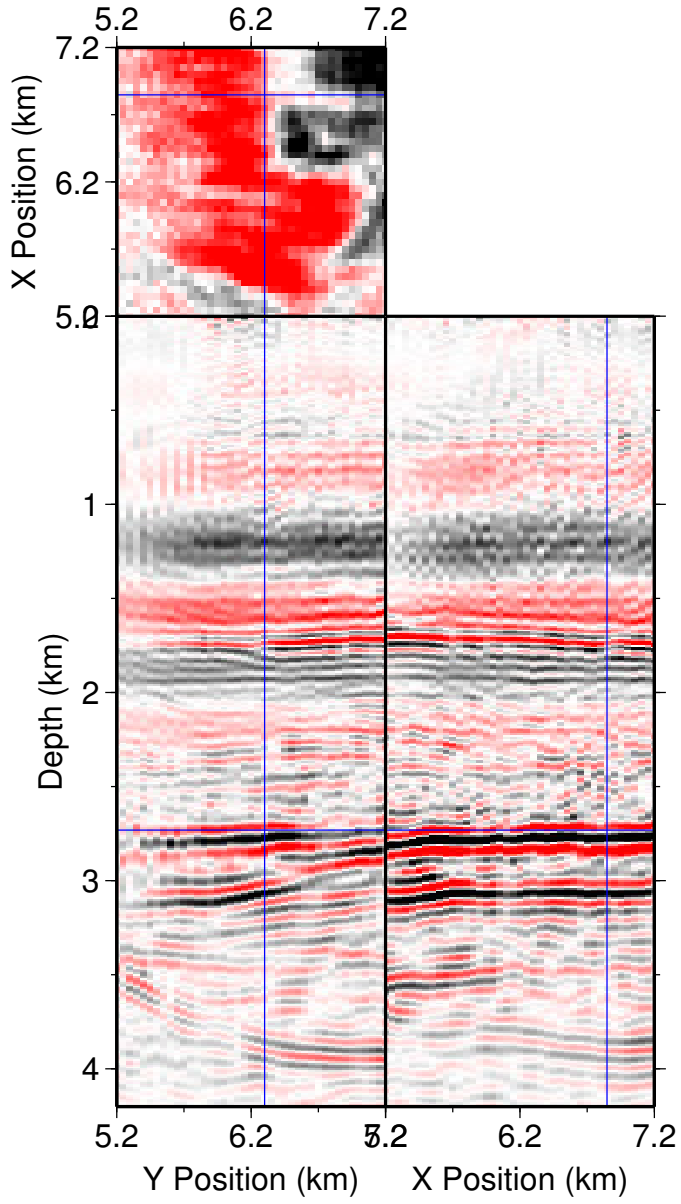

Figure 5.11: Valhall LoFS project migrated image for survey 9.

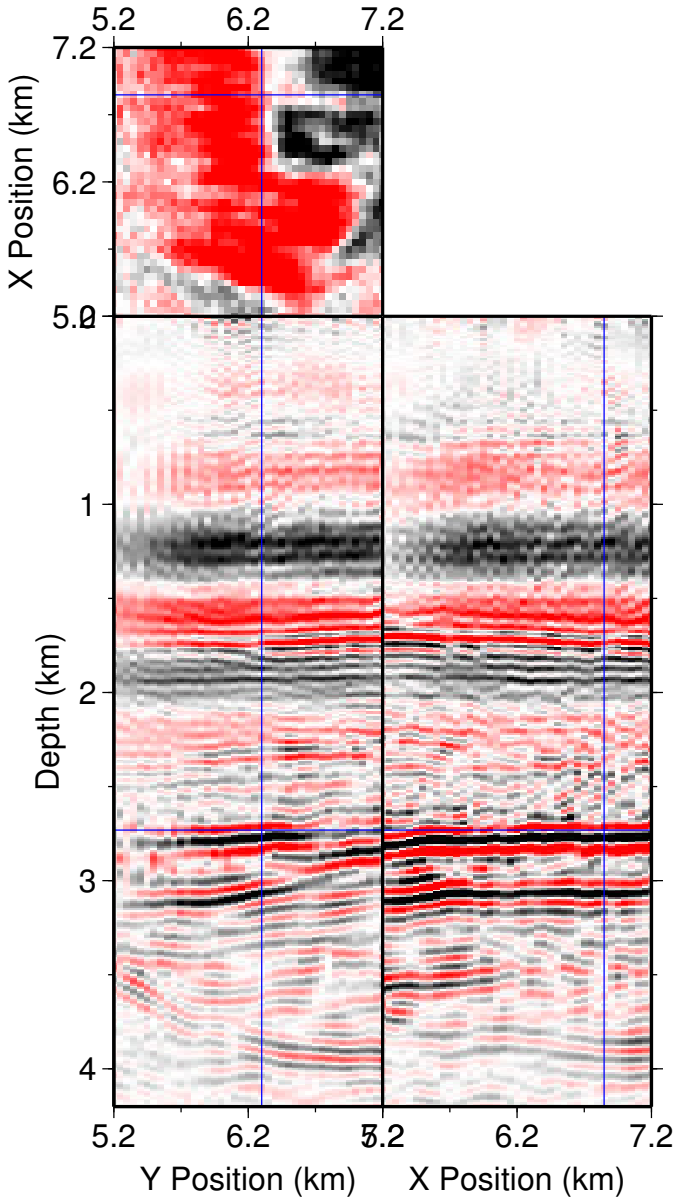

Figure 5.12: Valhall LoFS project migrated image for survey 10.

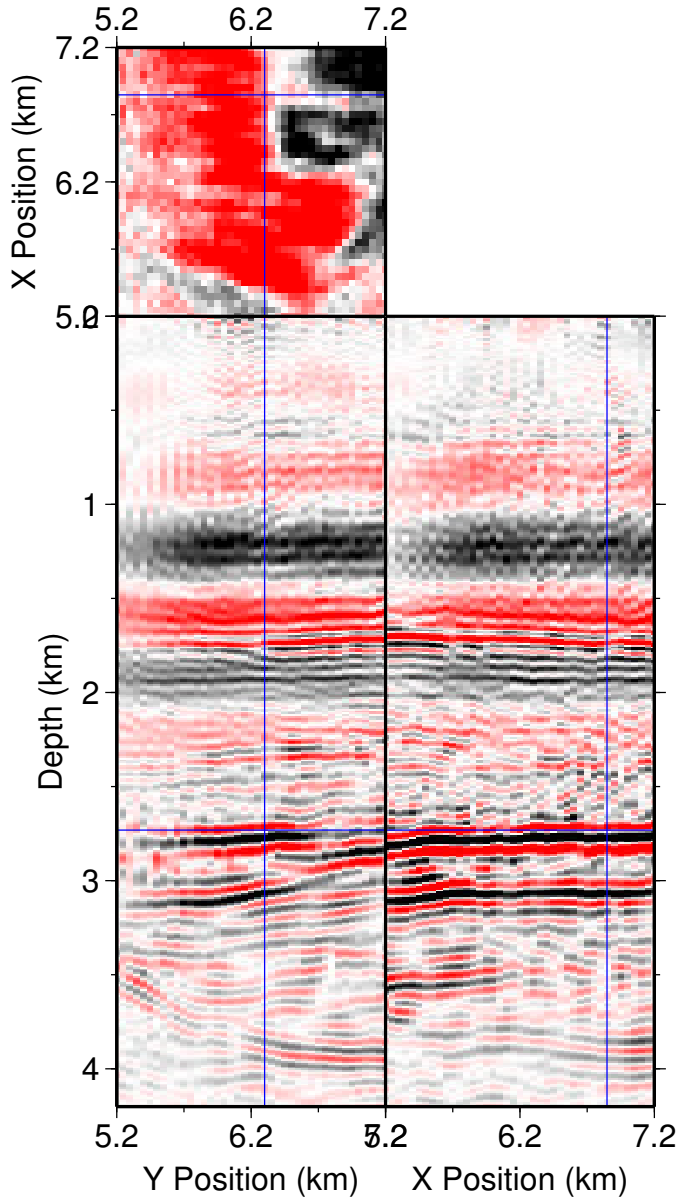

Figure 5.13: Valhall LoFS project migrated image for survey 11.

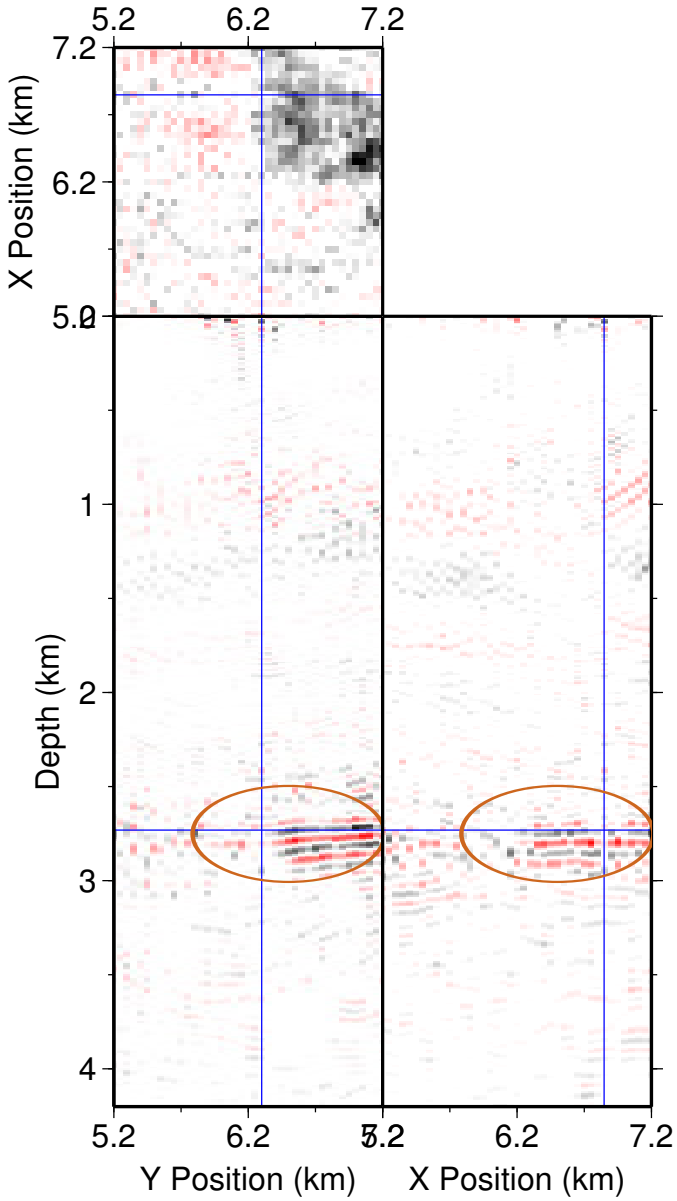

Figure 5.14: Valhall LoFS project time-lapse difference image for survey 9.

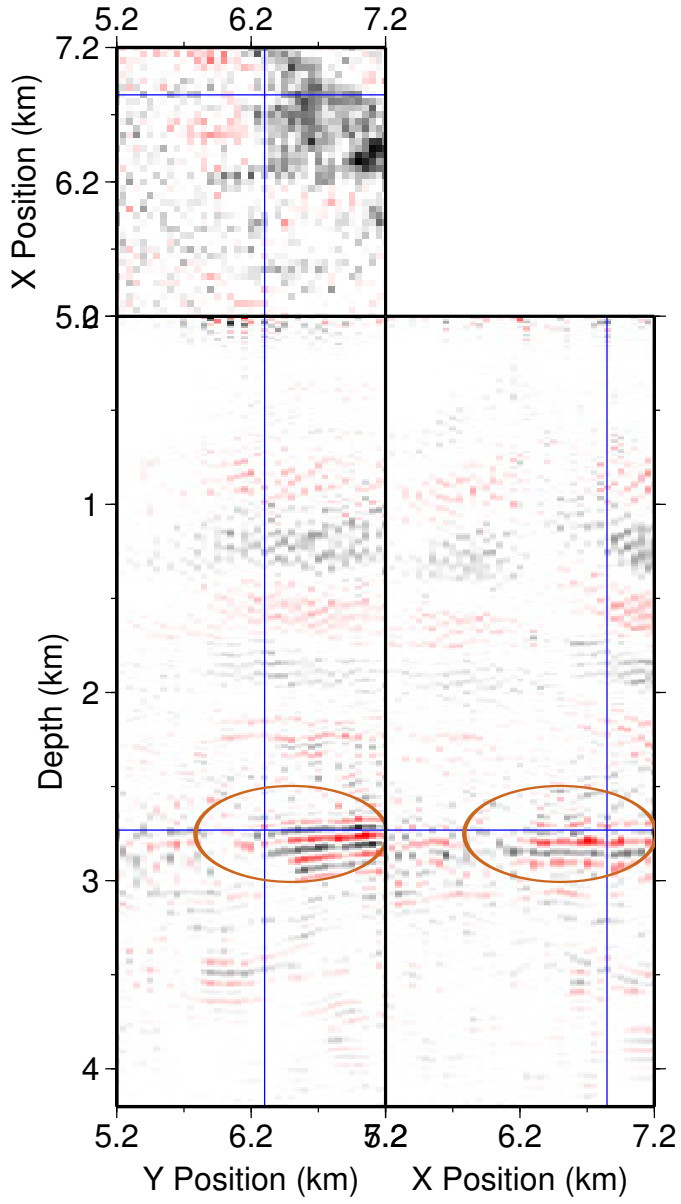

Figure 5.15: Valhall LoFS project time-lapse difference image for survey 10.

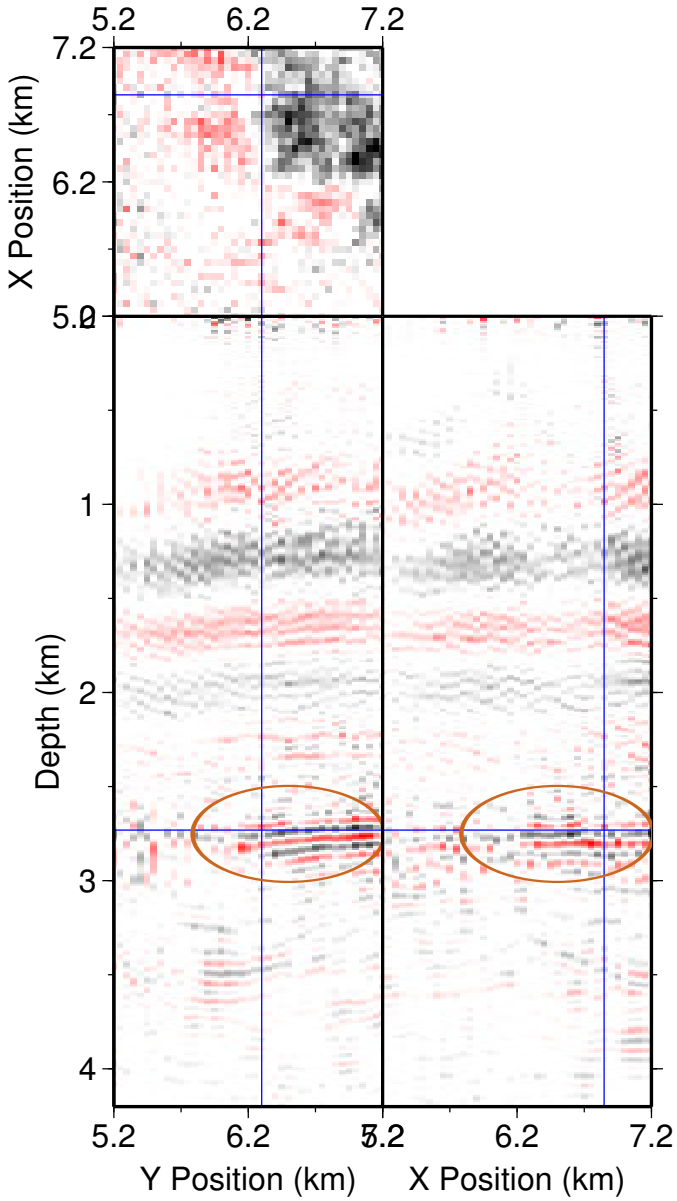

Figure 5.16: Valhall LoFS project time-lapse difference image for survey 11.

5.5 Quasi-Continuous Time-Lapse Monitoring 1

To demonstrate the efficiency of my data-estimation-based time-lapse monitoring approach on field data I use data subsets from Valhall LoFS surveys 9, 10, and 11. These are the 33% sparse datasets described in Section 5.3. Prior to estimating the discarded datasets, I create 4D sparse time-lapse data volumes by concatenating receiver gathers from the different surveys along the slow-time direction. I use the 1D Fourier transforms of these sparse time-lapse data volumes as the input to the MWNI algorithm. Sample estimated datasets are shown in Figures 5.17 through 5.19. Compare the estimated datasets in Figures 5.17 through 5.16 with the true datasets shown in Figures 5.7 through 5.9. The differences between the estimated and true datasets are shown in Figures 5.20 through 5.22. Estimation errors occur primarily in the form of incoherent noise, which implies that the reflectors are reconstructed with a high degree of accuracy.

The time-lapse difference images obtained by migrating the estimated images and computing the time-lapse amplitude changes are shown in Figures 5.23 through 5.25. Comparing the images from the estimated datasets (Figures 5.23 through 5.25) to the images obtained from the complete true datasets (Figures 5.14 through 5.16), we see that the approach does a good job at delineating the true time-lapse reservoir changes.

I present the data absolute amplitude ratio and depth-shift errors for the estimated datasets in Tables 5.1 and 5.2. Unlike in the synthetic examples, some of the absolute amplitude ratios for the estimated field data are larger than 1. This is caused by an overestimation of noise amplitudes in the estimated field data. Table 5.2 shows that the depth-shift errors are very small. The error estimates shown in Tables 5.1 and 5.2 indicate that the data reconstruction approach used does a good job at estimating the discarded traces.

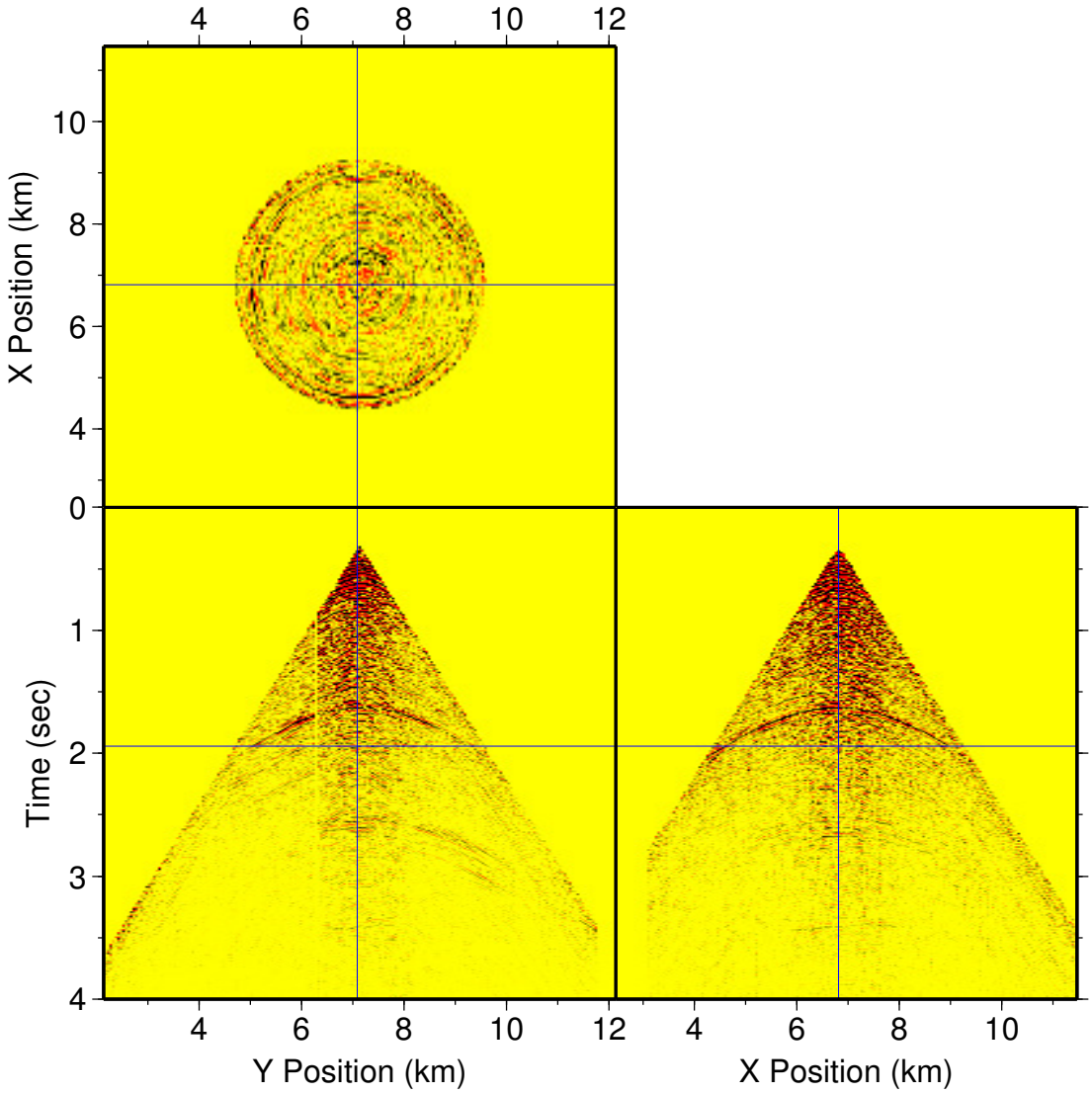

Figure 5.17: Slices through the estimated data obtained for a receiver gather from survey 9 using data estimated from an accumulated time-lapse data volume consisting of 33% sparse data from surveys 9 and 10.

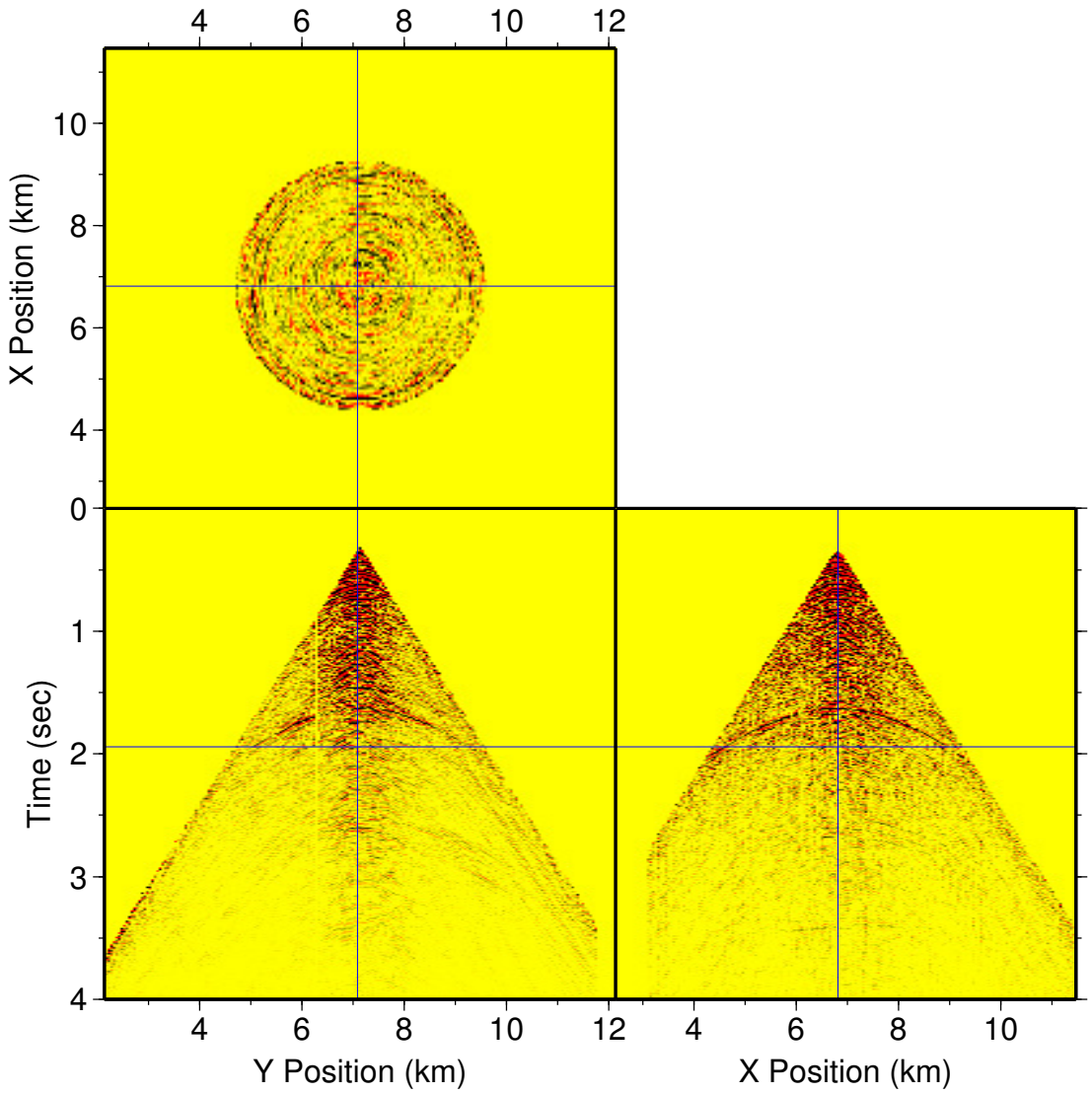

Figure 5.18: Slices through the estimated data obtained for a receiver gather from survey 10 using using data estimated from an accumulated time-lapse data volume consisting of 33% sparse data from surveys 9, 10, and 11.

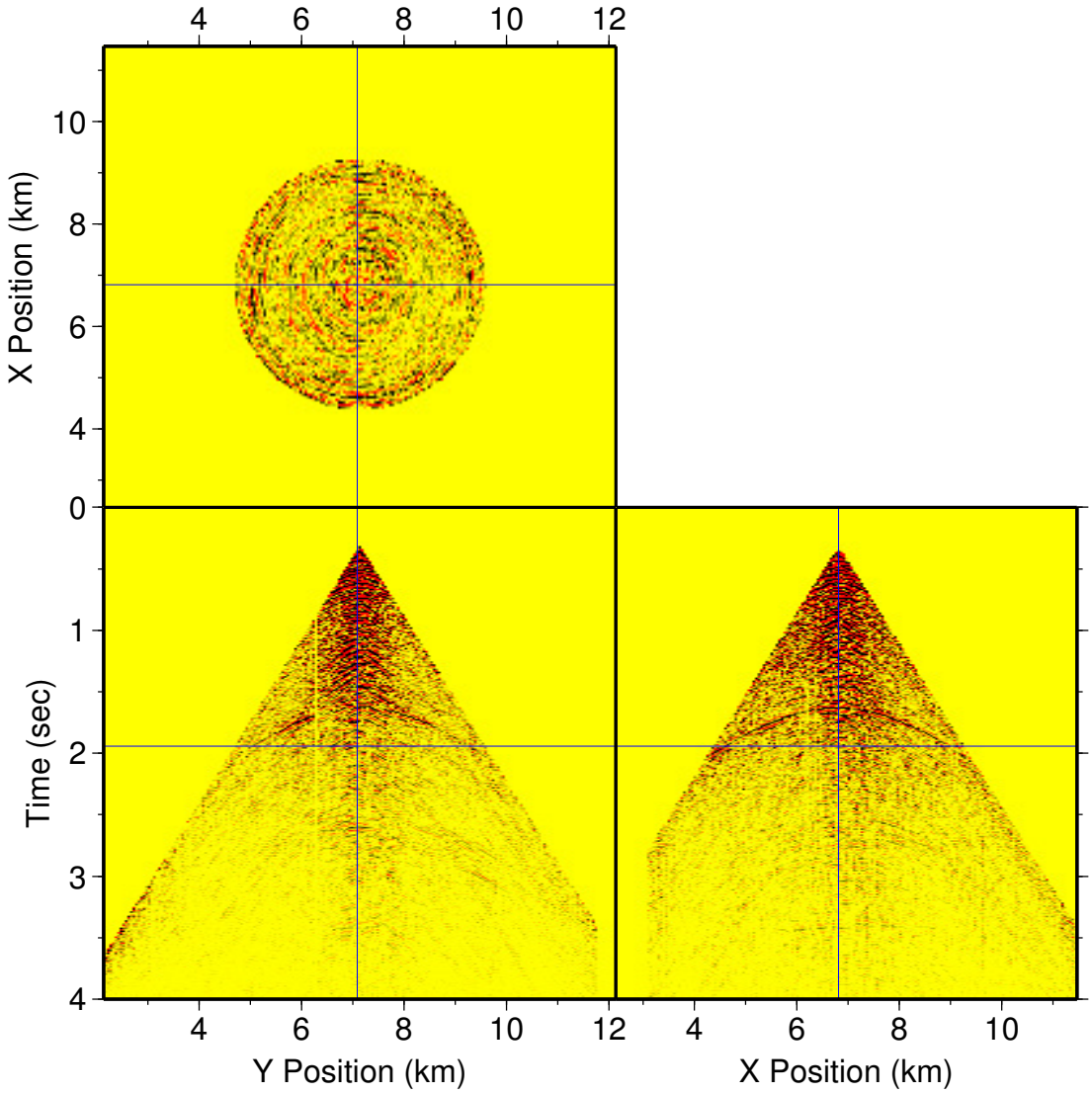

Figure 5.19: Slices through the estimated data obtained for a receiver gather from survey 11 using using data estimated from an accumulated time-lapse data volume consisting of 33% sparse data from surveys 9, 10, and 11.

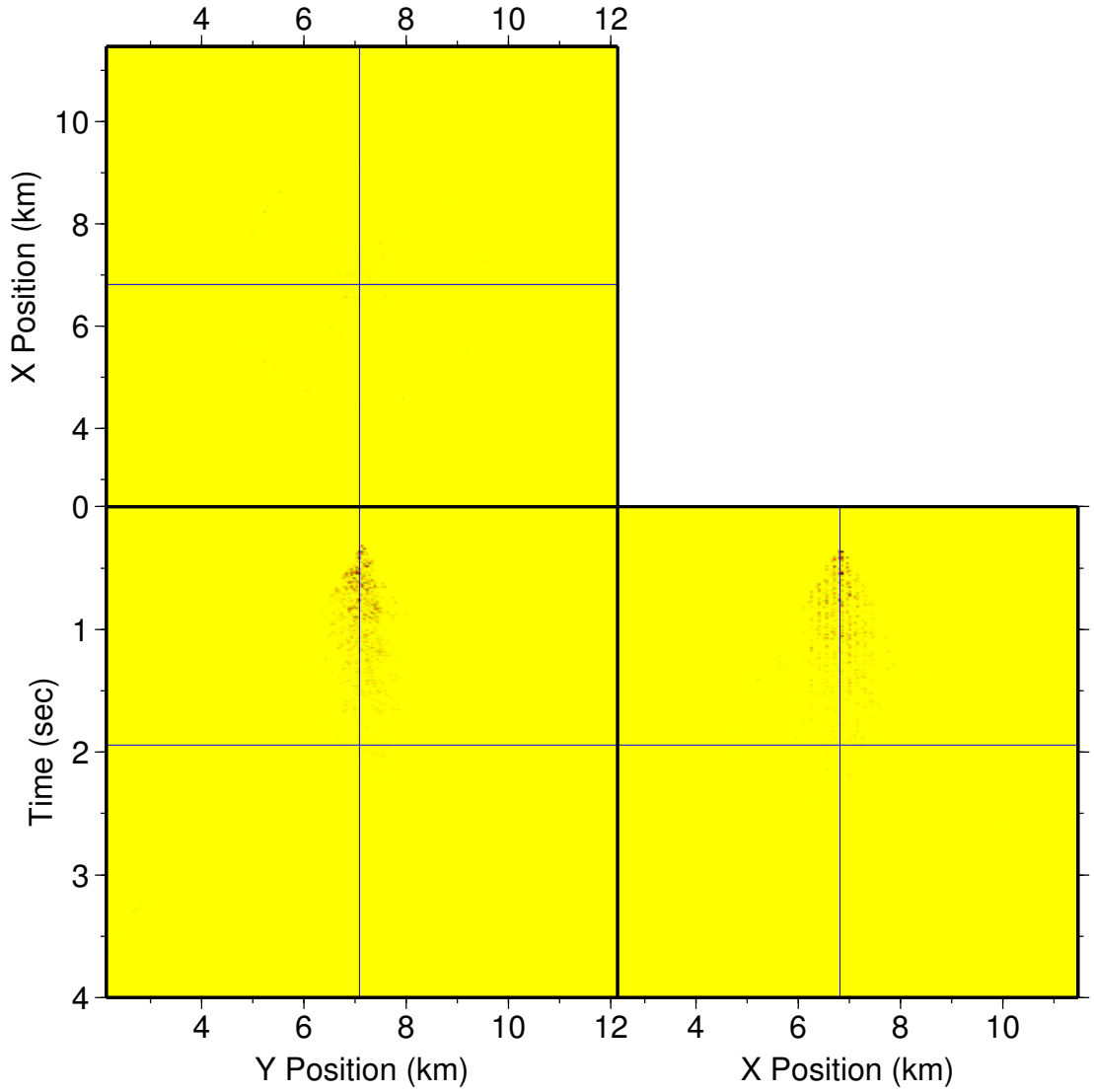

Figure 5.20: Slices through the difference between the true and estimated data obtained for the receiver gather from survey 9 shown in Figure 5.17.

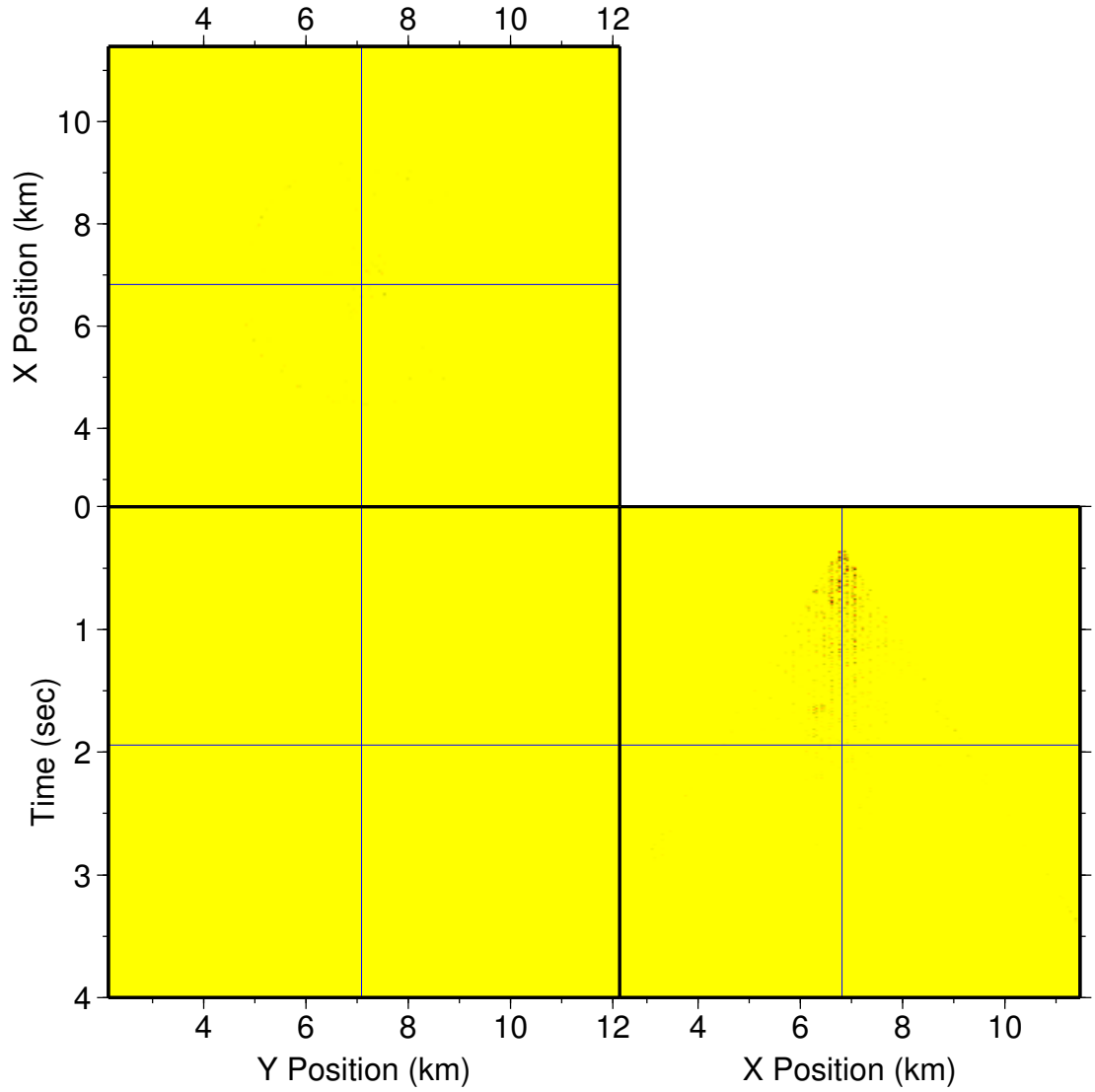

Figure 5.21: Slices through the difference between the true and estimated data obtained for the receiver gather from survey 10 shown in Figure 5.18.

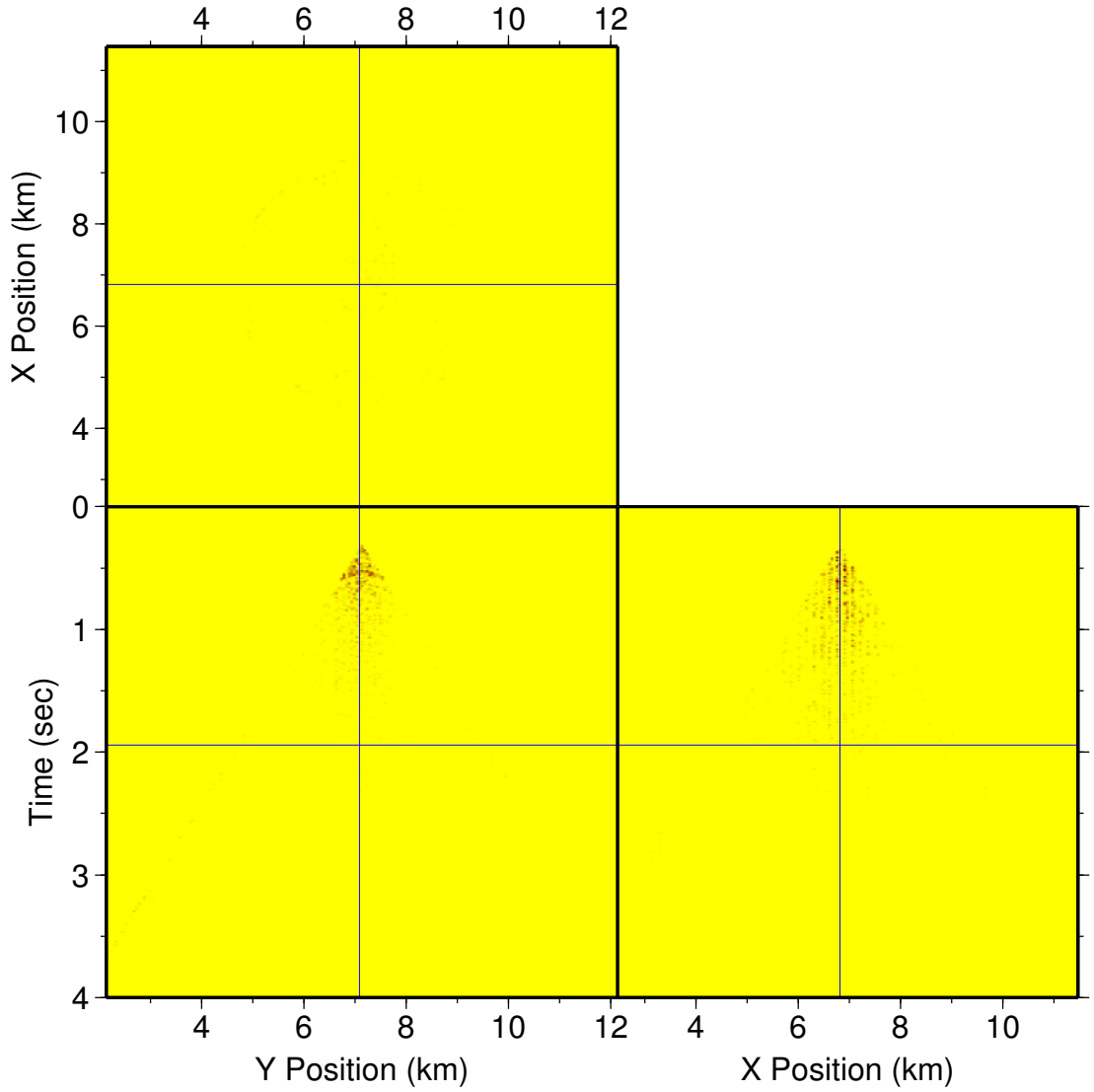

Figure 5.22: Slices through the difference between the true and estimated data obtained for the receiver gather from survey 11 shown in Figure 5.19.

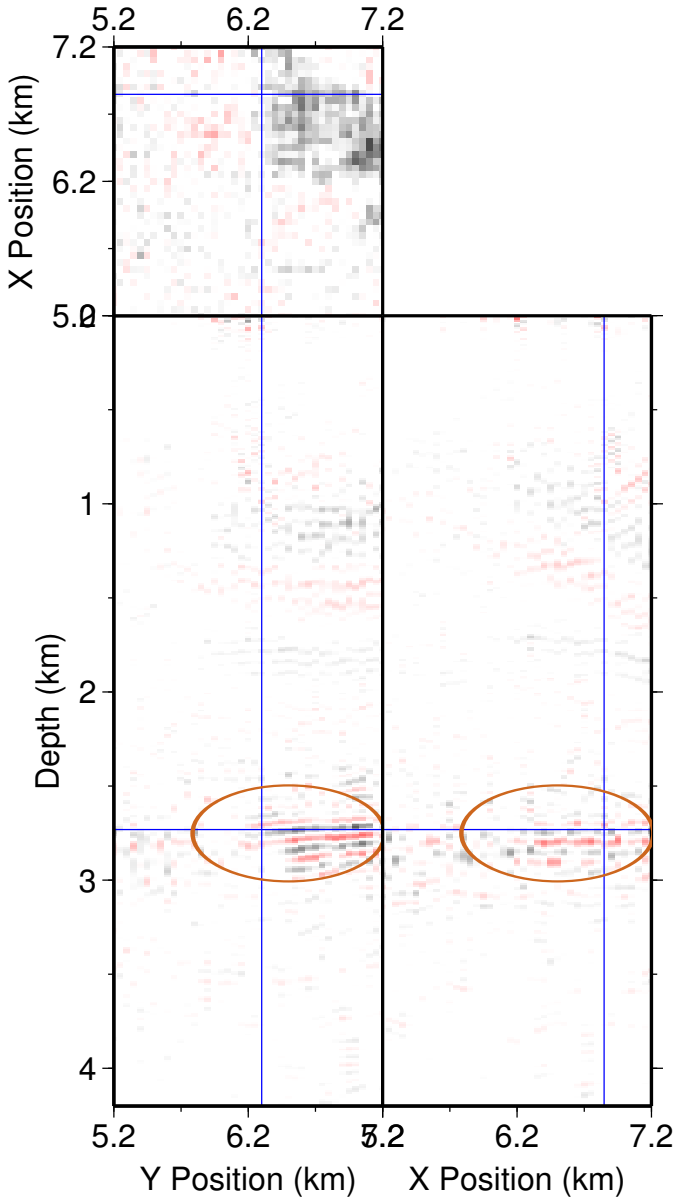

Figure 5.23: The time-lapse difference image obtained for survey 9 using data estimated from an accumulated time-lapse data volume consisting of 33% sparse data from surveys 9 and 10.

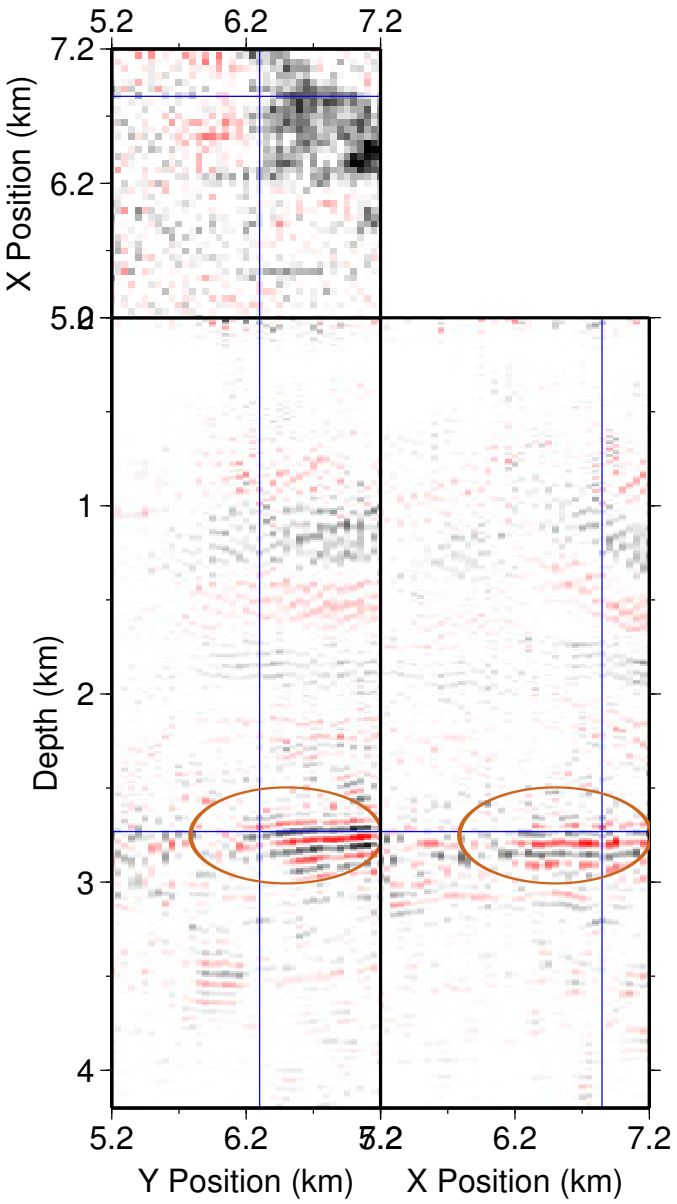

Figure 5.24: The time-lapse difference image obtained for survey 10 using data estimated from an accumulated time-lapse data volume consisting of 33% sparse data from surveys 9, 10 and 11.

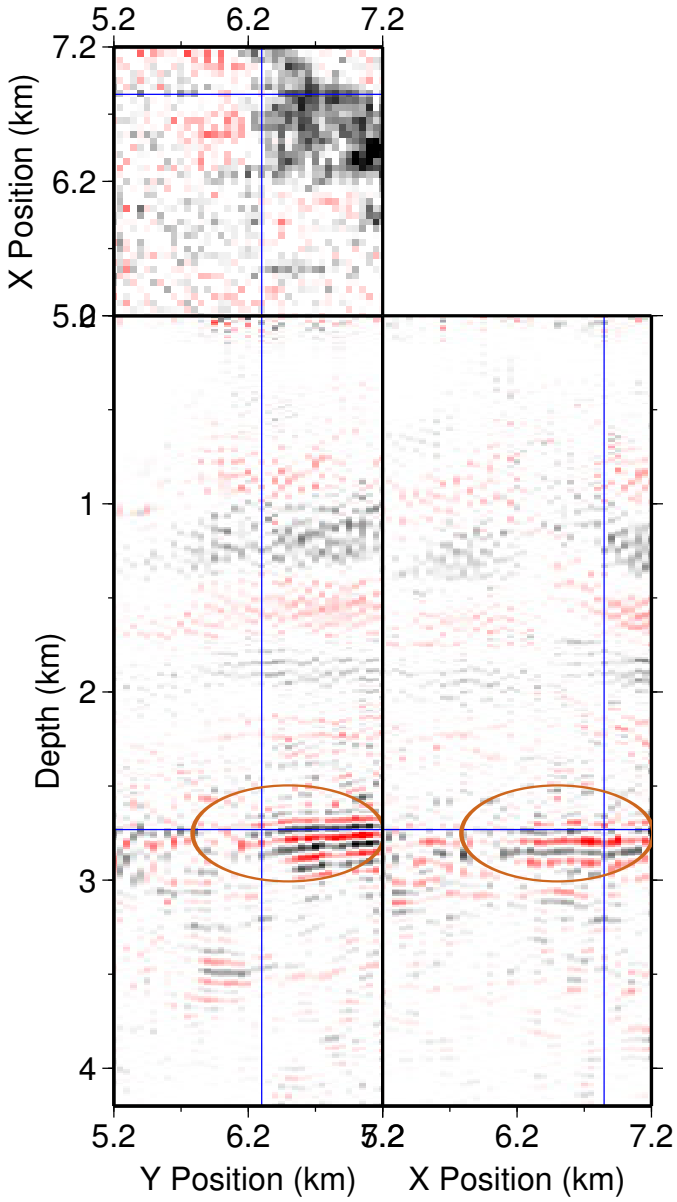

Figure 5.25: The time-lapse difference image obtained for the survey 11 using data estimated from an accumulated time-lapse data volume consisting of 33% sparse data from surveys 9, 10 and 11.

ESL / IT	0 Months	6 Months	12 Months
Survey 9	1.063	0.997	0.917
Survey 10	1.166	1.008	
Survey 11	1.119		

ESL - Estimation Slow-time Lag

IT - Image Time

Table 5.1: Absolute amplitude ratios for the estimated-data images (see Section 1.4 on page 9).

$x10^{-1}m$

ESL / IT	0 Months	6 Months	12 Months
Survey 9	-6.565	-5.613	-3.191
Survey 10	-4.626	0.093	
Survey 11	-7.061		

ESL - Estimation Slow-time Lag

IT - Image Time

Table 5.2: depth-shift errors in the estimated-data images.

5.6 Quasi-Continuous Time-Lapse Monitoring 2

An ideal quasi-continuous monitoring acquisition strategy at the Valhall Field will extend the acquisition time of each survey, such that data subsets can be used for monitoring at smaller-scale survey times. I simulate this scenario with data from the fourth Valhall LoFS survey by splitting the complete dataset into three groups of partial surveys, as shown in Figure 1.4. Figure 5.26 shows a receiver gather from the fourth Valhall LoFS survey, and Figures 5.27 through 5.29 show the data in Figure 5.26 split into three data subsets, based on shot times. Since the source boat travels continuously in the inline direction, data sparsity occurs primarily along the crossline direction.

I create 4D sparse time-lapse data volumes by concatenating receiver gathers from different surveys along the slow-time direction. I use the 1D Fourier transforms of these time-lapse data volumes as the input to the MWNI algorithm. Estimated data sections are shown in Figures 5.30 through 5.32. After estimating the unavailable traces for each subset, I migrate the estimated dataset. The resulting time-lapse difference images are shown in Figures 5.33 and 5.34. No observable time-lapse changes in the images are seen in the reservoir over the 45-day time-interval considered. This could occur if injection or production operations did not affect the portion of the reservoir imaged, or if data-acquisition parameters such as source-receiver spacing or data-sampling frequency are not adequate to detect any reservoir changes.

5.7 Summary

In this chapter, I applied the quasi-continuous strategy introduced in Chapter 1 to field surface-seismic data. I used the Valhall LoFS dataset provided by BP. The Valhall LoFS project was implemented to monitor injected water during secondary recovery at the Valhall Field off the coast of Norway. I presented a case for quasi-continuous monitoring using my approach with two example cases. In the first case, I subsampled data from three Valhall LoFS surveys to produce sparse datasets

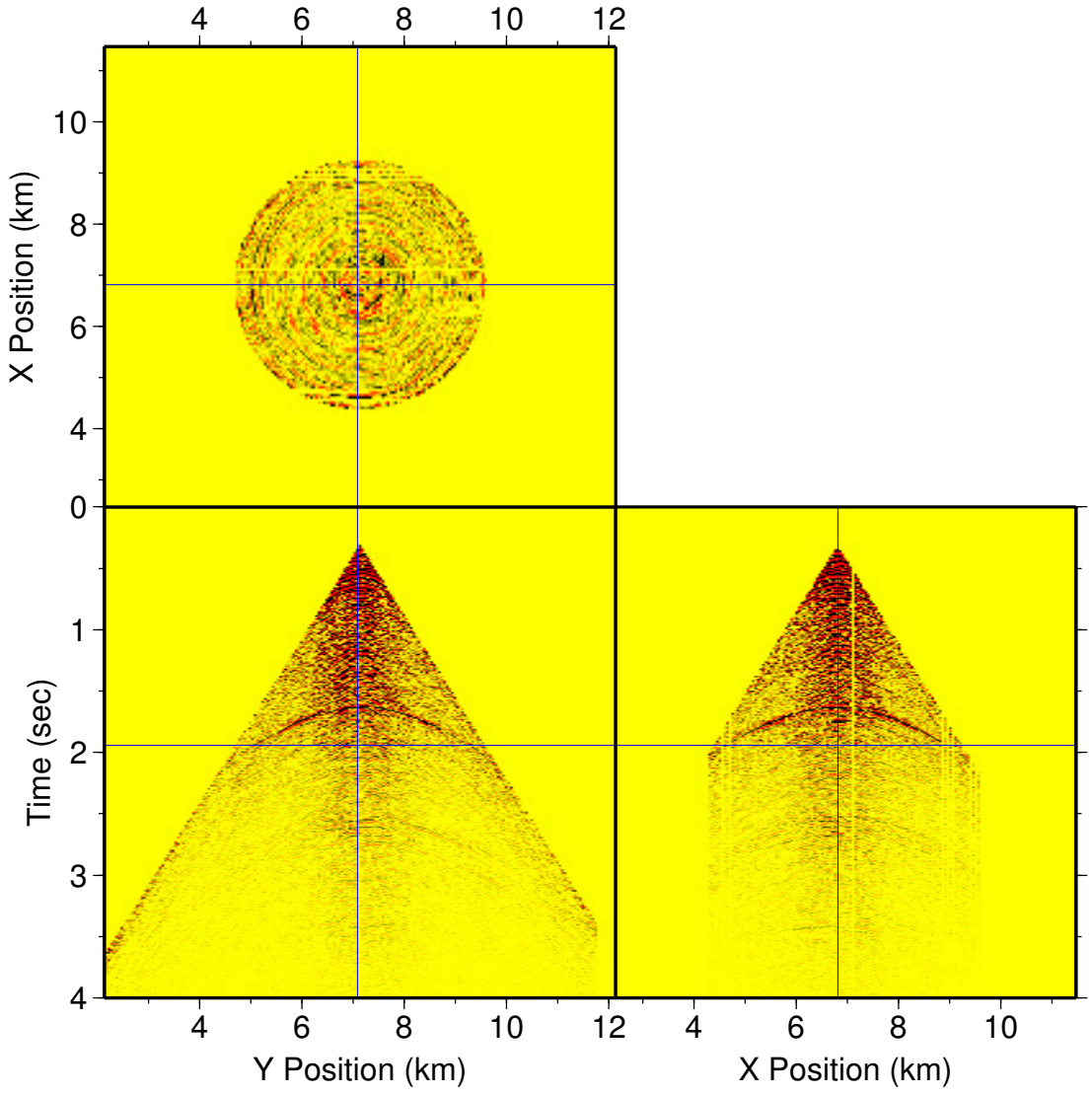

Figure 5.26: Sample complete receiver gather from the fourth Valhall LoFS survey.

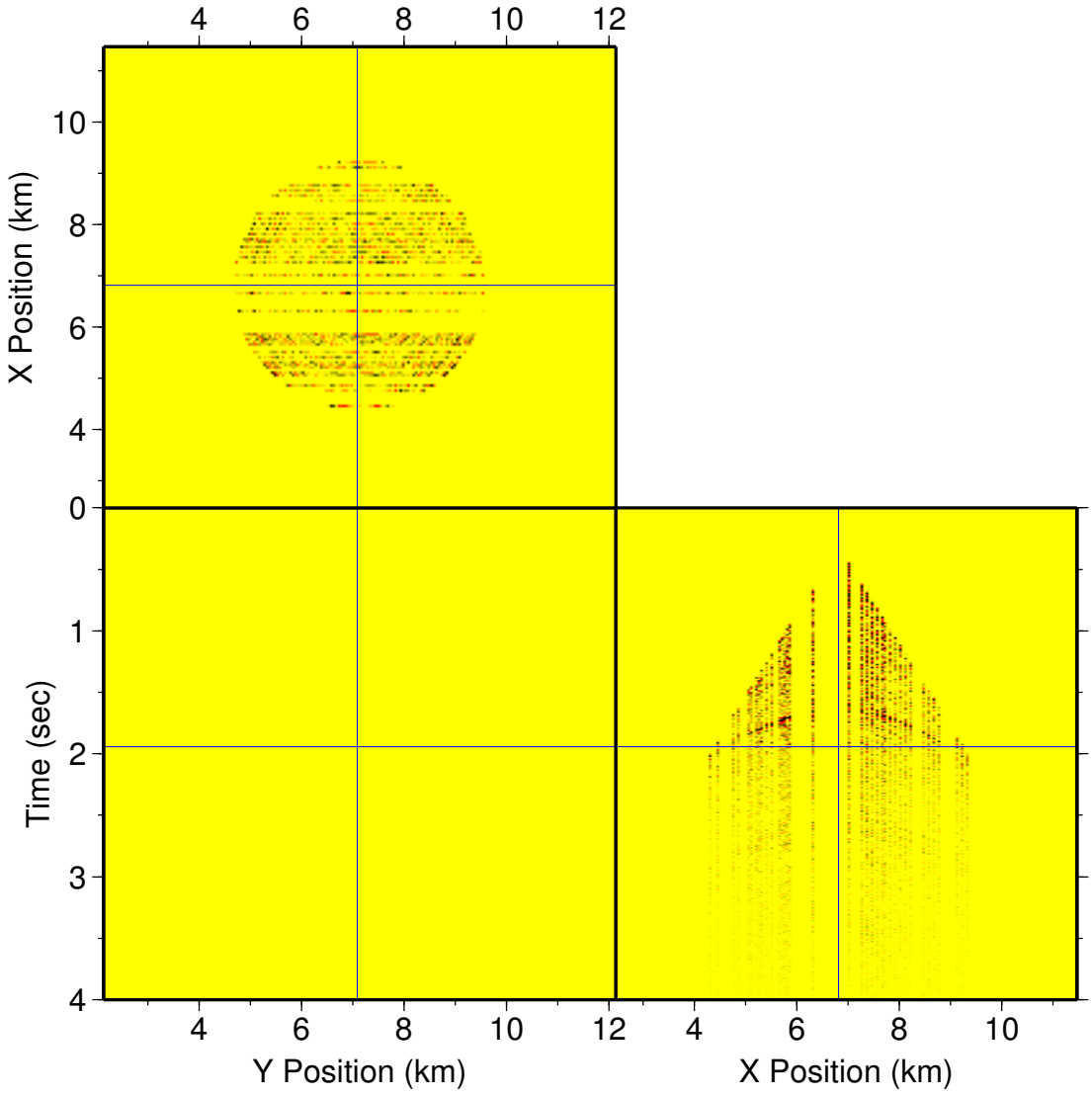

Figure 5.27: The first subset from the data shown in Figure 5.26.

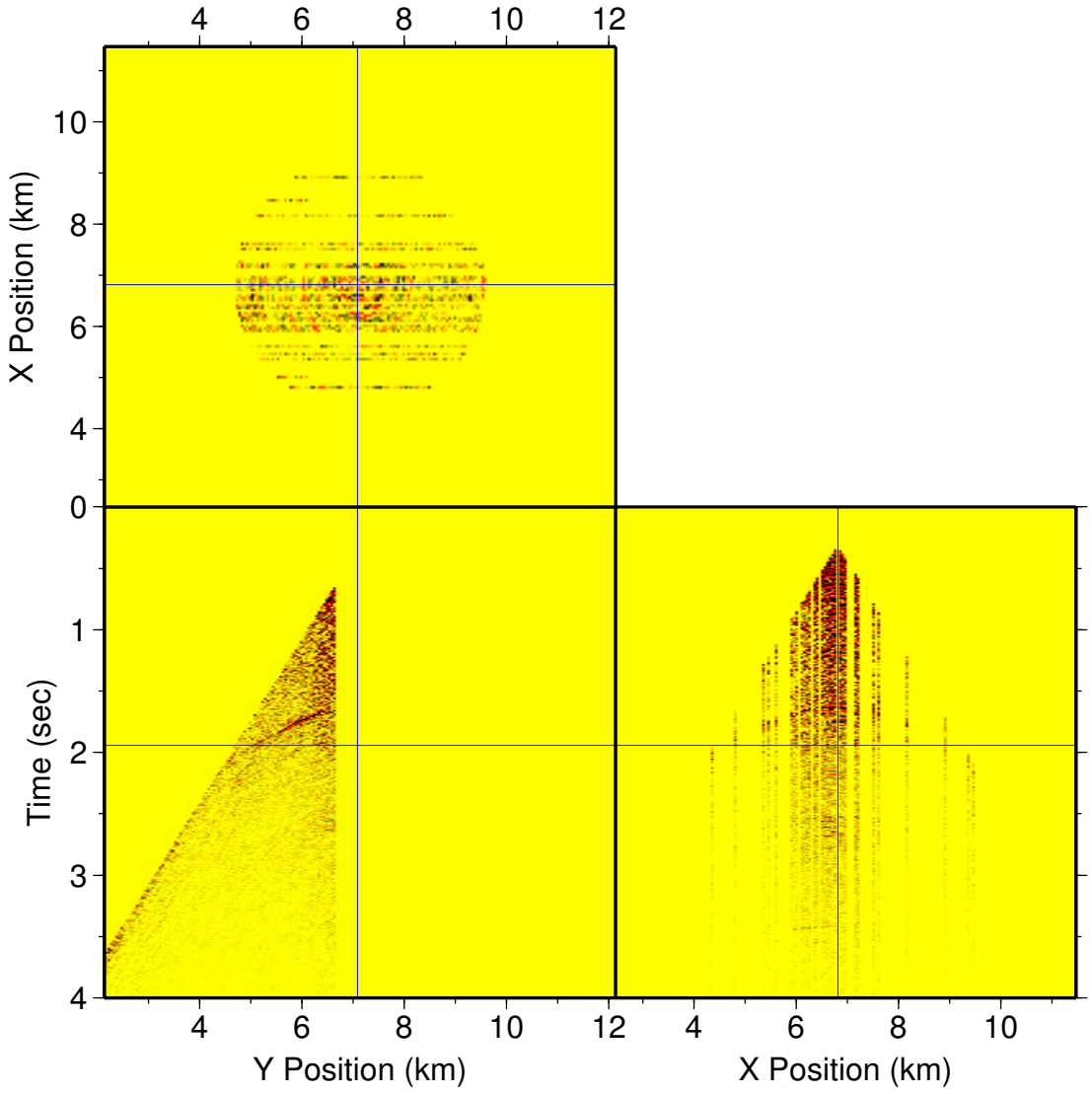

Figure 5.28: The second subset from the data shown in Figure 5.26.

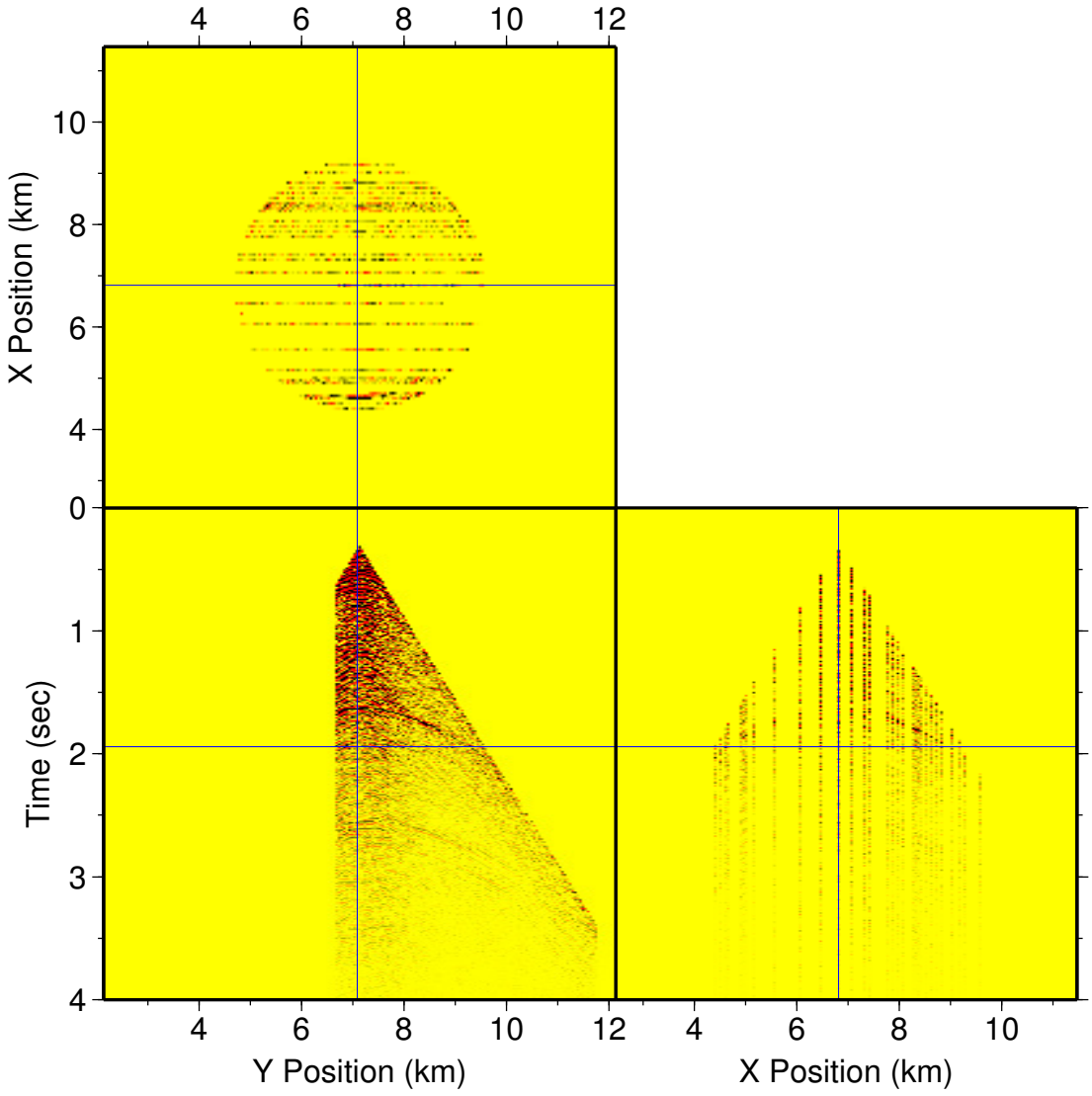

Figure 5.29: The third subset from the data shown in Figure 5.26.

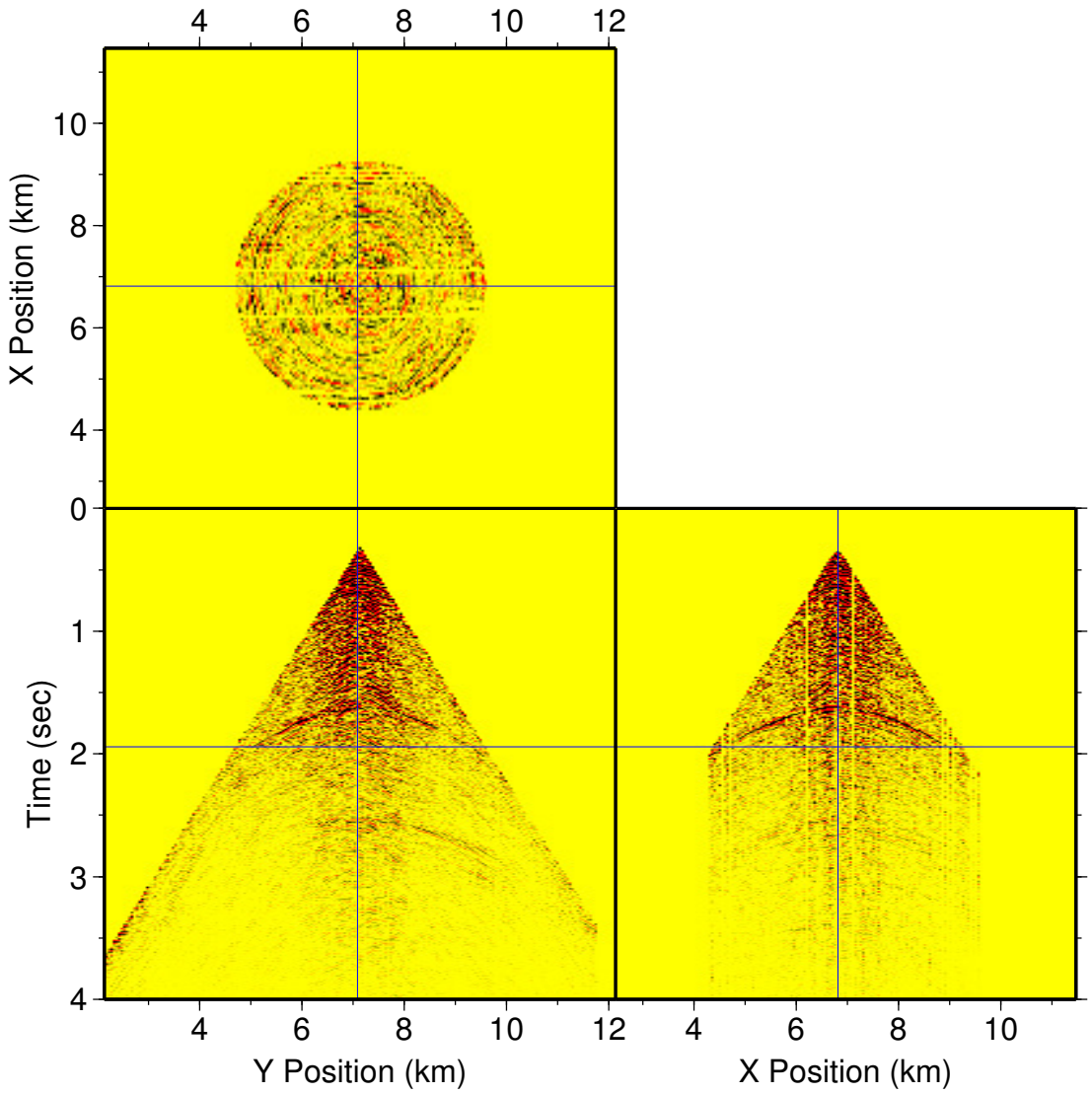

Figure 5.30: Estimated receiver gather from the sparse receiver gather in Figure 5.27. I estimate the unknown data using the baseline data and the monitor data shown in Figure 5.27.

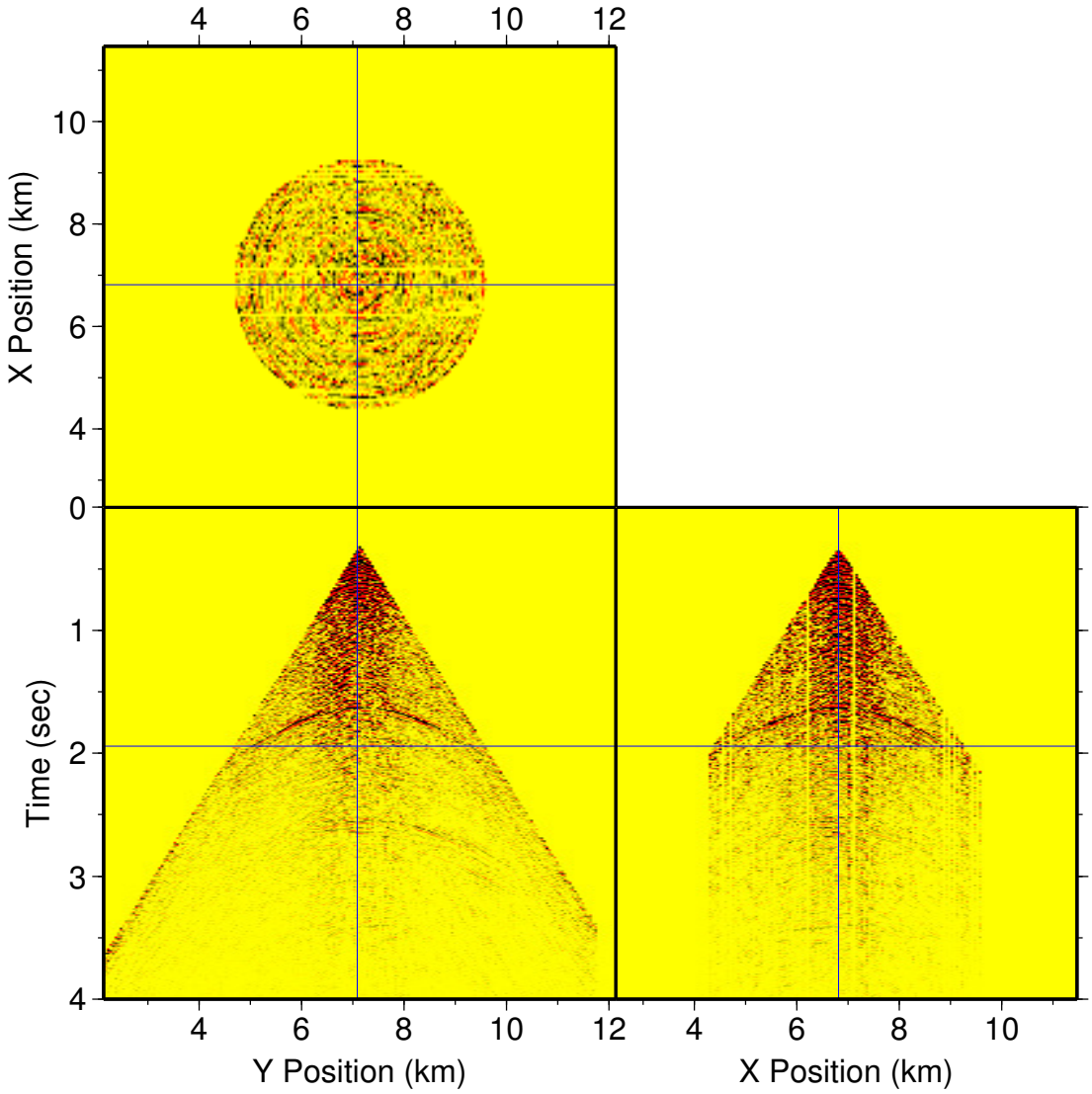

Figure 5.31: Estimated receiver gather from the sparse receiver gather in Figure 5.28. I estimate the unknown data using the baseline data and the monitor data shown in Figures 5.27 and 5.28.

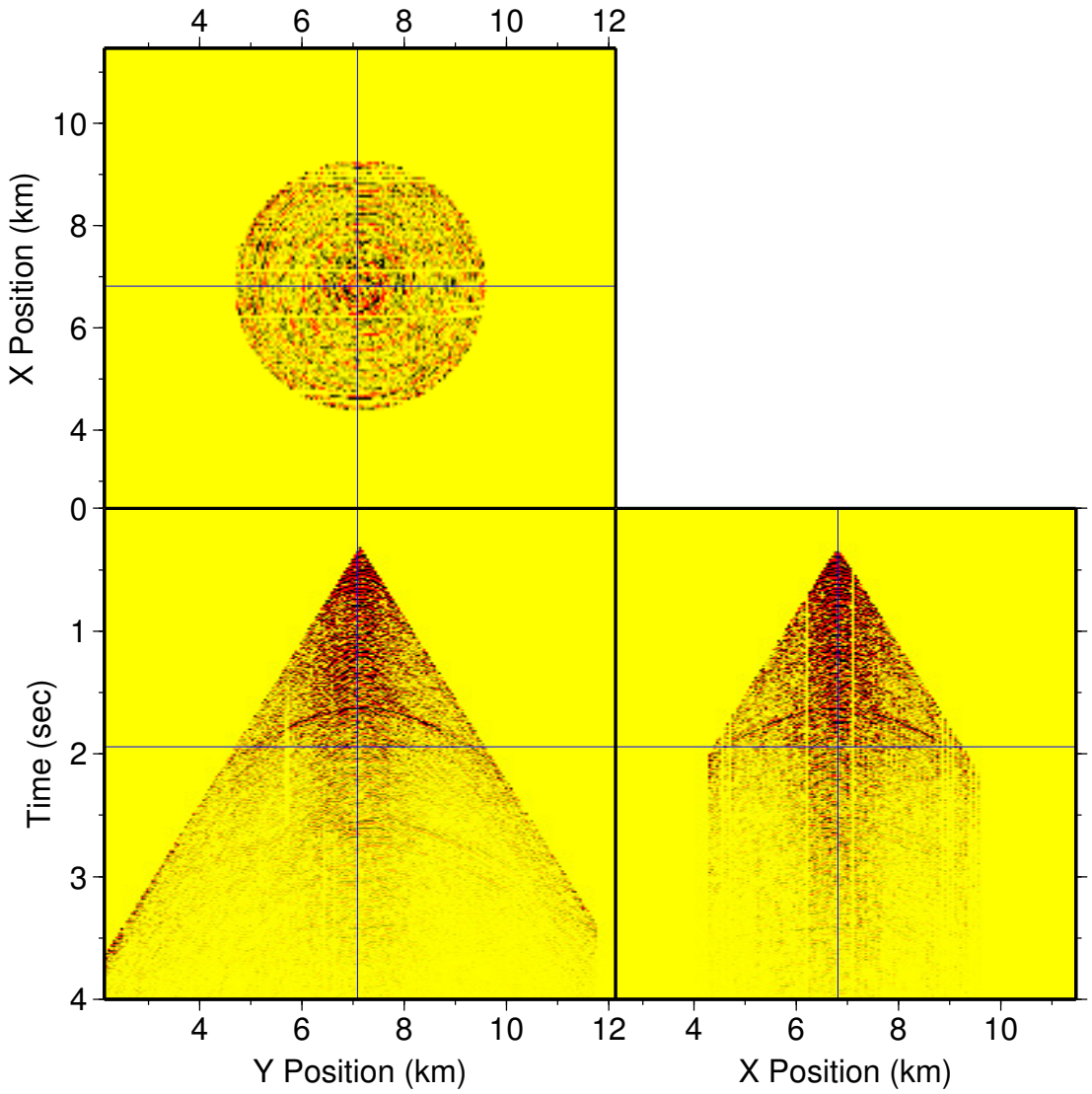

Figure 5.32: Estimated receiver gather from the sparse receiver gather in Figure 5.29. I estimate the unknown data using the baseline data and the monitor data shown in Figures 5.27, 5.28, and 5.29.

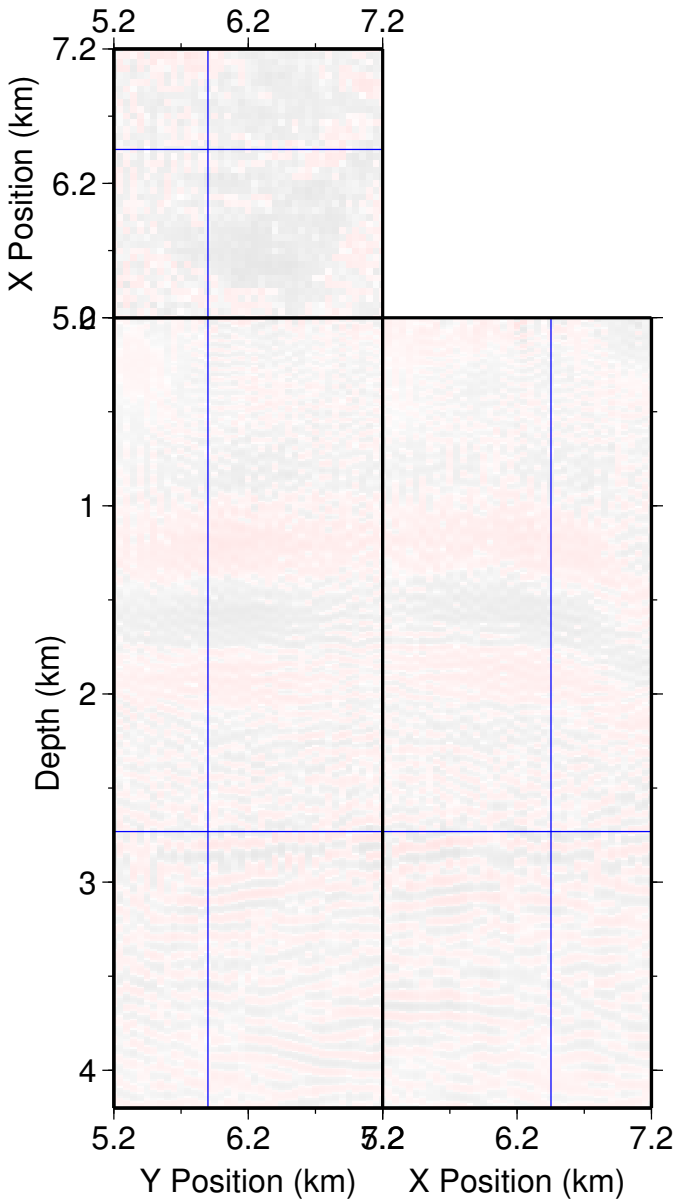

Figure 5.33: The time-lapse difference image obtained after 30 days of the fourth Valhall LoFS survey. There are no delineated reservoir changes in the portion of the reservoir studied during this time.

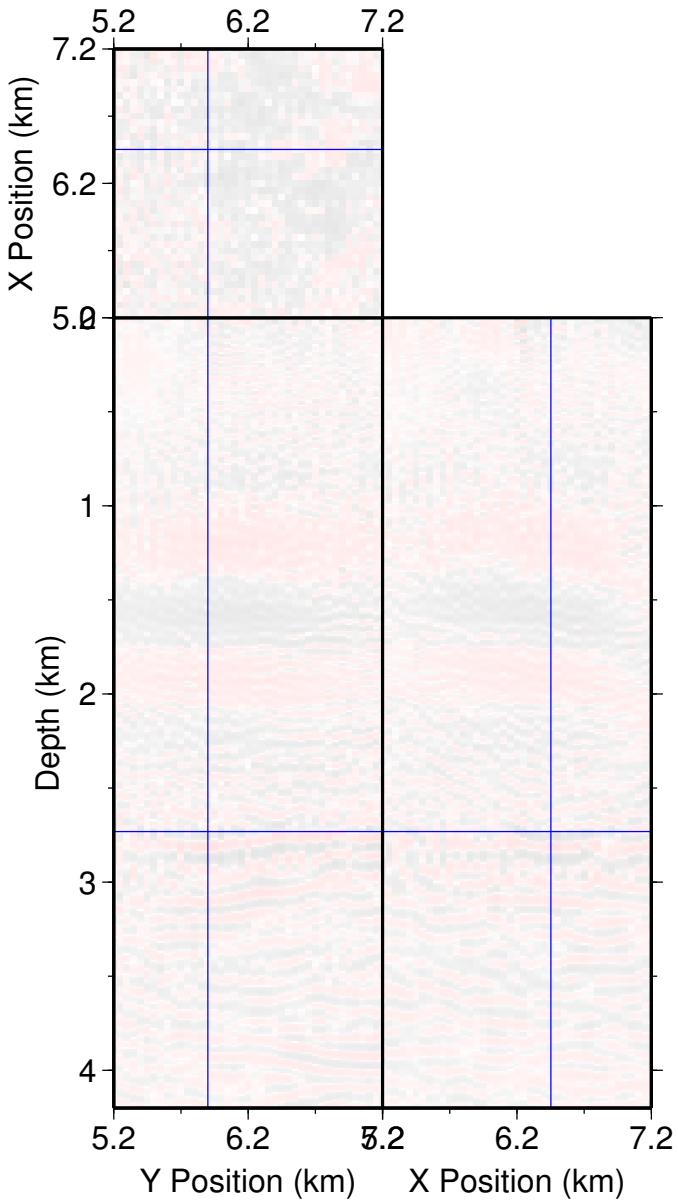

Figure 5.34: The time-lapse difference image obtained after 45 days of the fourth Valhall LoFS survey. There are no delineated reservoir changes in the portion of the reservoir studied during this time.

at each survey time. I estimated the discarded traces using accumulated sparse data. The estimated datasets were then migrated to produce images of the subsurface. Results show that the estimated datasets worked as well as the complete true datasets in delineating the spatial extent of changes in the reservoir. In the second case, I split a conventional 3D seismic volume into three partial data volumes, based on seismic shot times. The grouping represents data collected within 15-day intervals. I estimated the unavailable data in each partial dataset with accumulated datasets and migrated the results. An assessment of the estimation inaccuracies using the method described in Section 2.2 shows that estimation errors are very low.

Acknowledgements

I would like to thank BP and the Valhall partnership (BP Norge AS, Amerada Hess Norge, Total E&P Norge AS and A/S Norske Shell) for providing the Valhall LoFS dataset.

Chapter 6

Conclusions

This dissertation addresses the problem of quasi-continuous reservoir monitoring with seismic data. It tackles the problem by recognizing the impact of crew mobilization and equipment deployment, during seismic data acquisition, on reservoir monitoring frequency. The time it takes to acquire a complete 3D survey imposes a limit on the time interval between surveys in a time-lapse monitoring project. In addition, more time is used to preprocess large amounts of data, thereby prolonging the time interval between data acquisition and data interpretation.

I circumvent this problem by proposing that a combination of recorded and estimated data be used to produce an image of the subsurface at a particular time. This is done by recording survey subsets in small slow-time intervals and using all accumulated data to estimate unavailable data. Recording in this manner constitutes sparse spatial sampling. This provides the freedom to vary the slow-time sampling interval. Naturally, reducing the spatial sampling leads to reduced spatial resolution. This is the trade-off for the increased slow-time temporal resolution. By reconstructing unavailable data at each survey time, I can improve the spatial resolution of the data. With a small slow-time sampling interval, a more accurate reconstruction of the unavailable data is possible.

I noted in Chapter 1 that my approach trades spatial resolution for slow-time temporal resolution. In general, seismic images of the subsurface are produced so that they can be interpreted. While it is important for an estimated dataset to be as

close as possible to its corresponding true dataset, the ultimate test of efficiency is in interpreting the resulting images. Do we get the same interpretation from estimated datasets as we would get from complete, true datasets? The examples presented in this dissertation show that, using my approach, the answer to that question is yes.

The primary contribution of this dissertation is the presentation of a seismic time-lapse monitoring strategy that allows easy variability in slow-time temporal resolution. It has the potential to be the foundation for continuous seismic reservoir monitoring. The proposed approach can be applied to traveltime and full-trace seismic data. In Chapter 2, I present a new error-analysis tool that provides a way to quantitatively measure the estimation inaccuracies in estimated seismic datasets whose true values are known. This tool is particularly useful in tracking trends in a series of estimation results obtained using different input parameters.

In Chapter 3, I show an example of an application of the quasi-continuous monitoring strategy to synthetic and field crosswell traveltime data. I use the synthetic examples to illustrate how my method can be used in a CO_2 sequestration project to monitor the buried CO_2 plume and to detect leaks. Although it is not an ideal field dataset for this approach, I show an application of my proposed approach for time-lapse monitoring with sparse data using the McElroy Field crosswell-seismic data. In Chapter 4, I show 2D and 3D synthetic surface-seismic examples. As in the crosswell traveltime example, I use the 2D example to illustrate how surface-seismic surveys can be used to quasi-continuously monitor a CO_2 sequestration reservoir. I use the 3D example to illustrate how the quasi-continuous approach can be used to monitor a reservoir during secondary recovery.

In Chapter 5, I apply my approach to BP's Valhall LoFS project data. This is a field-data example illustrating how the approach can be used to monitor a reservoir during enhanced recovery. I present two examples. The first uses a time-scale on the order of months and is an argument for the implementation of this approach at the Valhall Field. The second uses a time-scale on the order of weeks and shows that the time-scale of the reservoir changes should be taken into consideration when designing a quasi-continuous reservoir monitoring project.

For the approach presented in this dissertation to be practical, surveys should

be repeatable, since the slow-time axis is used in the data-estimation process. Permanent installation of seismic sources and receivers facilitates repeatability. It also shortens turn-around time, since equipment deployment time is eliminated.

In this dissertation, I implemented the data-estimation-based approach using static missing-data estimation schemes. This is definitely a first step toward proving the practicality and efficiency of the approach. The next step should be an implementation with dynamic missing-data estimation schemes. Of special interest is the Kalman filter algorithm (Kalman, 1960), which updates previous estimates of the model parameters as new data become available. Such an algorithm is well suited for my approach, since data are acquired at increments and are used to estimate unavailable data at previous survey times.

Bibliography

Abma, R., and N. Kabir, 2006, 3D interpolation of irregular data with a POCS algorithm: Geophysics, **71**, E91–E97. 1.2

Ajo-Franklin, J. B., J. Urban, and J. M. Harris, 2005, Temporal integration of seismic traveltime tomography: 75th Annual Meeting and International Exposition, SEG, Expanded Abstracts. 1.2

Arogunmati, A., and J. M. Harris, 2009, An approach for quasi-continuous time-lapse seismic monitoring with sparse data: 79th Annual Meeting and International Exposition, SEG, Expanded Abstracts. 1.6, 2.2.1

———, 2010, A data-estimation based approach for quasi-continuous reservoir monitoring using sparse surface seismic data: 72nd EAGE Conference & Exhibition, Extended Abstracts. 1.6

Arts, R., O. Eiken, A. Chadwick, P. Zweigel, L. van der Meer, and B. Zinszner, 2004, Monitoring of CO_2 injected at Sleipner using time-lapse seismic data: Energy, **29**, 1383–1392. 1.1, 1.1

Barkved, O. I., K. Beuer, T. G. Kristiansen, R. M. Kjelstadli, and J. H. Kommedal, 2005, Permanent seismic monitoring of the Valhall Field, Norway: IPTC 10902. 1.1, 1.6

Barkved, O. I., and T. Kristiansen, 2005, Seismic time-lapse effects and stress changes: Examples from a compacting reservoir: The Leading Edge, **24**, 1244–1248. 5.2

Benson, S., P. Cook, J. Anderson, S. Bachu, H. B. Nimir, and B. Basu, 2005, Underground geological storage, *in* IPCC Special Report on Carbon Dioxide Capture and Storage: Cambridge University Press, 195–276. 1.3

Biondi, B., 2007, Distinguished instructor series, number 10: Concepts and applications in 3D seismic imaging: Society of Exploration Geophysicists. 4.2.2

Burkhart, T., A. R. Hoover, and P. B. Flemings, 2000, Case history: Time-lapse (4-D) seismic monitoring of primary production of turbidite reservoirs at South Timbalier Block 295, offshore Louisiana, Gulf of Mexico: Geophysics, **65**, 351–367. 1.1

Cabrera, S. D., and T. W. Parks, 1991, Extrapolation and spectral estimation with iterative weighted norm modification: IEEE Transactions on signal processing, **39**, 842–851. 2.1.2

Cameron, K., and P. Hunter, 2002, Using spatial models and kriging techniques to optimize long-term ground-water monitoring networks: A case study: Environmetrics, **13**, 629–656.

Candès, E. J., and J. Romberg, 2007, Sparsity and incoherence in compressive sampling: Inverse Problems, **23**, 969–985. 1.1

Candès, E. J., and M. B. Wakin, 2008, An introduction to compressive sampling: IEEE Signal Processing Magazine, **21**. 1.1

Castle, R. J., 1994, A theory of normal moveout: Geophysics, **59**, 983–999. 2.1.1

Claerbout, J. F., 1998, Multidimensional recursive filters via a helix: Geophysics, **63**, 1532–1541. 2.1.1, 2.1.1.1, 2.1.1.1, 2.2.1

———, 2008, Image estimation by example: Geophysical soundings image construction: Multidimensional autoregression: online. (last accessed March 12, 2008). 2.1.2.2

Clapp, R., 2001, Geologically constrained migration velocity analysis: PhD thesis, Stanford University.

Clarke, R., O. J. Askim, K. Pursley, and P. Vu, 2005, 4D rapid turnaround for permanent 4C installation: 75th Annual Meeting and International Exposition, SEG, Expanded Abstracts. 1.1

Crawley, S., 2000, Seismic trace interpolation with nonstationary prediction-error filters: PhD thesis, Stanford University. 1.2, 2.2.1

Cressie, N., 1993, Statistics for spatial data: Wiley. 2.1.1

Curry, W., 2008, Interpolation with prediction-error filters and training data: PhD

thesis, Stanford University. 1.2, 2.1, 2.2.1

de Bazelaire, E., 1988, Normal moveout revisited: Inhomogeneous media and curved interfaces: Geophysics, **53**, 143–157. 2.1.1

De-Cesare, L., D. E. Myers, and D. Posa, 2001, Product-sum covariance for space-time modeling: An environmental application: Environmetrics, **12**, 11–23.

Devaney, A. J., 1982, A filtered back propagation algorithm for diffraction tomography: Ultrasonic Imaging, **4**, 336–350.

Ebrom, D., X. Li, and D. Sukup, 2000, Facilitating technologies for permanently instrumented oil fields: The Leading Edge, **19**, 282–285. 1.1

Fomel, S., and J. F. Claerbout, 2003, Multidimensional recursive filter preconditioning in geophysical estimation problems: Geophysics, **68**, 577–588. 2.4

Foster, D., S. Fowler, J. McGarrity, M. Riviere, N. Robinson, R. Seaborne, and P. Watson, 2008, Building on BP's large-scale OBC monitoring experience - The Clair and Chirag-Azeri projects: The Leading Edge, **27**, 1632–1637. 1.1, 1.6

Gilgen, H., 2006, Univariate time series in geosciences: Springer. 2.1.1

Guitton, A., 2003, Multidimensional seismic noise attenuation: PhD thesis, Stanford University. 2.1.1

Hamilton, D., and R. L. Meehan, 1971, Ground rupture in the Baldwin Hills: Science, **23**, 333–344. 1.3

Hansen, P. C., 1998, Rank-deficient & discrete ill-posed problems: Numerical aspects of linear inversion: SIAM. 2.1.2

Hansen, T. M., and K. Mosegaard, 2008, VISIM: Sequential simulation for linear inverse problems: Computers and Geosciences, **34**, 53–76.

Hanson, K., 1987, Bayesian and related methods in image reconstruction from incomplete data: Image Recovery: Theory and Application, 79–125.

Hardie, R. C., K. J. Barnard, and E. E. Armstrong, 1997, Joint MAP registration and high-resolution image estimation using a sequence of undersampled images: IEEE Transactions on Image Processing, **6**, 1621–1633. 1.2

Harris, J. M., 1992, Initial value raytracing in smoothly varying heterogeneous media: Annual Report vol. 3, no. 1, Paper I, Stanford Tomography Project.

———, 2004, Geophysical monitoring of geologic sequestration: Technical report,

Global Climate and Energy Project.

Harris, J. M., R. C. Nolen-Hoeksema, R. T. Langan, M. van Schaack, S. K. Lazaratos, and J. W. Rector III, 1995, High resolution crosswell imaging of a West Texas carbonate reservoir: Part l-Project summary and interpretation: Geophysics, **60**, 667–681. 1.1, 3.3

Harris, J. M., M. D. Zoback, A. R. Kovscek, and F. M. Orr, 2007, Geologic storage of co2, *in* Global Climate and Energy Project 2007 Technical Report.

———, 2008, Geologic storage of co2, *in* Global Climate and Energy Project 2008 Technical Report.

Hatchell, P. A., A. van den Beukel, M. Molenaar, K. P. Maron, C. J. Kenter, J. G. F. Stammeijer, J. J. van der Velde, and C. M. Sayers, 2003, Whole-earth 4D: Reservoir monitoring geomechanics: 73rd Annual International Meeting, SEG, Expanded Abstracts, 1330–1333. 2.2.2

Herrmann, F. J., and G. Hennenfent, 2008, Non-parametric seismic data recovery with curvelet frames: Geophysical Journal International, **173**, 233–248. 1.1

Hestenes, M. R., and E. Stiefel, 1952, Methods of conjugate gradients for solving linear systems: Journal of Research of the National Bureau of Standards, **49**, 409–436. 2.1.1.1, 2.1.2

Hiriyannaiah, H. P., M. Satyaranjan, and K. R. Ramakrishnan, 1996, Reconstruction from incomplete data in cone-beam tomography: Optical Engineering, **35**, 2748–2760.

Hole, J. A., and B. C. Zelt, 1995, 3-D finite-difference reflection traveltimes: Geophysical Journal International, **121**, 427–443. 3.2.1

Hottman, W. E., and M. P. Curtis, 2001, Borehole seismic sensors in the instrumented oil field: The Leading Edge, **20**, 630–634. 1.1

Houston, M., and N. Grumman, 2003, Requirements, constraints and advantages of fiber optic sensor arrays for permanent offshore applications: paper OTC 15072. 1.6

Huang, S. W., and P. C. Li, 2004, Computed tomography sound velocity reconstruction using incomplete data: IEEE Transactions on Ultrasonics, Ferroelectrics and Frequency Control, **51**, 329–342.

Iooss, B., D. Geraets, T. Mukerji, Y. Samuelides, M. Touati, and A. Galli, 2003, Inferring the statistical distribution of velocity heterogeneities by statistical traveltime tomography: Geophysics, **68**, 1714–1730.

Jain, A. K., 1998, Fundamentals of digital image processing: Prentice Hall. 2.1.1, 2.1.1

Journel, A., and C. J. Huijbregts, 1978, Mining geostatistics: Academic Press. 2.1.1

Kalman, R. E., 1960, A new approach to linear filtering and prediction problems: Transactions of the ASME–Journal of Basic Engineering, **82**, 35–45. 6

Kling, G. W., M. A. Clary, H. R. Compton, J. D. Devine, W. C. Evans, A. M. Humphrey, E. J. Koenigsberg, J. P. Lockwood, M. L. Tuyrle, and G. N. Wagner, 1987, The 1986 Lake Nyos gas disaster in Cameroon, West Africa: Science, **236**, 169–175. 1.3

Knapp, C. H., and G. C. Carter, 1976, The generalized correlation method for estimation of time delay: IEEE Transactions on Acoustics, Speech and Signal Processing, **24**, 320–327. 2.2.2

Koster, K., P. Gabriels, M. Hartung, J. Verbeek, G. Deinum, and R. Staples, 2000, Time-lapse seismic surveys in the North Sea and their business impact: The Leading Edge, 286–293. 1.1

Landrø, M., 2001, Discrimination between pressure and fluid saturation changes from time-lapse seismic data: Geophysics, **66**, 836–844.

Landrø, M., O. A. Solheim, E. Hilde, B. O. Ekren, and L. K. Strønen, 1999, The Gullfaks 4D seismic study: Petroleum Geoscience, **5**, 213–226. 1.1

Lazarotos, S. K., and B. P. Marion, 1997, Crosswell seismic imaging of reservoir changes caused by CO_2 injection: The Leading Edge, **16**, 1300–1306. 3.3

Li, C., and R. Nowack, 2004, Application of autoregressive extrapolation to seismic tomography: Bulletin of the Seismological Society of America, **94**, 1456–1466.

Liu, B., 2004, Multi-dimensional reconstruction of seismic data: PhD thesis, University of Alberta. 2.1.2

Liu, B., and M. D. Sacchi, 2004, Minimum weighted norm interpolation of seismic records: Geophysics, **69**, 1560–1568. 2.1.2, 2.2.1

Lumley, D., 2001, Time-lapse seismic reservoir monitoring: Geophysics, **66**, 50–53. 1.1

MacLeod, M. K., R. A. Hanson, C. R. Bell, and S. McHugo, 1999, The Alba Field ocean bottom cable seismic survey: Impact on development: paper SPE 56977. 1.6

Mathisen, M. E., A. A. Vasiliou, P. Cunningham, J. Shaw, J. H. Justice, and N. J. Guinzy, 1995, Time-lapse crosswell seismic tomogram interpretation: Implications for heavy oil reservoir characterization, thermal recovery process monitoring, and tomographic imaging technology: Geophysics, **60**, 631–650. 1.1

Mavko, G., T. Mukerji, and J. Dvorkin, 1998, The rock physics handbook: Tools for seismic analysis in porous media: Cambridge University Press. 4.2, 4.3

Maxwell, S. C., and T. I. Urbancic, 2001, The role of passive microseismic monitoring in the instrumented oil field: The Leading Edge, **20**, 636–639. 1.1

Menke, W., 1984, Geophysical data analysis: Discrete inverse theory: Academic Press. 2.1

Munns, J. W., 1985, The Valhall Field: A geological overview: Marine and Petroleum Geology, **2**, 23–43. 5.2, 5.1

Myers, S., and C. Schultz, 2000, Improving sparse network seismic location with Bayesian kriging and teleseismically constrained calibration events: Bulletin of the Seismological Society of America, **90**, 199–211. 2.1.1

Naeini, E. Z., H. Hoeber, G. Poole, and H. R. Siahkoohi, 2009, Simultaneous multivintage time-shift estimation: Geophysics, **74**, 109–121. 2.2.2, 2.2.2

Peng, H., and H. Stark, 1989, One-step image reconstruction from incomplete data in computer tomography: IEEE transactions on medical imaging, **8**, 16–31.

Pernice, M., and F. Walker, 1998, NITSOL: A Newton iterative solver for non-linear systems: SIAM Journal on Scientific Computing, **19**, 302–318.

Porsani, M., 1999, Seismic trace inteprolation using half step prediction filters: Geophysics, **64**, 1461–1467.

Quan, Y., and J. M. Harris, 2008, Stochastic seismic inversion using both waveform and traveltime data and its application to time-lapse monitoring: 78th Annual Meeting and International Exposition, SEG, Expanded Abstracts. 1.2

Rickett, J. E., and D. E. Lumley, 2001, Cross-equalization data processing for time-lapse seismic reservoir monitoring: A case study from the Gulf of Mexico: Geophysics, **66**, 1015–1025. 1.1

Rouhani, S., and H. Wackernagel, 1990, Multivariate geostatistical approach to space-time data analysis: Water Resources Research, **26**, 585–591.

Santos, E., and J. M. Harris, 2008, DynaSIRT: A robust dynamic imaging method applied to CO_2 sequestration monitoring: 78th Annual Meeting and International Exposition, SEG, Expanded Abstracts. 1.2

Schultz, C., S. Myers, J. Hipp, and Y. Christopher, 1998, Nonstationary Bayesian kriging: A predictive technique to generate spatial corrections for seismic detection, location and identification: Bulletin of the Seismological Society of America, **88**, 1275–1288. 2.1.1

Schultz, R. R., and R. L. Stevenson, 1996, Extraction of high-resolution frames from video sequences: IEEE Transactions on Image Processing, **5**, 996–1011. 1.2

Sirgue, L., O. I. Barkved, J. Dellinger, J. Etgen, U. Albertin, and J. H. Kommedal, 2010, Thematic set: Full waveform inversion: the next leap forward in imaging at Valhall: First Break, **28**, 65–70. 5.2, 5.2

Soares, A., 2001, Direct sequential simulation and cosimulation: Mathematical Geology, **33**, 911–926.

Spitz, S., 1991, Seismic trace interpolation in the F-X domain: Geophysics, **56**, 785–794. 1.2, 2.1.2, 2.2.1

Stork, C., 1992, Reflection tomography in the postmigrated domain: Geophysics, **66**, 50–53.

Takanami, T., and G. Kitagawa, 1991, Estimation of the arrival times of seismic waves by multivariate time series model: Annals of the Institute of Statistical Mathematics, **43**, 407–433. 2.1.1

Tarantola, A., 1987, Inverse problem theory: Methods for data fitting and model parameter estimation: Elsevier. 2.1

Thomson, D., G. Hennenfent, H. Modzelewski, and F. J. Herrmann, 2006, A parallel windowed fast discrete curvelet transform applied to seismic processing: Presented at the SEG Extended Abstracts, Society of Exploration Geophysicists.

1.2

Tsvankin, I., 1995, Normal moveout from dipping reflectors in anisotropic media: Geophysics, **60**, 268–284. 2.1.1

van Gestel, J. P., J. H. Kommedal, O. I. Barkved, I. Mundal, R. Bakke, and K. D. Best, 2008, Continuous seismic surveillance of Valhall Field: The Leading Edge, **27**, 1616–1621. 1.6, 5.2

Vidale, J., 1990, Finite-difference calculation of traveltimes in three dimensions: Geophysics, **55**, 521–526.

Wang, Y., 2002, Seismic trace interpolation in the f-x-y domain: Geophysics, **67**, 1232–1239. 2.1.2

Wang, Z., and A. Nur, 1988, Effect of temperature on wave velocities in sands and sandstones with heavy hydrocarbons: SPE Reservoir Engineering, **3**, 158–164. 4.3

Wu, C., 2005, Efficient seismic modeling in multi-scale heterogeneous media: PhD thesis, Stanford University. 4.2

Wynn, D., 2003, Survey of geophysical monitoring methods for monitoring CO_2 sequestration in aquifers: Master's thesis, Stanford University. 1.1

Yau, S. F., and Y. H. Chiu, 2000, Iterative method for tomographic reconstruction of time-varying objects: Journal of Electronic Imaging, **9**, 5–15.

Yilmaz, O., 1987, Seismic data processing: Society of Exploration Geophysicists, Tulsa. 1.1, 2.1.1

———, 2001, Seismic data analysis: Processing, inversion, and interpretation of seismic: Society of Exploration Geophysicists, Tulsa. 1.1

Zelt, C. A., and P. J. Barton, 1998, 3D seismic refraction tomography: A comparison of two methods applied to data from the Faeroe Basin: Journal of Geophysical Research, **103**, 7187–7210. 3.2.1, 3.3.1

Zwartjes, P., and A. Gisolf, 2007, Fourier reconstruction with sparse inversion: Geophysical Prospecting, **55**, 199–221. 1.2